

AD-763 489

LATE-TIME SOURCES FOR CLOSE-IN EMP

David A. Sargis, et al

Science Applications, Incorporated

Prepared for:

Defense Nuclear Agency

August 1972

DISTRIBUTED BY:

**NTIS**

National Technical Information Service  
U. S. DEPARTMENT OF COMMERCE  
5285 Port Royal Road, Springfield Va. 22151

AD 763489

**DNA 3064F**

August 1972

SAI-72-556-LJ

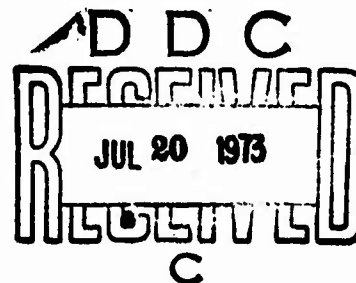
## LATE-TIME SOURCES FOR CLOSE-IN EMP

### FINAL REPORT

3 May 1971 through 2 August 1972

by

D. A. Sargis  
E. R. Parkinson  
J. N. Wood  
R. E. Dietz  
C. A. Stevens



**HEADQUARTERS**  
**Defense Nuclear Agency**  
**Washington, D.C. 20305**

Reproduced by  
**NATIONAL TECHNICAL**  
**INFORMATION SERVICE**

U S Department of Commerce  
Springfield VA 22151

**Contract DASA01-71-C-0155**

**Approved for public release; distribution unlimited.**



SCIENCE APPLICATIONS, LA JOLLA, CALIFORNIA  
ALBUQUERQUE • ANN ARBOR • ARLINGTON • BOSTON • CHICAGO • HUNTSVILLE • LOS ANGELES  
PALO ALTO • ROCKVILLE • SUNNYVALE • TUCSON

P.O. Box 2351, 1250 Prospect Street, La Jolla, California 92037

322

**UNCLASSIFIED**

Security Classification

**DOCUMENT CONTROL DATA - R & D**

(Security classification of title, body of abstract and indexing annotation must be entered when the overall report is classified)

1. ORIGINATING ACTIVITY (Corporate author) <b>Science Applications, Inc. P. O. Box 2351, 1200 Prospect Street LaJolla, California 92037</b>		2a. REPORT SECURITY CLASSIFICATION <b>UNCLASSIFIED</b>	
3. REPORT TITLE <b>Late-Time Sources For Close-In EMP</b>		2b. GROUP	
4. DESCRIPTIVE NOTES (Type of report and inclusive dates) <b>Final Report</b>			
5. AUTHOR(S) (First name, middle initial, last name) <b>David A. Sargis, Ernest R. Parkinson, John N. Wood, Ronald E. Dietz, Charles A. Stevens</b>			
6. REPORT DATE <b>August 1972</b>	7a. TOTAL NO. OF PAGES <b>325 323</b>	7b. NO. OF REFS <b>13</b>	
8a. CONTRACT OR GRANT NO. <b>DAS01-71-C-0155</b>	9a. ORIGINATOR'S REPORT NUMBER(S) <b>SAI-72-556-LJ</b>		
b. PROJECT NO. <b>NWED Subtask Code EA094</b>	9b. OTHER REPORT NO(S) (Any other numbers that may be assigned this report) <b>DNA 3064F</b>		
c. Work Unit Code 03			
d.			
10. DISTRIBUTION STATEMENT <b>Approved for public release; distribution unlimited.</b>			
11. SUPPLEMENTARY NOTES		12. SPONSORING MILITARY ACTIVITY <b>Director Defense Nuclear Agency Washington, D. C. 20305</b>	
13. ABSTRACT <p>This report describes calculations of ionization rates and electric currents in air and ground resulting from neutron sources. In particular, this report describes the numerical methods, nuclear data, and computer programs employed and presents results for a typical thermonuclear neutron spectrum. A discussion of fitting of earlier electromagnetic pulse (EMP) source calculations is also presented.</p> <p>The latest ENDF/B neutron transport and gamma ray production data for air and ground are used and sensitivity of EMP calculations to cross section changes have been estimated. A new source energy band version of the Monte Carlo code 05RNIES has been developed which makes it possible to compute EMP sources by folding in various desired neutron spectra. New analytical approaches have also been introduced to accurately treat neutron capture events in air to times as late as one second. Analytical gamma-ray transport calculations away from the air-ground interface are also used. Various neutron and gamma-ray contributions to ionization rates and electric currents have been tabulated as functions of fast and thermal reactions to assist in fitting of these quantities.</p> <p>Calculations are presented for three heights of burst, 0 meters, 200 meters, and 500 meters. The early time mesh, below 0.1 <math>\mu</math>sec, is more detailed for the HoB = 0 m calculation than in previous calculations.</p>			

**DD FORM 1473**  
1 NOV 650  
1**UNCLASSIFIED**  
Security Classification

**UNCLASSIFIED**

Security Classification

14 KEY WORDS	LINK A		LINK B		LINK C	
	ROLE	WT	ROLE	WT	ROLE	WT
NEUTRON TRANSPORT (AIR-OVER-GROUND) MONTE CARLO ELECTROMAGNETIC PULSE (EMP) IONIZATION RATES ELECTRON CURRENTS						

..  
//

**UNCLASSIFIED**

Security Classification



## ABSTRACT

This report describes calculations of ionization rates and electric currents in air and ground resulting from neutron sources. In particular, this report describes the numerical methods, nuclear data, and computer programs employed and presents results for a typical thermonuclear neutron spectrum. A discussion of fitting of earlier electromagnetic pulse (EMP) source calculations is also presented.

The latest ENDF/B neutron transport and gamma ray production data for air and ground are used and sensitivity of EMP calculations to cross section changes have been estimated. A new source energy band version of the Monte Carlo code 05RNIES has been developed which makes it possible to compute EMP sources by folding in various desired neutron spectra. New analytical approaches have also been introduced to accurately treat neutron capture events in air to times as late as one second. Analytical gamma-ray transport calculations away from the air-ground interface are also used. Various neutron and gamma-ray contributions to ionization rates and electric currents have been tabulated as functions of fast and thermal reactions to assist in fitting of these quantities.

Calculations are presented for three heights of burst, 0 meters, 200 meters, and 500 meters. The early time mesh, below  $0.1 \mu\text{sec}$ , is more detailed for the  $H_oB = 0$  m calculation than in previous calculations.

## CONTENTS

Section	Page
ABSTRACT . . . . .	iii
LIST OF ILLUSTRATIONS . . . . .	v
LIST OF TABLES . . . . .	xviii
1. INTRODUCTION . . . . .	1
2. DISCUSSION AND RESULTS FOR A TYPICAL THERMONUCLEAR NEUTRON SPECTRUM . . . . .	3
3. CURVE FIT REPRESENTATION OF TRANSPORT RESULTS . . . . .	105
3.1 General Remarks . . . . .	105
3.2 The Transport Data . . . . .	107
3.3 The Fitting Procedure . . . . .	108
3.4 The Time Domain Fits . . . . .	108
3.5 The Interpolation Procedure . . . . .	110
3.6 The Curve Fitting Code NF . . . . .	138
3.7 The Neutron Induced Source Subroutine NSOURCE . . . . .	139
4. THE O5RNIES PROGRAM . . . . .	155
4.1 General Remarks . . . . .	155
4.2 Source Energy Band Version . . . . .	156
4.3 Late-Time EMP Drivers . . . . .	161
4.4 Biasing Techniques . . . . .	184
4.5 Nuclear Cross Sections . . . . .	187
4.6 Instructions for Using O5RNIES . . . . .	202
REFERENCES . . . . .	304

## ILLUSTRATIONS

Figure	Page
2.1. Radial dependence of ionization due to thermo-nuclear source on ground, $\cos \theta = 0 - 0.05$ . . . . .	10
2.2. Radial dependence of ionization due to thermo-nuclear source for HoB = 200 m, altitude = 0 - 50 meters. . . . .	12
2.3. Radial dependence of ionization due to thermo-nuclear source for HoB = 500 m, altitude = 0 - 50 meters. . . . .	13
2.4. Radial dependence of ionization due to thermo-nuclear source for HoB = 0 and HoB = 200 m, $\cos \theta = 0.5 - 1.0$ . . . . .	14
2.5. Geometrical explanation for polar angle dependence. . . . .	16
2.6. Polar angle variation of total ionization at radius 450 - 550 meters, due to thermonuclear source on ground. . . . .	17
2.7. Polar angle variation of neutron ionization at radius 450 - 550 meters, due to thermonuclear source on ground. . . . .	18
2.8. Polar angle variation of gamma ray ionization at radius 450 - 550 meters, due to thermonuclear source on ground. . . . .	19
2.9. Polar angle variation of total ionization at radius 450 - 550 meters, due to thermonuclear source for 200 m HoB. . . . .	21

Figure	Page
2.10. Polar angle variation of neutron ionization at radius 450 - 550 meters, due to thermonuclear source for 200 m HoB. . . . .	22
2.11. Polar angle variation of gamma ray ionization at radius 450 - 550 meters, due to thermonuclear source for 200 m HoB. . . . .	23
2.12. Ionization vs. depth at radius 450 - 550 meters, due to thermonuclear source for HoB = 0, HoB = 200, and HoB = 500 meters. . . . .	24
2.13. Ionization rate for thermonuclear source at radius = 450 - 550 meters, for HoB = 0 m, $\cos \theta = 0 - 0.05$ , and at HoB = 200 m, elevation = 0 - 50 m. . . . .	26
2.14. Ionization rate at radius 450 - 550 meters, elevation = 0 - 50 m, for thermonuclear source at HoB = 200 and HoB = 500 m. . . . .	27
2.15. Total ionization rate at radius 450 - 550 meters, $\cos \theta = 0.5 - 1.0$ , due to thermonuclear source at HoB = 0 meters. . . . .	29
2.16. Ionization rate due to neutrons at radius 450 - 550 meters, $\cos \theta = 0.5 - 1.0$ , due to thermonuclear source at HoB = 0 meters. . . . .	30
2.17. Ionization rate due to gamma rays at radius 450 - 550 meters, $\cos \theta = 0.5 - 1.0$ , due to thermonuclear source at HoB = 0 meters. . . . .	31
2.18. Total ionization rate at radius 450 - 550 meters, $\cos \theta = 0.5 - 1.0$ , due to thermonuclear source at HoB = 500 meters. . . . .	32
2.19. Ionization rate due to neutrons at radius 450 - 550 meters, $\cos \theta = 0.5 - 1.0$ , due to thermonuclear source at HoB = 500 meters. . . . .	33

Figure	Page
2.20. Ionization rate due to gamma rays at radius 450 - 550 meters, $\cos \theta = 0.5 - 1.0$ , due to thermonuclear source at HoB = 500 meters. . . . .	34
2.21. Radial current at radius 450 - 550 meters, $\cos \theta = 0 - 0.05$ , due to thermonuclear source on ground. . . . .	36
2.22. Theta current at radius 450 - 550 meters, $\cos \theta = 0 - 0.05$ , due to thermonuclear source on ground. . . . .	37
2.23. Radial current at radius 450 - 550 meters, $\cos \theta = 0 - 0.1$ , due to thermonuclear source for HoB = 200 meters. . . . .	39
2.24. Radial current at radius 450 - 550 meters, $\cos \theta = 0 - 0.1$ , due to thermonuclear source for HoB = 500 meters. . . . .	40
2.25. Ionization rate at radius 450 - 550 meters, $\cos \theta = 0.5 - 1.0$ , due to thermonuclear source at HoB = 0 and HoB = 200 meters. . . . .	42
2.26. Ionization rate in ground, depth = 0 - 2 cm, radius = 450 - 550 meters, due to thermonuclear source at HoB = 0 and HoB = 200 meters. . . . .	43
2.27. Ionization rate in ground, depth = 0 - 2 cm, radius = 450 - 550 meters, due to thermonuclear source at HoB = 200 and HoB = 500 meters. . . . .	44
2.28. Ionization rate in ground, depth = 90 - 120 cm, radius = 450 - 550 meters, due to thermonuclear source at HoB = 0 and HoB = 200 meters. . . . .	46
2.29. Ionization rate in ground, depth = 90 - 120 cm, radius = 450 - 550 meters, due to thermonuclear source at HoB = 200 and HoB = 500 meters. . . . .	47

Figure	Page
2.30. Geometrical explanation for the effect of source altitude on ground ionization rates. . . . .	49
2.31. Comparison of new and old ionization rate calculations at radius = 550 - 650 meters, elevation = 0 - 50 meters due to thermonuclear source at HoB = 200 m. . . . .	51
2.32. Comparison of new and old vertical current densities at radius = 550 - 650 meters, elevation = 0 - 50 meters due to a thermonuclear source at HoB = 200 m. . . . .	52
2.33. Ionization rate at radius = 850 - 1050 meters, $\cos \theta = 0.0 - 0.05$ , due to thermonuclear source on ground. . . . .	54
2.34. Radial current density vs. time at radius 850 - 1050 m, $\cos \theta = 0.0 - 0.05$ , due to thermonuclear source on ground. . . . .	55
2.35. Theta current density vs. time at radius = 850 - 1050 m, $\cos \theta = 0.0 - 0.05$ , due to thermonuclear source on ground. . . . .	56
2.36. Ionization rate vs. time at radius = 1900 - 2100 m, $\cos \theta = 0.0 - 0.05$ , due to thermonuclear source on ground. . . . .	57
2.37. Radial current density vs. time at radius = 1900 - 2100 m, $\cos \theta = 0.0 - 0.05$ , due to thermonuclear source on ground. . . . .	58
2.38. Theta current density vs. time at radius = 1900 - 2100 m, $\cos \theta = 0.0 - 0.05$ , due to thermonuclear source on ground. . . . .	59
2.39. Ionization rate vs. time at radius = 1900 - 2100 m, $\cos \theta = 0.5 - 1.0$ , due to thermonuclear source on ground. . . . .	60

Figure	Page
2.40. Radial current density vs. time at radius = 1900 - 2100 m, $\cos \theta = 0.5 - 1.0$ , due to thermonuclear source on ground. . . . .	61
2.41. Ionization rate vs. time at radius = 2700 - 3100 m, $\cos \theta = 0.0 - 0.05$ , due to thermonuclear source on ground. . . . .	62
2.42. Radial current density vs. time at radius = 2700 - 3100 m, $\cos \theta = 0.0 - 0.05$ , due to thermonuclear source on ground. . . . .	63
2.43. Theta current density vs. time at radius = 2700 - 3100 m, $\cos \theta = 0.0 - 0.05$ , due to thermonuclear source on ground. . . . .	64
2.44. Ionization rate vs. time at radius = 2700 - 3100 m, $\cos \theta = 0.5 - 1.0$ , due to thermonuclear source on ground. . . . .	65
2.45. Radial current density vs. time at radius = 2700 - 3100 m, $\cos \theta = 0.5 - 1.0$ , due to thermonuclear source on ground. . . . .	66
2.46. Ionization rate vs. time at radius = 4000 - 5000 m, $\cos \theta = 0.0 - 0.05$ , due to thermonuclear source on ground. . . . .	67
2.47. Radial current density vs. time at radius = 4000 - 5000 m, $\cos \theta = 0.0 - 0.05$ , due to thermonuclear source on ground. . . . .	68
2.48. Ionization rate vs. time at radius = 4000 - 5000 m, $\cos \theta = 0.5 - 1.0$ , due to thermonuclear source on ground. . . . .	69
2.49. Radial current density vs. time at radius = 4000 - 5000 m, $\cos \theta = 0.5 - 1.0$ , due to thermonuclear source on ground. . . . .	70

Figure	Page
2.50. Ionization rate vs. time at radius = 850 - 1050 m, elevation = 0 - 50 m, due to thermonuclear source at HoB = 200 m. . . . .	71
2.51. Vertical current density vs. time at radius = 850 - 1050 m, elevation = 0 - 50 m, due to thermonuclear source at HoB = 200 m. . . . .	72
2.52. Horizontal current density vs. time at radius = 850 - 1050 m, elevation = 0 - 50 m, due to thermonuclear source at HoB = 200 m. . . . .	73
2.53. Ionization rate vs. time at radius = 850 - 1050 m, $\cos \theta = 0.5 - 1.0$ , due to thermonuclear source at HoB = 200 m. . . . .	74
2.54. Radial current density vs. time at radius = 850 - 1050 m, $\cos \theta = 0.5 - 1.0$ , due to thermonuclear source at HoB = 200 m. . . . .	75
2.55. Ionization rate vs. time at radius = 1900 - 2100 m, elevation = 0 - 50 m, due to thermonuclear source at HoB = 200 m. . . . .	76
2.56. Vertical current density vs. time at radius = 1900 - 2100 m, elevation = 0 - 50 m, due to thermonuclear source at HoB = 200 m. . . . .	77
2.57. Horizontal current density vs. time at radius = 1900 - 2100 m, elevation = 0 - 50 m, due to thermonuclear source at HoB = 200 m. . . . .	78
2.58. Ionization rate vs. time at radius = 1900 - 2100 m, $\cos \theta = 0.5 - 1.0$ , due to thermonuclear source at HoB = 200 m. . . . .	79
2.59. Radial current density vs. time at radius = 1900 - 2100 m, $\cos \theta = 0.5 - 1.0$ , due to thermonuclear source at HoB = 200 m. . . . .	80



Figure	Page
2.60. Ionization rate vs. time at radius = 2700 - 3100 m, elevation 0-50 m, due to thermonuclear source at HoB = 200 m. . . . .	81
2.61. Horizontal current density vs. time at radius = 2700 - 3100 m, elevation = 0 - 50 m, due to thermonuclear source at HoB = 200 m. . . . .	82
2.62. Ionization rate vs. time at radius = 2700 - 3100 m, $\cos \theta = 0.5 - 1.0$ , due to thermonuclear source at HoB = 200 m. . . . .	83
2.63. Radial current density vs. time at radius = 2700 - 3100, $\cos \theta = 0.5 - 1.0$ , due to thermonuclear source at HoB = 200 m. . . . .	84
2.64. Ionization rate vs. time at radius = 4000 - 5000 m, $\cos \theta = 0.5 - 1.0$ , due to thermonuclear source at HoB = 200 m. . . . .	85
2.65. Ionization rate vs. time at radius = 4000 - 5000 m, elevation = 0 - 50 m, due to thermonuclear source at HoB = 200 m. . . . .	86
2.66. Ionization rate vs. time at radius = 850 - 1050 m, elevation = 0 - 50 m, due to thermonuclear source at HoB = 500 m. . . . .	87
2.67. Vertical current density vs. time at radius = 850 - 1050 m, elevation = 0 - 50 m, due to thermonuclear source at HoB = 500 m. . . . .	88
2.68. Horizontal current density vs. time at radius = 850 - 1050 m, elevation = 0 - 50 m, due to thermonuclear source at HoB = 500 m. . . . .	89
2.69. Ionization rate vs. time at radius = 850 - 1050 m, $\cos \theta = 0.5 - 1.0$ , due to thermonuclear source at HoB = 500 m. . . . .	90

Figure		Page
2.70.	Radial current density vs. time at radius = 850 - 1050 m, $\cos \theta = 0.5 - 1.0$ , due to thermo- nuclear source at HoB = 500 m. . . . .	91
2.71.	Ionization rate vs. time at radius = 1900 - 2100 m, elevation = 0 - 50 m, due to thermo- nuclear source at HoB = 500 m. . . . .	92
2.72.	Vertical current density vs. time at radius = 1900 - 2100 m, elevation = 0 - 50 m, due to thermonuclear source at HoB = 500 m. . . . .	93
2.73.	Horizontal current density vs. time at radius = 1900 - 2100 m, elevation = 0 - 50 m, due to thermonuclear source at HoB = 500 m. . . . .	94
2.74.	Ionization rate vs. time at radius = 1900 - 2100 m, $\cos \theta = 0.5 - 1.0$ , due to thermonuclear source at HoB = 500 m. . . . .	95
2.75.	Radial current density vs. time at radius = 1900 - 2100 m, $\cos \theta = 0.5 - 1.0$ , due to thermo- nuclear source at HoB = 500 m. . . . .	96
2.76.	Ionization rate vs. time at radius = 2700 - 3100 m, elevation 0 - 50 m, due to thermonuclear source at HoB = 500 m. . . . .	97
2.77.	Vertical current density vs. time at radius 2700 - 3100 m, elevation = 0 - 50 m, due to thermonuclear source at HoB = 500 m. . . . .	98
2.78.	Horizontal current density vs. time at radius = 2700 - 3100 m, elevation = 0 - 50 m, due to thermo- nuclear source at HoB = 500 m. . . . .	99
2.79.	Ionization rate vs. time at radius = 2700 - 3100 m, $\cos \theta = 0.5 - 1.0$ , due to thermonuclear source at HoB = 500 m. . . . .	100

Figure	Page
2.80. Radial current density vs. time at radius = 2700 - 3100 m, $\cos \theta = 0.5 - 1.0$ , due to thermo- nuclear source at HoB = 500 m. . . . .	101
2.81. Ionization rate vs. time at radius = 4000 - 5000 m, $\cos \theta = 0.5 - 1.0$ , due to thermo- nuclear source at HoB = 500 m. . . . .	102
2.82. Ionization rate vs. time at radius = 4000 - 5000 m, elevation = 0 - 50 m, due to thermo- nuclear source at HoB = 500 m. . . . .	103
3.1. Curve fits for dose rates for typical thermo- nuclear source on ground, range = 200 meters, $\cos \theta = 0.05$ . . . . .	112
3.2. Curve fits for radial current densities for typical thermonuclear source on ground, range = 200 meters, $\cos \theta = 0.05$ . . . . .	113
3.3. Curve fits for theta current densities for typical thermonuclear source on ground, range = 200 meters, $\cos \theta = 0.05$ . . . . .	114
3.4. Curve fits for dose rates for typical thermo- nuclear source on ground, range = 500 meters, $\cos \theta = 0.05$ . . . . .	115
3.5. Curve fits for radial current densities for typical thermonuclear source on ground, range = 500 meters, $\cos \theta = 0.05$ . . . . .	116
3.6. Curve fits for theta current densities for typical thermonuclear source on ground, range = 500 meters, $\cos \theta = 0.05$ . . . . .	117
3.7. Curve fits for dose rates for typical thermo- nuclear source on ground, range = 1000 meters, $\cos \theta = 0.05$ . . . . .	118
3.8. Curve fits for radial current densities for typical thermonuclear source on ground, range = 1000 meters, $\cos \theta = 0.05$ . . . . .	119

Figure	Page
3.9. Curve fits for theta current densities for typical thermonuclear source on ground, range = 1000 meters, $\cos \theta = 0.05$ . . . . .	120
3.10. Curve fits for dose rates for typical thermonuclear source on ground, range = 2000 meters, $\cos \theta = 0.05$ . . . . .	121
3.11. Curve fits for radial current densities for typical thermonuclear source on ground, range = 2000 meters, $\cos \theta = 0.05$ . . . . .	122
3.12. Curve fits for dose rates for typical thermonuclear source on ground, range = 3000 meters, $\cos \theta = 0.05$ . . . . .	123
3.13. Curve fits for radial current densities for typical thermonuclear source on ground, range = 3000 meters, $\cos \theta = 0.05$ . . . . .	124
3.14. Curve fits for dose rates for typical thermonuclear source on ground, range = 200 meters, $\cos \theta = 0.30$ . . . . .	125
3.15. Curve fits for radial current densities for typical thermonuclear source on ground, range = 200 meters, $\cos \theta = 0.30$ . . . . .	126
3.16. Curve fits for theta current densities for typical thermonuclear source on ground, range = 200 meters, $\cos \theta = 0.30$ . . . . .	127
3.17. Curve fits for dose rates for typical thermonuclear source on ground, range = 500 meters, $\cos \theta = 0.30$ . . . . .	128
3.18. Curve fits for radial current densities for typical thermonuclear source on ground, range = 500 meters, $\cos \theta = 0.30$ . . . . .	129
3.19. Curve fits for theta current densities for typical thermonuclear source on ground, range = 500 meters, $\cos \theta = 0.30$ . . . . .	130

Figure	Page
3.20. Curve fits for dose rates for typical thermo-nuclear source on ground, range = 1000 meters, $\cos \theta = 0.30$ . . . . .	131
3.21. Curve fits for radial current densities for typical thermonuclear source on ground, range = 1000 meters, $\cos \theta = 0.30$ . . . . .	132
3.22. Curve fits for theta current densities for typical thermonuclear source on ground, range = 1000 meters, $\cos \theta = 0.30$ . . . . .	133
3.23. Curve fits for dose rates for typical thermo-nuclear source on ground, range = 2000 meters, $\cos \theta = 0.30$ . . . . .	134
3.24. Curve fits for radial current densities for typical thermonuclear source on ground, range = 2000 meters, $\cos \theta = 0.30$ . . . . .	135
3.25. Curve fits for dose rates for typical thermo-nuclear source on ground, range = 3000 meters, $\cos \theta = 0.30$ . . . . .	136
3.26. Curve fits for radial current densities for typical thermonuclear source on ground, range = 3000 meters, $\cos \theta = 0.30$ . . . . .	137
4.1. Comparison of the typical thermonuclear spectrum in the original 17-group structure and in the new 13-band version. . . . .	159
4.2. Comparison of neutron ionization rate calculations using ENDF/B and older data at 480 meters. . . . .	196
4.3. Comparison of gamma ray ionization rate calculations using ENDF/B and older data at 480 meters. . .	197
4.4. Comparison of total ionization rate calculations using ENDF/B and older data at 480 meters. . . . .	198

Figure		Page
4.5.	Comparison of radial Compton current calculations using ENDF/B and older data at 480 meters. . . . .	199
4.6.	Typical O5RNIES output. . . . .	225
4.7.	Block diagram of history-generating subroutines in O5RNIES. . . . .	231
4.8.	Analysis routines in O5RNIES. . . . .	232
4.9.	Flowchart for subroutine BANKR. . . . .	236
4.10.	Flowchart for subroutine CHARGE. . . . .	238
4.11.	Flowchart for subroutine DEP. . . . .	240
4.12.	Flowchart for subroutine DOSEN. . . . .	242
4.13.	Flowchart for subroutine GATR. . . . .	244
4.14.	Flowchart for subroutine INELIN. . . . .	246
4.15.	Flowchart for subroutine KINNY. . . . .	248
4.16.	Flowchart for subroutine NIES. . . . .	250
4.17.	Flowchart for subroutine RAGE. . . . .	252
4.18.	Flowchart for subroutine RDIFF. . . . .	254
4.19.	Flowchart for subroutine ROUTIN. . . . .	256
4.20.	Flowchart for subroutine SEARCH. . . . .	258
4.21.	Flowchart for subroutine SOURCE. . . . .	260
4.22.	Flowchart for subroutine SSTART. . . . .	262
4.23.	Flowchart for subroutine TAUM. . . . .	264
4.24.	Flowchart for subroutine UPDATE. . . . .	266

Figure	Page
4.25. Flowchart for subroutine XINIT. . . . .	268
4.26. Subroutines called by O5NPT. . . . .	288
4.27. Flowchart for the O5NPT program. . . . .	290
4.28. Flowchart for the O5NPT program. . . . .	291
4.29. Flowchart for subroutine PLOTTER. . . . .	294
4.30. Flowchart for the subroutine SUMOBD. . . . .	296

## TABLES

	Page
1. Energy Distribution for Thermonuclear Source . . . . .	4
2. Bin Structures for Zero Meter HoB Transport Problems . . . . .	7
3. Bin Structures for 200 Meter HoB Transport Problems . . . . .	8
4. Bin Structures for 500 meter HoB Transport Problems . . . . .	9
5. Bin Structures for Transport Problems . . . . .	106
6. Comparison of the Typical Thermonuclear Neutron Source Spectrum in the Original 17-Group Structure and in the New 13-Band Source Version . . . . .	158
7. Typical Input for an O5RNIES Production Run . . . . .	215
8. KCOUNT Array . . . . .	226
9. ZCOUNT Array . . . . .	228



## 1. INTRODUCTION

Calculations are presented of electromagnetic pulse (EMP) sources for a typical thermonuclear neutron source spectrum. The ionization rates and Compton currents resulting from the neutron source are required for the prediction of free field EMP environments. The calculations are performed for a point source of neutrons in an air-over-ground configuration. Three low level heights of burst are considered; 0, 200, and 500 meters. A time-dependent tabulation of ionization rates and Compton currents is made in two dimensions in both air and ground.

New analytical methods have been developed to take into consideration the very late-time neutron capture reactions in air. These events, which can introduce sources at times as late as one second, have been included in our calculations for the first time. A description of the new version of the Monte Carlo code O5RNIES, which incorporates these air capture reactions, is included in a later section. A new energy band treatment enables the user to efficiently fold in an arbitrary neutron spectrum once the initial production runs are completed.

The calculations presented here are similar to previous results.<sup>(1-3)</sup> A complete treatment of neutron transport in both air and ground is included. The inclusion of late-time air capture reactions represents a significant improvement over earlier treatments which neglected these events. Thermal neutrons are also followed back and forth from ground to air in the new calculations, as opposed to previous results which approximated the air by vacuum. Comparisons made between the new late-time program and the previous version of O5RNIES indicate that the new version yields substantially higher ionization rates than the conventional program in the time interval between 1 millisecond and 1 second. In this

time span air capture events, which are neglected in the earlier version of O5RNIES, become important and enhance the late-time ionization rates as computed in the new code. Furthermore, ionization rates and currents in the ground, but very close to the air-ground interface, also appear to be enhanced relative to the conventional treatment. This is due in part to the fact that the conventional version of the code does not allow thermal neutrons escaping from the ground into the air to return to the ground, whereas the late-time models follow the neutrons from one medium into another.

Another important change has been made in the O5RNIES code. Previously, only the total ionization rate and Compton current were edited as output. In the new version, contributions are separated according to their origin. Thus, for current rate we tabulate, in addition to the total, the separate contributions from thermal neutron capture gamma rays and from fast neutron capture and inelastic gamma rays. For ionization rate, the contribution from neutron collisions is also tabulated separately as fast and thermal neutron induced ionization. These separate contributions will give greater understanding of which reaction types are most important at different times. This additional knowledge is most useful when selecting biasing techniques and will make it much easier to fit the results because the behavior of the separate components is easier to describe with simple functions than is the sum of the components.

The results presented here incorporate the latest ENDF/B neutron transport and gamma ray production cross sections for air and ground. Sensitivity of EMP calculations to changes in cross sections has also been estimated.

The calculations are carried out to local times of one second and to ranges of five kilometers. However, the time-dependent data at ranges beyond about three kilometers are somewhat erratic with large statistical uncertainties.

## 2. DISCUSSION AND RESULTS FOR A TYPICAL THERMONUCLEAR NEUTRON SPECTRUM

EMP source calculations are presented in this section for three low altitude nuclear explosions. The three heights of burst (HoB's) selected were at 0, 200, and 500 meter altitudes. The neutron source spectrum chosen for these calculations was a typical thermonuclear spectrum which has been used in other transport calculations.<sup>(4)</sup> The typical thermonuclear spectrum is shown in Table 1 in a seventeen group structure. The actual calculations were performed using thirteen energy bands as will be discussed in Section 4.2.

We have produced a total of more than 5,000 ionization rate and current plots on microfilm for the thermonuclear source. It is apparent that we can only present a very small fraction of these results in this report. However, we do present a representative sampling of these data and have stored the complete plotted and tabulated results on microfilm and tape where they may be processed for use in EMP field codes. Furthermore, the basic production runs are available on tape for each height of burst so that other neutron spectra may easily be folded in to obtain various desired EMP drivers.

Ionization rates and Compton currents were obtained in air and ground and extend to ranges of 5 kilometers in air. Biasing in the form of path length stretching of neutrons and gammas is mandatory to obtain results at these distances with reasonable amounts of computer time.

Table 1

ENERGY DISTRIBUTION FOR  
THERMONUCLEAR SOURCE

<u>Energy (MeV)</u>	<u>Number Fraction in Group</u>
12.2 - 15.0	7.06(-2) <sup>a</sup>
10.0 - 12.2	2.56(-2)
8.19 - 10.0	1.41(-2)
6.36 - 8.19	1.47(-2)
4.97 - 6.36	1.80(-2)
4.07 - 4.97	1.70(-2)
3.01 - 4.07	2.60(-2)
2.46 - 3.01	1.90(-2)
2.35 - 2.46	5.00(-3)
1.83 - 2.35	2.80(-2)
1.11 - 1.83	6.20(-2)
0.55 - 1.11	8.50(-2)
0.11 - 0.55	1.02(-1)
3.35(-3) - 0.110	3.65(-1)
5.83(-4) - 3.35(-3)	1.22(-1)
1.01(-4) - 5.83(-4)	2.40(-2)
2.90(-5) - 1.01(-4)	2.00(-3)
<2.90(-5)	0

---

<sup>a</sup>Read as  $7.06 \times 10^{-2}$

Even with biasing, the spatial results beyond 3 kilometers in air, and also at great depths in the ground, become sporadic. However, it is felt that most of the spatial positions of interest in EMP studies have been obtained with reasonable statistical accuracy.

The calculations described here were acquired with a new late-time version of the Monte Carlo code O5RNIES, which is discussed in detail in Section 4. The latest ENDF/B neutron and gamma ray production data were used and the sensitivity of calculations to cross section changes is considered in Section 4.5. The accurate treatment of very late-time air capture reactions represents a significant improvement in the calculational models used in generating EMP sources. The new late-time results are generally higher than previous results in air in the time range from 1 millisecond to 1 second, where air capture events become important. The accurate tracking of thermal neutrons back and forth from ground to air in the new code also generally results in larger EMP sources at positions in the ground but near the air-ground interface.

The O5RNIES code tabulates results in spherical coordinates above the source, and in cylindrical coordinates below it. This coordinate system is selected for consistency with the EMP field codes which use the O5RNIES results as input.

In each of the three HoB calculations discussed here, a total of 195,000 neutron histories were followed. These neutrons, through various inelastic scattering, capture, charged particle, and other reactions, produce gamma rays which are also followed. For each HoB, production runs were performed with unit neutron sources in each of thirteen energy bands. The desired neutron source spectra were then folded in using the auxiliary folding and plotting code O5NPT. The production runs required approximately 22 hours, 17 hours, and 15 hours

of computer time on the CDC 6600 for the HoB = 0 m, HoB = 200 m, and HoB = 500 m runs, respectively. The higher altitude bursts are performed more rapidly since the new faster analytic routines in O5RNIES can be employed more frequently at the higher elevations. The auxiliary folding code O5NPT required approximately 30 minutes of CDC 6600 time to fold in an arbitrary neutron spectrum for each HoB.

The bin structures used for scoring for the three heights of burst are indicated in Tables 2 - 4. The results are obtained to distances of 5 kilometers and to times of 1 second. For the HoB = 0 m calculations, there are  $39 \times 19 \times 14 = 10,374$  individual scoring bins. Similarly, for the HoB = 200 m and HoB = 500 m problems we score time dependent quantities in 9120 and 9690 bins, respectively. It is apparent that with the large number of bins in each problem, good statistical results could not be obtained at each position. However, it is felt that all of the important spatial positions are adequately represented in the results described here.

Time integrated ionization data are considered in the first twelve figures. Following these, time dependent ionization rate and Compton current calculations are presented. All of the figures are normalized to one source neutron. In some of the figures, contributions due to thermal and fast neutron reactions are separately plotted. Because of space limitations, the statistical error bars which depict standard deviations from the mean values are only shown for the total quantities. The separation into fast and thermal components was made to assist in fitting of these data and to further understanding of the importance of various reaction mechanisms in different time regimes.

In Fig. 2.1 the ionization vs. radius is shown for an angular bin having polar angle limits of  $\cos \theta = 0.0$  to  $\cos \theta = 0.05$  for a source on

Table 2

## BIN STRUCTURES FOR ZERO METER HOB TRANSPORT PROBLEMS

Radial Intervals (meters)	Depth Intervals (cm)	Polar Angle Intervals (cos $\theta$ )	Local Time Intervals ( $\mu$ sec)	Height Intervals (meters)
0 - 150	0 - 2	0 - 0.05	0	0.015
150 - 250	2 - 6	0.05 - 0.1	0.015 -	0.02
250 - 350	6 - 14	0.1 - 0.2	0.02 -	0.03
350 - 450	14 - 30	0.2 - 0.5	0.03 -	0.04
450 - 550	30 - 50	0.5 - 1.0	0.04 -	0.06
550 - 650	50 - 90		0.06 -	0.08
650 - 850	90 - 120		0.08 -	0.10
850 - 1050	120 - 180		0.10 -	0.14
1050 - 1300	180 - 250		0.14 -	0.2
1300 - 1500			0.2 -	0.3
1500 - 1700			0.3 -	0.4
1700 - 1900			0.4 -	0.6
1900 - 2100			0.6 -	0.8
2100 - 2300			0.8 -	1
2300 - 2700			1 -	2
2700 - 3100			2 -	3
3100 - 3500			3 -	4
3500 - 4000			4 -	5
4000 - 5000			5 -	7.5
			7.5 -	10
			10 -	20
			20 -	30
			30 -	50
			50 -	75
			75 -	100
			100 -	200
			200 -	300
			300 -	500
			500 -	1,000
			1,000 -	1,500
			1,500 -	3,000
			3,000 -	6,000
			6,000 -	10,000
			10,000 -	30,000
			30,000 -	60,000
			60,000 -	100,000
			100,000 -	300,000
			300,000 -	600,000
			600,000 -	1,000,000

Table 3

## BIN STRUCTURES FOR 200 METER HOB TRANSPORT PROBLEMS

Radial Intervals (meters)	Depth Intervals (cm)	Polar Angle Intervals ( $\cos \theta$ )	Local Time Intervals ( $\mu\text{sec}$ )	Height Intervals (meters)
0 - 150	0 - 2	0 - 0.1	0 -	0 - 50
150 - 250	2 - 6	0.1 - 0.2	0.2 -	50 - 100
250 - 350	6 - 14	0.2 - 0.5	0.4 -	100 - 200
350 - 450	14 - 30	0.5 - 1.0	0.6 -	
450 - 550	30 - 50		0.8 -	
550 - 650	50 - 90		1 -	
650 - 850	90 - 120		2 -	
850 - 1050	120 - 180		3 -	
1050 - 1300	180 - 250		4 -	
1300 - 1500			5 -	
1500 - 1700			7.5 -	
1700 - 1900			10 -	
1900 - 2100			20 -	
2100 - 2300			30 -	
2300 - 2700			50 -	
2700 - 3100			75 -	
3100 - 3500			100 -	
3500 - 4000			200 -	
4000 - 5000			300 -	
			500 -	
			1,000 -	
			1,500 -	
			3,000 -	
			6,000 -	
			10,000 -	
			30,000 -	
			60,000 -	
			100,000 -	
			300,000 -	
			600,000 -	
			1,000,000 -	



Table 4

## BIN STRUCTURES FOR 500 METER HOB TRANSPORT PROBLEMS

Radial Intervals (meters)	Depth Intervals (cm)	Polar Angle Intervals (cos $\theta$ )	Local Time Intervals ( $\mu$ sec)	Height Intervals (meters) (Applicable only to HoB = 200 meter problem)
0 - 150	0 - 2	0 - 0.1	0 -	0 - 50
150 - 250	2 - 6	0.1 - 0.2	0.2 -	50 - 100
250 - 350	6 - 14	0.2 - 0.5	0.4 -	100 - 300
350 - 450	14 - 30	0.5 - 1.0	0.6 -	300 - 500
450 - 550	30 - 50		0.8 -	
550 - 650	50 - 90		1 -	
650 - 850	90 - 120		2 -	
850 - 1050	120 - 180		3 -	
1050 - 1300	180 - 250		4 -	
1300 - 1500			5 -	
1500 - 1700			7.5 -	
1700 - 1900			10 -	
1900 - 2100			20 -	
2100 - 2300			30 -	
2300 - 2700			50 -	
2700 - 3100			75 -	
3100 - 3500			100 -	
3500 - 4000			200 -	
4000 - 5000			300 -	
			500 -	
			1,000 -	
			1,500 -	
			3,000 -	
			6,000 -	
			10,000 -	
			30,000 -	
			60,000 -	
			100,000 -	
			300,000 -	
			600,000 -	
			1,000,000 -	

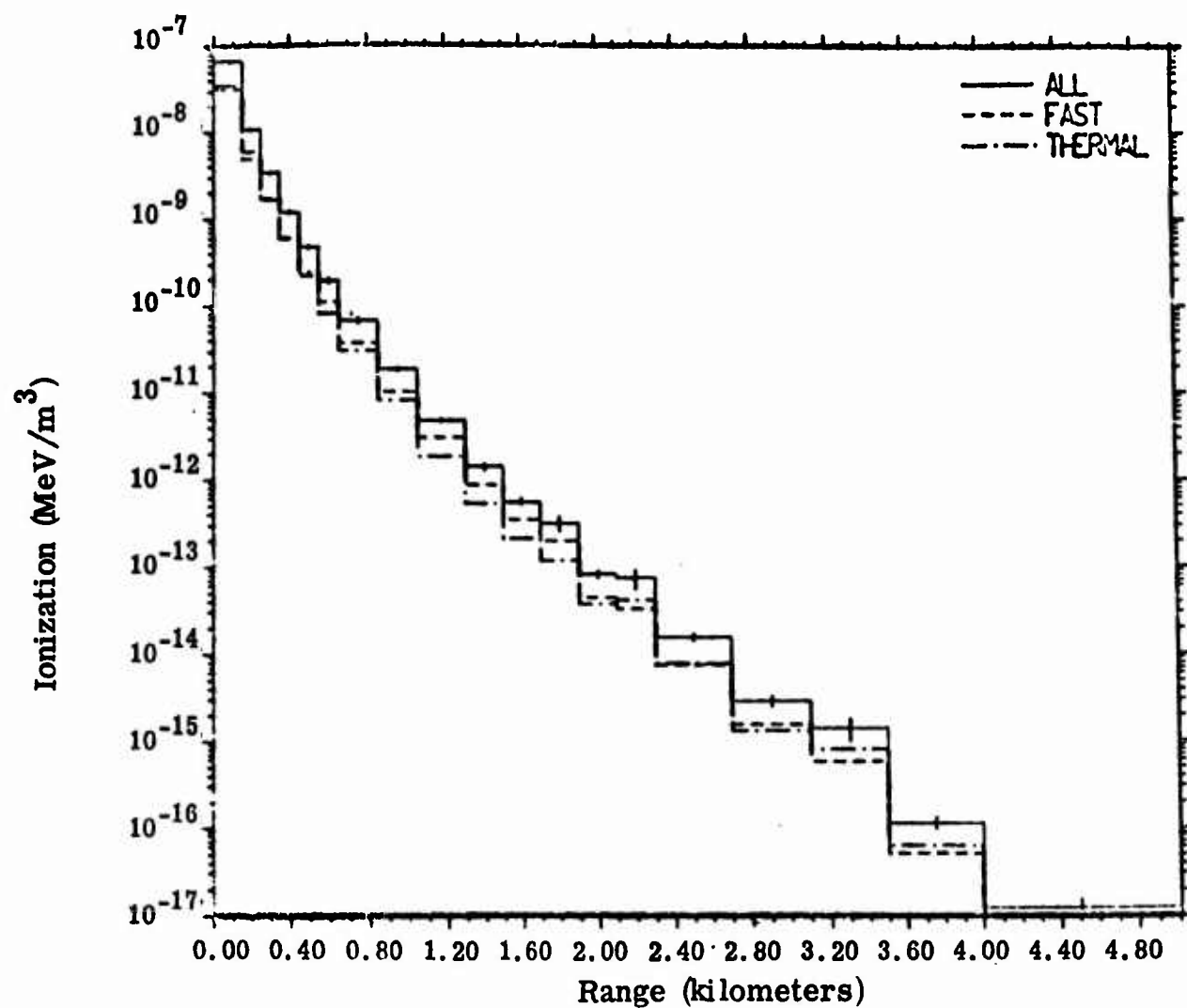


Figure 2.1. Radial dependence of ionization due to thermo-nuclear source on ground,  $\cos \theta = 0 - 0.05$ .

the ground. The ionization is due to both neutrons and gamma rays and the solid histogram depicts the total dose. The dashed histogram represents contributions to the ionization from fast neutron ionization processes and from gamma rays which are produced from fast neutron reactions. The dashed-dotted histogram similarly indicates ionization produced by thermal neutron energy deposition and by photons which are produced by thermal neutron reactions.

Figure 2.2 shows the ionization vs. radius for the 200 m HoB for a height bin extending from the air-ground interface to an elevation of 50 meters. These bins represent approximately the same spatial positions as the angular bins of Fig. 2.1, namely spatial regions close to the air-ground interface. Comparing the 0 and 200 meter HoB results along the air-ground interface indicates that there are differences in the time integrated ionization rate results. At close-in ranges out to a few hundred meters, the 0 meter results are substantially higher while at greater distances the 200 meter HoB results appear to be generally higher.

In Fig. 2.3 the time integrated ionization rate vs. radial position is shown for the 500 meter HoB for the elevation bin extending from the ground to an altitude of 50 meters. The 500 meter HoB results are much lower than the 200 meter HoB calculations for the first few radial bins extending to several hundred meters. The 500 and 200 meter HoB results are then fairly close to one another, with the 200 meter results generally higher, out to about 2 kilometers, beyond which the 500 meter calculations surpass the lower HoB data.

A comparison of the 0 and 200 meter HoB time integrated ionization rates vs. radius for the angular bin  $\cos \theta = 0.5 - 1.0$  is shown in Fig. 2.4. The values for the HoB = 0 source are generally

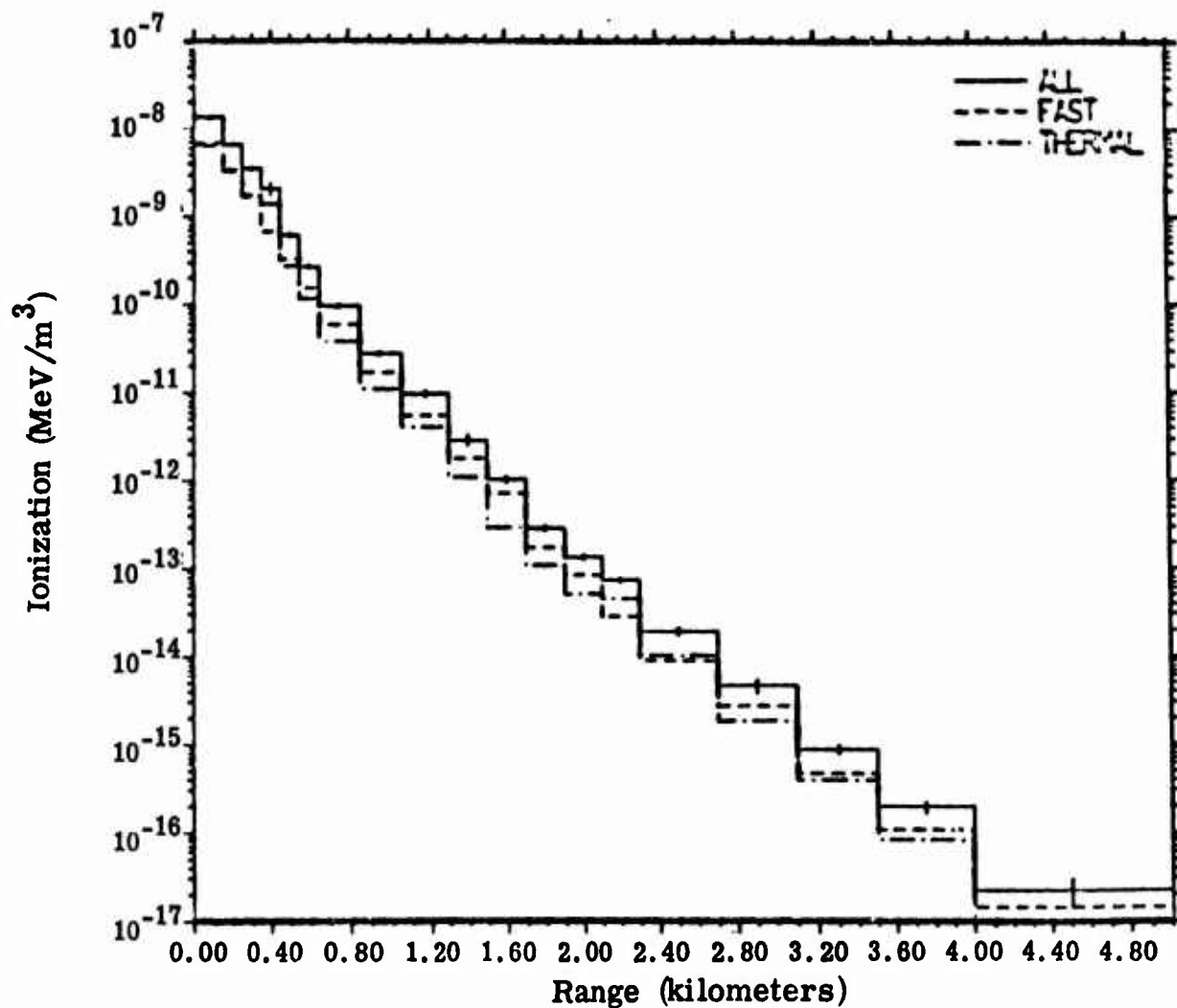


Figure 2.2. Radial dependence of ionization due to thermonuclear source for HoB = 200 m, altitude = 0 - 50 meters.

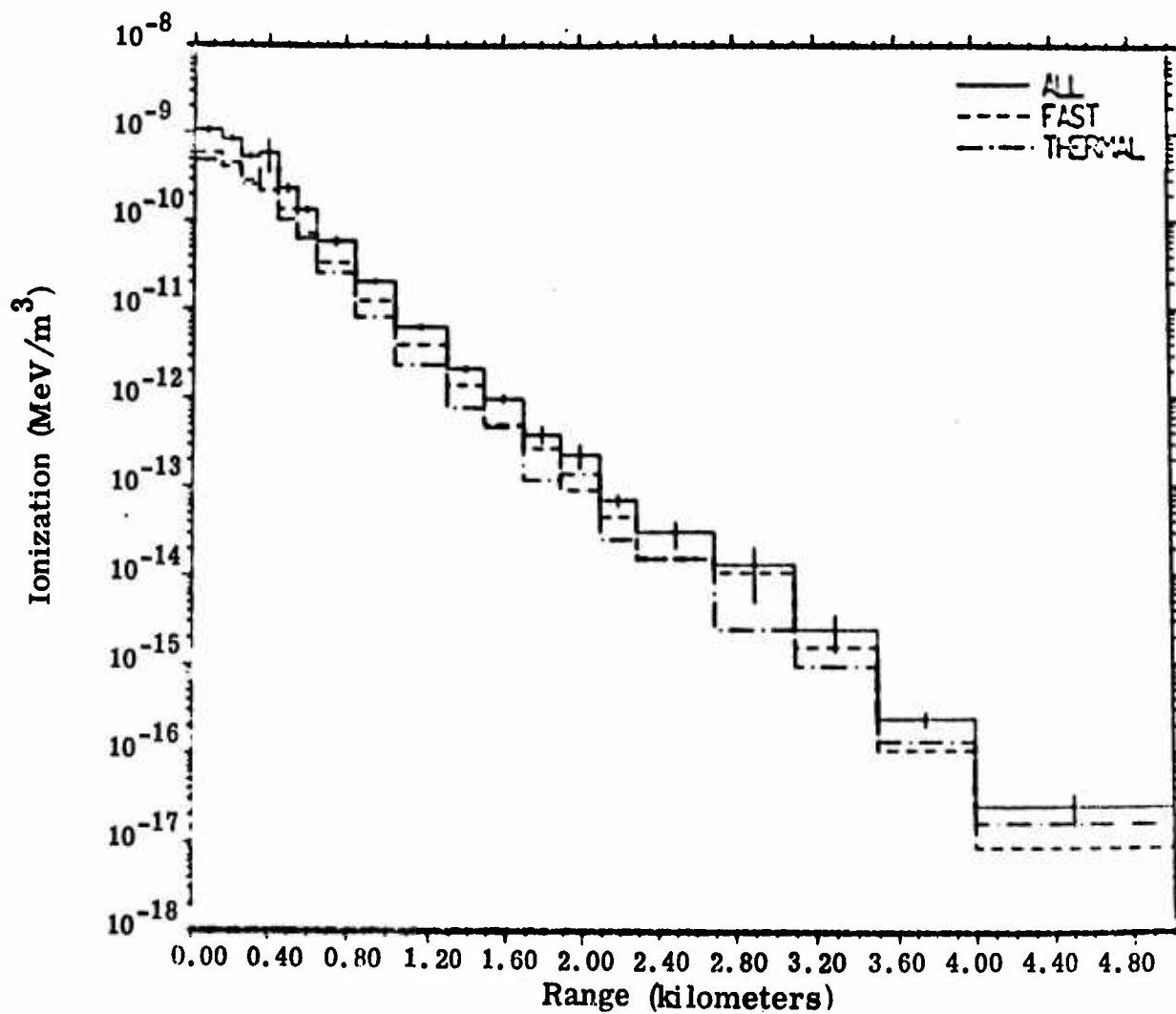


Figure 2.3. Radial dependence of ionization due to thermonuclear source for HoB = 500 m, altitude = 0 - 50 meters.

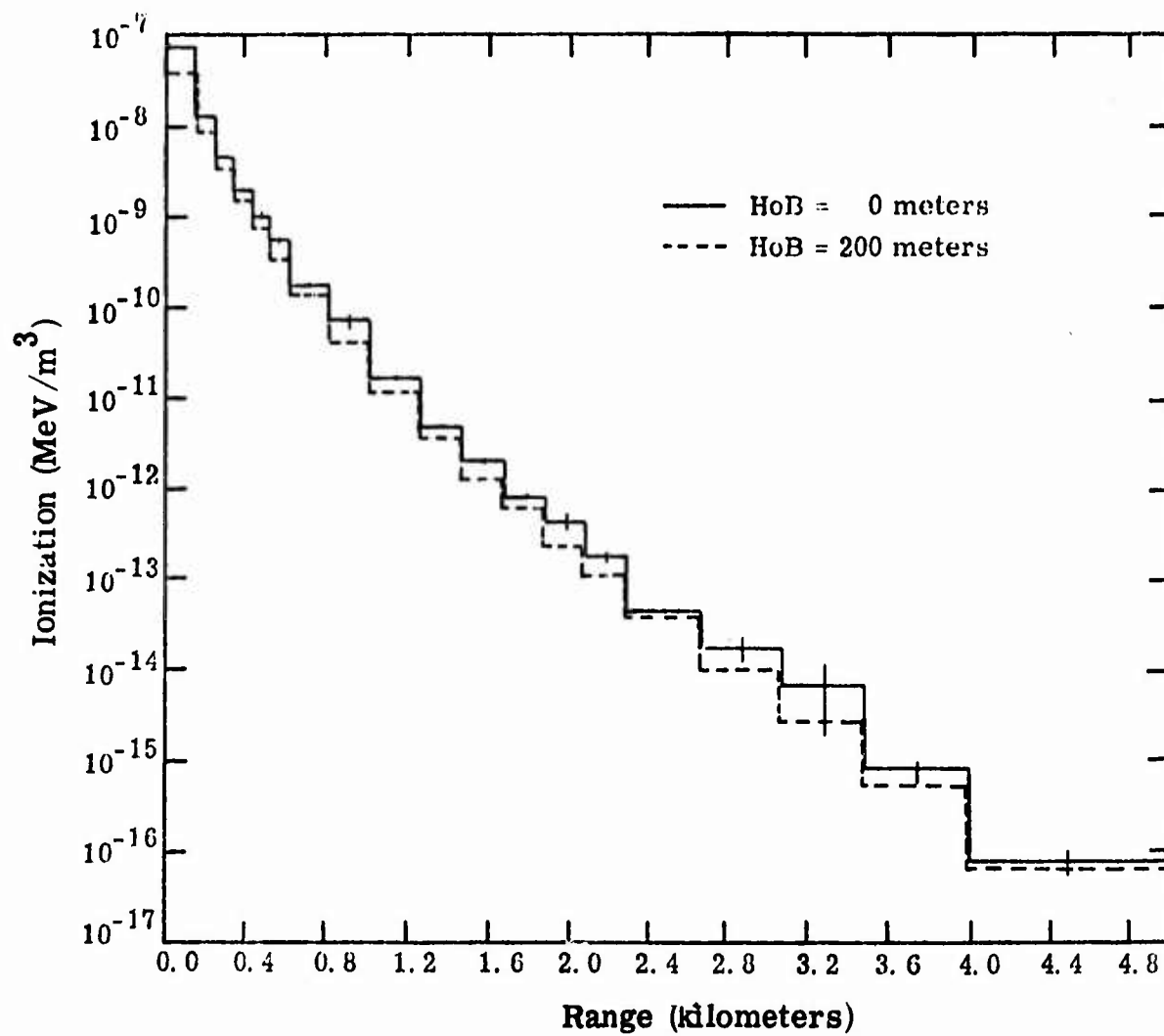
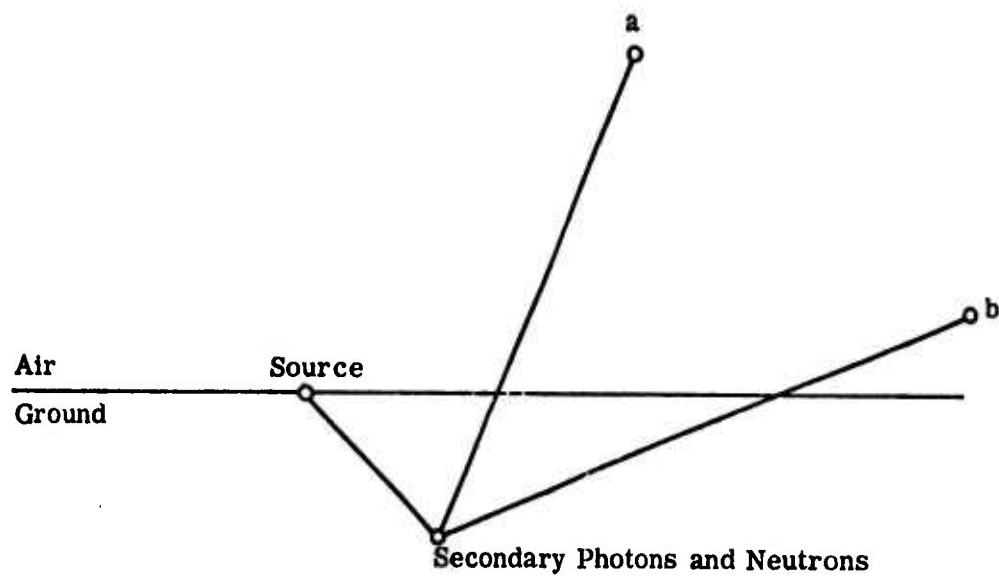


Figure 2.4. Radial dependence of ionization due to thermo-nuclear source for HoB = 0 and HoB = 200 m,  $\cos \theta = 0.5 - 1.0$ .

higher than the HoB = 200 m results for all ranges. A similar comparison was made between the 200 meter HoB and the 500 meter HoB for the  $\cos \theta = 0.5 - 1.0$  bins. For these two cases virtually identical results were obtained for all ranges which implies that for HoB's above 200 meters, the ground plays little role in determining the dose deposited in air at small polar angles.

The reason for the differences between the 0 and 200 meter HoB results shown in Fig. 2.4 can be explained with the aid of Fig. 2.5-2.11. From Fig. 2.5 it is clear that secondary photons which are produced in the ground by a HoB = 0 meter source must traverse more ground to reach an observer at b than an observer at a. Therefore, the energy deposited by gamma rays at small polar angles in air should be larger than the energy deposited at larger angles. A similar argument can be presented for the source neutrons from a ground burst. A large fraction of the source neutrons produce secondary neutrons in the ground through inelastic scattering reactions. The energy deposited by these neutrons is again larger for small polar angles because there is less ground to traverse than for the large polar angles.

The polar angle dependence of the ionization for the ground burst is shown in Figs. 2.6-2.8. In Fig. 2.6 the total neutron plus photon ionization as a function of the polar angle is presented for a radial bin extending from 450 to 550 meters. The ionization due to both fast and thermal reactions is seen to increase with decreasing polar angle as would be expected from the previous geometrical arguments of Fig. 2.5. Figures 2.7 and 2.8 illustrate the ionization versus polar angle due to neutrons and gamma rays, respectively. For both types of particles, it is clear that the ionization increases with decreasing polar angle. Neutron and photon ionization produced by both fast and thermal



**Figure 2.5. Geometrical explanation for polar angle dependence.**



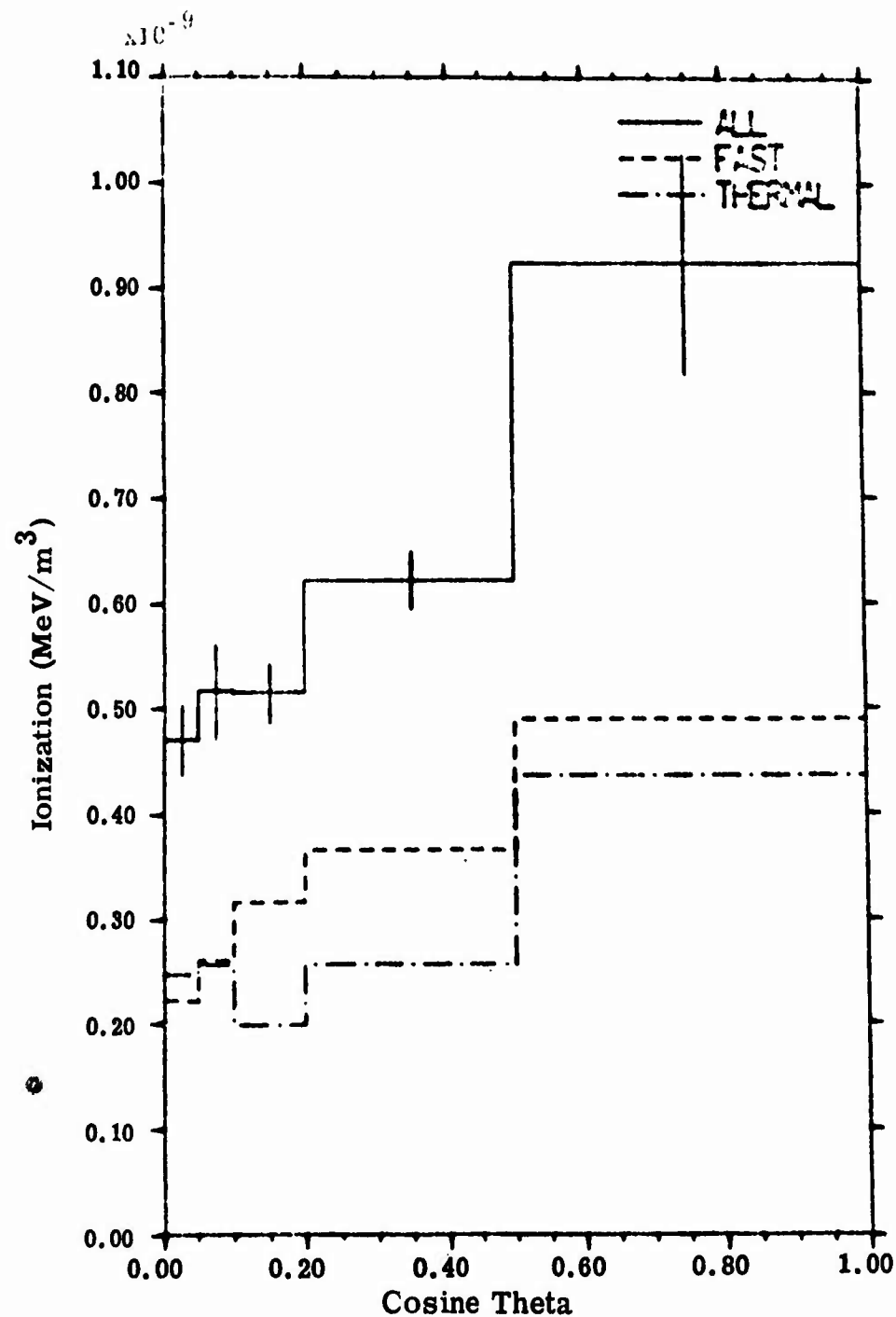


Figure 2. 6. Polar angle variation of total ionization at radius 450 - 550 meters, due to thermonuclear source on ground.

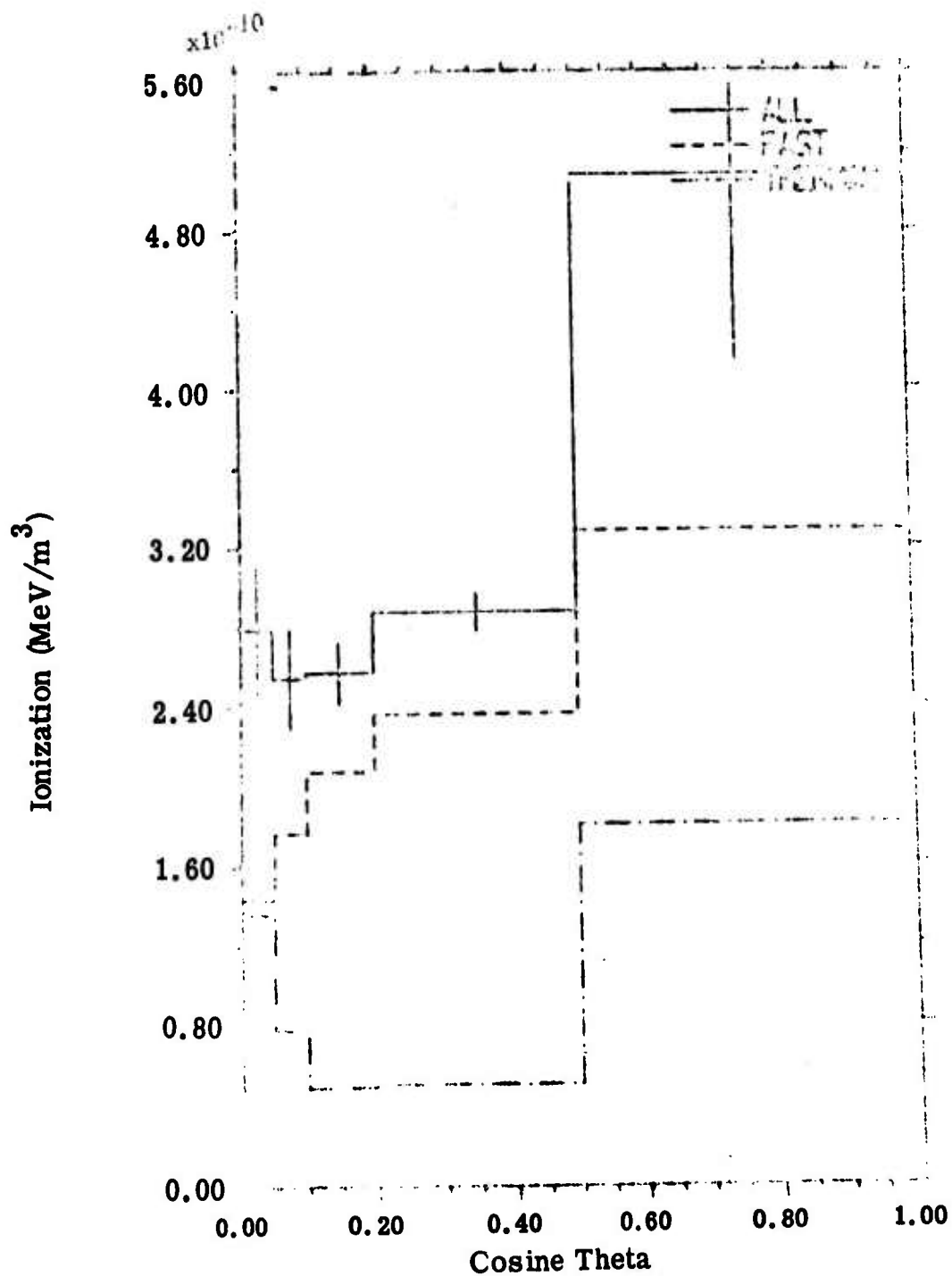


Figure 2.7. Polar angle variation of neutron ionization at radius 450 - 550 meters, due to thermonuclear source on ground.

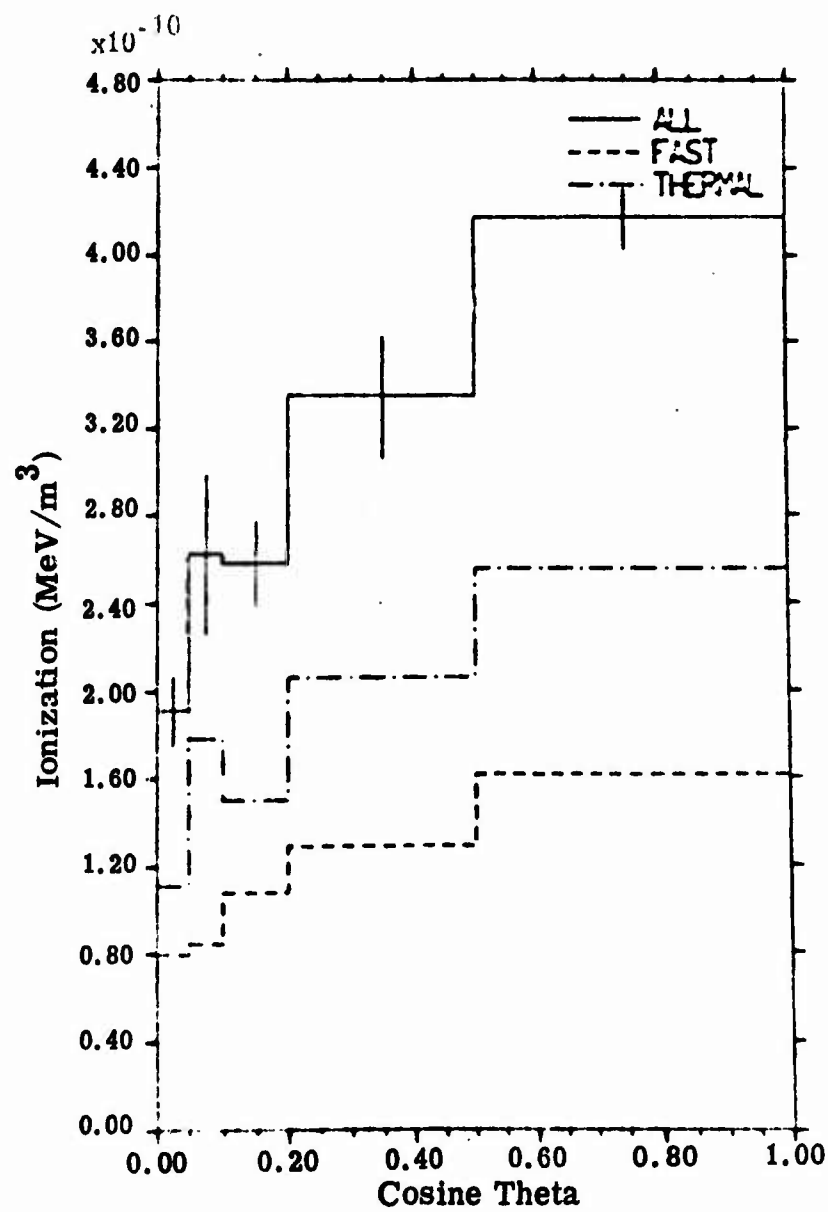


Figure 2.8. Polar angle variation of gamma ray ionization at radius 450 - 550 meters, due to thermonuclear source on ground.

neutron reactions demonstrate this angular dependence. Although these angular results are shown here only for one radial bin, the effect can be shown to be a general phenomenon at other ranges for a ground burst. For higher HoB's, the polar angle dependence is much flatter. In Figs. 2.9-2.11, the polar angle dependence of the ionization at the 450-550 meter radial bin is shown for the 200 meter HoB. The total ionization, neutron ionization, and photon ionization results are all flatter for the 200 meter HoB as a function of polar angle than the corresponding ground burst calculations. The polar angle dependence is much less pronounced for both the 200 m and 500 m HoB sources than for the ground burst because for the higher altitude calculations the secondary photons and neutrons produced in the ground are distributed over a wider area and furthermore, the ground plays a much smaller role in altering directions for source particles because of the greater distances involved. Therefore, for small polar angles, larger ionization values due to the ground burst, relative to the 200 m HoB, can be anticipated as illustrated in Fig. 2.4.

Figure 2.12 illustrates the effect of the height of the source upon ionization in the ground for the radial interval from 450-550 meters. The HoB = 200 m results are consistently higher than the ground burst calculations. In turn, the HoB = 0 m results are slightly higher than the higher altitude HoB = 500 m data. The HoB = 200 m calculations exceed the ground burst mainly due to the fact that uncollided neutrons can reach the ground, at this radial distance, from the 200 m burst but not from the ground burst. Therefore, the HoB = 0 m source neutrons are degraded in energy to a greater extent than the 200 m particles, and the ionization in the ground is therefore substantially reduced relative to the HoB = 200 m calculations. On the other hand, as even higher HoB sources are considered, the probability of energetic neutrons and gamma rays reaching the ground at the 450-550 m radius is reduced. This is demonstrated by the fact that the HoB = 500 m results are slightly lower at nearly all depths than the ground burst results, and much lower than the HoB = 200 m calculations.

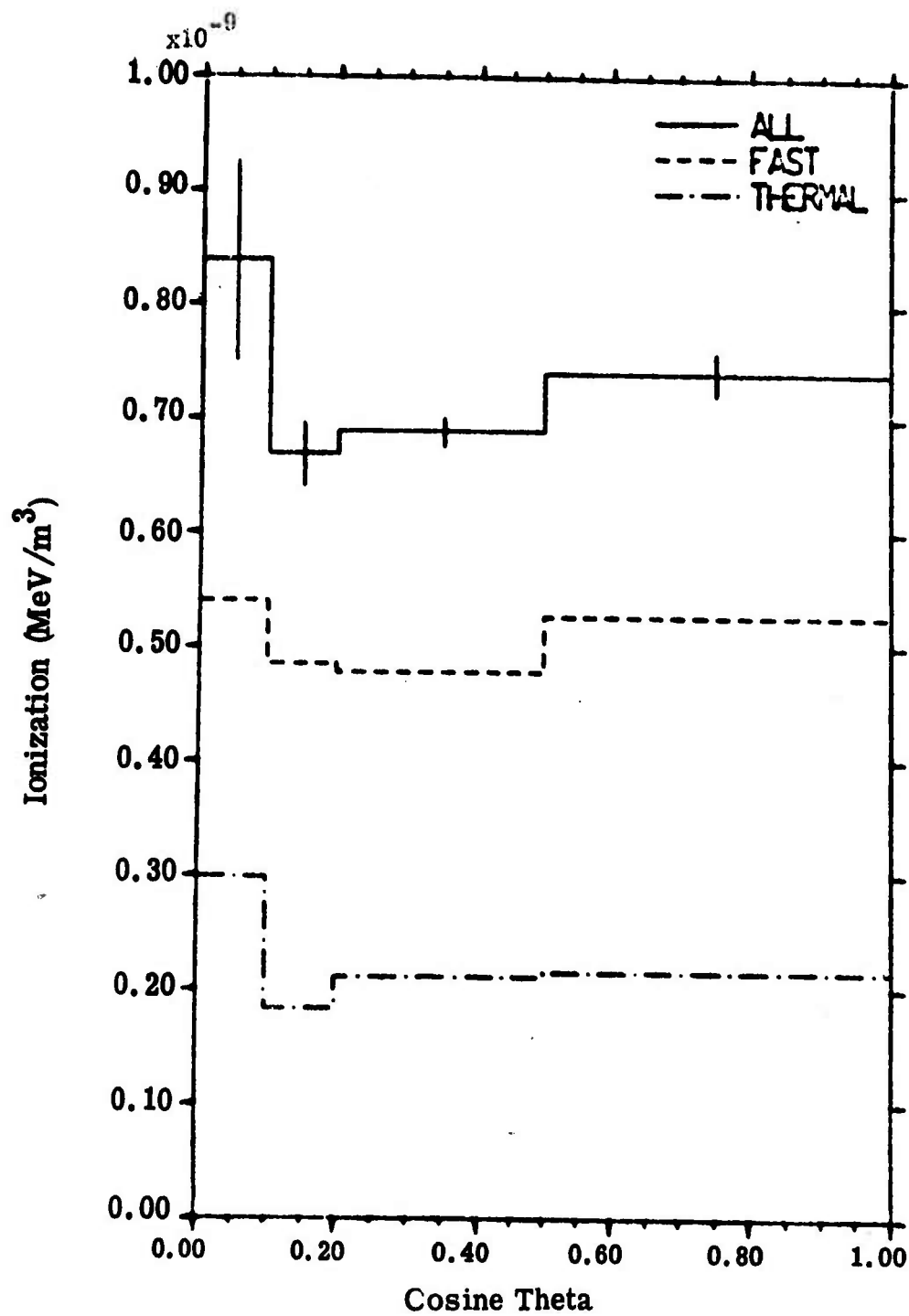


Figure 2. 9. Polar angle variation of total ionization at radius 450 - 550 meters, due to thermonuclear source for 200 m HoB.

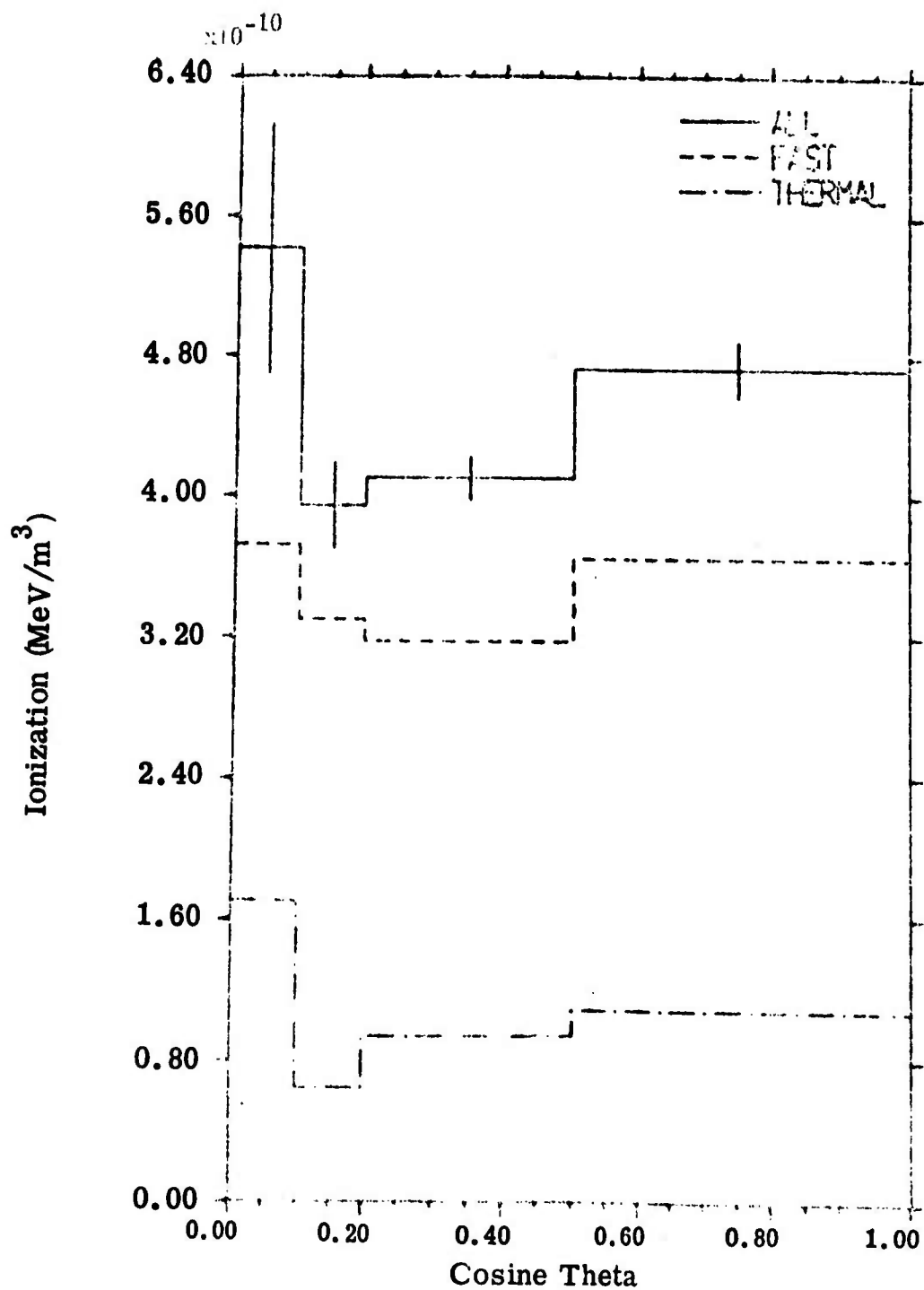


Figure 2.10. Polar angle variation of neutron ionization at radius 450 - 550 meters, due to thermonuclear source for 200 m HoB.

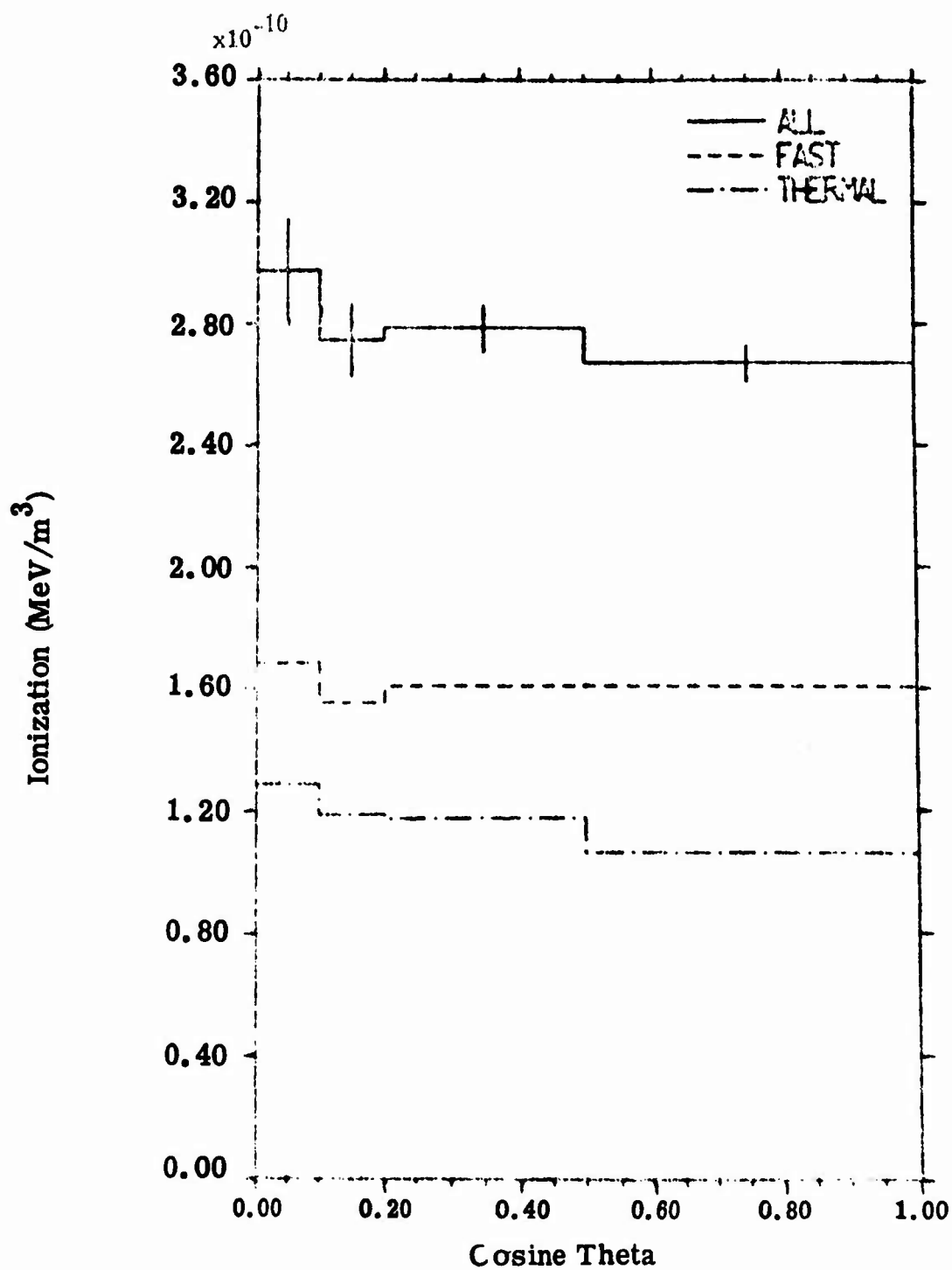


Figure 2.11. Polar angle variation of gamma ray ionization at radius 450 - 550 meters, due to thermonuclear source for 200 m HoB.

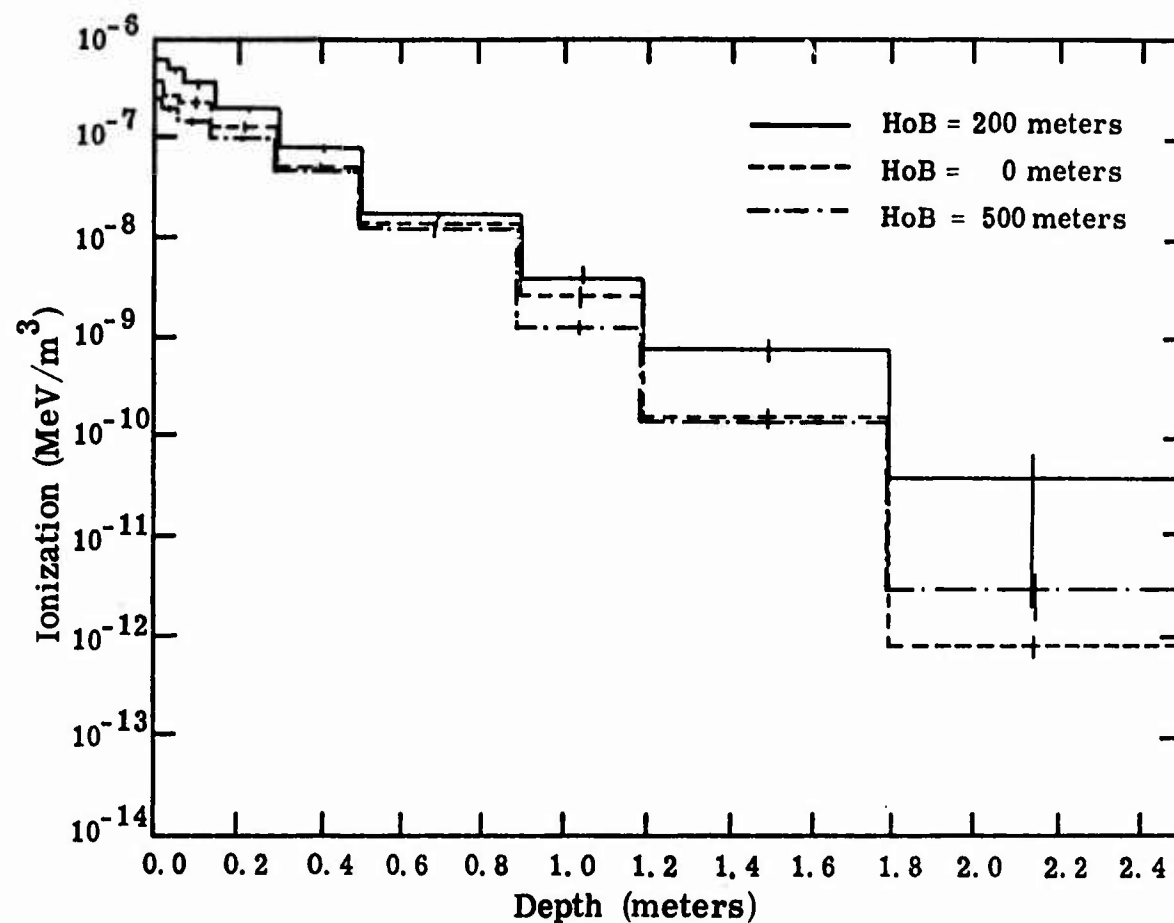


Figure 2.12. Ionization vs. depth at radius 450 - 550 meters, due to thermonuclear source for HoB = 0, HoB = 200, and HoB = 500 meters.



The next series of figures is concerned with various time dependent ionization rate and Compton current results at radial positions of 450 - 550 meters for the three heights of burst. In Fig. 2.13 the ionization rates in air just above the air-ground interface are displayed for the HoB = 0 m and HoB = 200 m calculations. The HoB = 200 m results are for a cylindrical bin extending from the ground to an elevation of 50 meters. The HoB = 0 m results are for a spherical bin extending from  $\cos \theta = 0.0$  to  $\cos \theta = 0.05$ . Although the two bins are of different shapes, they both refer to approximately the same spatial positions. The results presented in Fig. 2.13 indicate that there is very little difference between the two HoB calculations for the spatial positions considered here. The HoB = 0 m results are higher in the very early time intervals since neutrons are immediately converted to inelastic gammas for the ground source. Therefore, the HoB = 0 m calculations display an initial prompt spike which is absent in the higher altitude calculations. Both sources show another spike at approximately  $8 \mu\text{sec}$  local time which signals the arrival of 14 MeV neutrons. After the arrival of the neutron wave front, ionization is caused by both photons and neutrons, whereas at earlier times only secondary gamma rays were contributing to ionization.

In Fig. 2.14 a comparison between HoB = 200 m and HoB = 500 m ionization rates is made for the elevation bin 0 - 50 meters. Here the 500 meter results are lower than the HoB = 200 m calculations by about a factor of 2 for all the time intervals. The arrival of the 14 MeV neutron spike is also delayed for the HoB = 500 m calculations, falling into the 10 - 20  $\mu\text{sec}$  local time bin, since these neutrons must travel farther before reaching the observation bin than the lower altitude source neutrons.

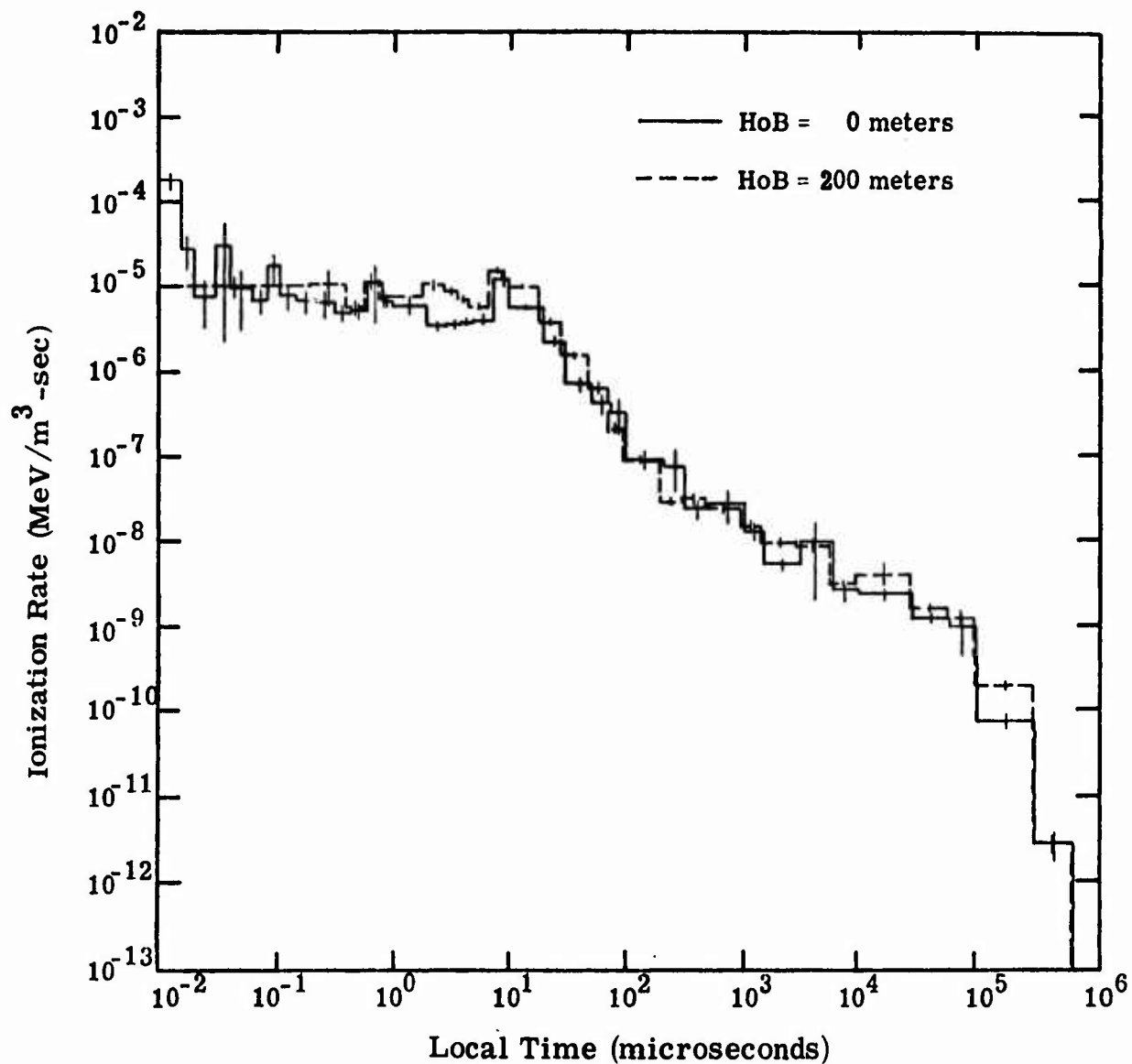


Figure 2.13. Ionization rate for thermonuclear source at radius = 450 - 550 meters, for HoB = 0 m,  $\cos \theta = 0 - 0.05$ , and at HoB = 200 m, elevation = 0 - 50 m.

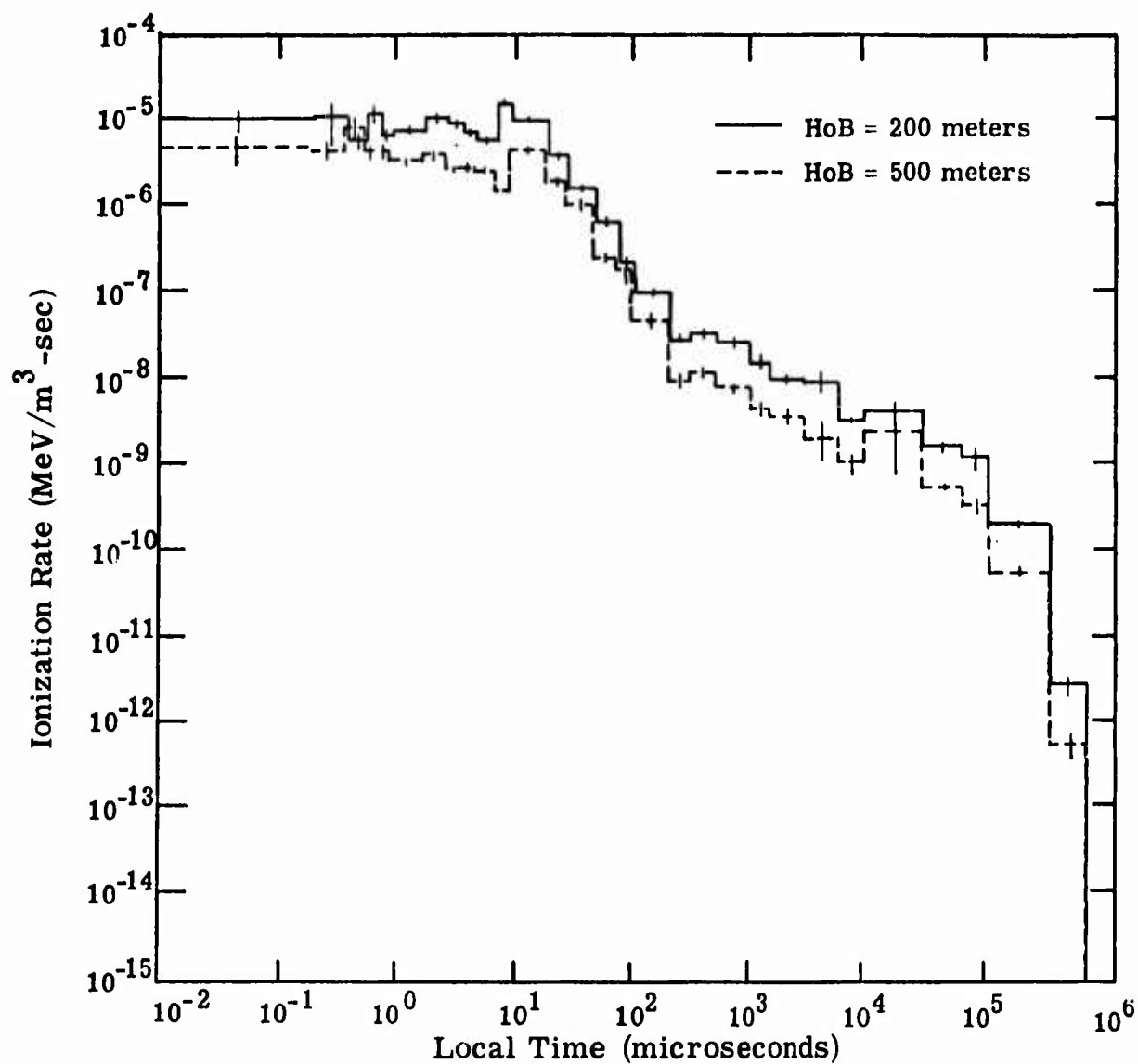


Figure 2.14. Ionization rate at radius 450 - 550 meters, elevation = 0 - 50 m, for thermonuclear source at HoB = 200 and HoB = 500 m.

Figure 2.15 shows the ionization rate in the air for a  $\cos \theta = 0.5 - 1.0$  bin due to a ground burst. The ionization rate is due to combined neutron and gamma ray energy deposition. Figures 2.16 and 2.17 display the ionization rates for this same angular bin due to separate neutron and gamma ray deposition processes. On all three plots, the ionization rate is further separated into components due to fast and thermal neutron reactions. By comparing the three figures, we can determine something about the effectiveness of the various deposition mechanisms in certain time intervals. It is apparent from Figs. 2.16 and 2.17 that the ionization is solely due to gamma rays initially. A prompt initial photon spike due to inelastic neutron scattering in the ground is displayed in the first time interval. Photon ionization due to thermal neutron captures does not appear until approximately  $4 \mu\text{sec}$  local time. The initial fast neutron energy deposition appears at about  $5 \mu\text{sec}$ , with significant deposition taking place in the next time bin, from  $7.5 - 10 \mu\text{sec}$ . From this time bin out to approximately  $100 \mu\text{sec}$ , the neutron ionization is larger than the photon contribution. The gamma ray ionization then becomes larger than the neutron component in the time range from  $100$  to  $10^4 \mu\text{sec}$ . At  $10^4 \mu\text{sec}$  thermal neutron capture in air becomes a factor, as can be seen from Fig. 2.16, and the neutron and photon components of the ionization rate become comparable from  $10^4$  to  $10^6 \mu\text{sec}$ .

Figures 2.18 - 2.20 show the total ionization rate, and the ionization rates due to the separate neutron and gamma ray processes for a source at an altitude of 500 m. The angular bin extending from  $\cos \theta = 0.5 - 1.0$  with radius 450 - 550 meters is again used. In comparing the HoB = 500 m results with the ground burst calculations of Figs. 2.15 - 2.17 we can draw a number of conclusions. Neutron ionization rates for the two sources are very similar for all time bins as might be anticipated

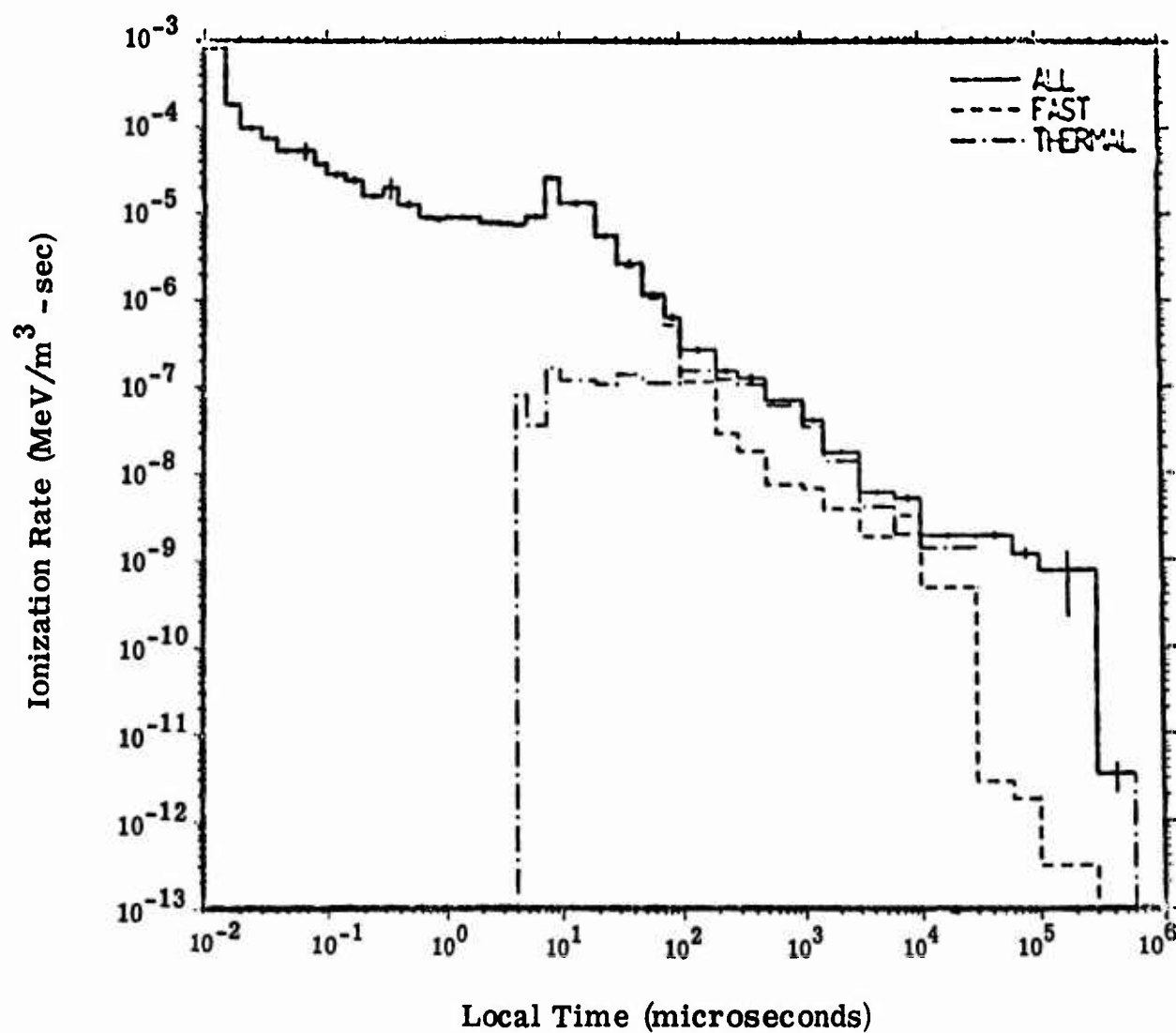


Figure 2.15. Total ionization rate at radius 450 - 550 meters,  $\cos \theta = 0.5 - 1.0$ , due to thermonuclear source at HoB = 0 meters.

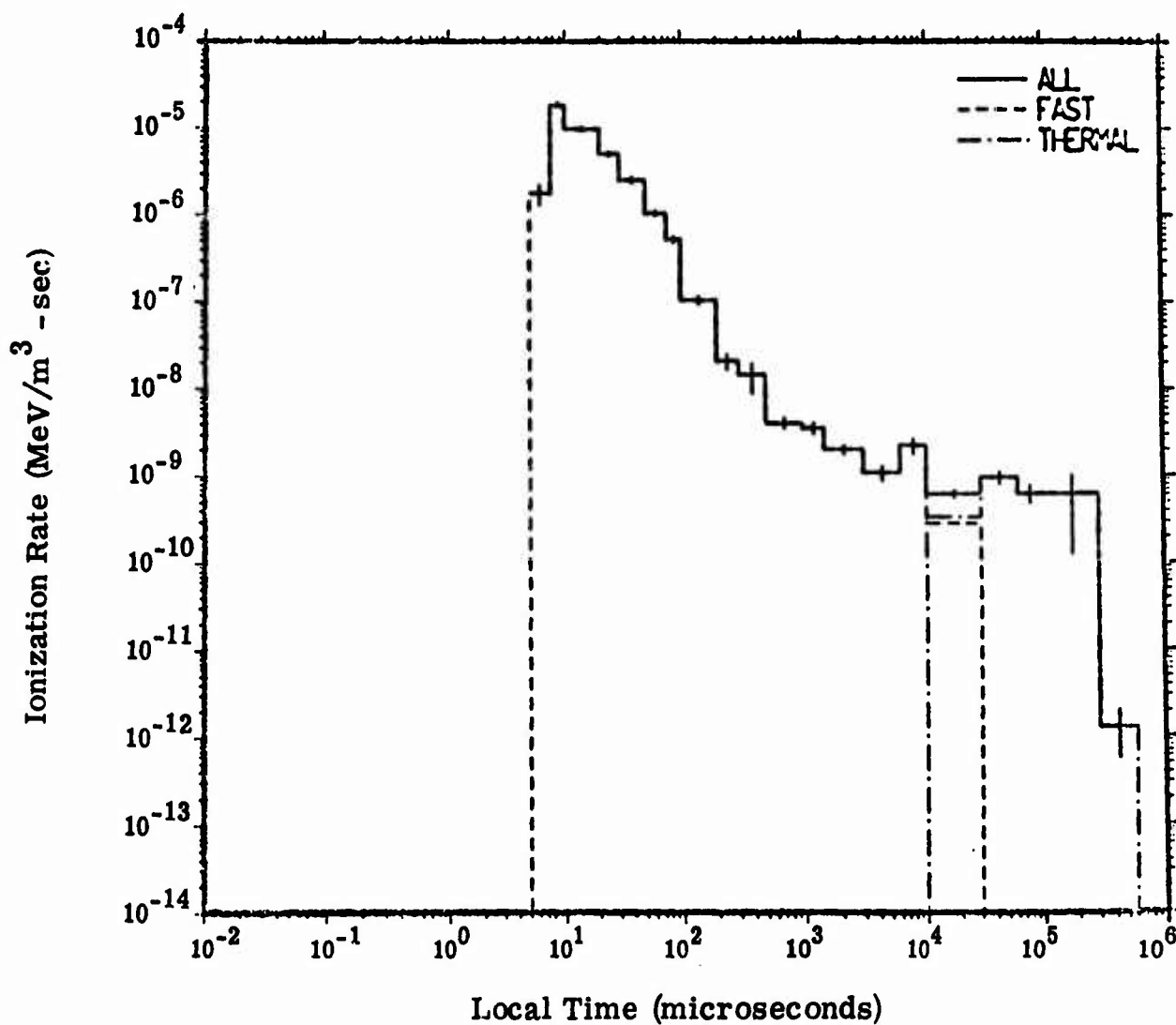


Figure 2.16. Ionization rate due to neutrons at radius 450 - 550 meters,  $\cos \theta = 0.5 - 1.0$ , due to thermonuclear source at HoB = 0 meters.

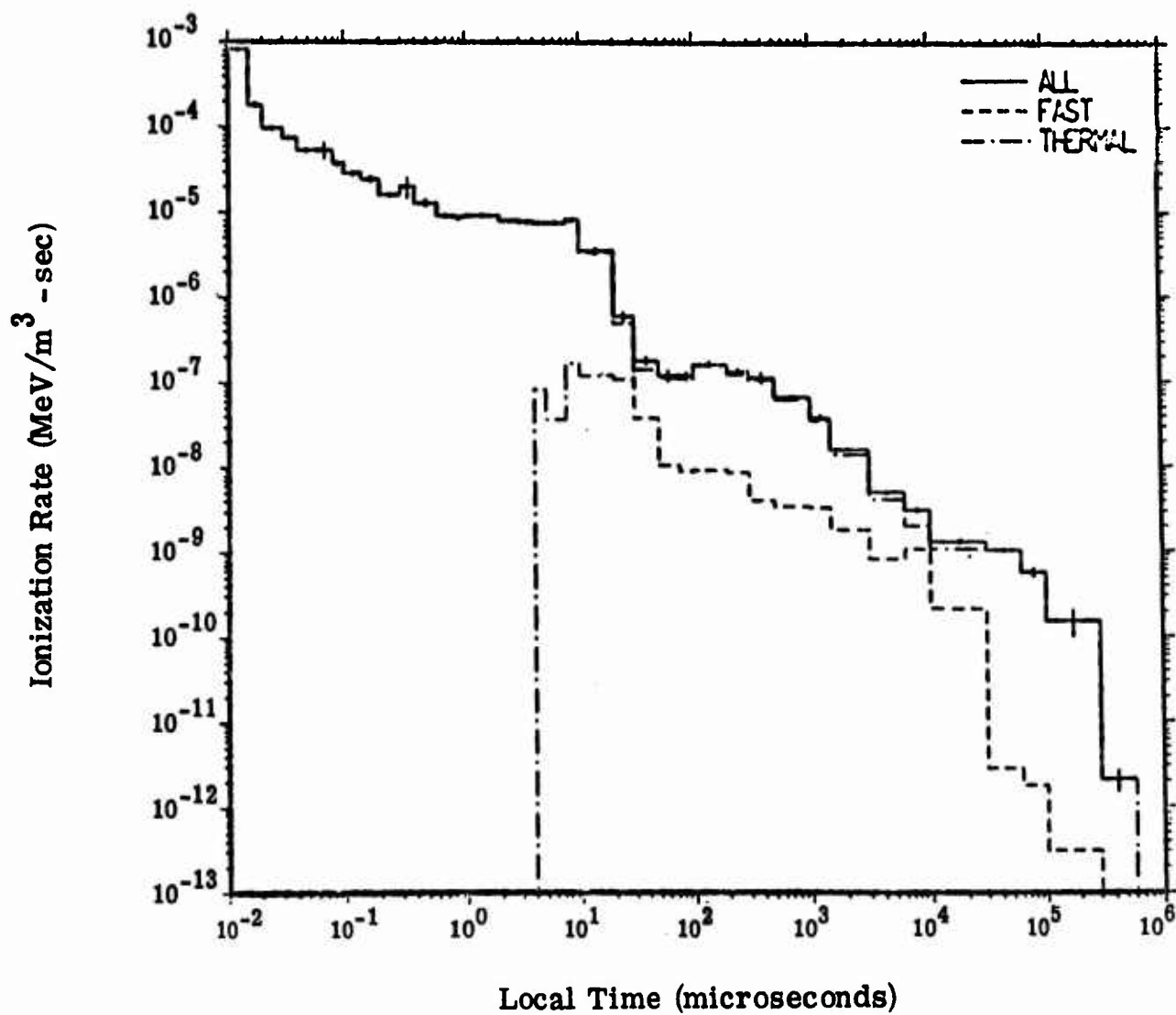


Figure 2.17. Ionization rate due to gamma rays at radius 450 - 550 meters,  $\cos \theta = 0.5 - 1.0$ , due to thermo-nuclear source at HoB = 0 meters.

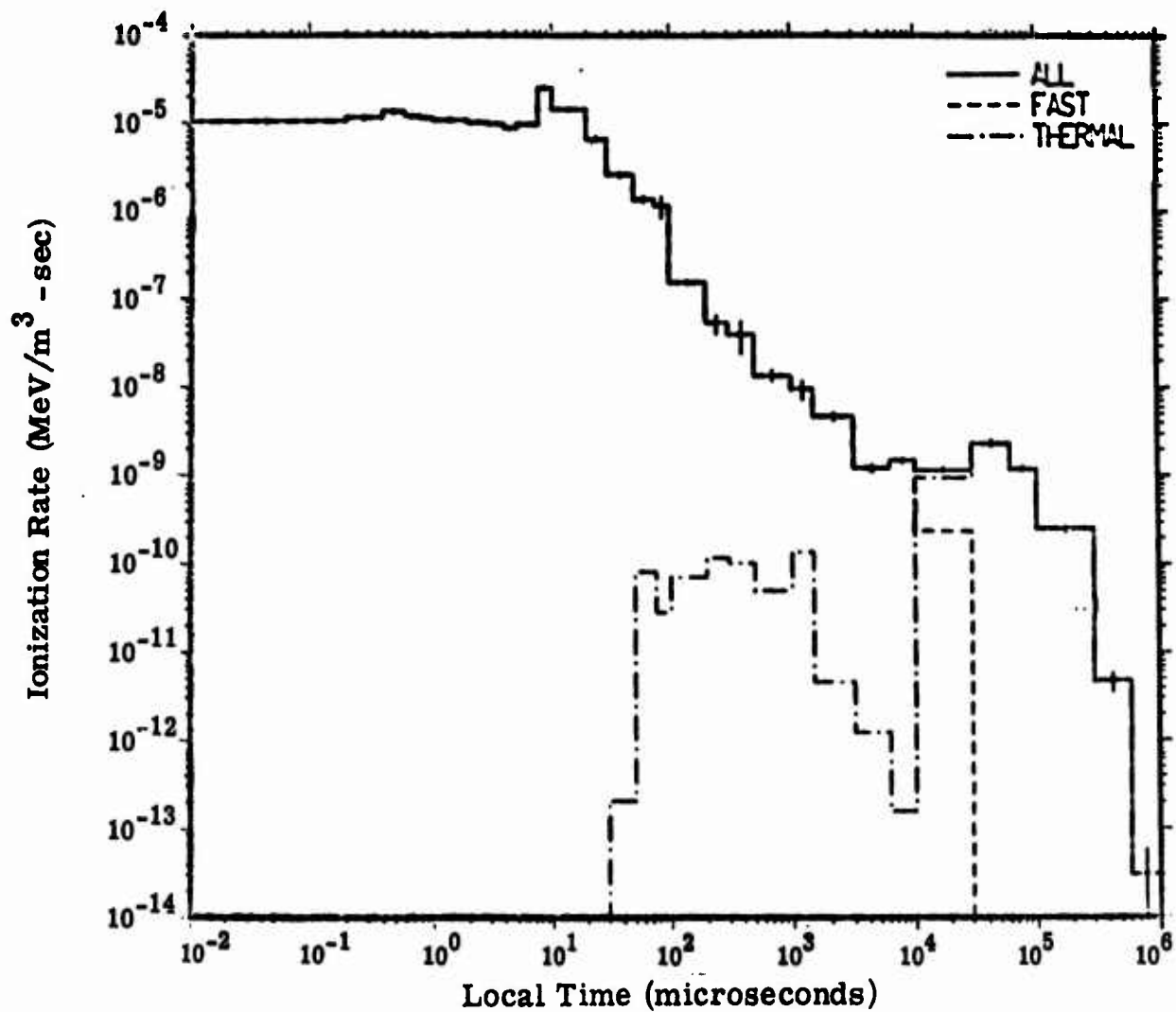


Figure 2.18. Total ionization rate at radius 450 - 550 meters,  $\cos \theta = 0.5 - 1.0$ , due to thermonuclear source at HoB = 500 meters.



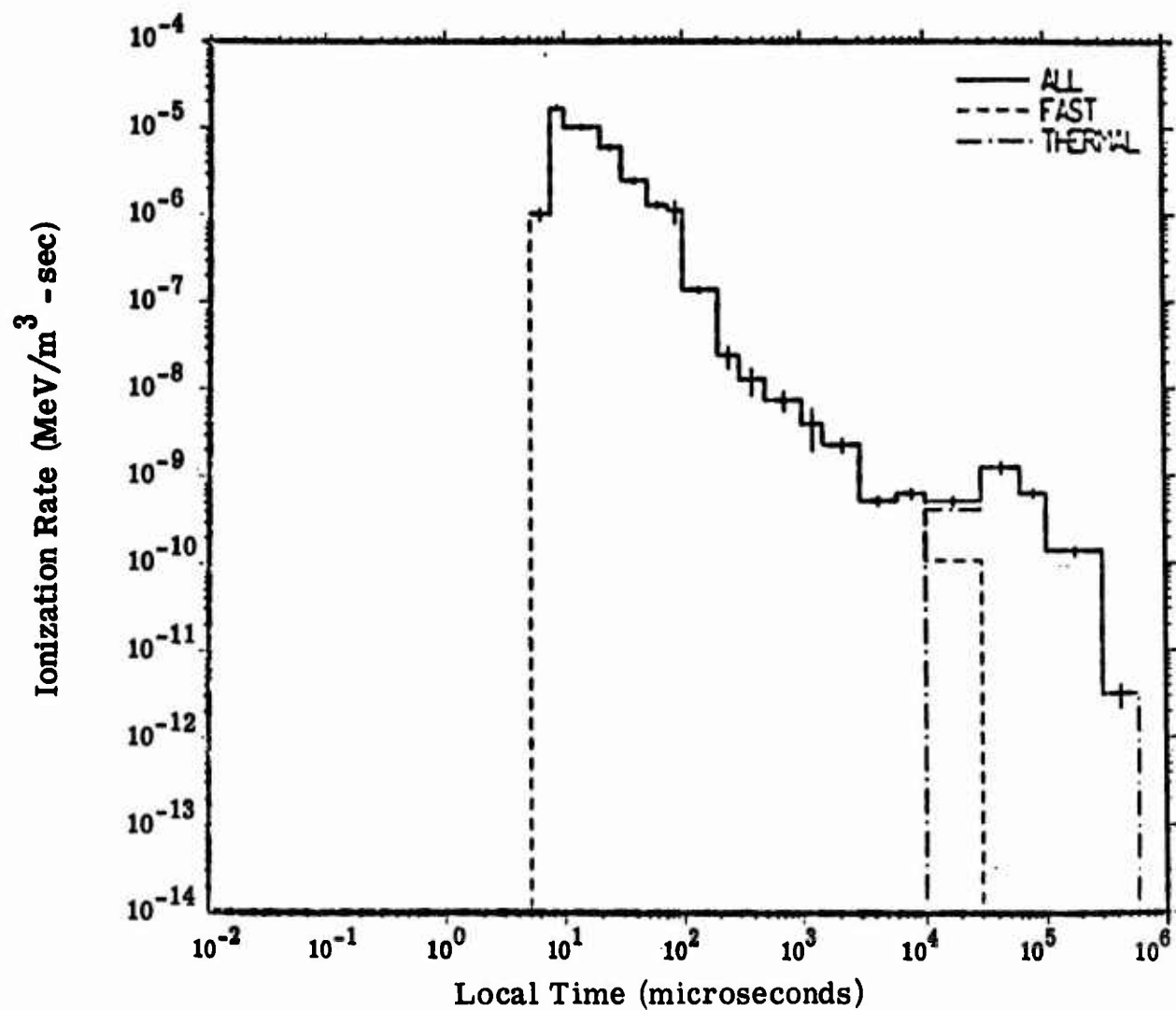


Figure 2.19. Ionization rate due to neutrons at radius 450 - 550 meters,  $\cos \theta = 0.5 - 1.0$ , due to thermonuclear source at HoB = 500 meters.

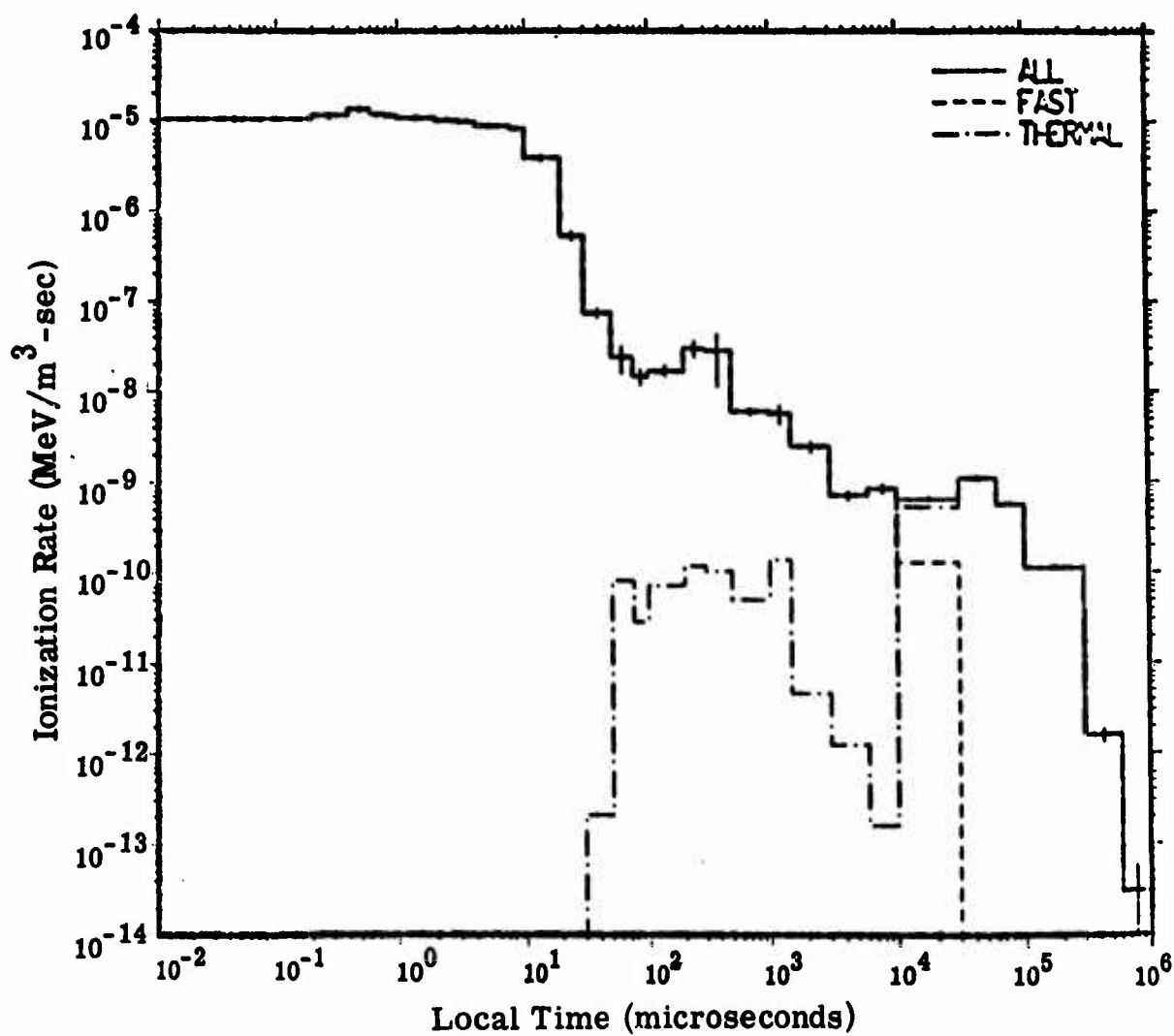


Figure 2.20. Ionization rate due to gamma rays at radius 450 - 550 meters,  $\cos \theta = 0.5 - 1.0$ , due to thermonuclear source at HoB = 500 meters.

since the spatial bin considered is in the air and distant from the air-ground interface. The higher altitude calculations again do not display the large prompt spike shown by the  $\text{HoB} = 0 \text{ m}$  calculations. Furthermore, the ground burst shows substantially higher ionization out to about  $0.4 \text{ } \mu\text{sec}$  where the two calculations are approximately equal. This is expected since the gamma rays from inelastic scattering in the ground are only possible from the  $\text{HoB} = 0 \text{ m}$  source in this time region. The  $\text{HoB} = 500 \text{ m}$  fast gamma rays are due solely to inelastic scattering in the air out to about  $10 \text{ } \mu\text{sec}$  where ground inelastic gammas become a possibility. The ionization due to photons is approximately the same for the two  $\text{HoB}$ 's from  $0.4 \text{ } \mu\text{sec}$  to  $3 \text{ } \mu\text{sec}$ . From  $3 \text{ } \mu\text{sec}$  to about  $10^4 \text{ } \mu\text{sec}$  the  $\text{HoB} = 0 \text{ m}$  results are about an order of magnitude larger than the  $500 \text{ m}$  calculations. Beyond  $10^4 \text{ } \mu\text{sec}$  the two results are comparable. It is interesting to note that a very large difference in photon ionization exists between the two calculations due to thermal photon contributions. The ground burst thermal photon ionization is about three orders of magnitude larger than the  $\text{HoB} = 500 \text{ m}$  calculation. The thermal gamma contributions also appear at earlier times,  $4 \text{ } \mu\text{sec}$  for the ground burst versus  $30 \text{ } \mu\text{sec}$  for the higher source. Differences in thermal gamma ionization rates between the two sources appear to be primarily responsible for the large deviations displayed in the total gamma ionization rates.

In Fig. 2.21 the radial Compton current due to the ground burst is shown for the angular bin extending from  $\cos \theta = 0.0$  to  $\cos \theta = 0.05$  and the range from  $450 - 550 \text{ m}$ . Figure 2.22 displays the theta current for the same angular bin. In both figures negative currents are indicated by the letter "N". The sign convention used on all figures in this report is that the electric current flows in the direction opposite to the electron

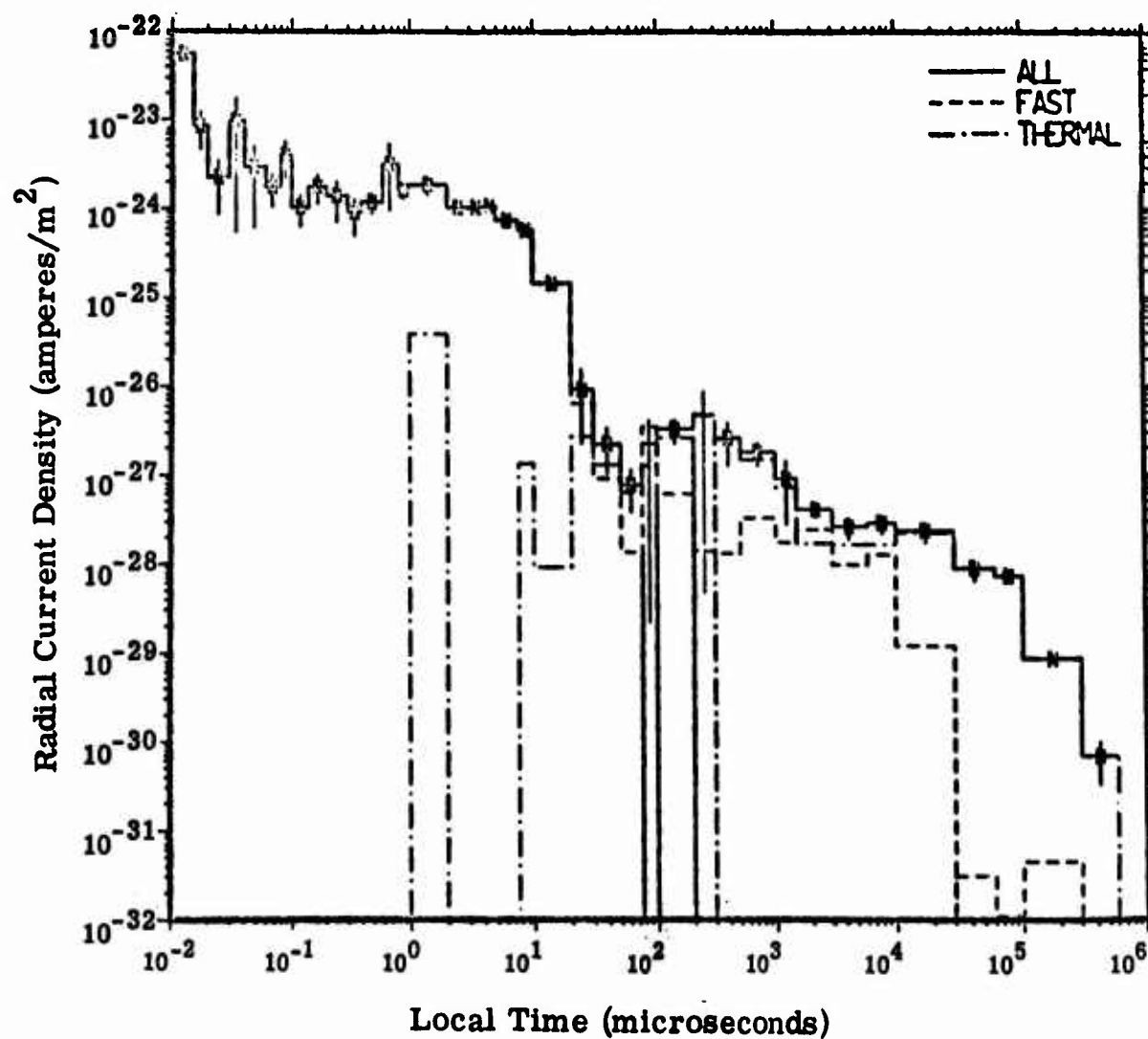


Figure 2.21. Radial current at radius 450 - 550 meters,  $\cos \theta = 0 - 0.05$ , due to thermonuclear source on ground.

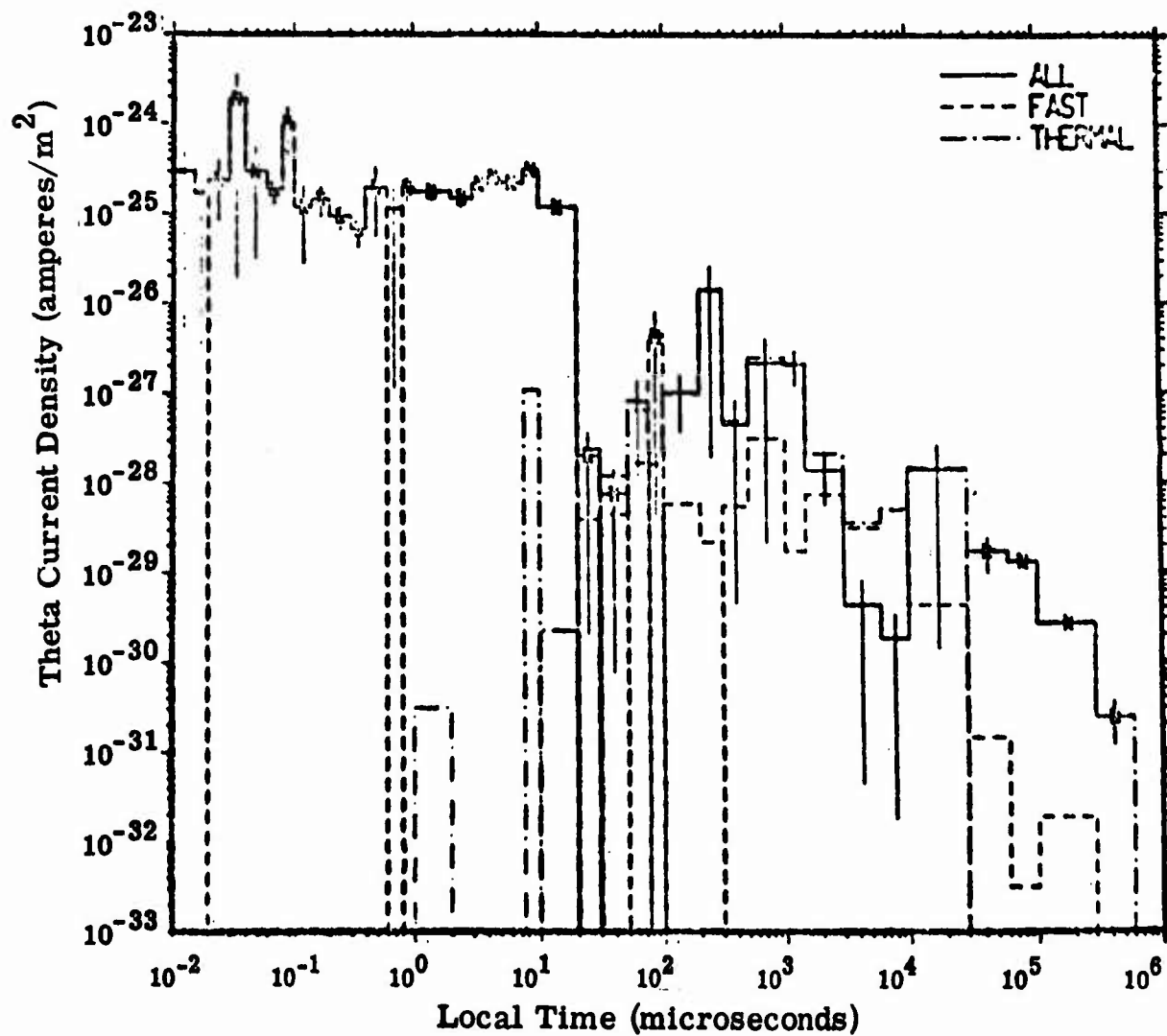


Figure 2.22. Theta current at radius 450 - 550 meters,  $\cos \theta = 0 - 0.05$ , due to thermonuclear source on ground.

flow. By including both air and ground capture gamma production in our calculations, electric currents are produced to much longer times than in previous studies <sup>(1-3)</sup>. The radial currents in Fig. 2.21 are essentially all negative as would be anticipated indicating that the photon current is in an outward direction at all times. On the other hand, the theta current is seen to undergo two distinct sign reversals. At early times to approximately 100  $\mu\text{sec}$ , the photon current is predominantly into the ground resulting in a negative theta current. For times extending to about  $3 \times 10^4 \mu\text{sec}$ , gamma rays are produced primarily in the ground and the transport of these photons into the air produces positive theta currents. At very late times, air capture gamma rays dominate, and photon currents directed toward the ground again result in negative theta currents. This very late time sign reversal of the theta current is a new phenomenon which was not observed in last year's calculations since air capture events were not considered at that time.

Figures 2.23 and 2.24 show the radial currents for the angular bins  $\cos \theta = 0.0 - 0.1$  and radial distances 450 - 550 m due to the HoB = 200 m and HoB = 500 m sources, respectively. The currents for the two sources are in reasonable agreement for nearly all time bins. Furthermore comparing the 200 m HoB with the ground burst of Fig. 2.21 again reveals good agreement for most time intervals. The ground burst of Fig. 2.21 again displays the initial prompt gamma spike due to inelastic collisions in the ground, whereas the two higher altitude bursts are smoother and of lower magnitude at very early times. Comparison of the theta currents for the two higher HoB's with the ground burst shows much larger discrepancies which may be partly due to larger statistical uncertainties. However, the theta currents for the higher bursts also display sign changes similar to those of Fig. 2.22, although the changes take place in different time bins for each source.

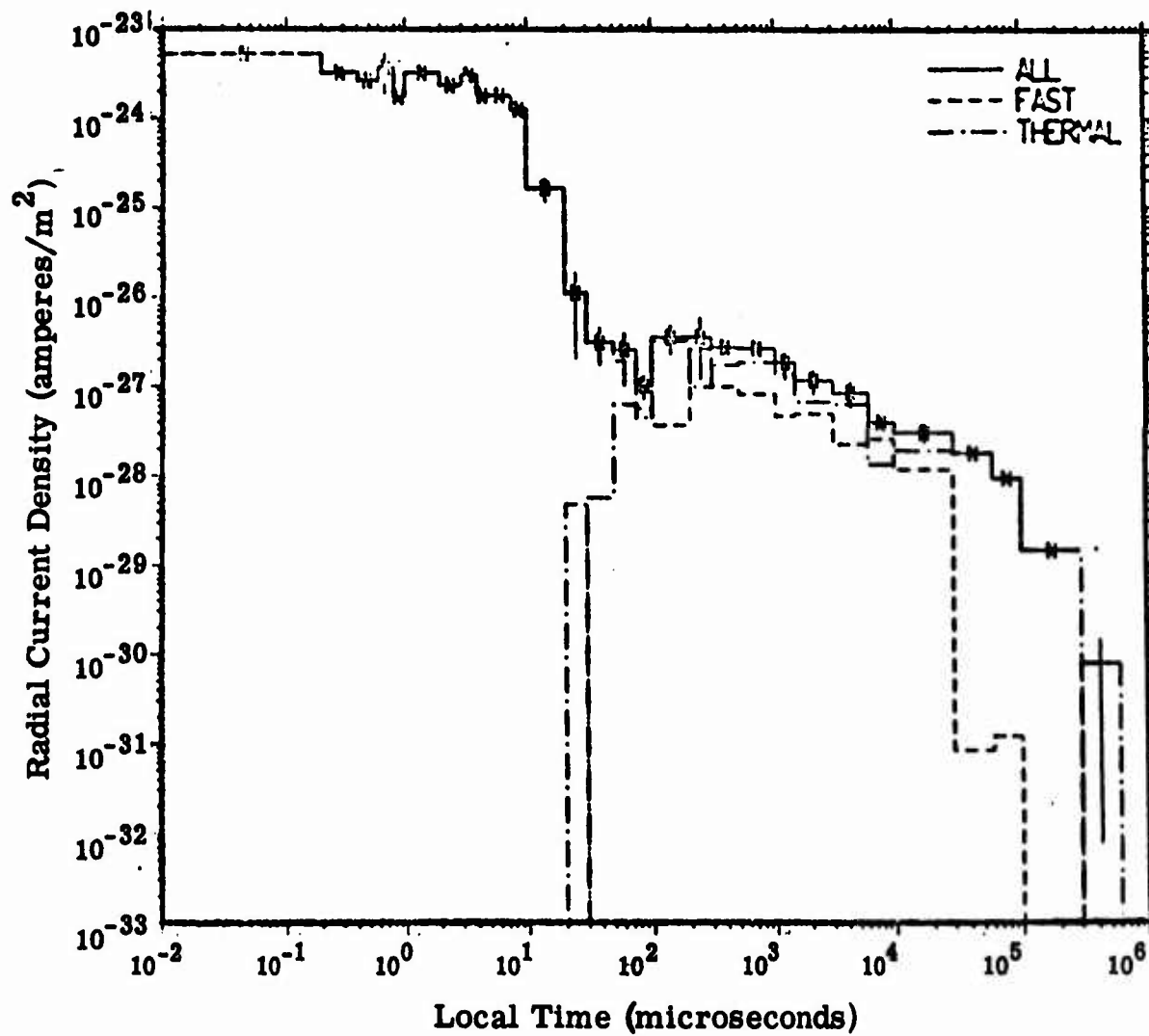


Figure 2.23. Radial current at radius 450 - 550 meters,  $\cos \theta = 0 - 0.1$ , due to thermonuclear source for  $H_oB = 200$  meters.

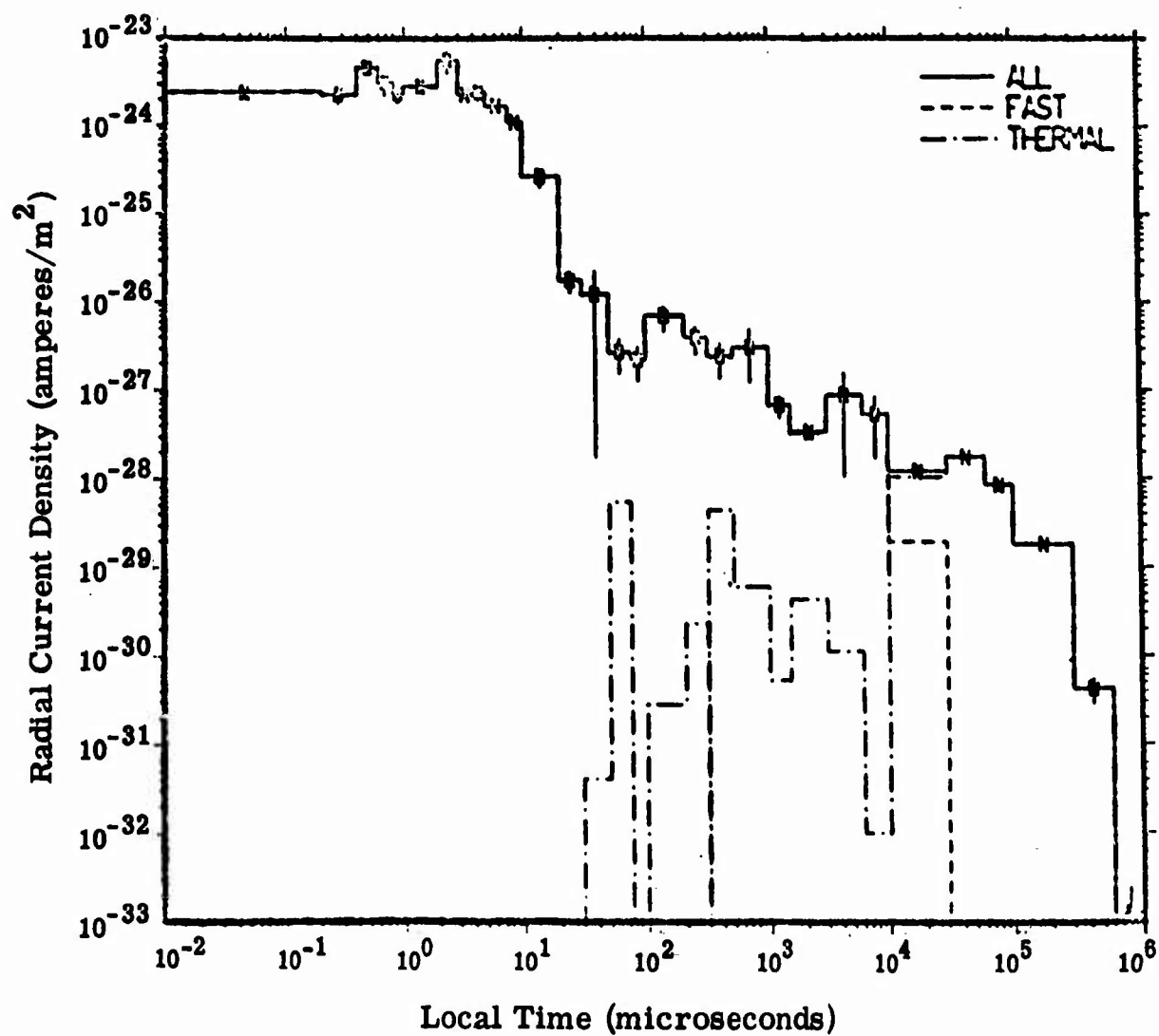


Figure 2.24. Radial current at radius 450 - 550 meters,  $\cos \theta = 0 - 0.1$ , due to thermonuclear source for HoB = 500 meters.



In Fig. 2.25 a comparison is made of the ionization rate for the  $\cos \theta = 0.5 - 1.0$  bin between the HoB = 0 m and HoB = 200 m sources. A radial range of 450 - 550 m is again used. The ionization rate at early times below 1  $\mu\text{sec}$  is again much higher for the ground burst. From 1  $\mu\text{sec}$  to 100  $\mu\text{sec}$  the two sources give very comparable results, while between 100 and  $10^4$   $\mu\text{sec}$  the HoB = 0 m source is again substantially higher. The results to  $10^4$   $\mu\text{sec}$  are basically consistent with conclusions drawn in comparing the two sources in last year's effort. <sup>(3)</sup> However, the deviations between the two sources in the time interval 100 -  $10^4$   $\mu\text{sec}$  appear to be somewhat larger in the previous work. Furthermore, beyond  $10^4$   $\mu\text{sec}$  the two sources yield approximately equal results. It appears that the inclusion of air capture events in the present calculations enhances the HoB = 200 m results relative to the ground burst calculations. We have also compared the HoB = 200 m source results with HoB = 500 m calculations for this angular bin and found close agreement between the two sources out to 100  $\mu\text{sec}$ . From 100  $\mu\text{sec}$  to  $3 \times 10^4$   $\mu\text{sec}$ , factor of 2 variations are observed with the 200 m HoB results higher, and good agreement is again seen at very late times. In general the agreement between the HoB = 200 m and HoB = 500 m sources is very good for this spatial bin.

The effects of the neutron source altitude on ionization rates in the ground is illustrated in the next four figures. In Fig. 2.26 a comparison is made between ionization rates due to a ground burst and due to the HoB = 200 m source for the 450 - 550 m radial bin and for a depth of 0-2 cm. Beyond the first few fractions of a microsecond, the HoB = 200 m rates appear to be generally higher than the ground source results. A comparison between HoB = 200 m and HoB = 500 m ionization rates for the same ground bin is presented in Fig. 2.27. Here the 500 m HoB is consistently lower than the 200 m source at all times. For this bin,

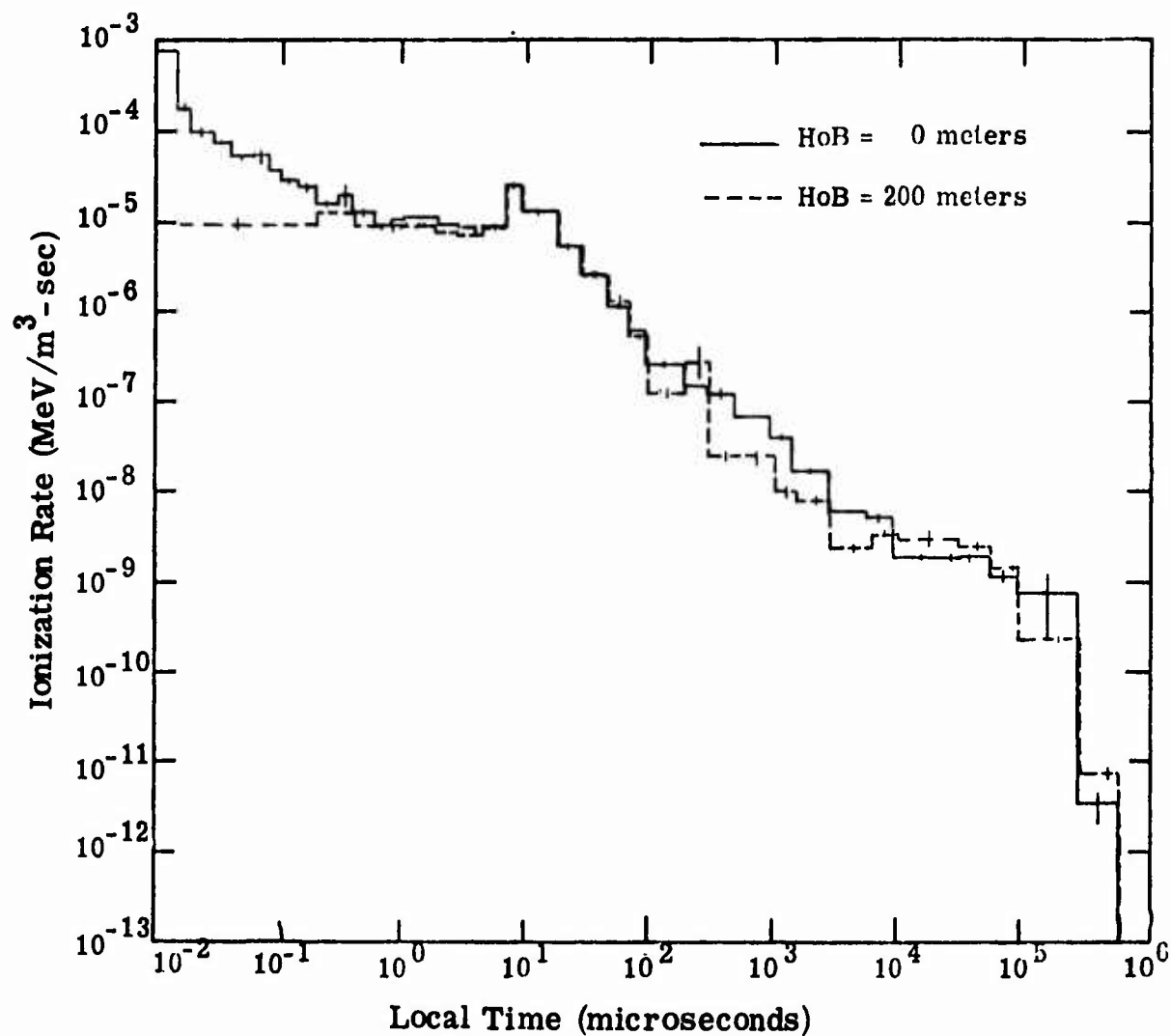
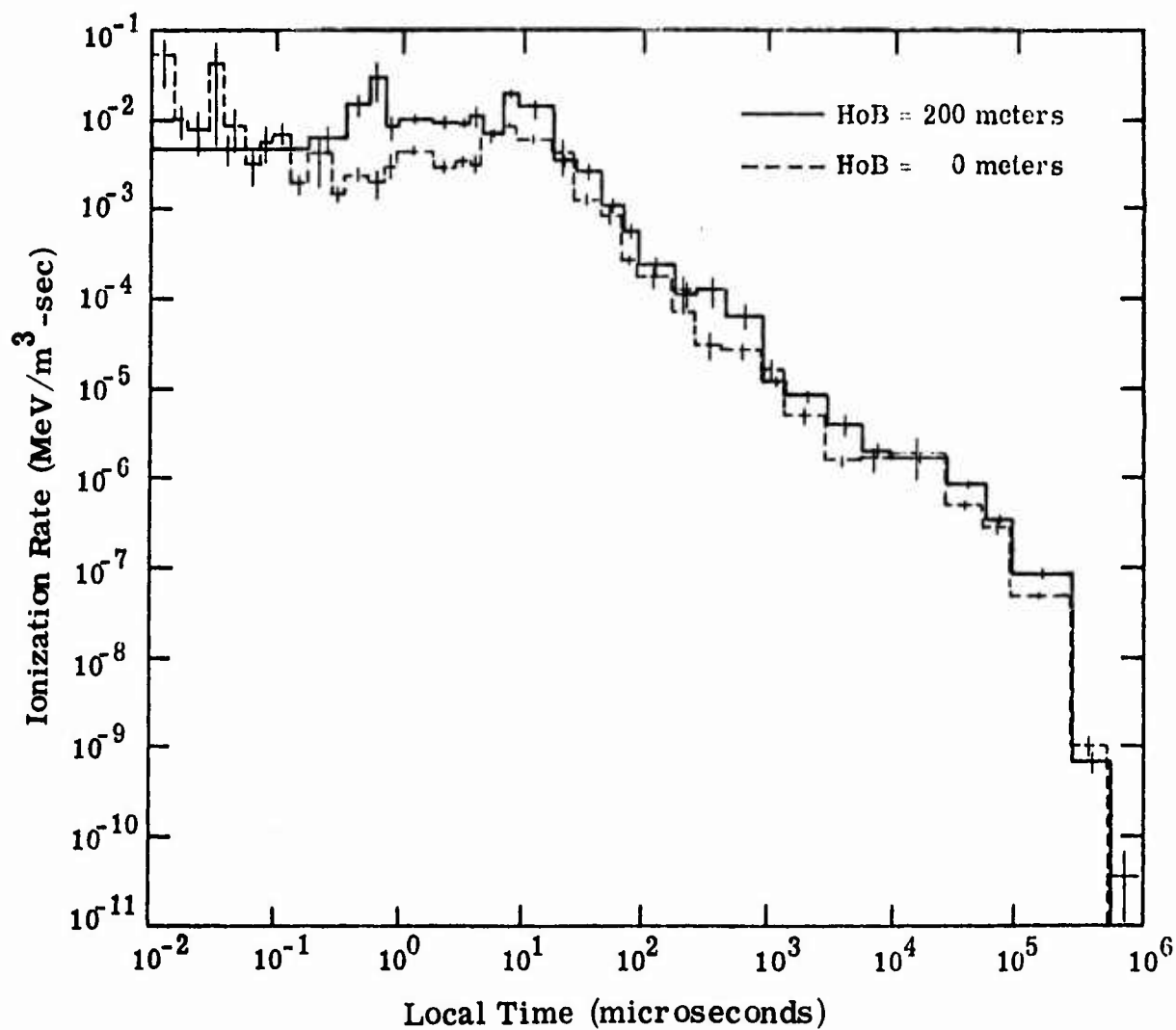


Figure 2.25. Ionization rate at radius 450 - 550 meters,  $\cos \theta = 0.5 - 1.0$ , due to thermonuclear source at HoB = 0 and HoB = 200 meters.



**Figure 2.26.** Ionization rate in ground, depth = 0 - 2 cm, radius = 450 - 550 meters, due to thermonuclear source at HoB = 0 and HoB = 200 meters.

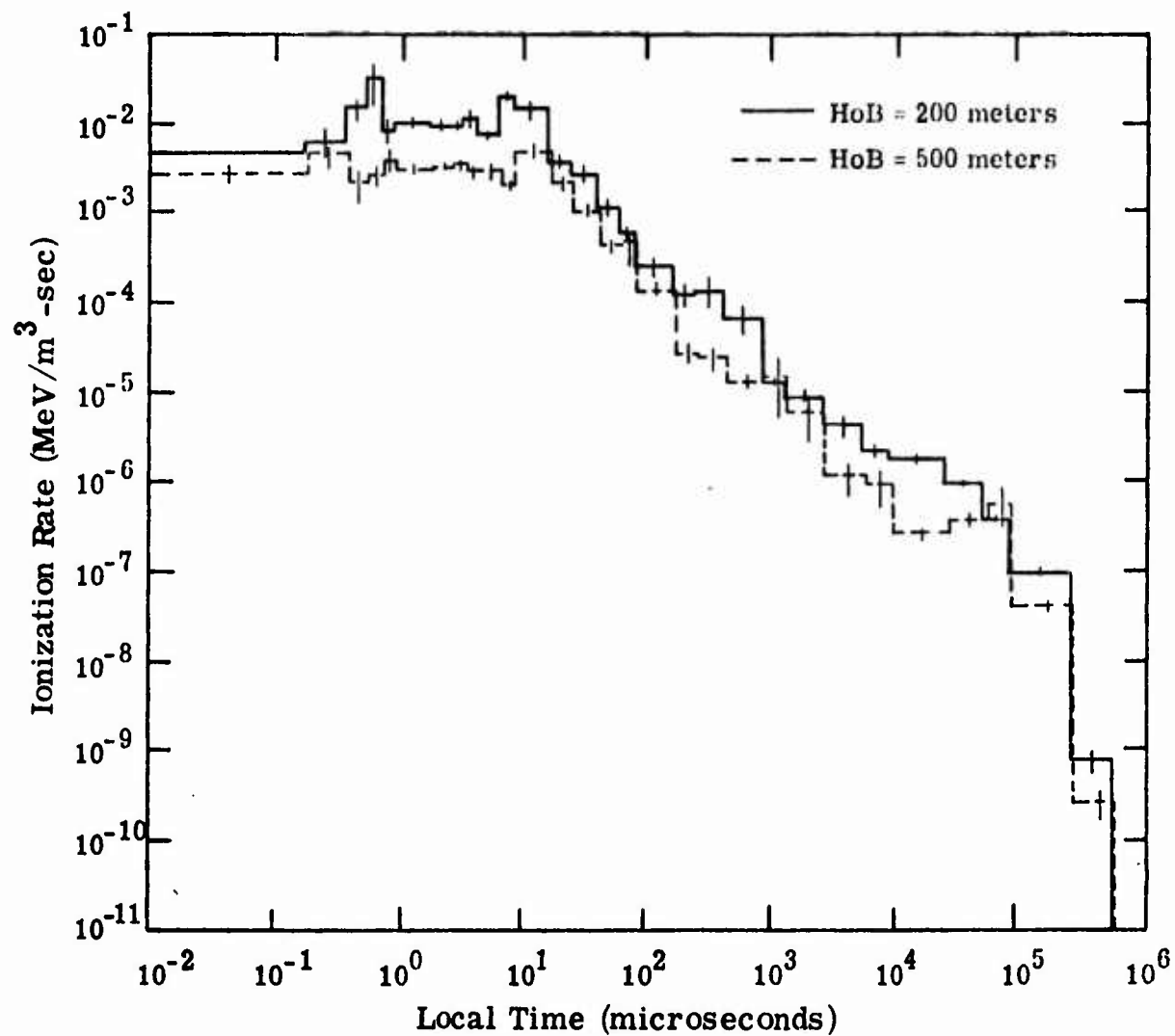


Figure 2.27. Ionization rate in ground, depth = 0 - 2 cm, radius = 450 - 550 meters, due to thermonuclear source at HoB = 200 and HoB = 500 meters.

the ionization rate due to the HoB = 200 m source exceeds the ground burst results since neutrons from the higher altitude source can reach the observation point without prior attenuating collisions in the ground. The ground burst source neutrons on the other hand are moderated to a greater extent by the ground at positions which are distant from the observation bin. Therefore, there is less neutron energy available for deposition in this bin. The probability of photon energy deposition is also reduced because the photons are born at positions which have smaller solid angle probabilities of eventually reaching the observation point. The HoB = 500 m ionization rates are generally lower than the 200 m source results because the higher altitude source neutrons are attenuated in the air to a greater extent than the HoB = 200 m neutrons. Therefore, the 500 m HoB neutron energy available for deposition in the 0 - 2 cm bin is less than the neutron energy available for the lower altitude source. Furthermore, the gamma ray energy deposited by the 500 m HoB source is lower than the HoB = 200 m results due to greater attenuation of gamma rays which are produced at the higher altitudes.

In Figs. 2.28 and 2.29 a comparison of the three source altitudes is made for the same range of 450 - 550 m, but for a deeper ground depth of 90 - 120 cm. Figure 2.28 compares the ground burst and the HoB = 200 m source for this bin. At very early times there is little ionization due to the ground source and the 200 m HoB ionization rate is much higher out to about 8  $\mu$ sec. Beyond 8  $\mu$ sec the differences between the two sources are much smaller. In Fig. 2.29 a comparison between the HoB = 500 m and HoB = 200 m sources for the 90 - 120 cm depth bin is made. In this case, the 500 m source gives larger ionization rates at early times to approximately 5  $\mu$ sec. Beyond 5  $\mu$ sec the ionization rate differences between the two sources are not very large with the HoB = 200 m source ionization rates generally higher.

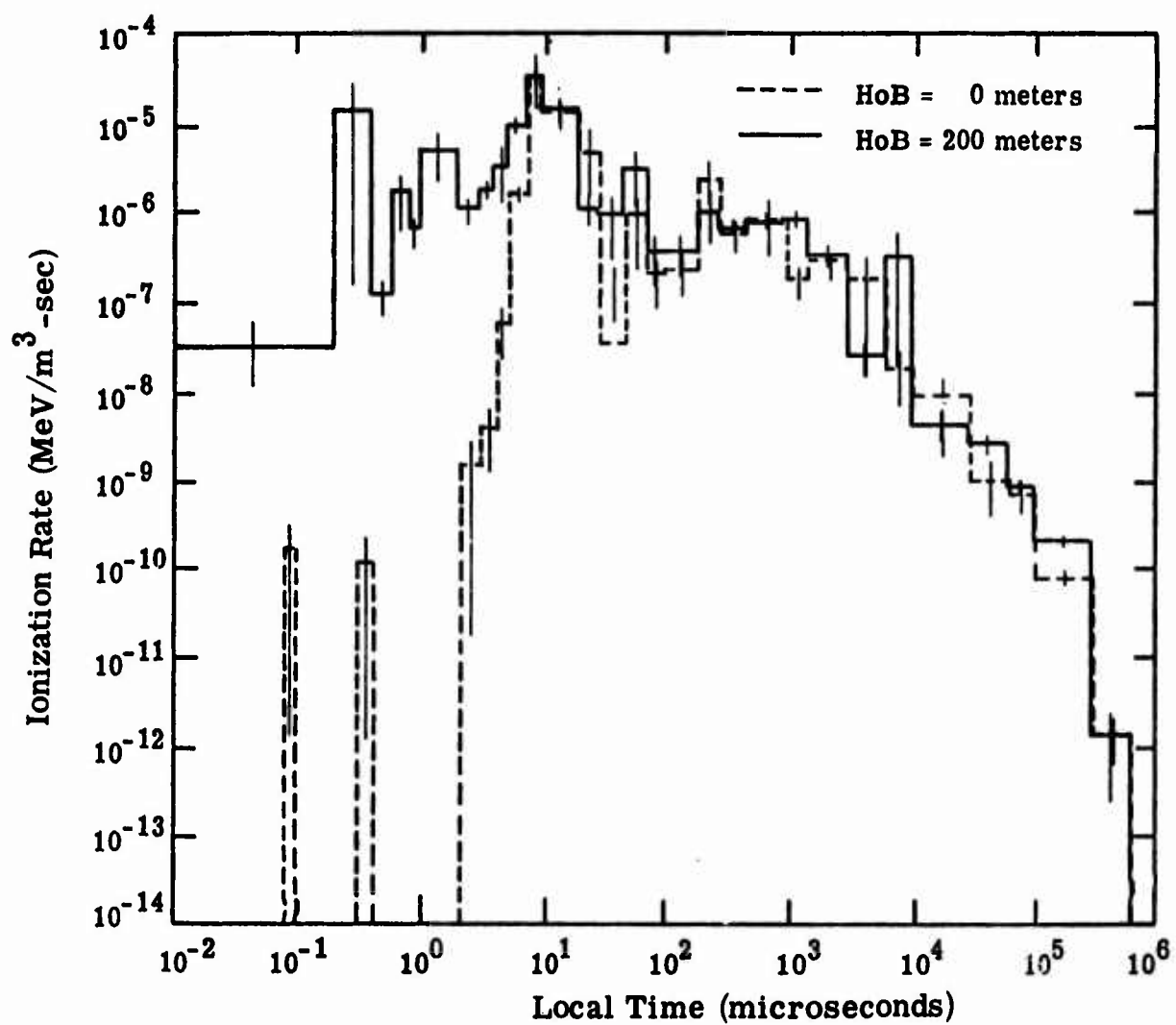
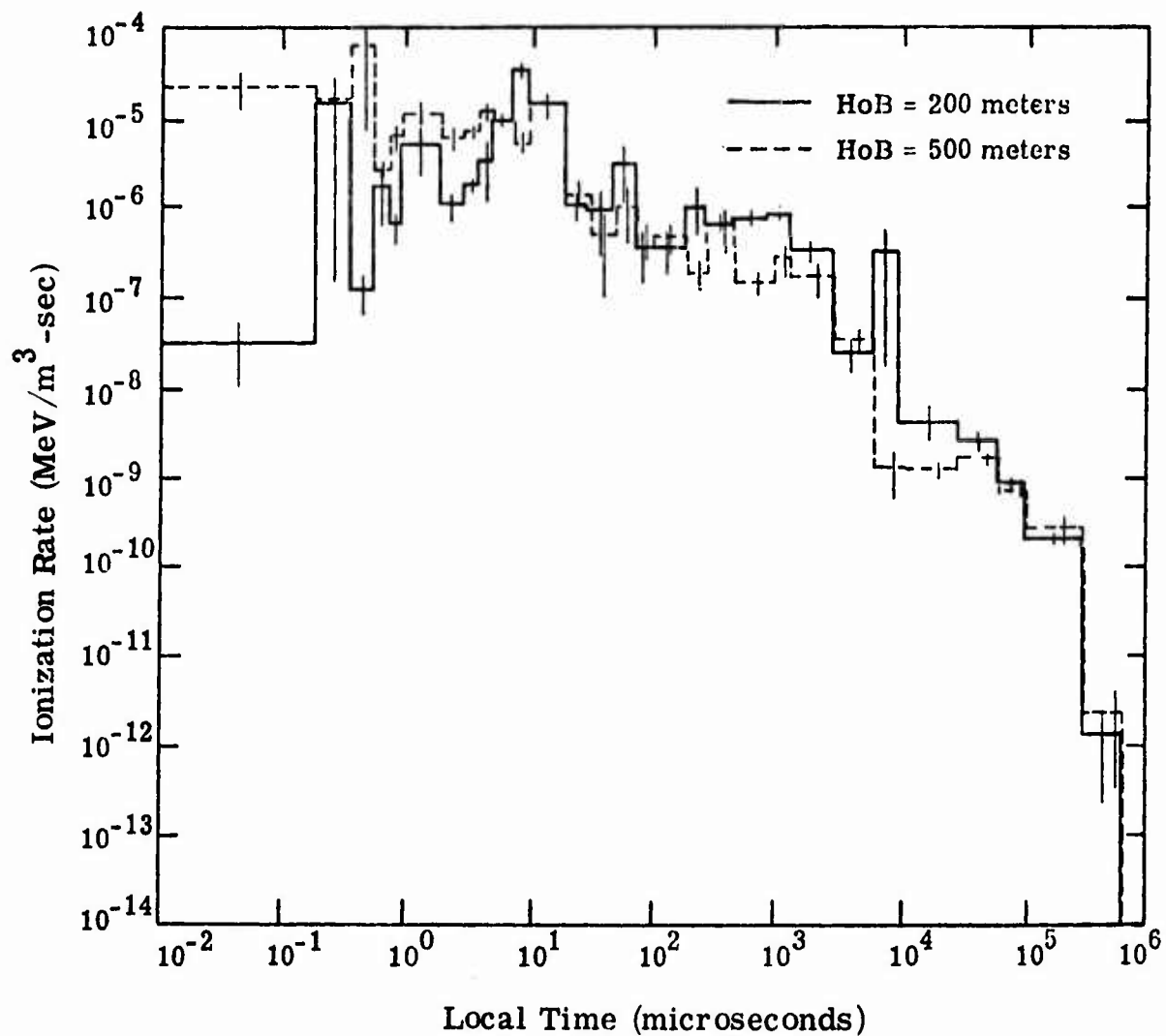


Figure 2.28. Ionization rate in ground, depth = 90 - 120 cm, radius = 450 - 550 meters, due to thermonuclear source at HoB = 0 and HoB = 200 meters.



**Figure 2.29.** Ionization rate in ground, depth = 90 - 120 cm, radius = 450 - 550 meters, due to thermonuclear source at HoB = 200 and HoB = 500 meters.

A geometrical explanation for the differences in ground ionization rates due to source altitude variations is shown in Fig. 2. 30. The point 0 represents an observation point below the air-ground interface at a range of approximately 500 m. At very early times the ionization at 0 is primarily due to photons which are produced close to the respective neutron source locations through inelastic scattering collisions. From the figure it is apparent that the prompt gamma rays born near the HoB = 500 m source must traverse less ground before reaching 0 than the prompt photons from the 200 m HoB. In turn, the HoB = 200 m prompt photons have far less ground to traverse than gamma rays born near the HoB = 0 m source. Therefore, at very early times we would expect the ionization rates for the HoB = 500 m source to be larger than the HoB = 200 m rates. In addition, the HoB = 200 m ionization rates at early times would be much larger than the HoB = 0 m results in which the prompt photons are attenuated to a great extent by the ground. At later times, source neutrons have migrated away from the respective source locations, so that photons produced by these neutrons will be distributed over wider areas. The ground distances that must be traversed by these photons to reach point 0, will not differ to as great an extent between the three sources as the prompt photons discussed above. Therefore, we would anticipate less deviation between ionization rates for the three sources for times later than several microseconds.

These remarks apply primarily to an observation point 0 which is deeply imbedded in the ground, e. g., the bin discussed above at a depth of 90 - 120 cm. In this case, the main factor in determining the ionization rate is the ground distance which must be traversed. For bins which are close to the air-ground interface, such as the 0 - 2 cm depth bin considered earlier, photons can contribute to the ionization rate



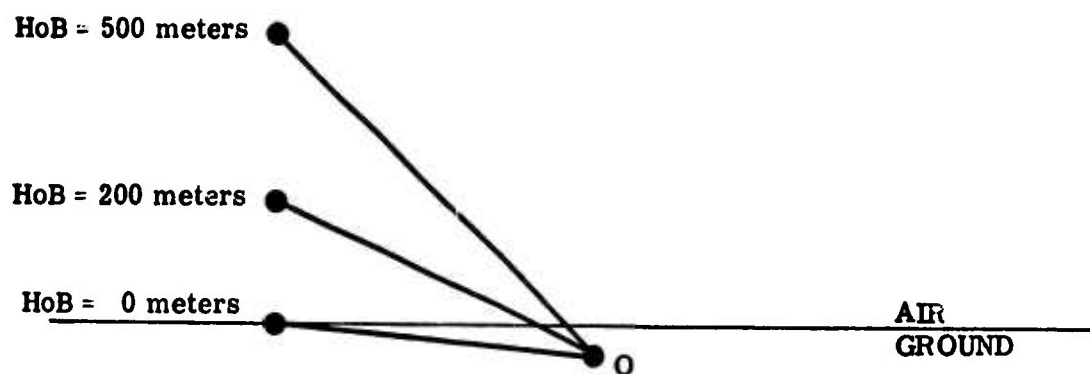


Figure 2.30. Geometrical explanation for the effect of source altitude on ground ionization rates.

without passing through the ground to any great degree. Furthermore, direct neutron contributions to the ionization rate become important for these bins, at local times of several microseconds, whereas for the deeper bins the ionization is dominated by photons due to their longer mean free path lengths. Therefore, the ionization rates for bins close to the air-ground interface are determined to some extent by the amount of air attenuation experienced by the photons and neutrons from the various sources.

From these and previous comments, it is clear that ionization rates as well as Compton currents are sensitive to source altitudes in some time and spatial bins and relatively insensitive in other cases. The same sensitivity and insensitivity can be seen for other radial positions as well. Arriving at general models to interpolate ionization rates and currents between HoB's appears to be a difficult task. Obtaining analytical fits to the data obtained for the three HoB's would be a useful initial step from which possible interpolation between the various altitudes might result. The effect of the source altitude is a very complicated function of the spatial bin of interest as well as the time interval under consideration. Further consideration of interpolation schemes could possibly result in general models which would eliminate lengthy computer calculations for intermediate burst heights.

In Figs. 2. 31 and 2. 32 we also include a brief comparison of the present O5RNIES calculations and the thermonuclear results obtained last year. A 200 m HoB is used in both calculations with a radial bin extending from 550 - 650 meters and an elevation bin extending from the ground to an altitude of 50 meters. Figure 2. 31 compares ionization rates for this bin while Fig. 2. 32 shows the vertical current densities for the two calculations. It is difficult to make a clean comparison between the

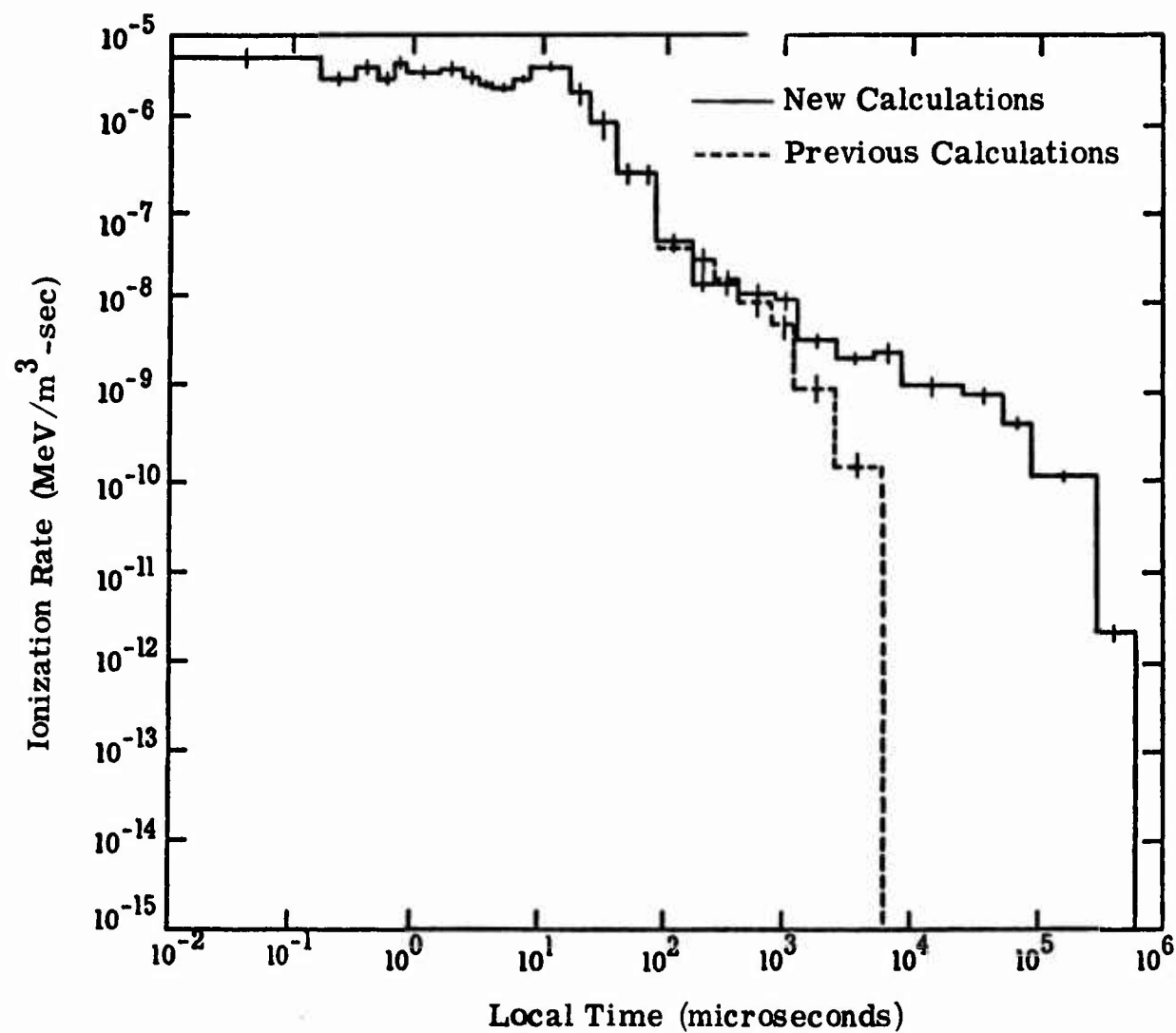


Figure 2. 31. Comparison of new and old ionization rate calculations at radius = 550 - 650 meters, elevation = 0 - 50 meters due to thermonuclear source at HoB = 200 m.

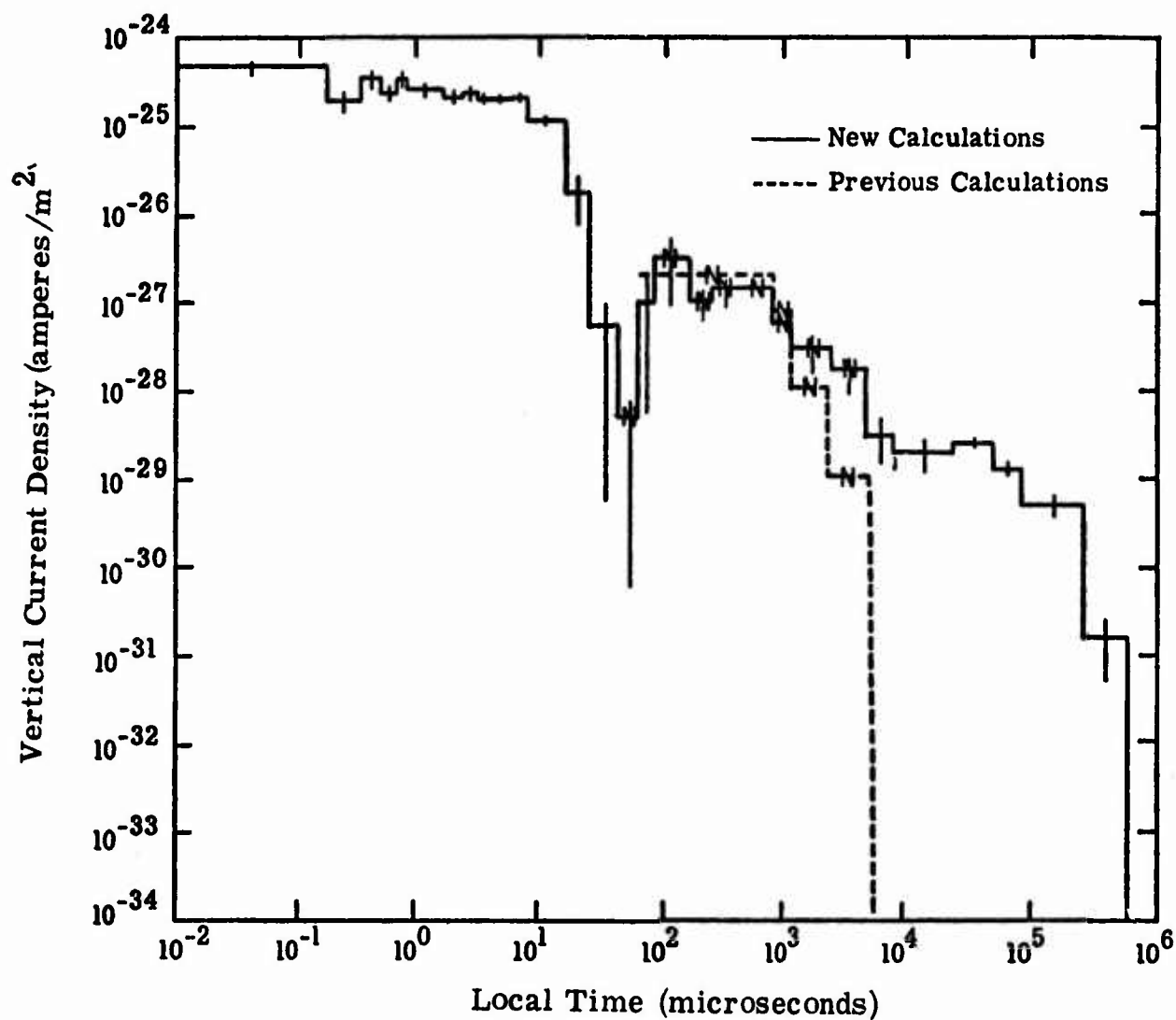


Figure 2.32. Comparison of new and old vertical current densities at radius = 550 - 650 meters, elevation = 0 - 50 meters due to a thermonuclear source at HoB = 200 m.

previous calculations and the new results since a new set of neutron and gamma ray production cross sections has been utilized. The sensitivity of transport and EMP calculations to cross section changes is discussed more completely in Section 4.5. However, from Figs. 2.31 and 2.32 it is apparent that the inclusion of air capture events in the new calculations results in much larger sources at very late times. At early times, the new and previous results are in reasonable agreement, and we have chosen to only show the previous results starting at approximately 100  $\mu$ sec. Beyond 100  $\mu$ sec the two sets of calculations begin to deviate substantially. These large differences at late times cannot be explained on the basis of cross section differences between the two calculations, but must be attributed to the treatment of air capture reactions in the new version of O5RNIES. The two comparisons presented here are representative of calculational trends in other spatial bins, namely reasonable agreement between the new and previous calculations at early times, and much higher EMP sources at late times in the new calculations.

The results presented to this point have been concerned primarily with the radial interval extending from 450 - 550 meters. We will now present a number of other radial intervals for the three HoB sources. The results at other ranges qualitatively display the same behavior discussed above for the 450 - 550 meter range. In Figs. 2.33 - 2.82 we present a number of new calculations at ranges of 850 - 1050 m, 1900 - 2100 m, and 2700 - 3100 m for the three neutron sources. We also display a few calculations for the bin at 4000 - 5000 m. For this last radial bin, the statistical uncertainties in general are large, since long computer execution times or extreme biasing schemes are required to obtain results with small error bars.

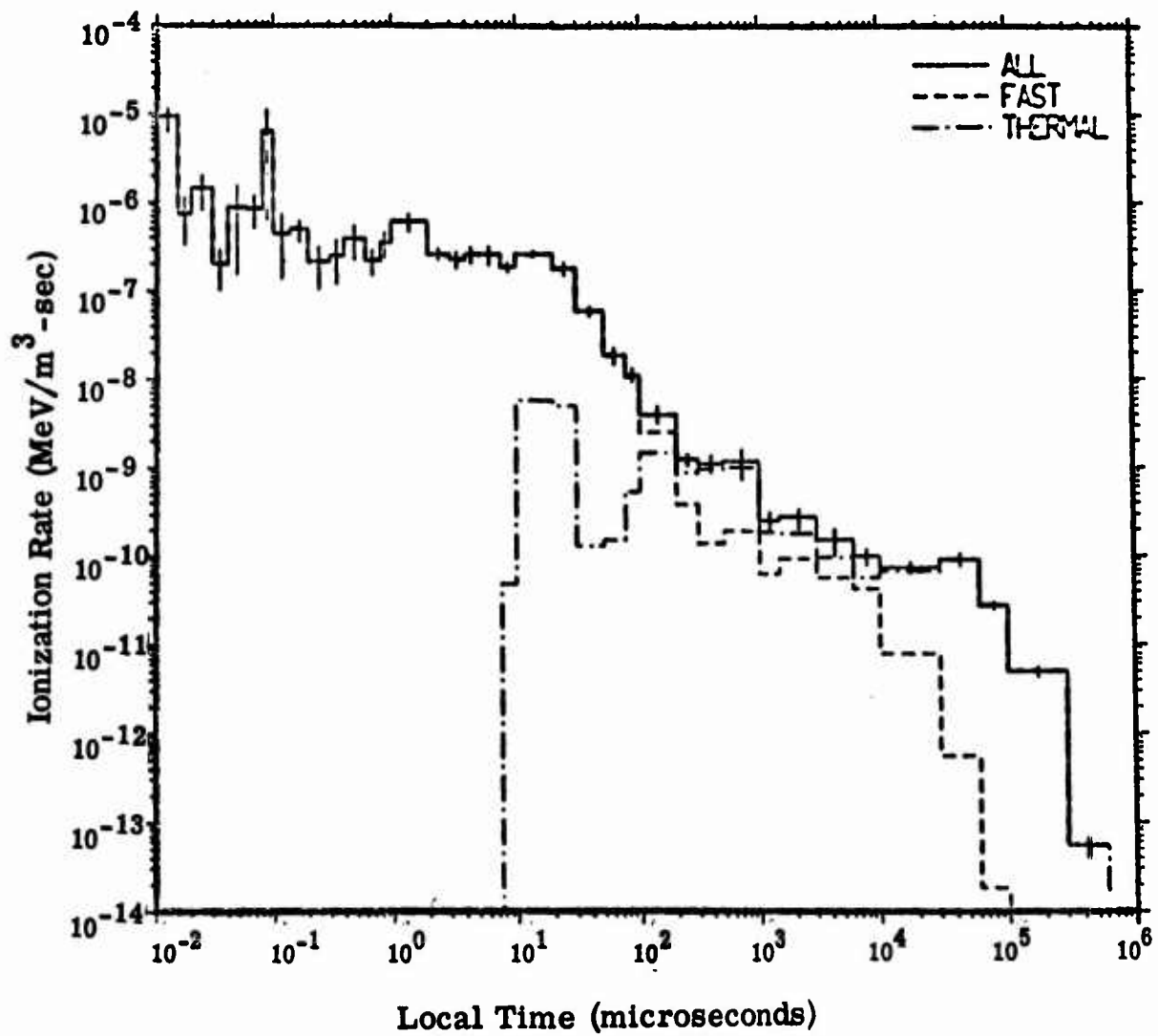


Figure 2.33. Ionization rate at radius = 850 - 1050 meters,  $\cos \theta = 0.0 - 0.05$ , due to thermonuclear source on ground.

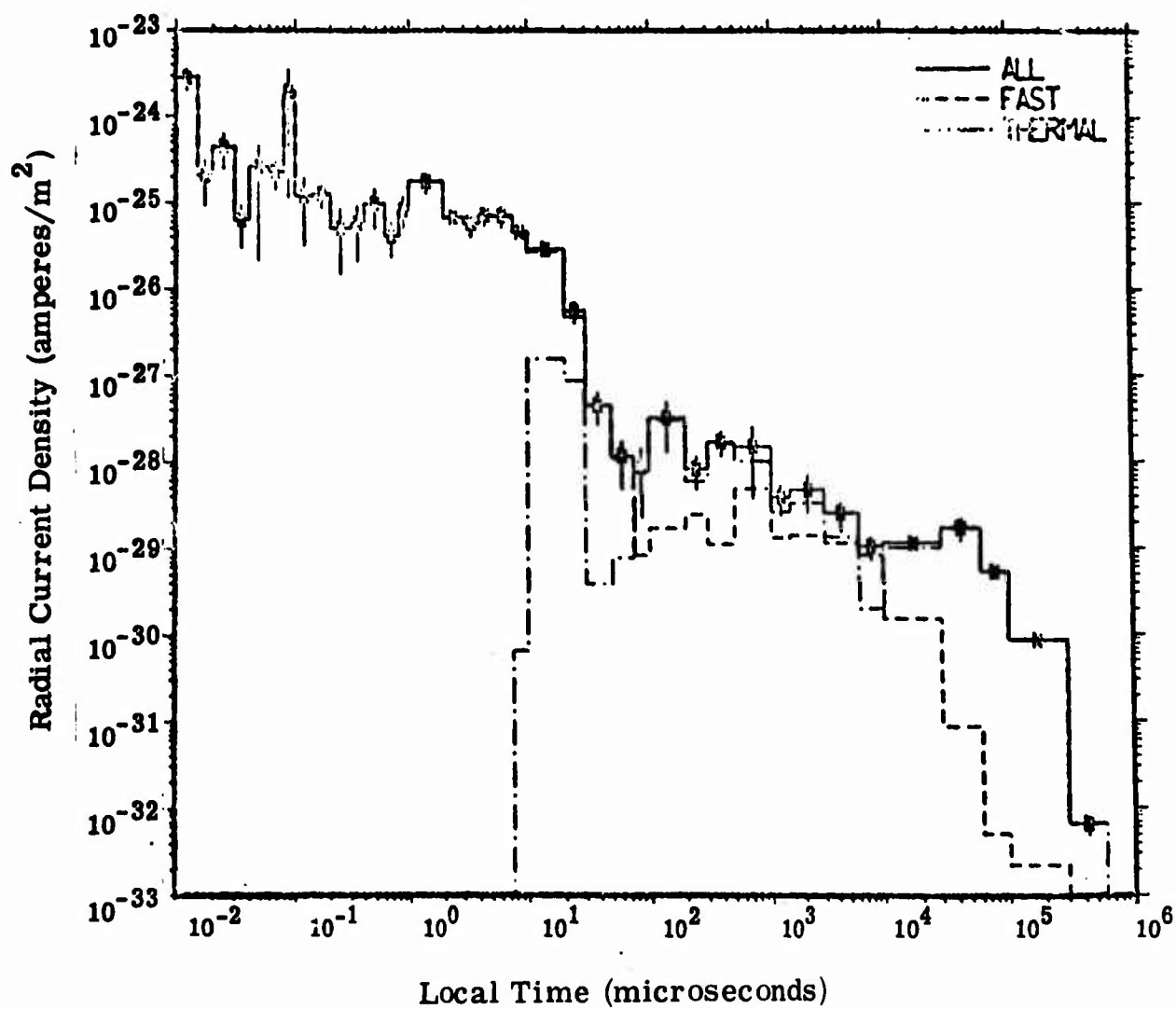


Figure 2.34. Radial current density vs. time at radius 850 - 1050 m,  $\cos \theta = 0.0 - 0.05$ , due to thermo-nuclear source on ground.

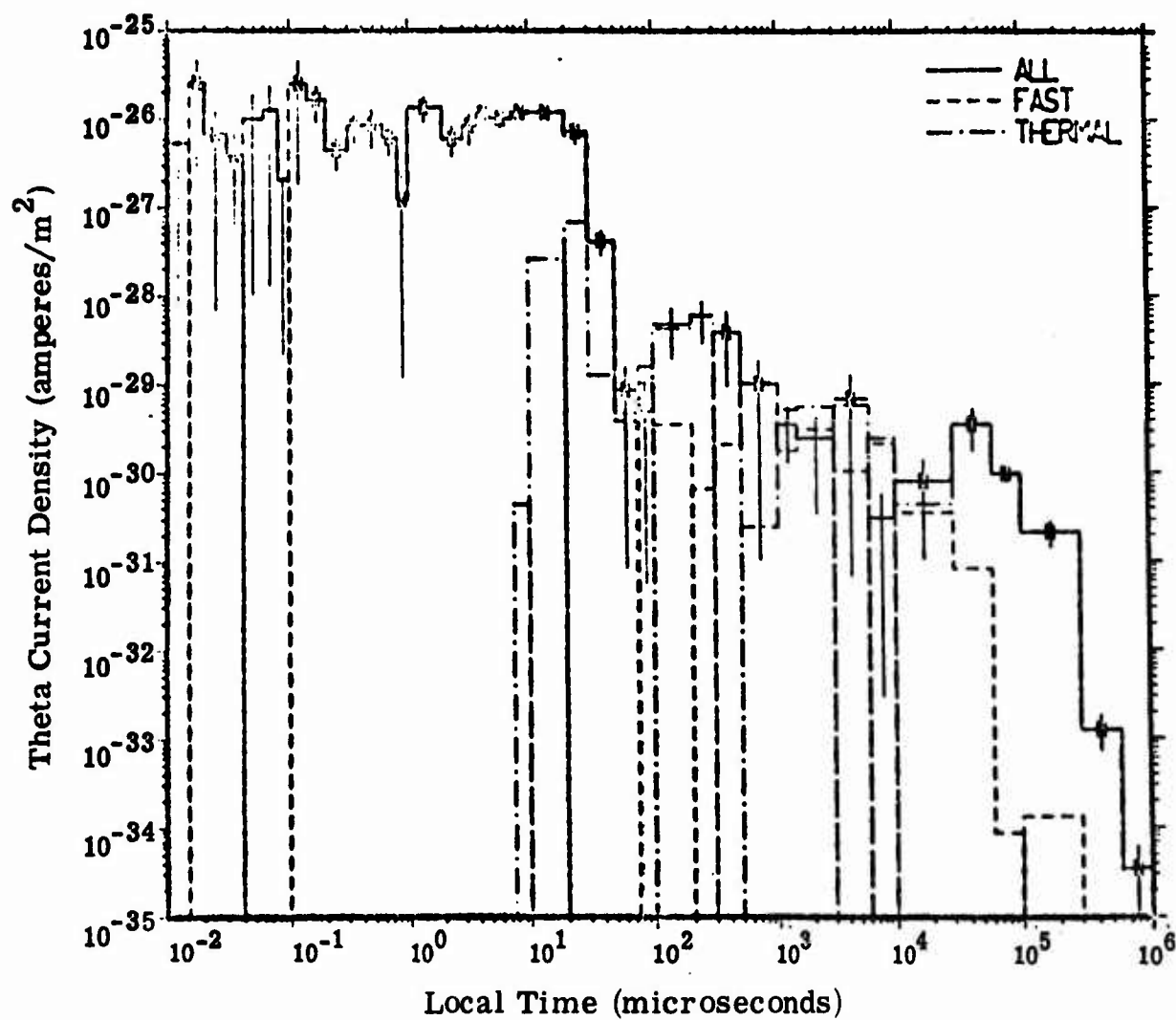


Figure 2.35. Theta current density vs. time at radius = 850 - 1050 m,  $\cos \theta = 0.0 - 0.05$ , due to thermonuclear source on ground.



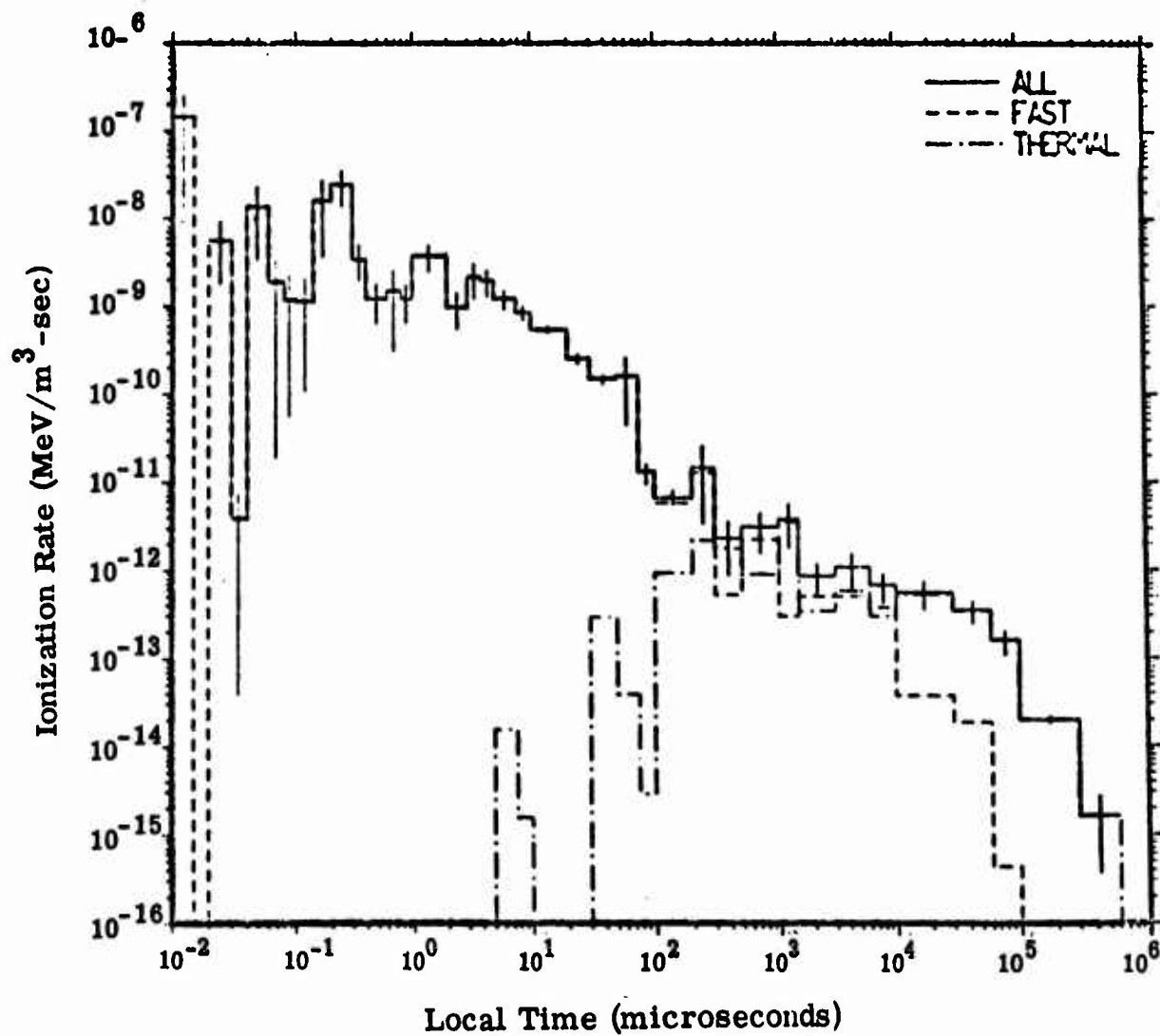


Figure 2.36. Ionization rate vs. time at radius = 1900 - 2100 m,  $\cos \theta = 0.0 - 0.05$ , due to thermonuclear source on ground.

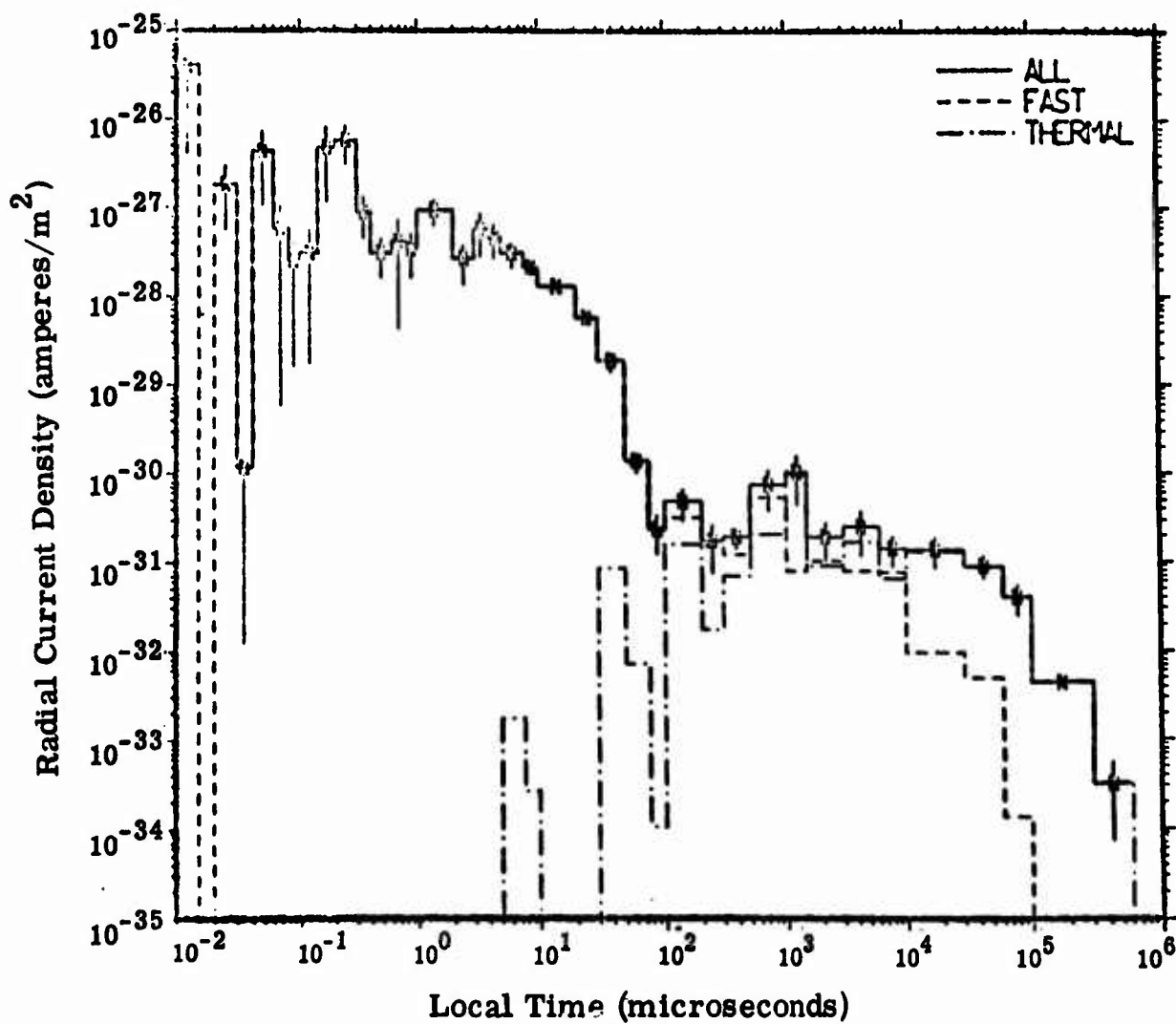


Figure 2.37. Radial current density vs. time at radius = 1900 - 2100 m,  $\cos \theta = 0.0 - 0.05$ , due to thermonuclear source on ground.

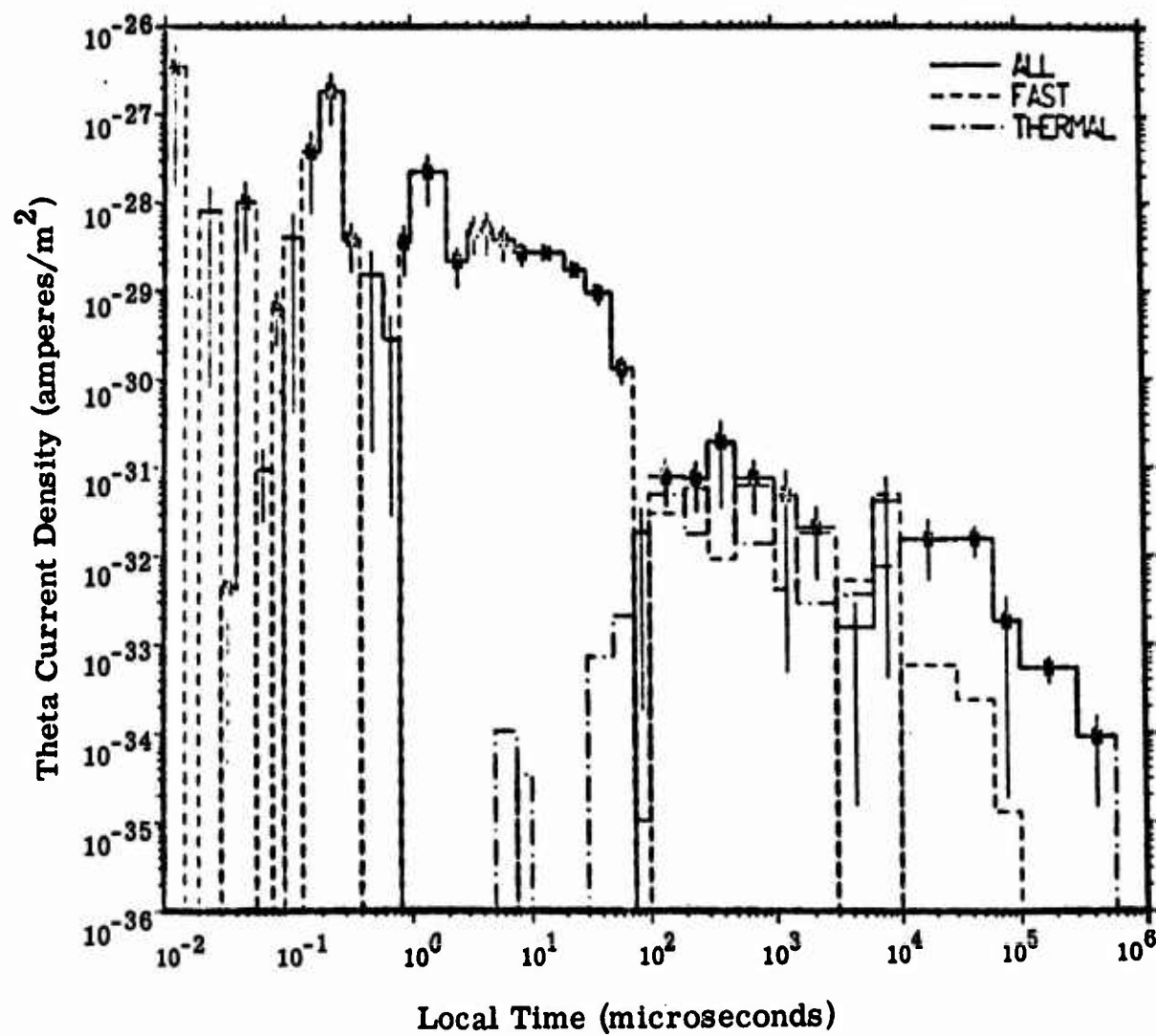


Figure 2.38. Theta current density vs. time at radius = 1900 - 2100 m,  $\cos \theta = 0.0 - 0.05$ , due to thermonuclear source on ground.

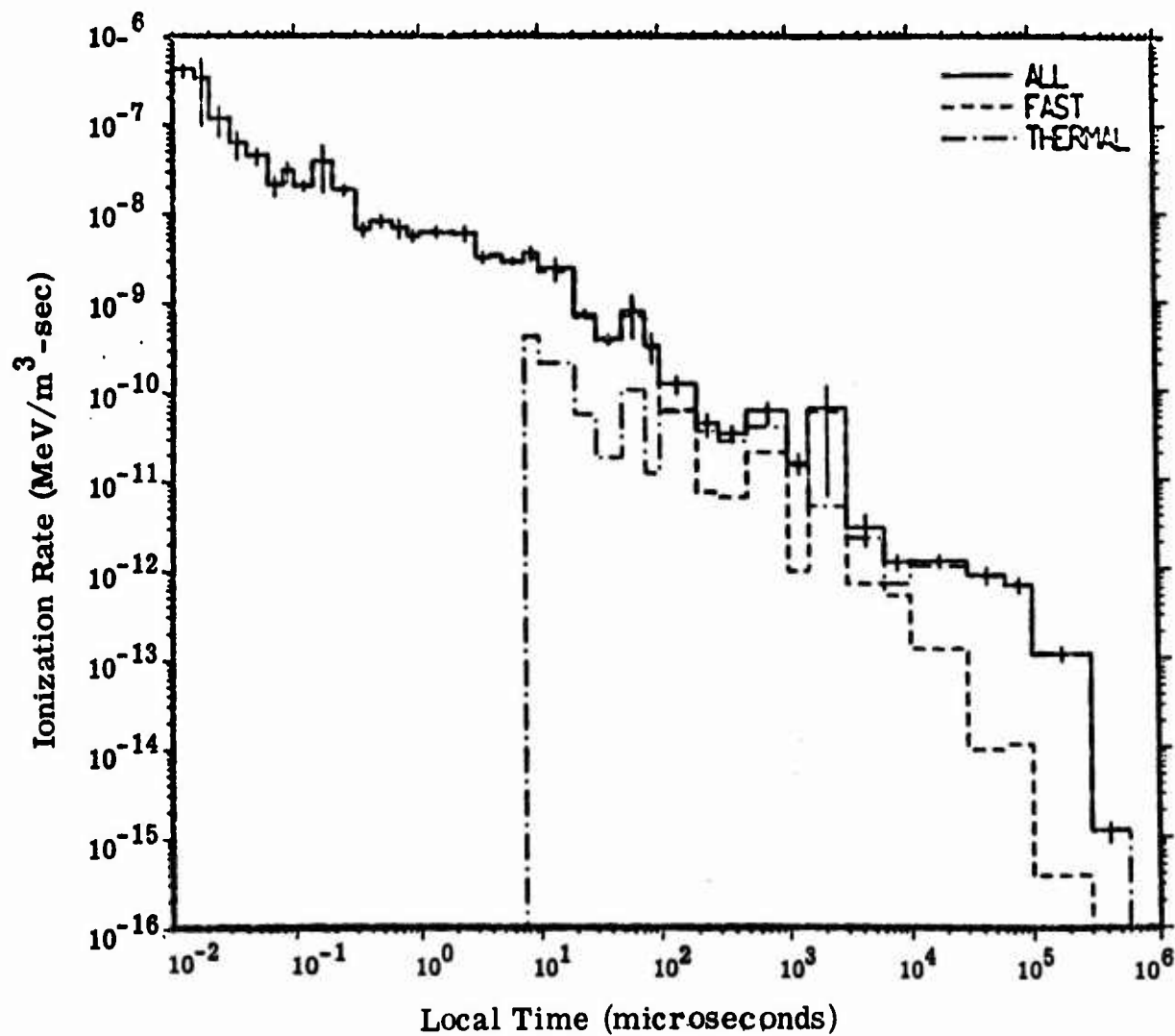


Figure 2.39. Ionization rate vs. time at radius = 1900 - 2100 m,  $\cos \theta = 0.5 - 1.0$ , due to thermonuclear source on ground.

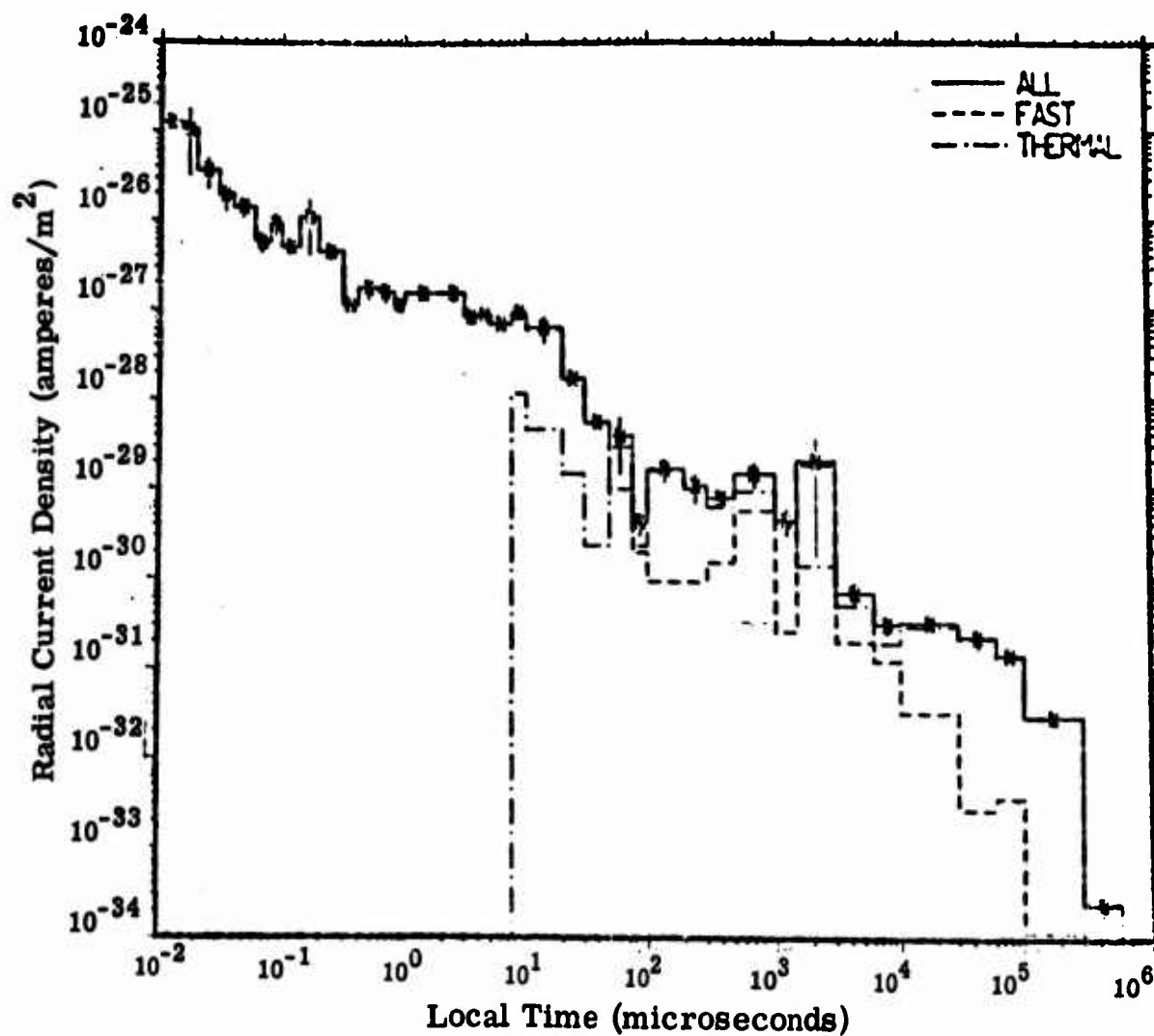


Figure 2.40. Radial current density vs. time at radius = 1900 - 2100 m,  $\cos \theta = 0.5 - 1.0$ , due to thermonuclear source on ground.

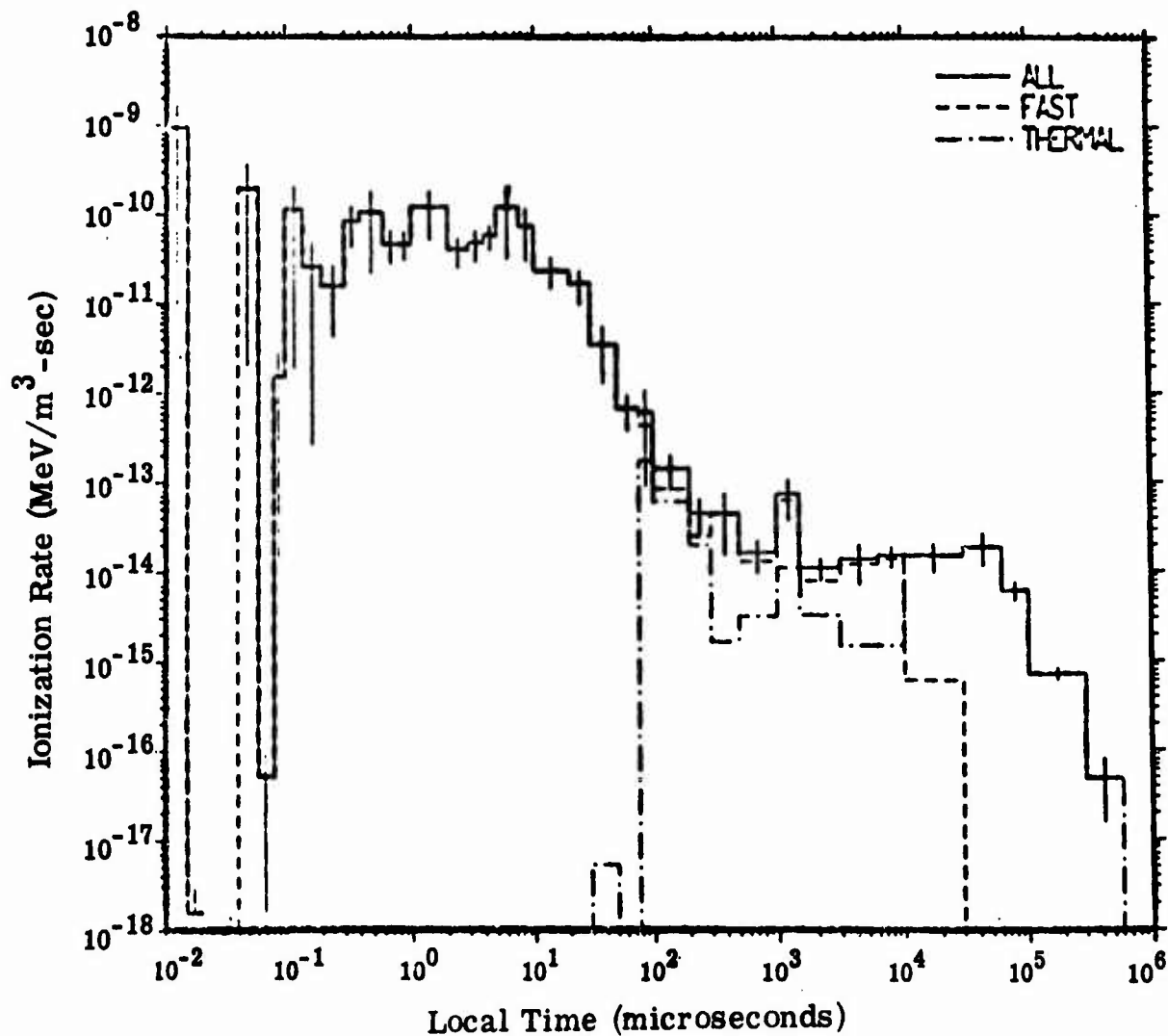


Figure 2.41. Ionization rate vs. time at radius = 2700 - 3100 m,  $\cos \theta = 0.0 - 0.05$ , due to thermonuclear source on ground.

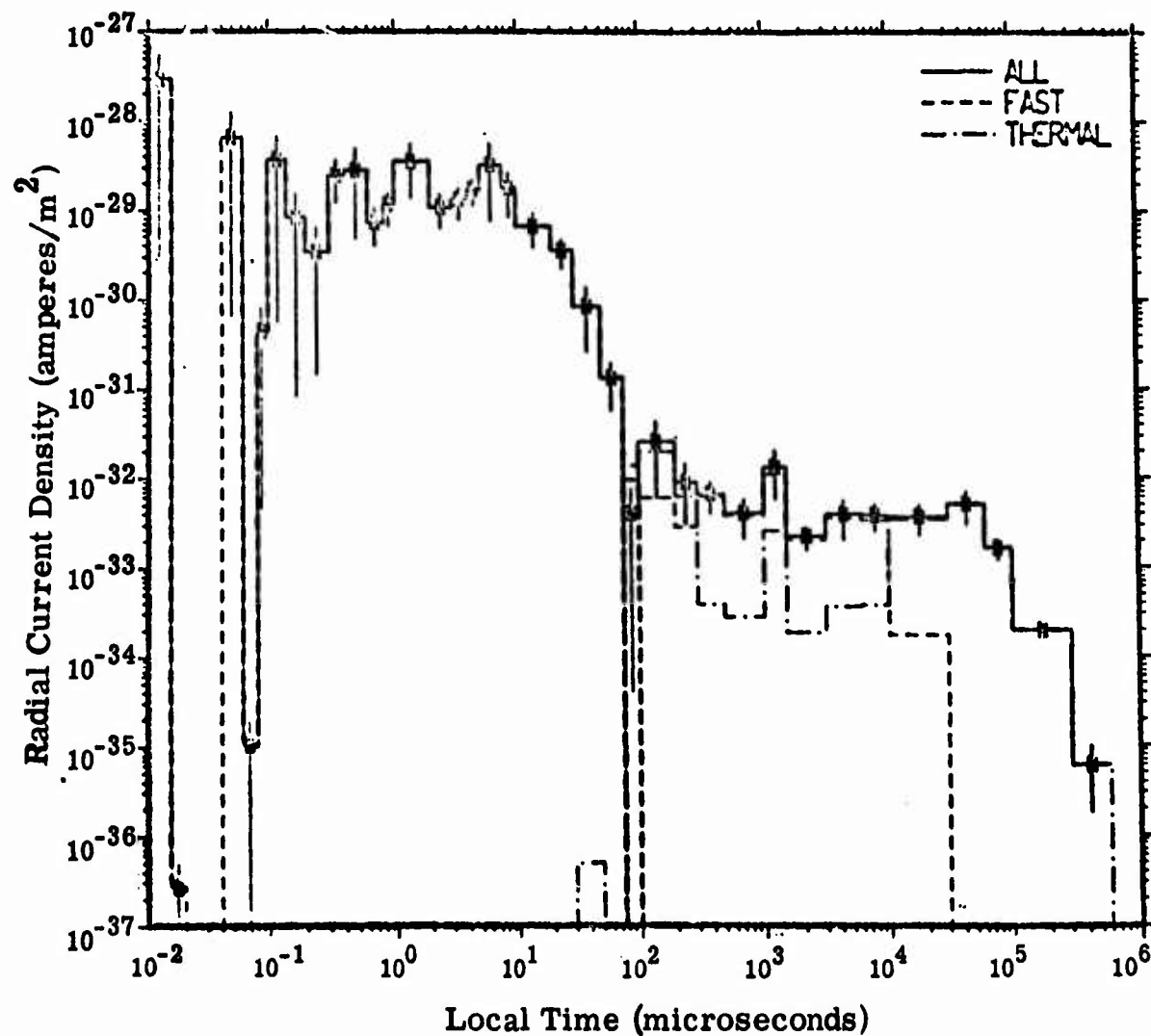


Figure 2.42. Radial current density vs. time at radius = 2700 - 3100 m,  $\cos \theta = 0.0 - 0.05$ , due to thermonuclear source on ground.

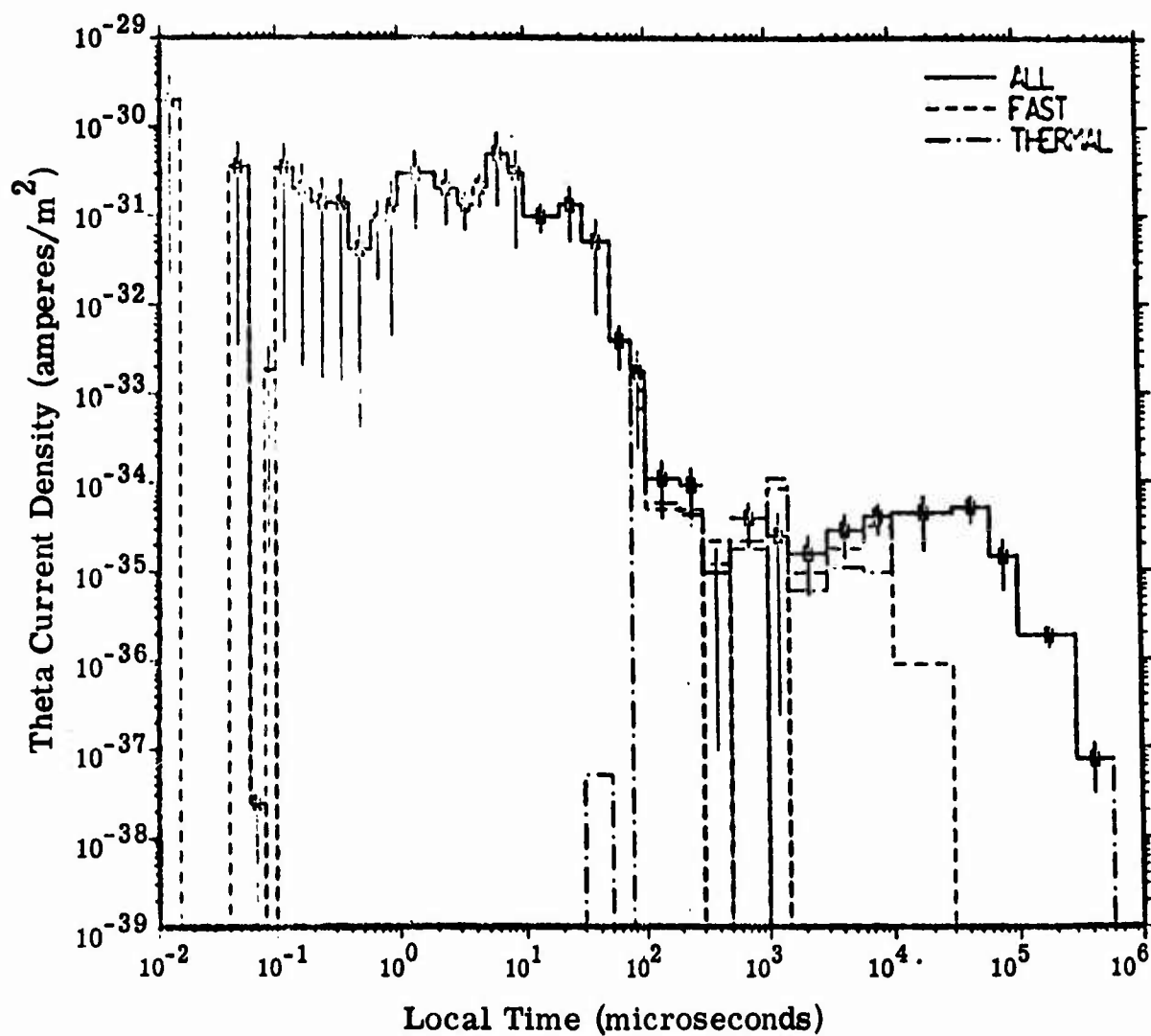


Figure 2.43. Theta current density vs. time at radius = 2700 - 3100 m,  $\cos \theta = 0.0 - 0.05$ , due to thermonuclear source on ground.



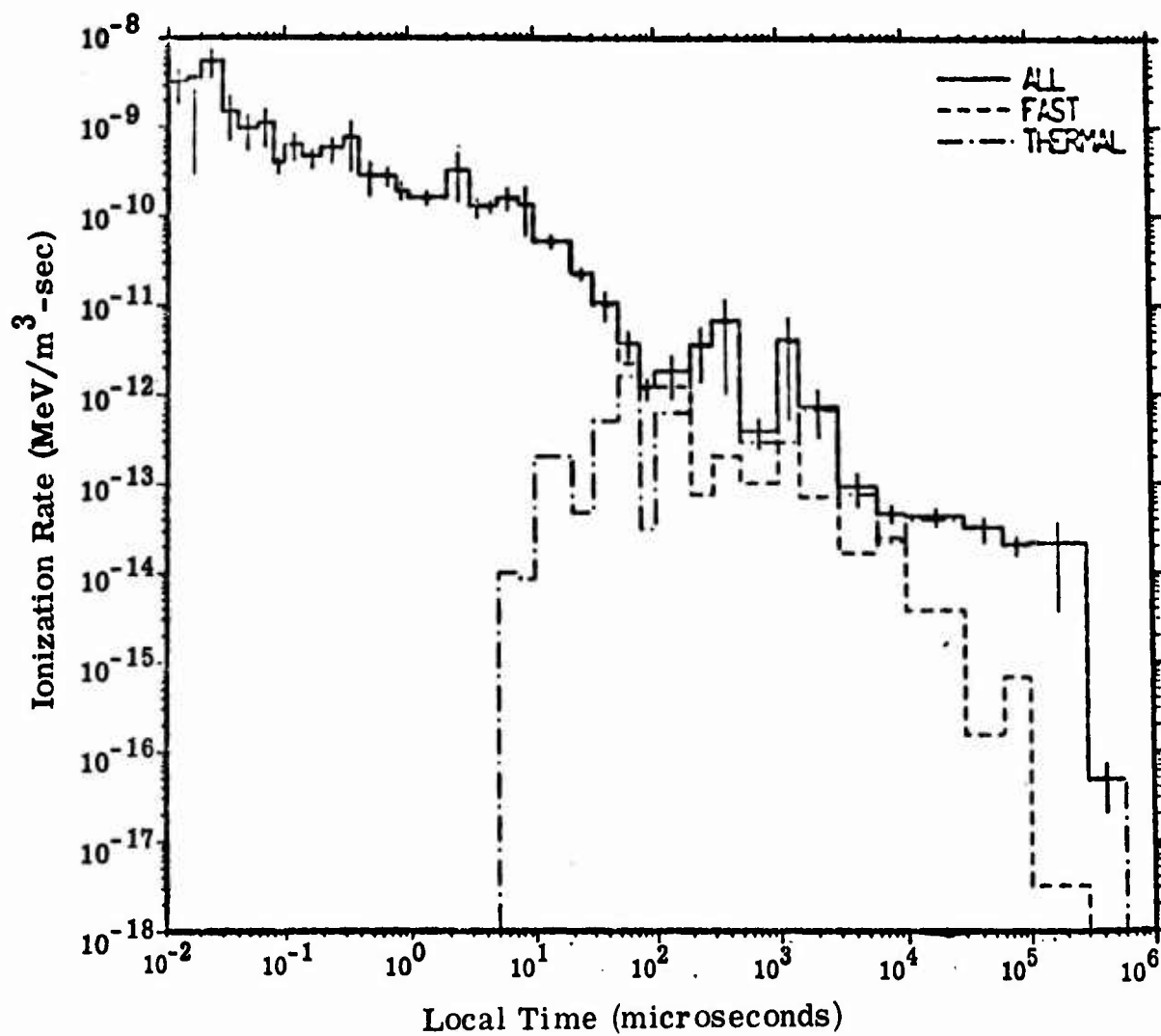


Figure 2.44. Ionization rate vs. time at radius = 2700 - 3100 m,  $\cos \theta = 0.5 - 1.0$ , due to thermo-nuclear source on ground.

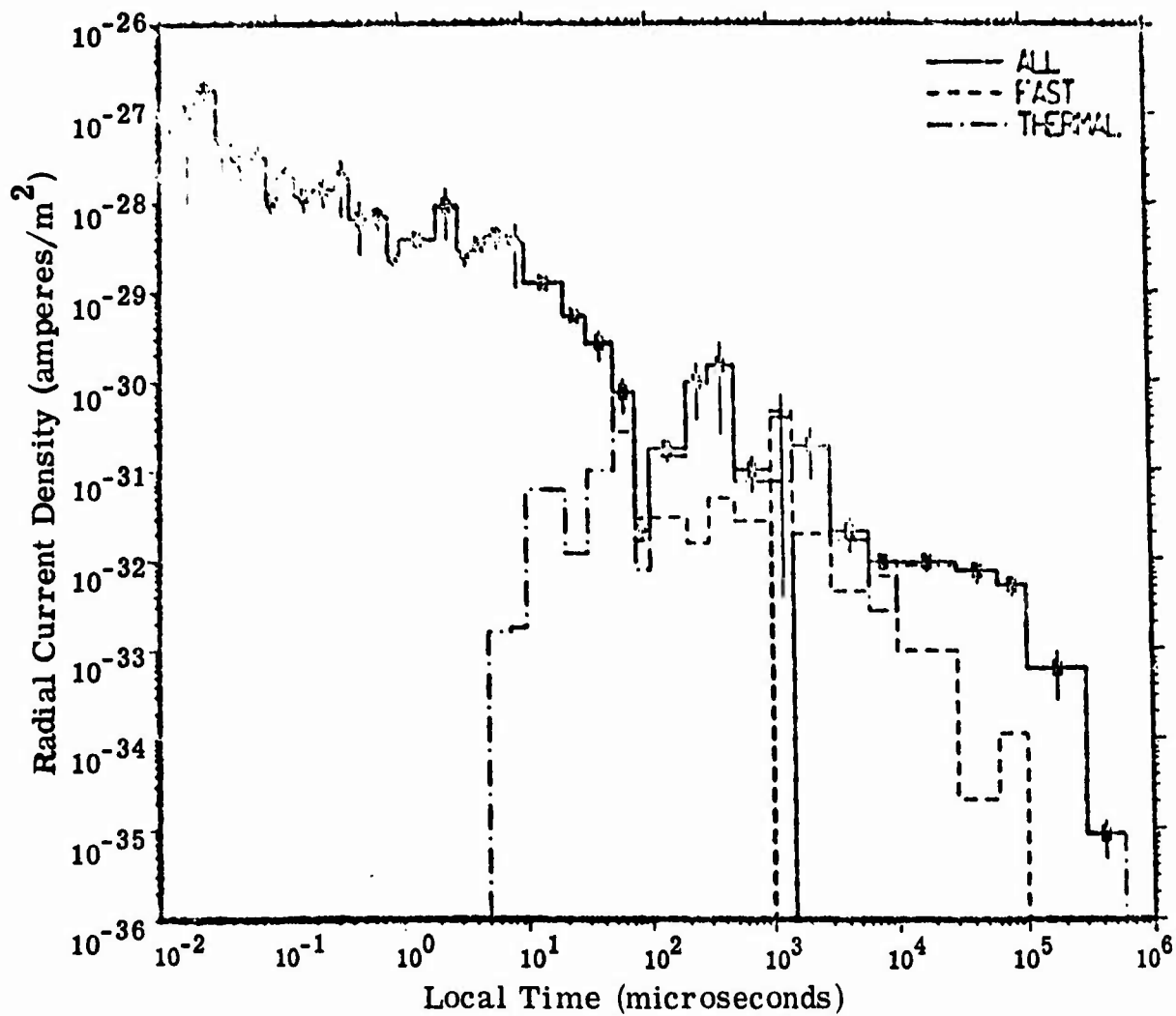


Figure 2.45. Radial current density vs. time at radius = 2700 - 3100 m,  $\cos \theta = 0.5 - 1.0$ , due to thermonuclear source on ground.

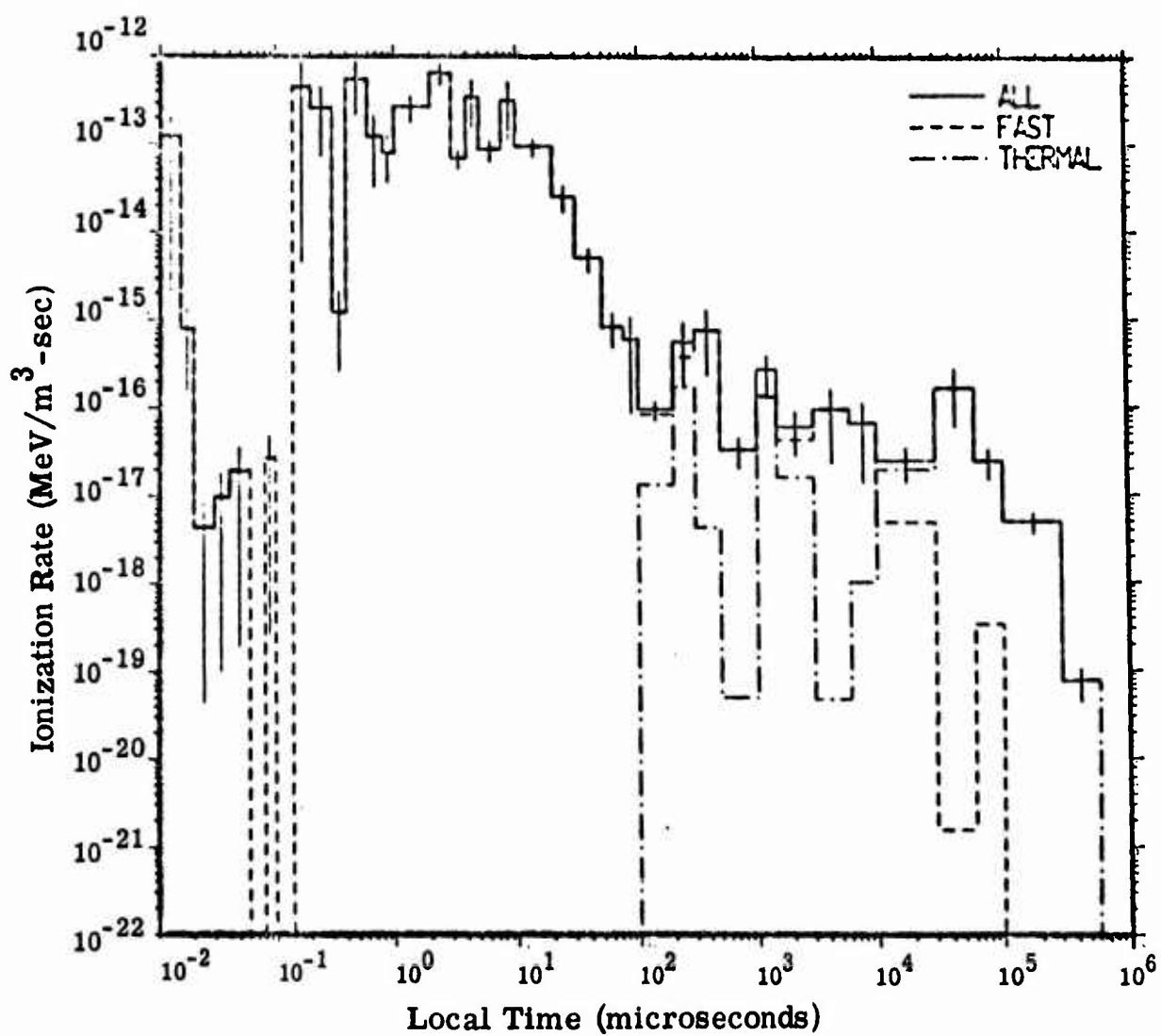


Figure 2.46. Ionization rate vs. time at radius = 4000 - 5000 m,  $\cos \theta = 0.0 - 0.05$ , due to thermonuclear source on ground.

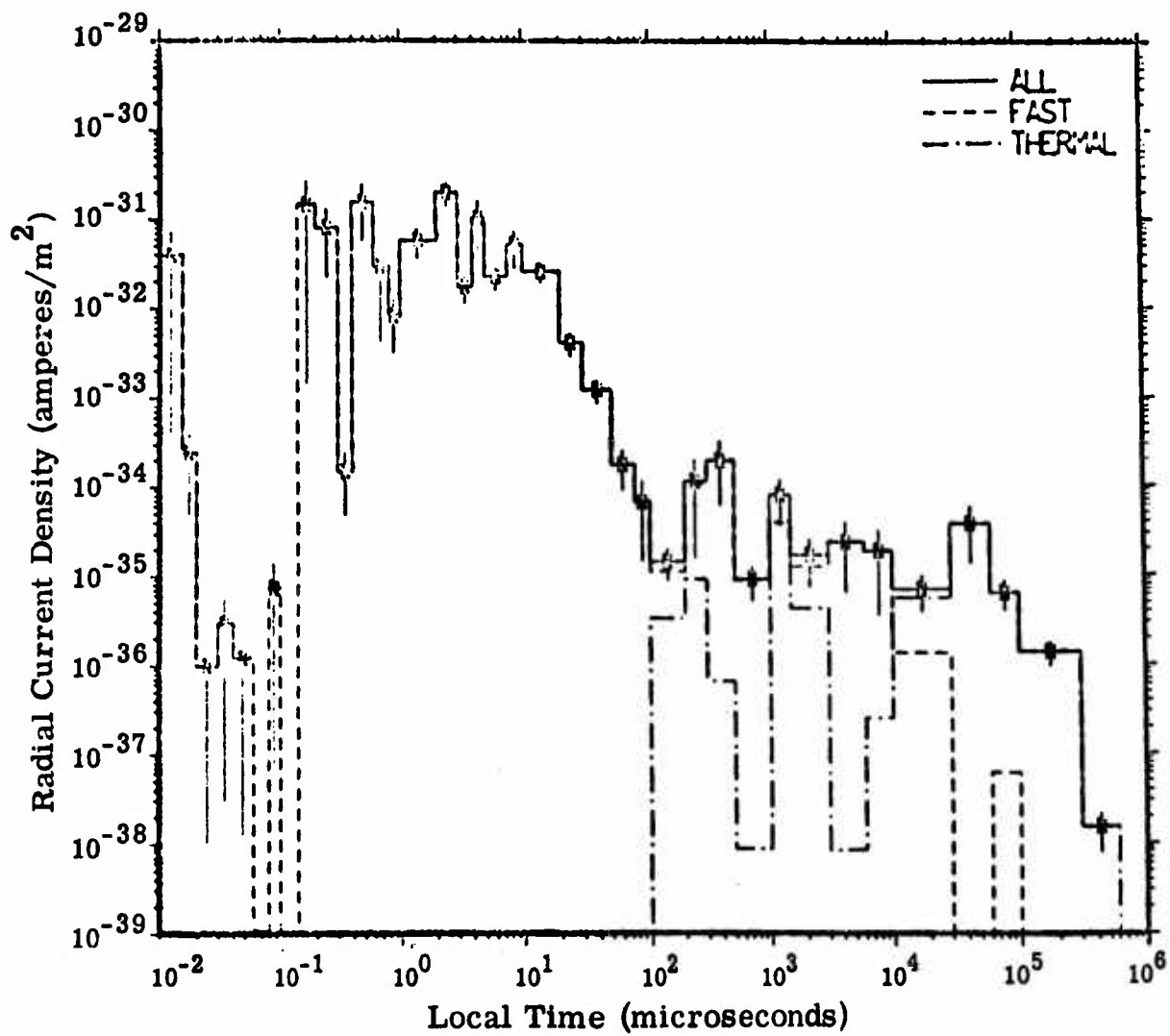


Figure 2.47. Radial current density vs. time at radius = 4000 - 5000 m,  $\cos \theta = 0.0 - 0.05$ , due to thermonuclear source on ground.

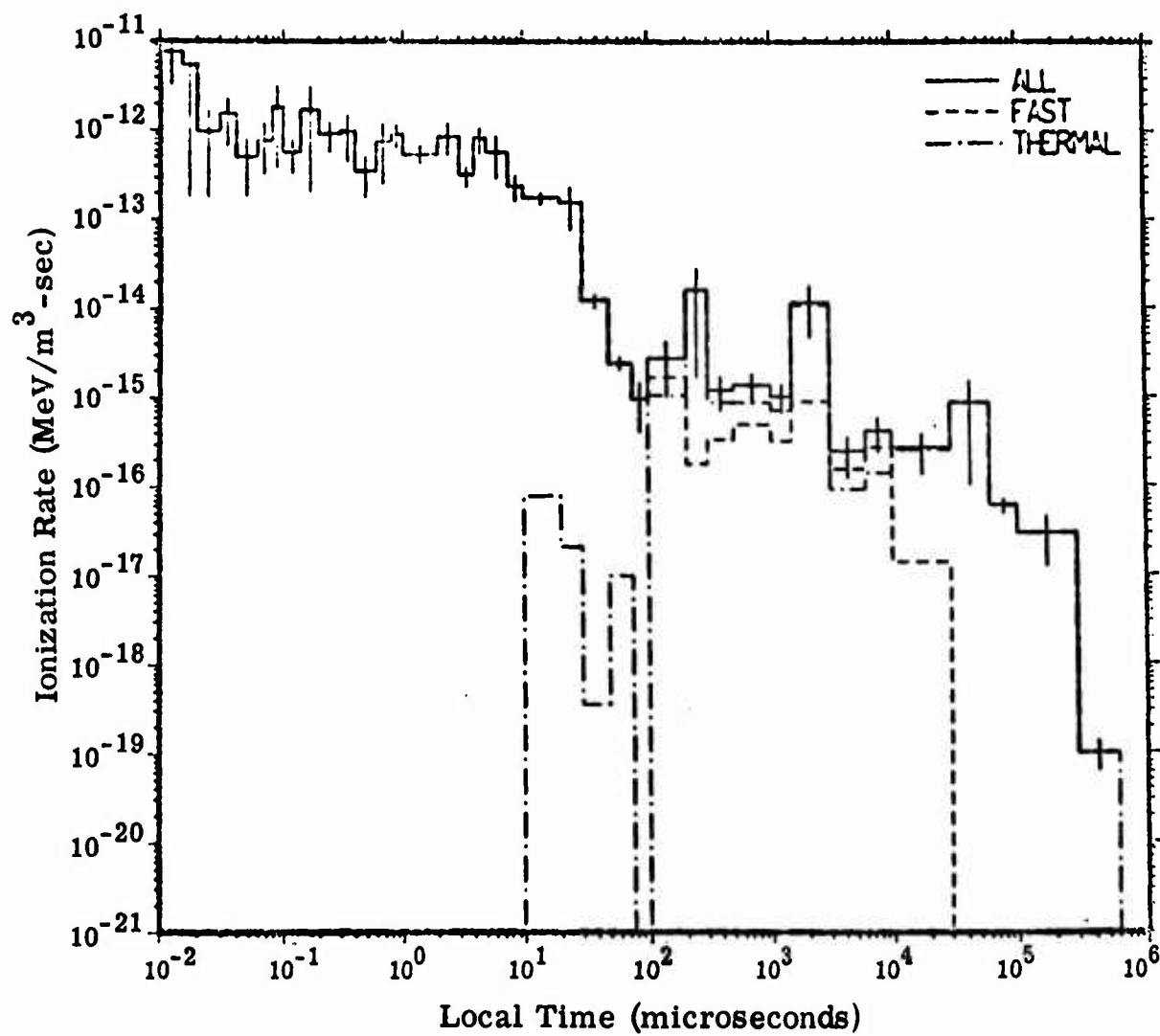


Figure 2.48. Ionization rate vs. time at radius = 4000 - 5000 m,  $\cos \theta = 0.5 - 1.0$ , due to thermonuclear source on ground.

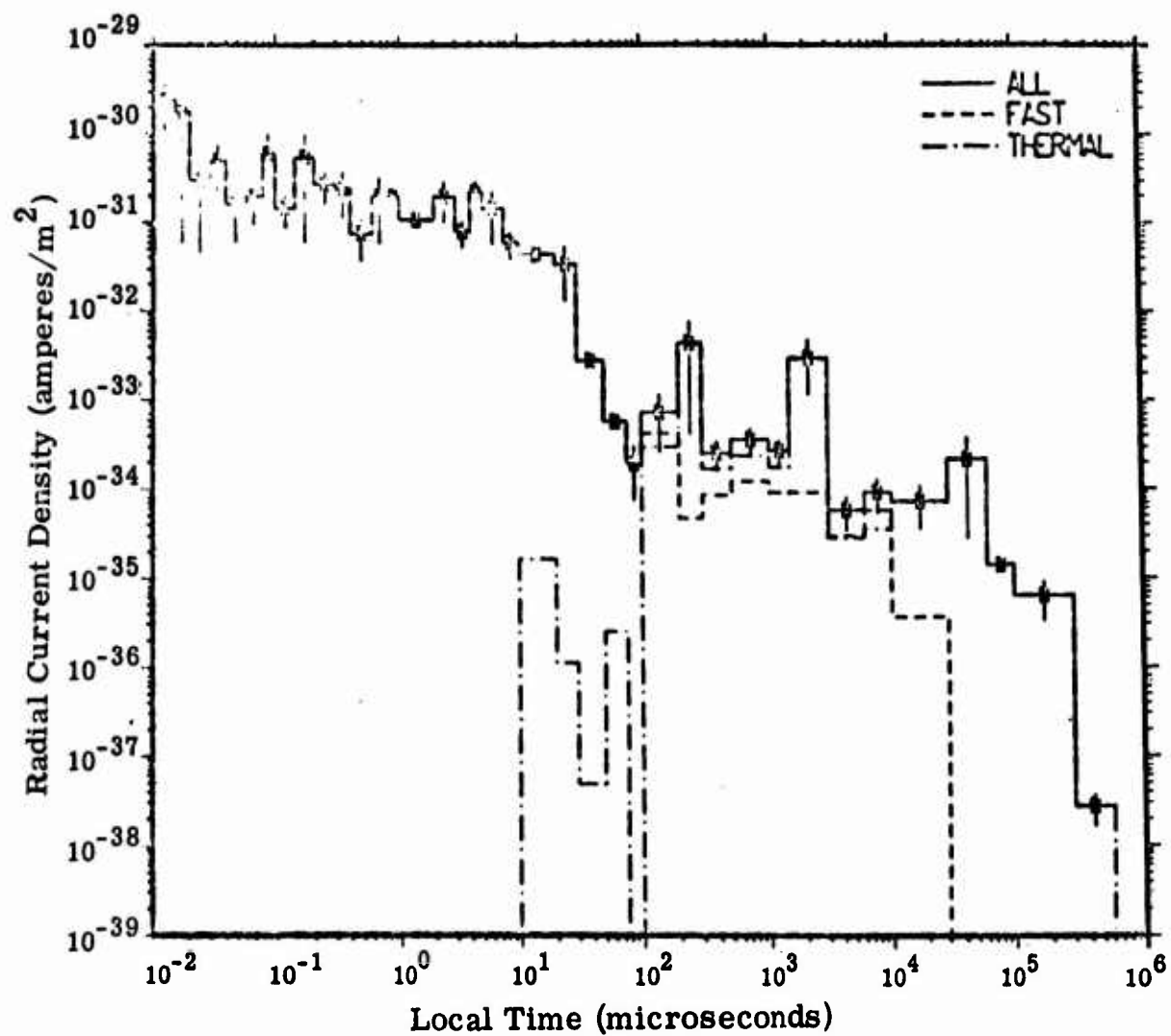


Figure 2.49. Radial current density vs. time at radius = 4000 - 5000 m,  $\cos \theta = 0.5 - 1.0$ , due to thermonuclear source on ground.

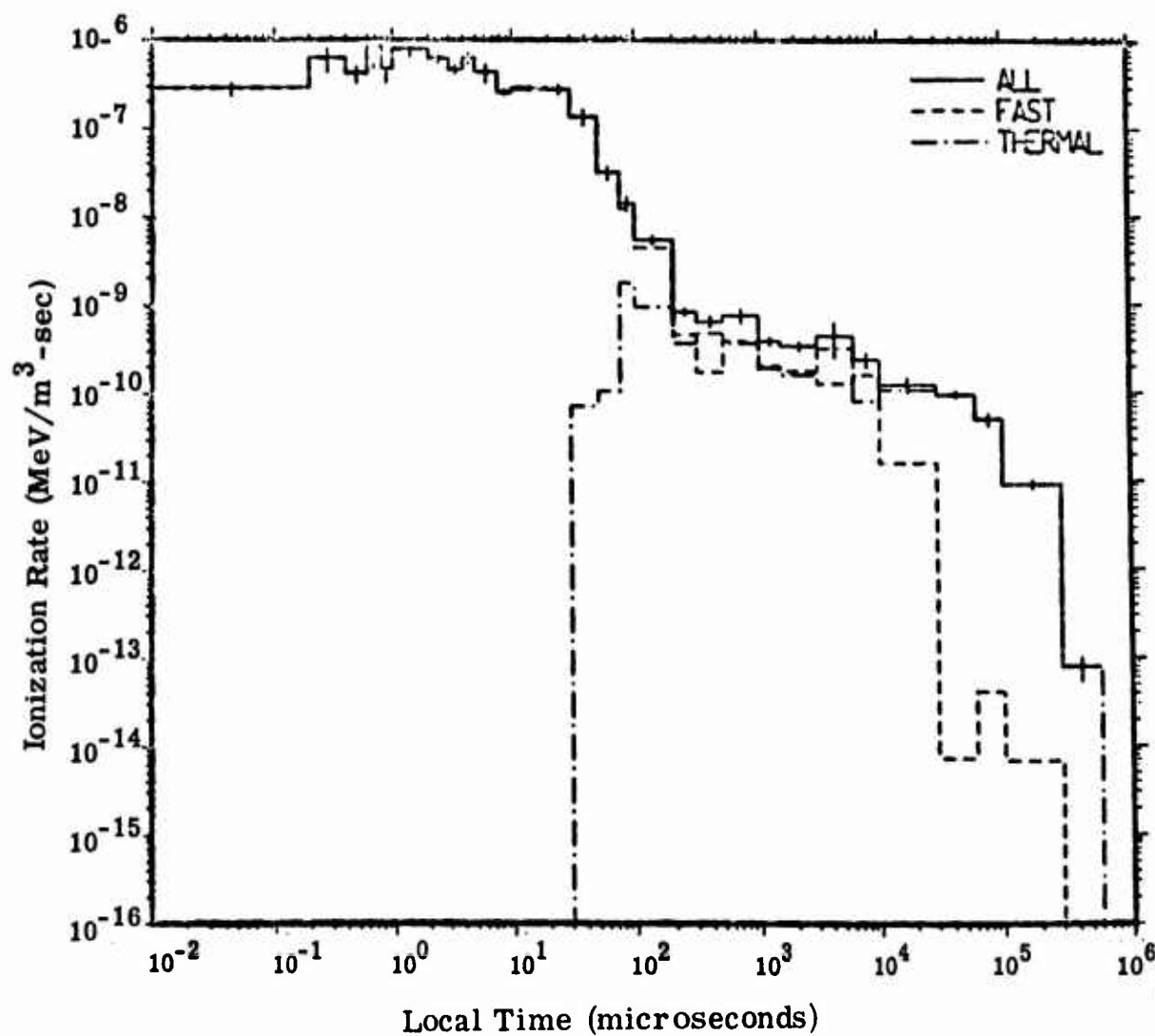


Figure 2.50. Ionization rate vs. time at radius = 850 - 1050 m, elevation = 0 - 50 m, due to thermo-nuclear source at HoB = 200 m.

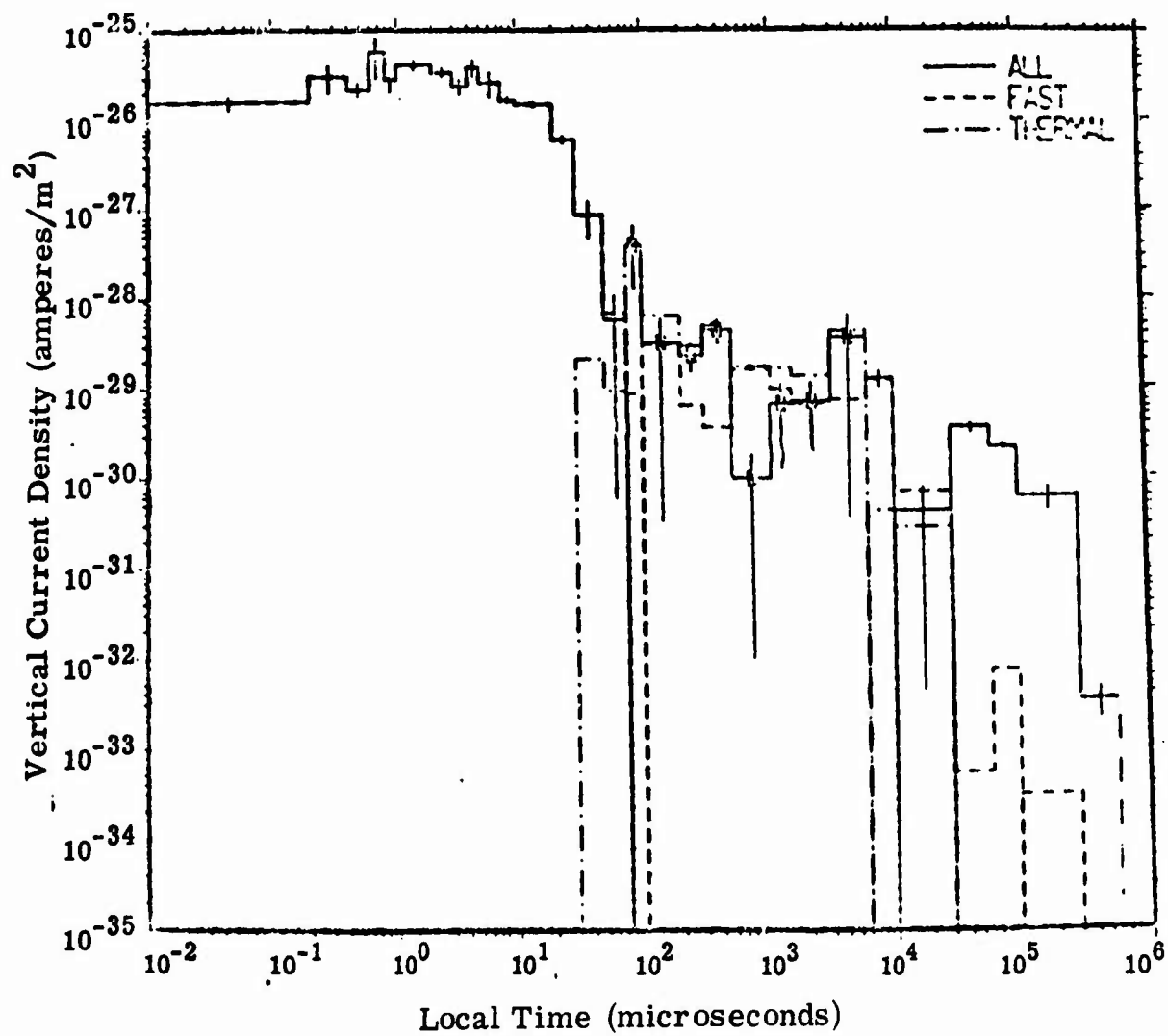


Figure 2.51. Vertical current density vs. time at radius = 850 - 1050 m, elevation = 0-50 m, due to thermo-nuclear source at HoB = 200 m.



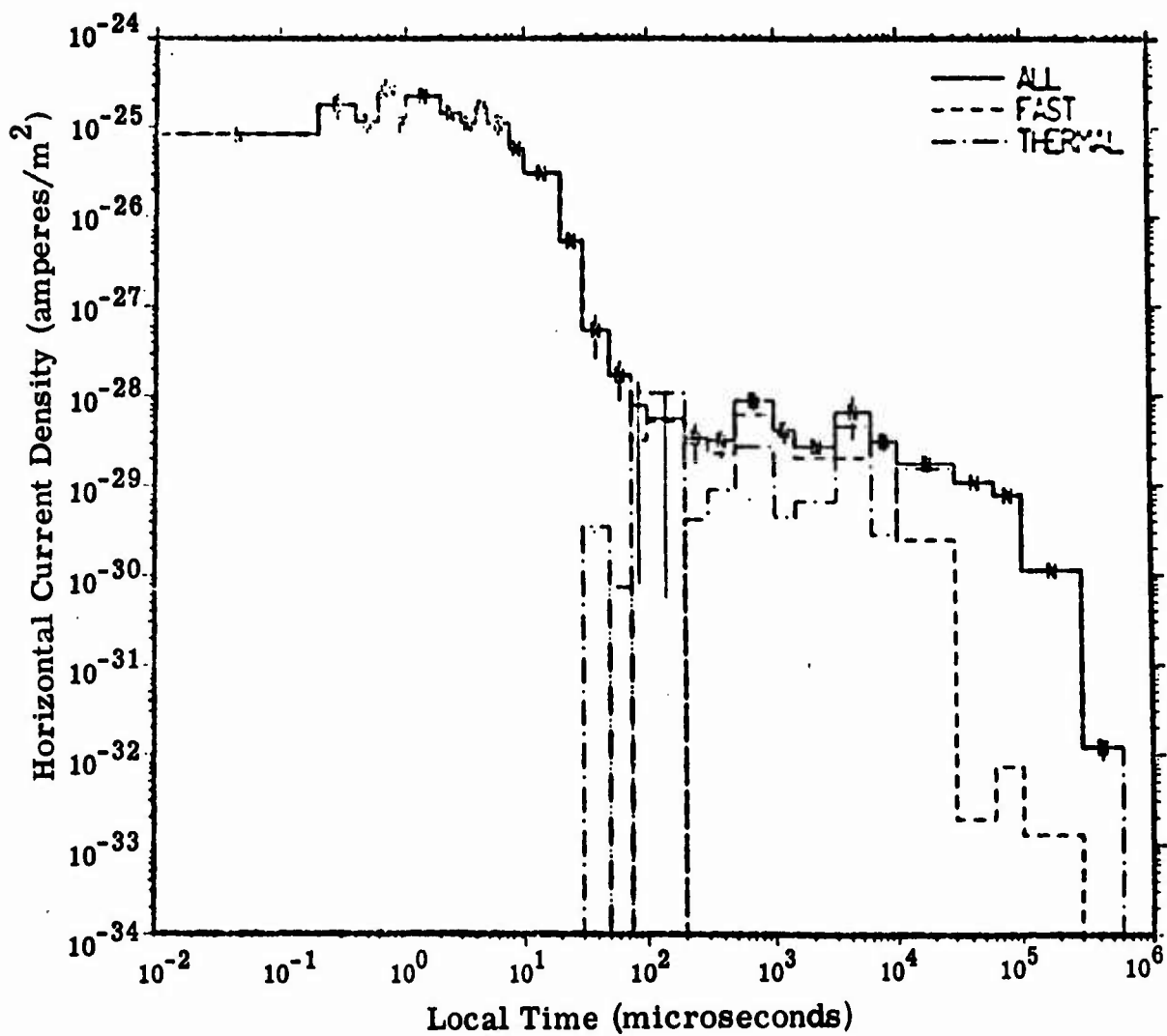


Figure 2.52. Horizontal current density vs. time at radius = 850 - 1050 m, elevation = 0-50 m, due to thermonuclear source at HoB = 200 m.

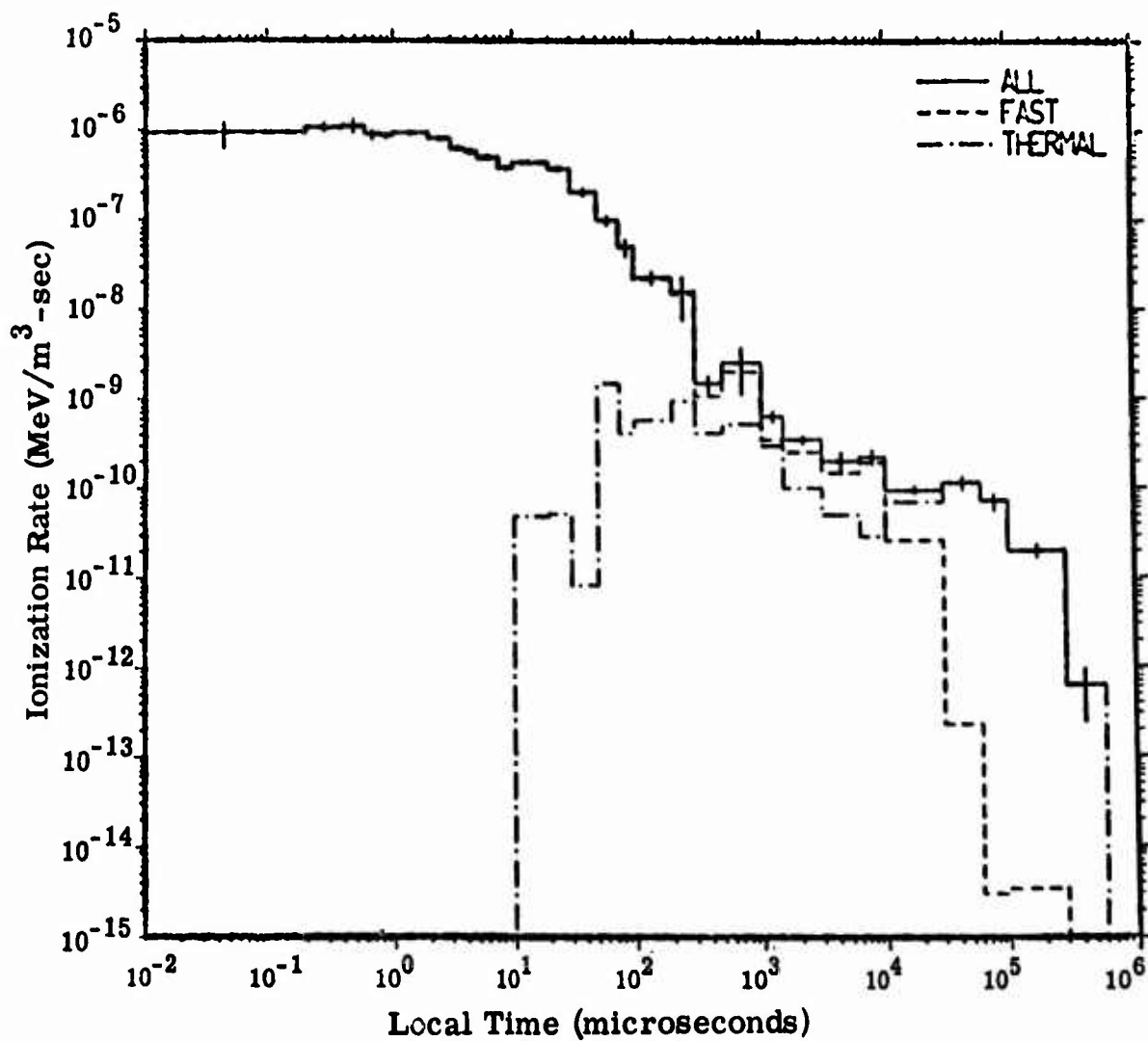


Figure 2.53. Ionization rate vs. time at radius = 850 - 1050 m,  $\cos \theta = 0.5 - 1.0$ , due to thermonuclear source at HoB = 200 m.

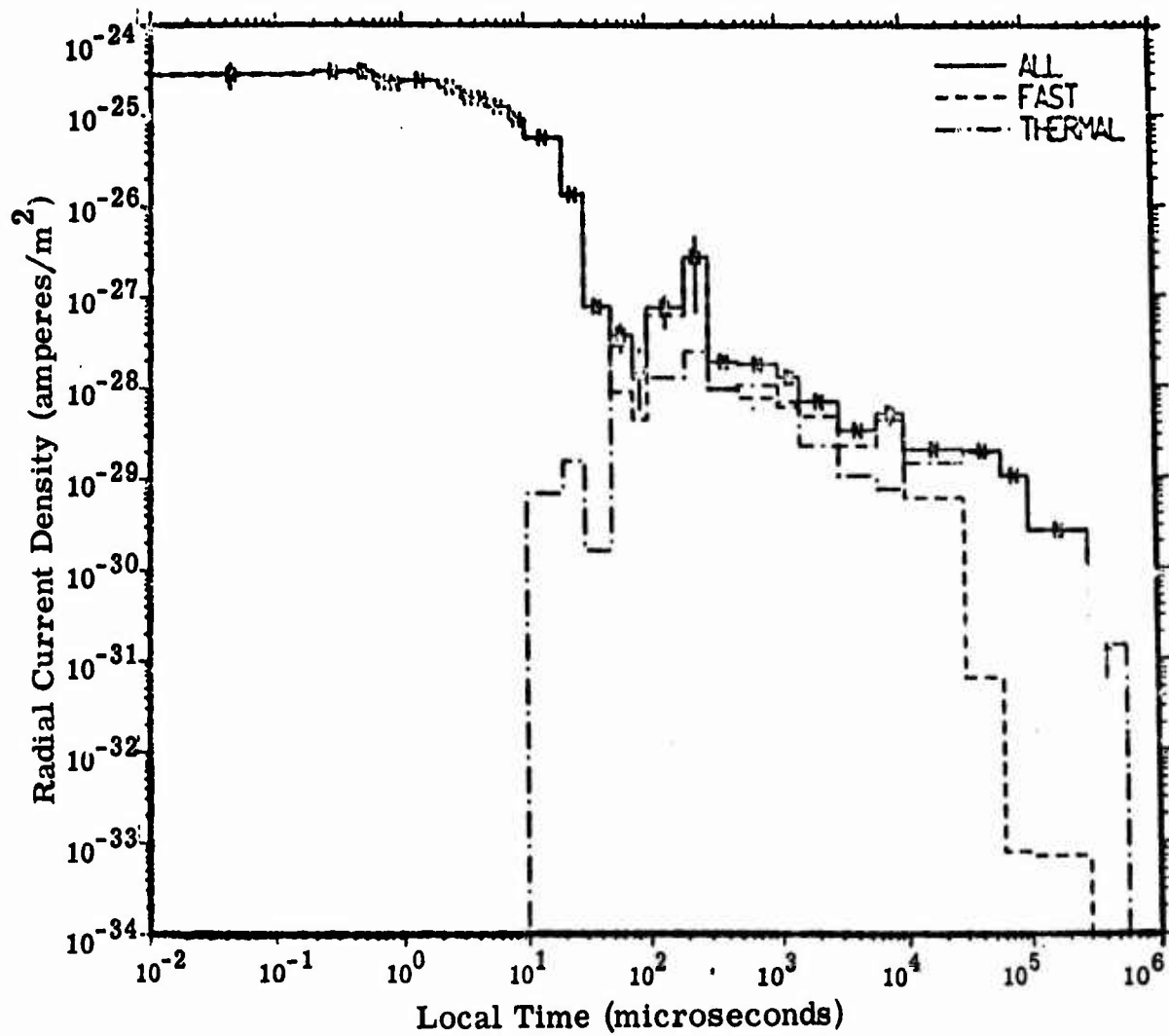


Figure 2.54. Radial current density vs. time at radius = 850 - 1050 m,  $\cos \theta = 0.5 - 1.0$ , due to thermo-nuclear source at HoB = 200 m.

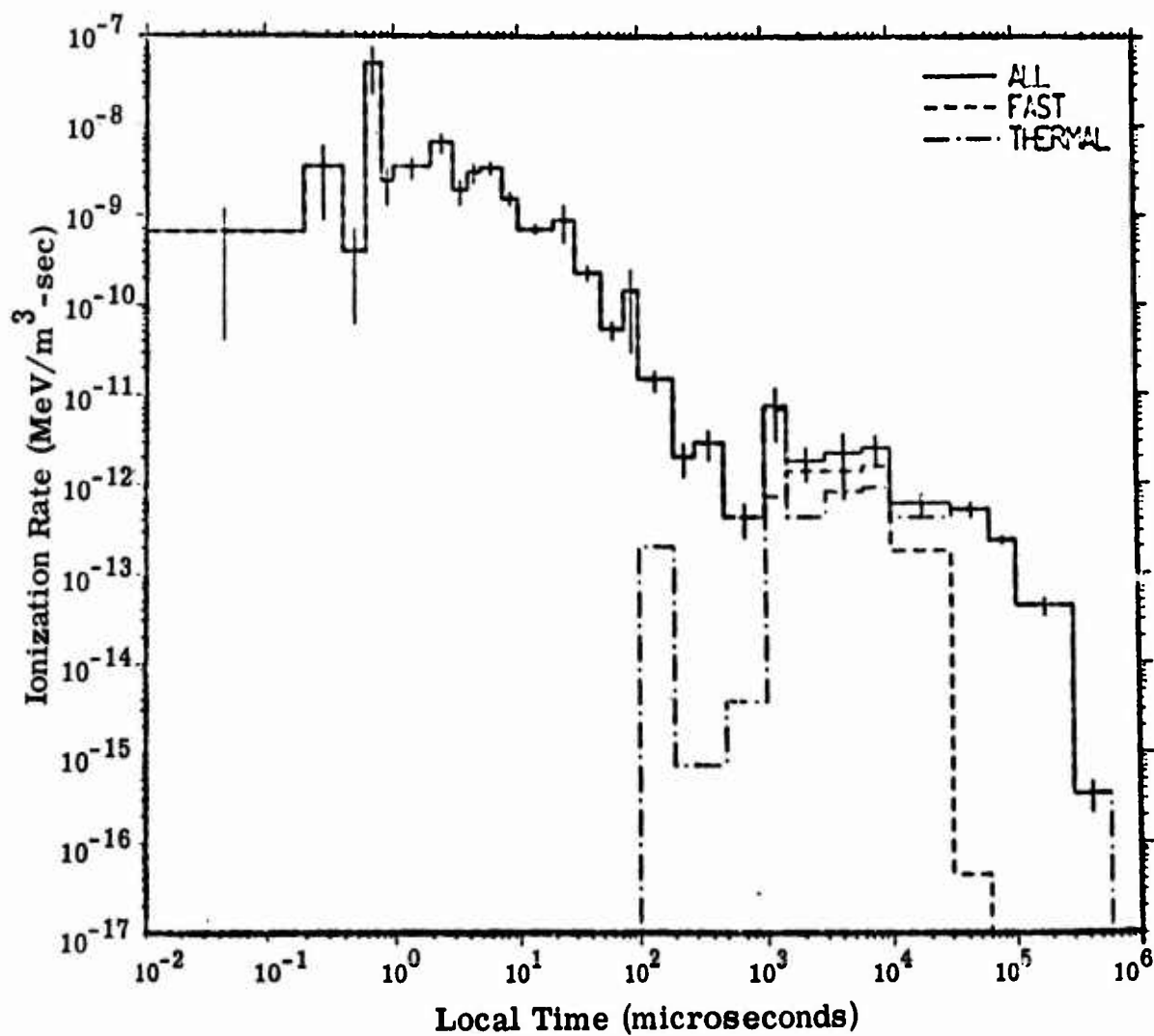


Figure 2.55. Ionization rate vs. time at radius = 1900 - 2100 m, elevation = 0 - 50 m, due to thermonuclear source at HoB = 200 m.

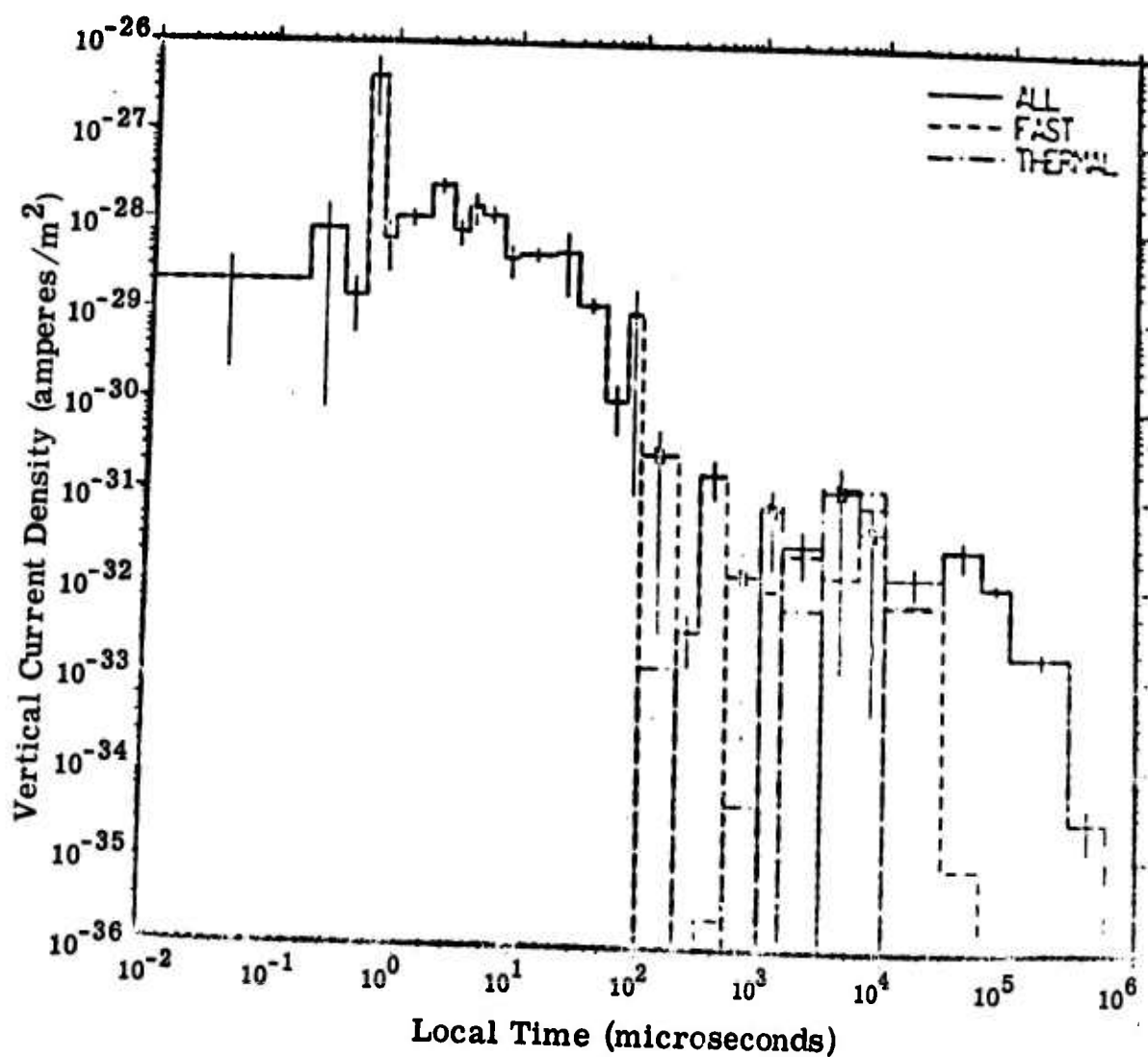


Figure 2.56. Vertical current density vs. time at radius = 1900 - 2100 m, elevation = 0 - 50 m, due to thermonuclear source at HoB = 200 m.

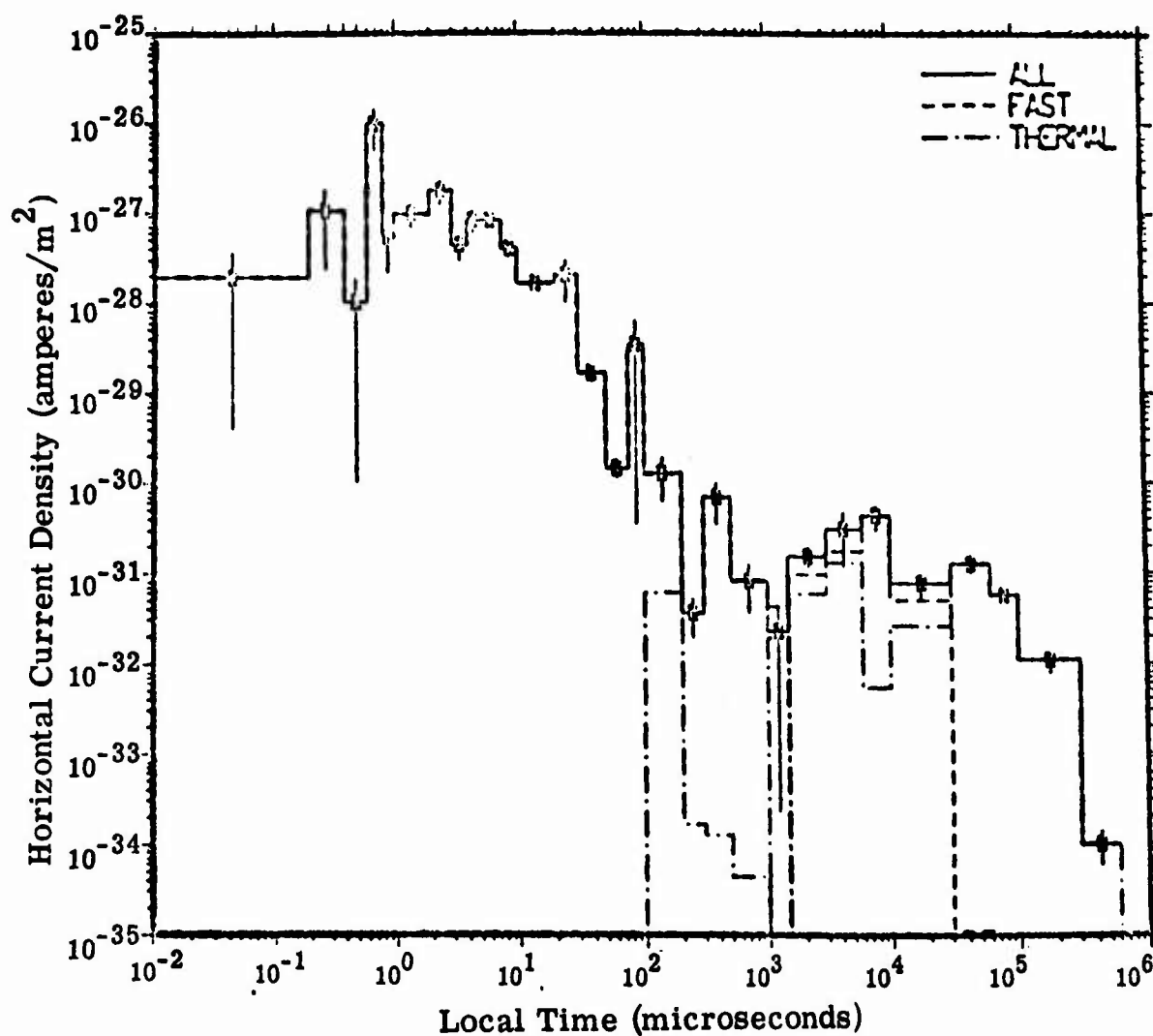


Figure 2.57. Horizontal current density vs. time at radius = 1900 - 2100 m, elevation = 0 - 50 m, due to thermonuclear source at HoB = 200 m.

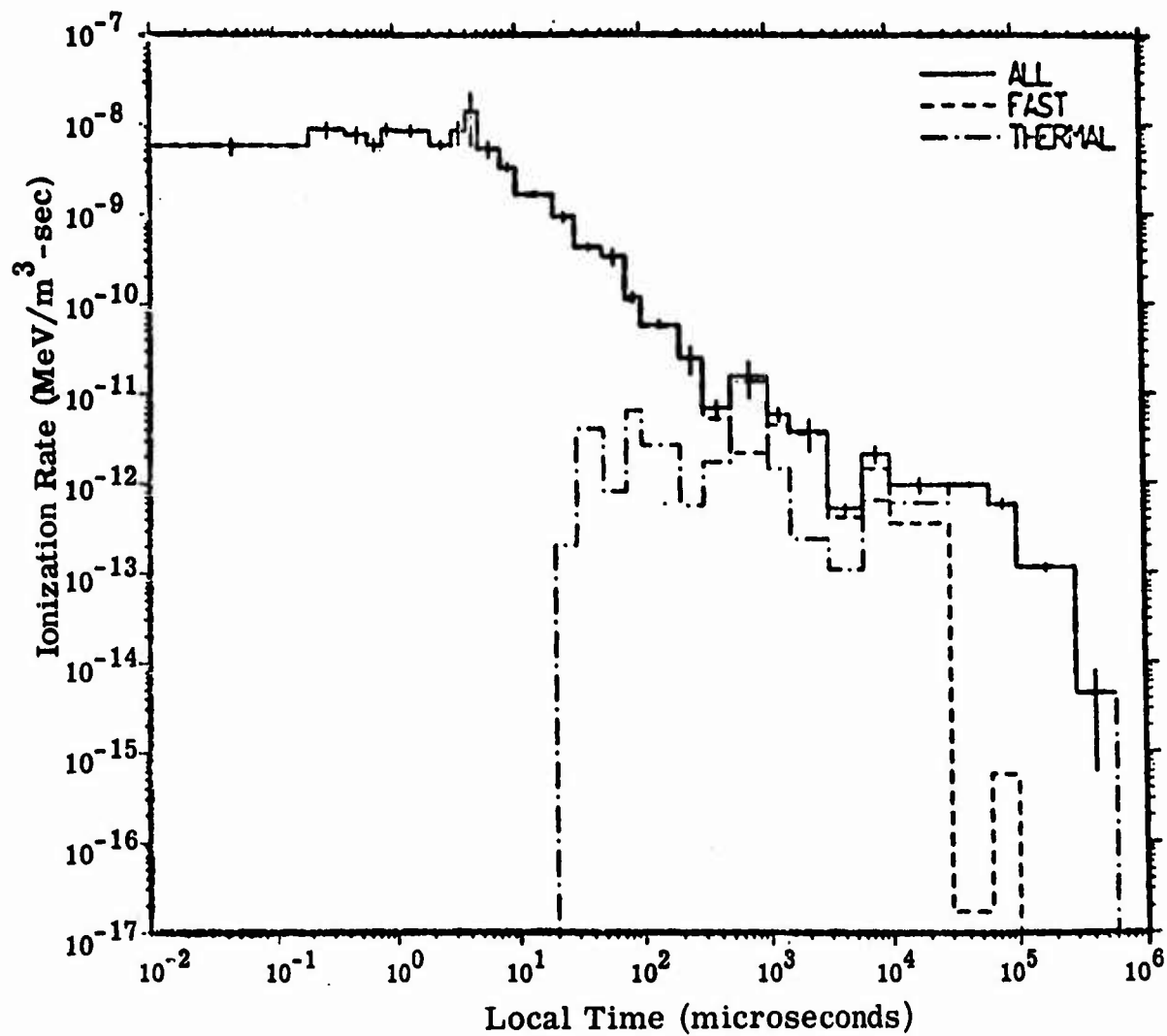


Figure 2.58. Ionization rate vs. time at radius = 1900 - 2100 m,  $\cos \theta = 0.5 - 1.0$ , due to thermonuclear source at HoB = 200 m.

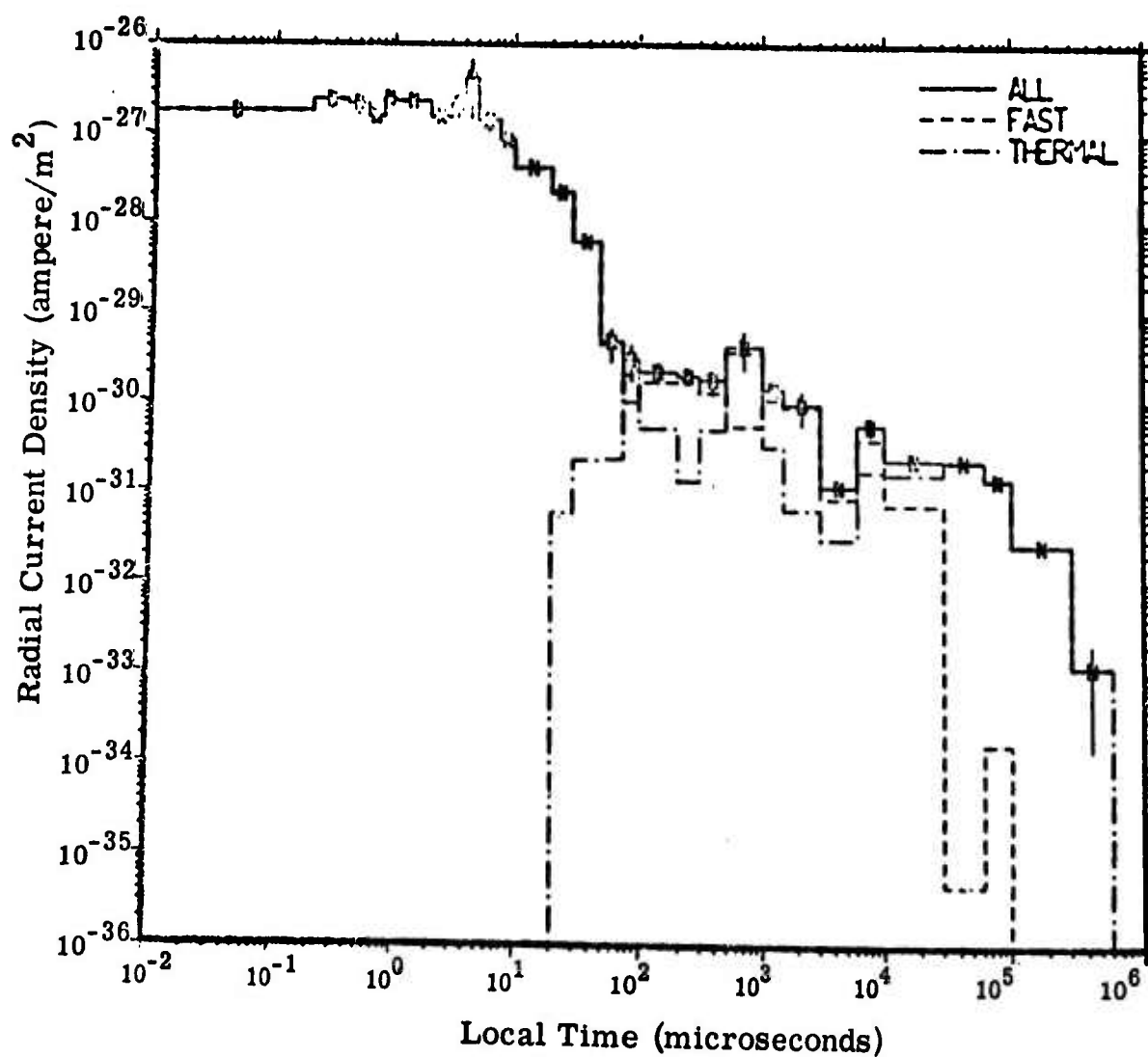


Figure 2.59. Radial current density vs. time at radius = 1900 - 2100 m,  $\cos \theta = 0.5 - 1.0$ , due to thermo-nuclear source at HoB = 200 m.



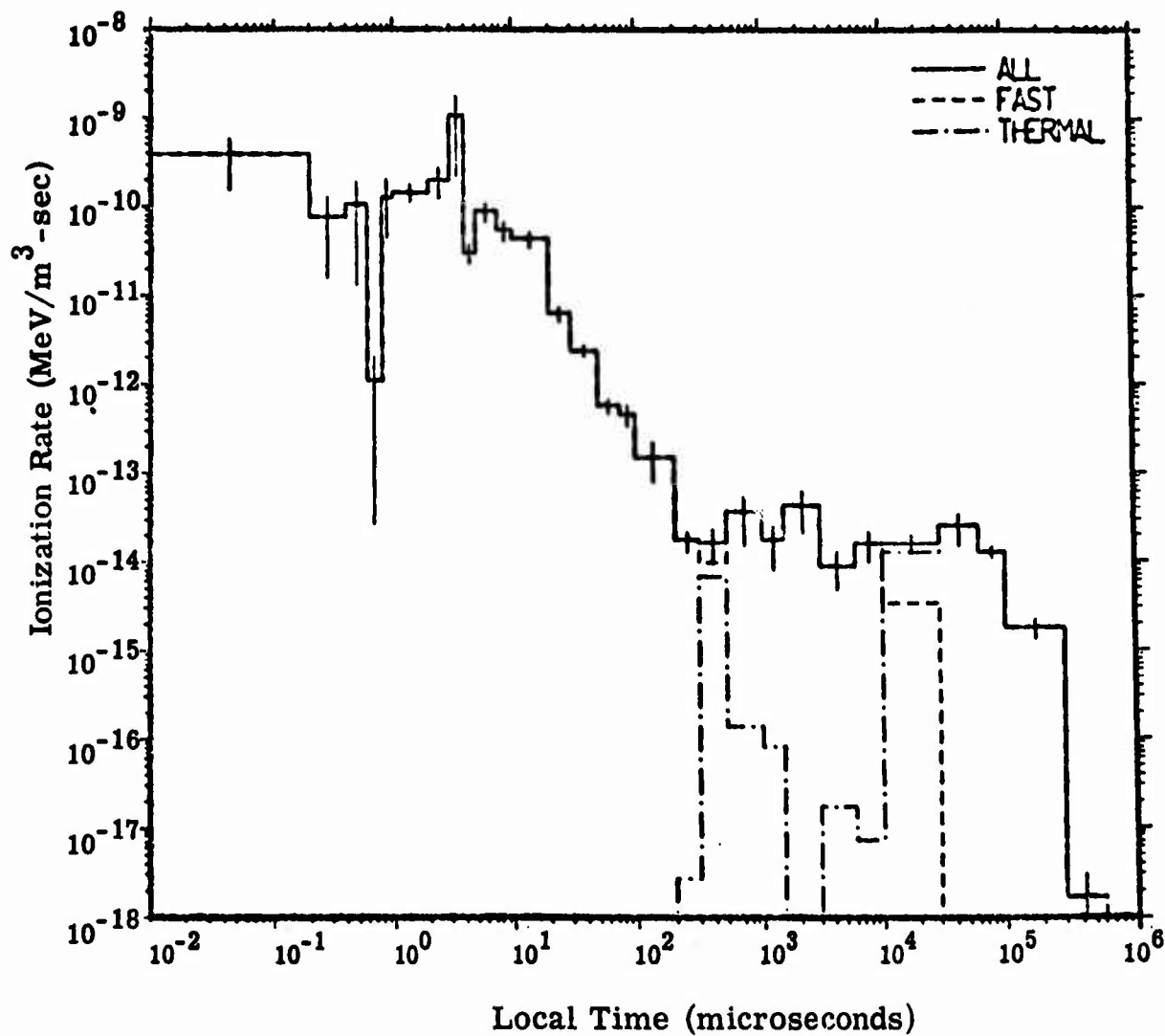


Figure 2. 60. Ionization rate vs. time at radius = 2700 - 3100 m, elevation 0-50 m, due to thermonuclear source at HoB = 200 m.

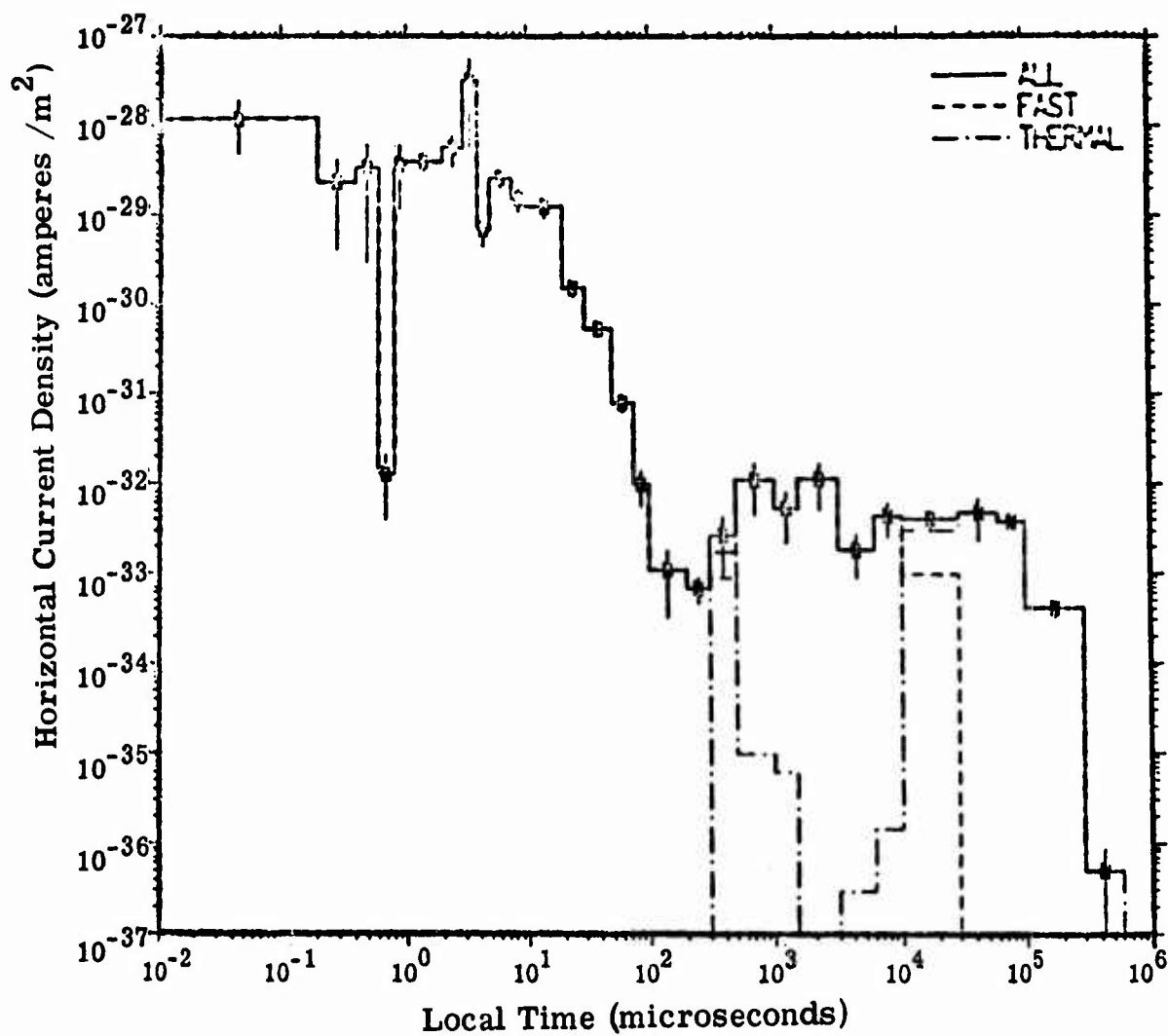


Figure 2. 61. Horizontal current density vs. time at radius = 2700 - 3100 m, elevation = 0 - 50 m, due to thermonuclear source at HoB = 200 m.

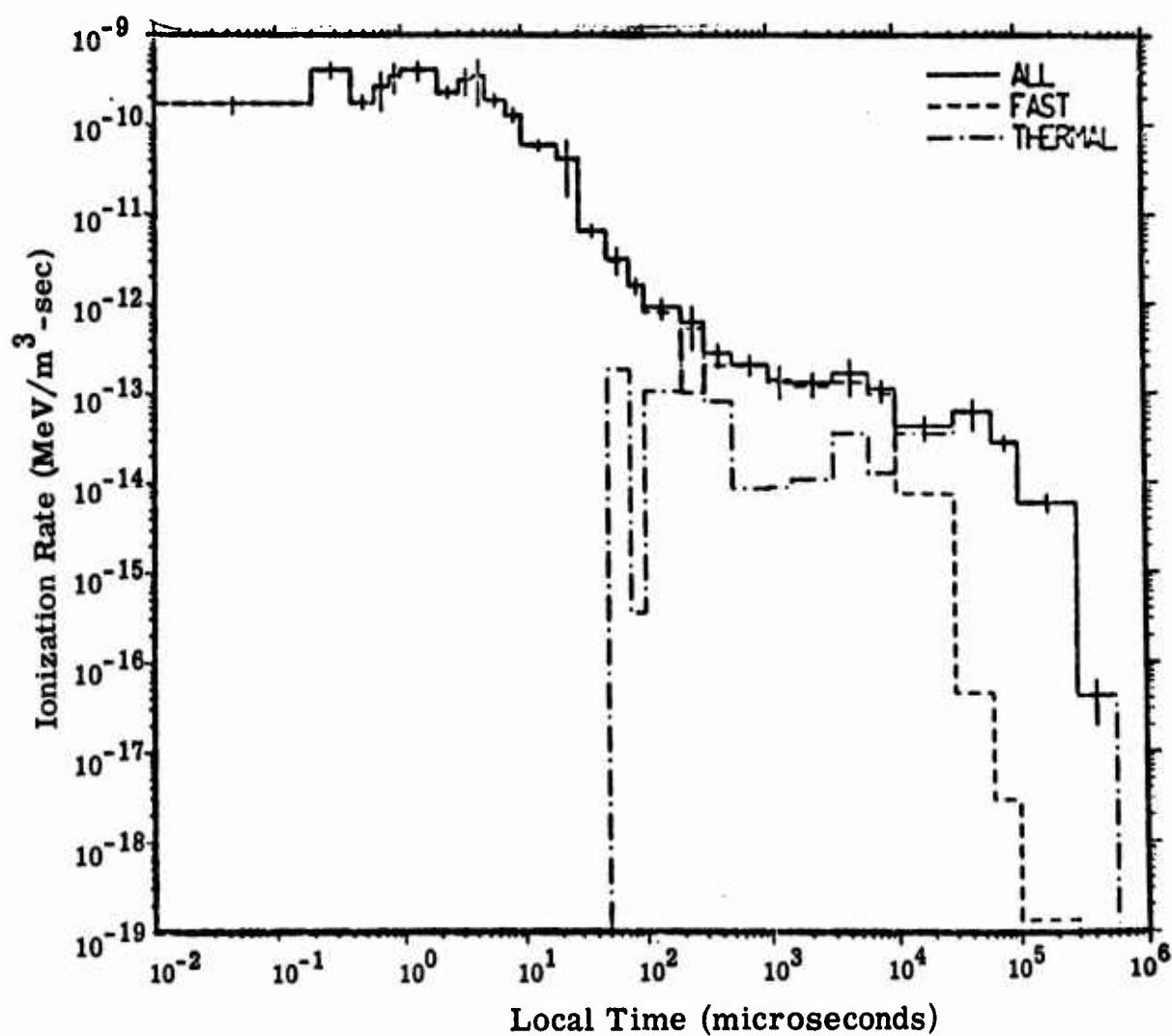


Figure 2. 62. Ionization rate vs. time at radius = 2700 - 3100 m,  $\cos \theta = 0.5 - 1.0$ , due to thermonuclear source at HoB = 200 m.

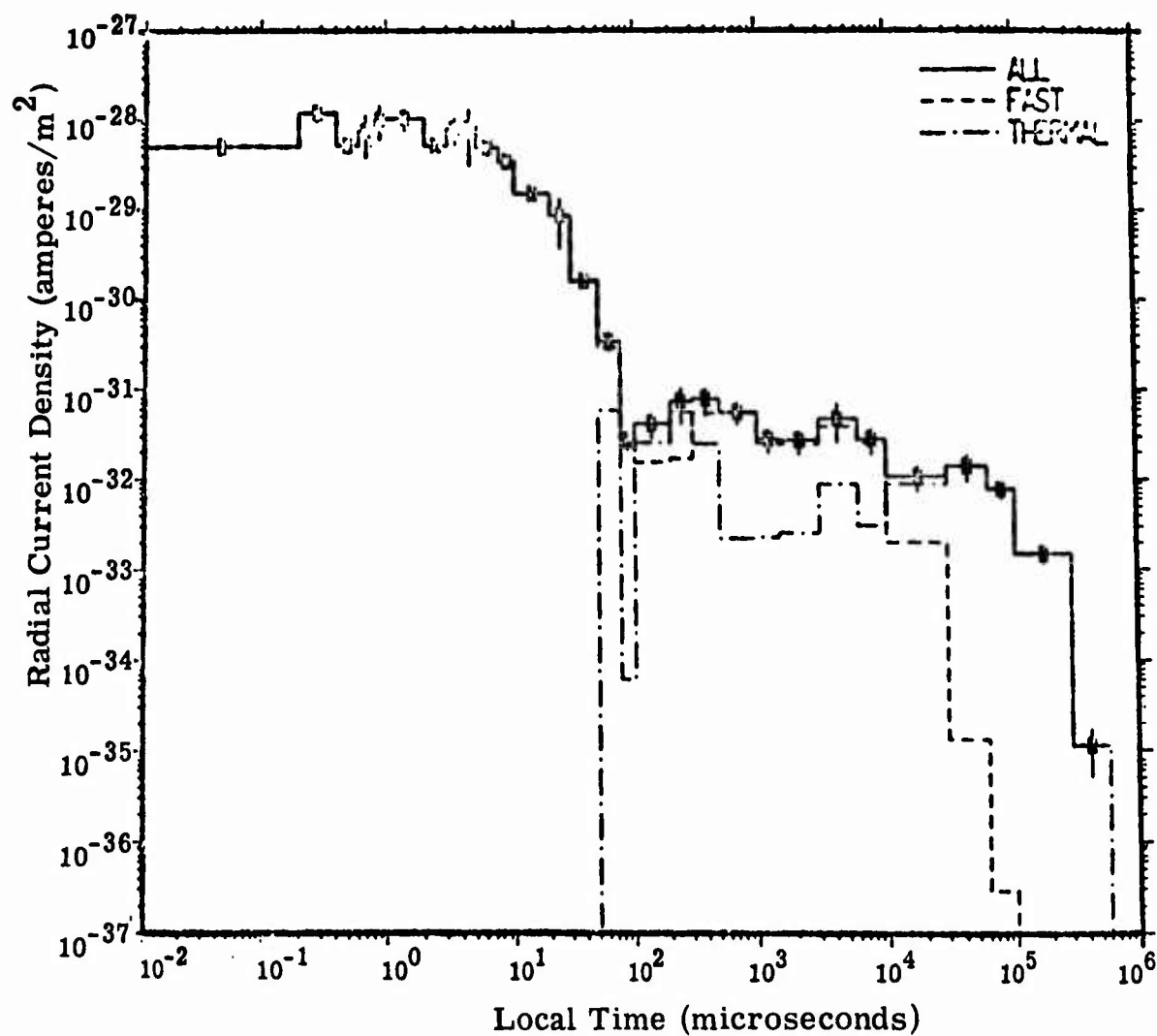


Figure 2. 63. Radial current density vs. time at radius = 2700 - 3100,  $\cos \theta = 0.5 - 1.0$ , due to thermonuclear source at HoB = 200 m.

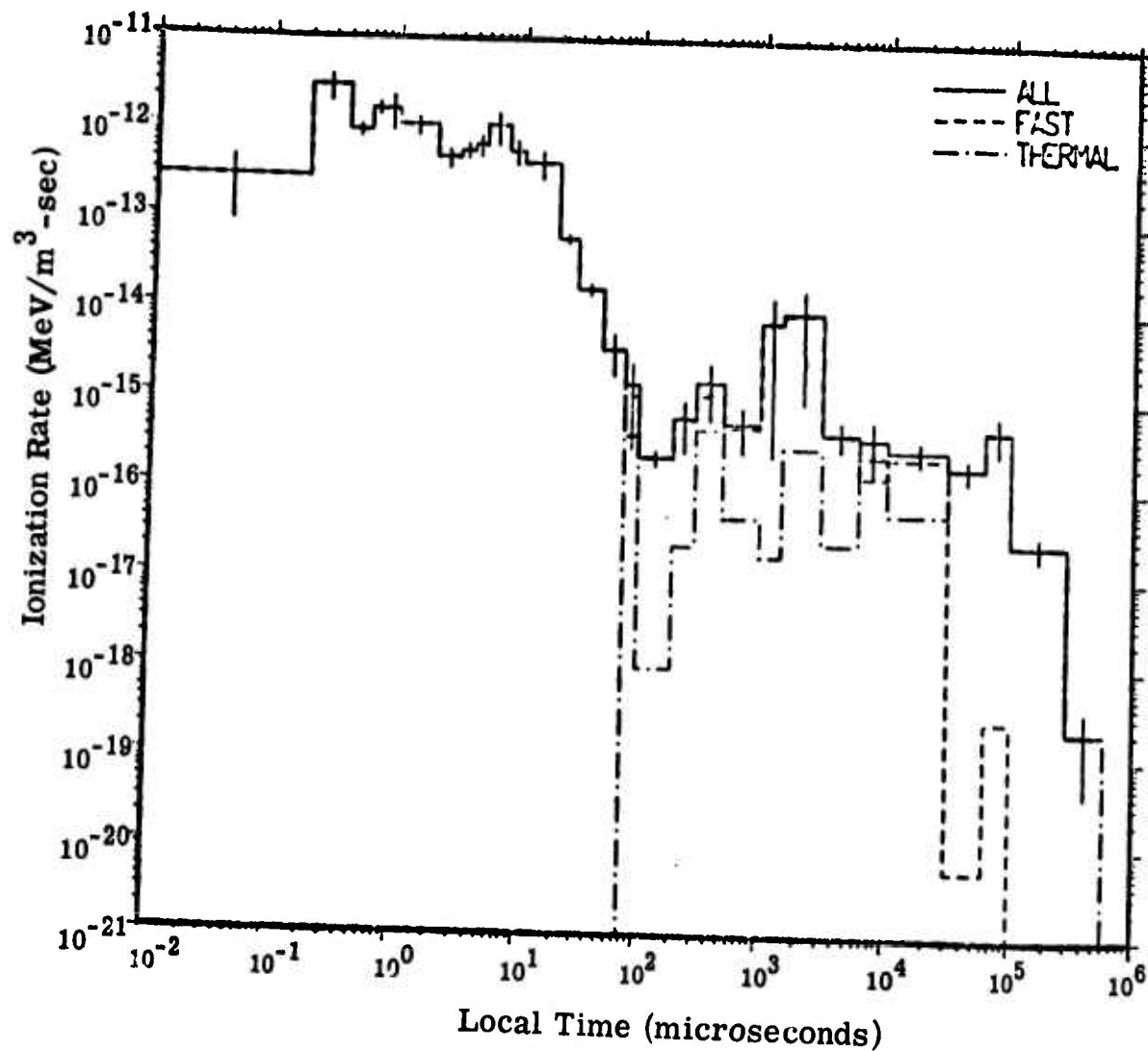


Figure 2. 64. Ionization rate vs. time at radius = 4000 - 5000 m,  $\cos \theta = 0.5 - 1.0$ , due to thermonuclear source at HoB = 200 m.

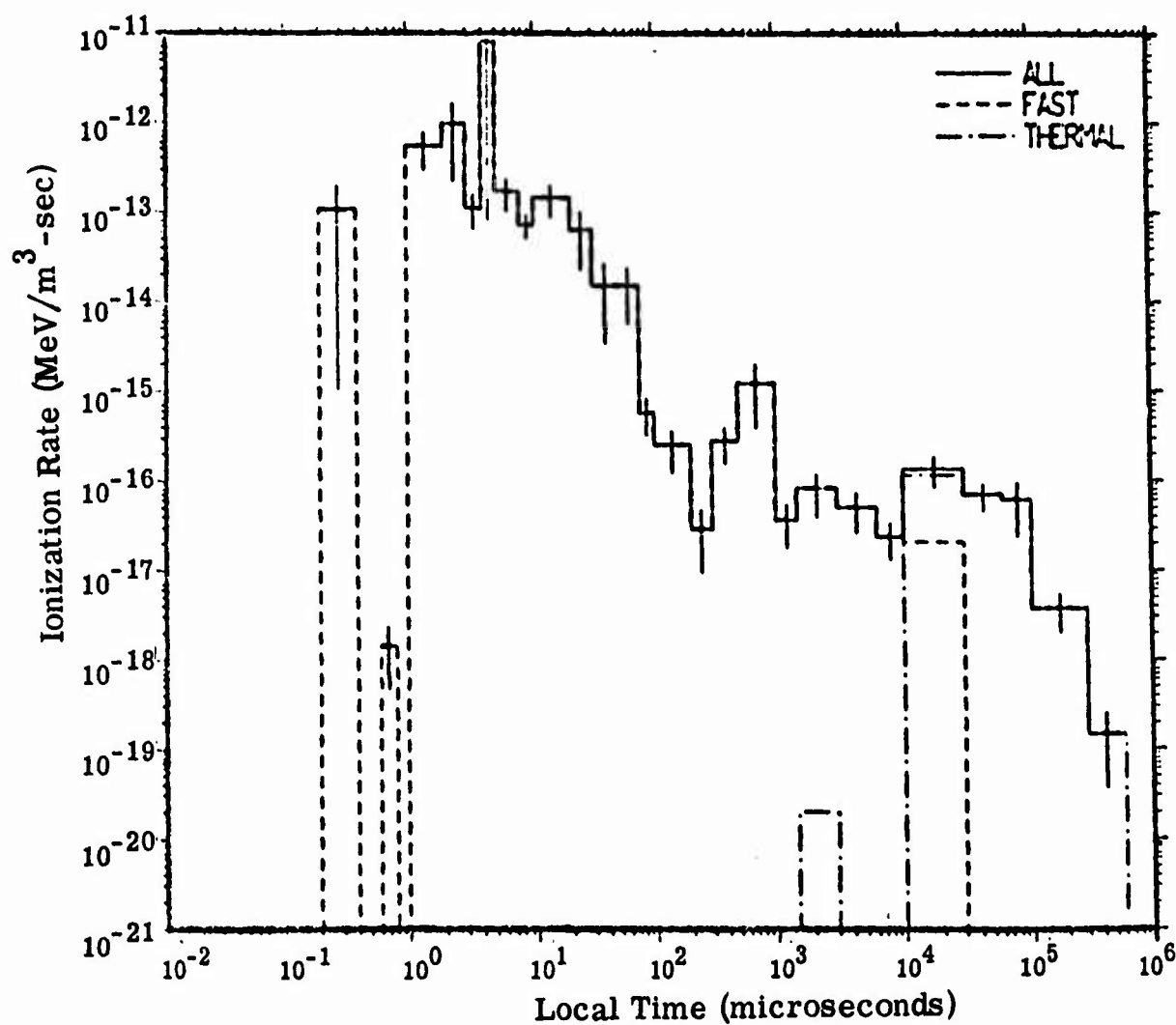


Figure 2. 65. Ionization rate vs. time at radius = 4000 - 5000 m, elevation = 0 - 50 m, due to thermonuclear source at HoB = 200 m.

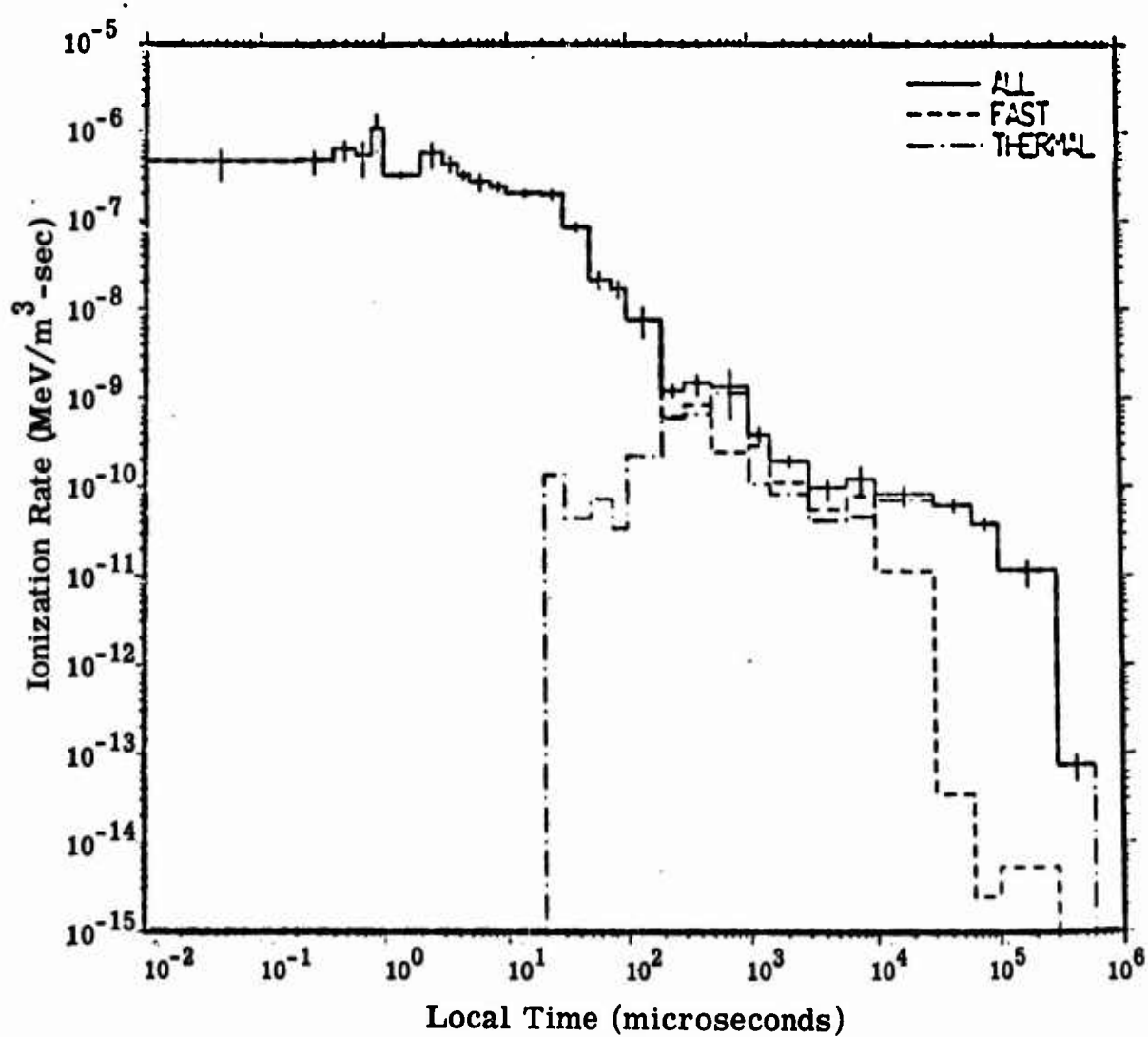


Figure 2. 66. Ionization rate vs. time at radius = 850 - 1050 m, elevation = 0 - 50 m, due to thermonuclear source at HoB = 500 m.

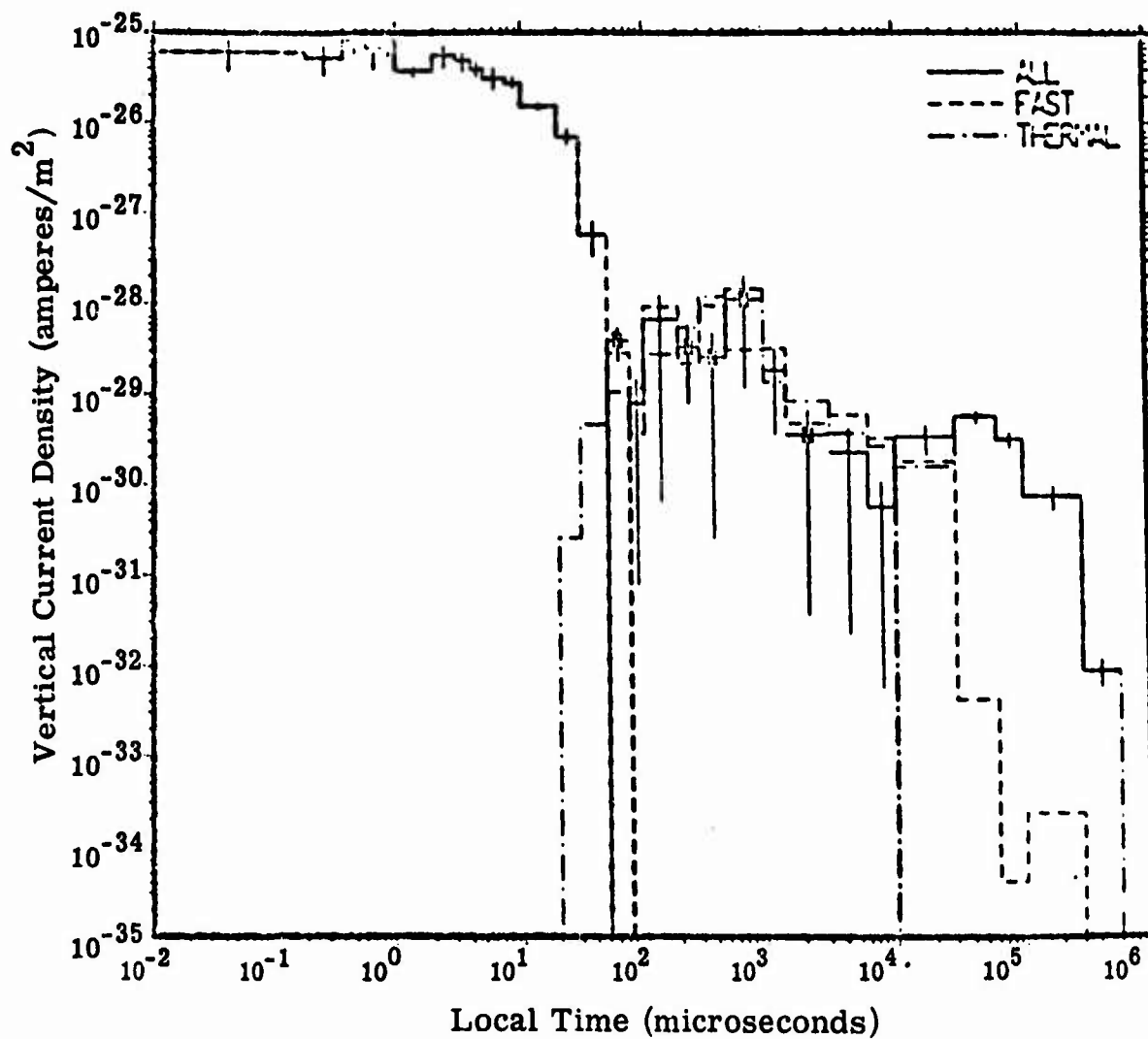


Figure 2. 67. Vertical current density vs. time at radius = 850 - 1050 m, elevation = 0 - 50 m, due to thermo-nuclear source at HoB = 500 m.



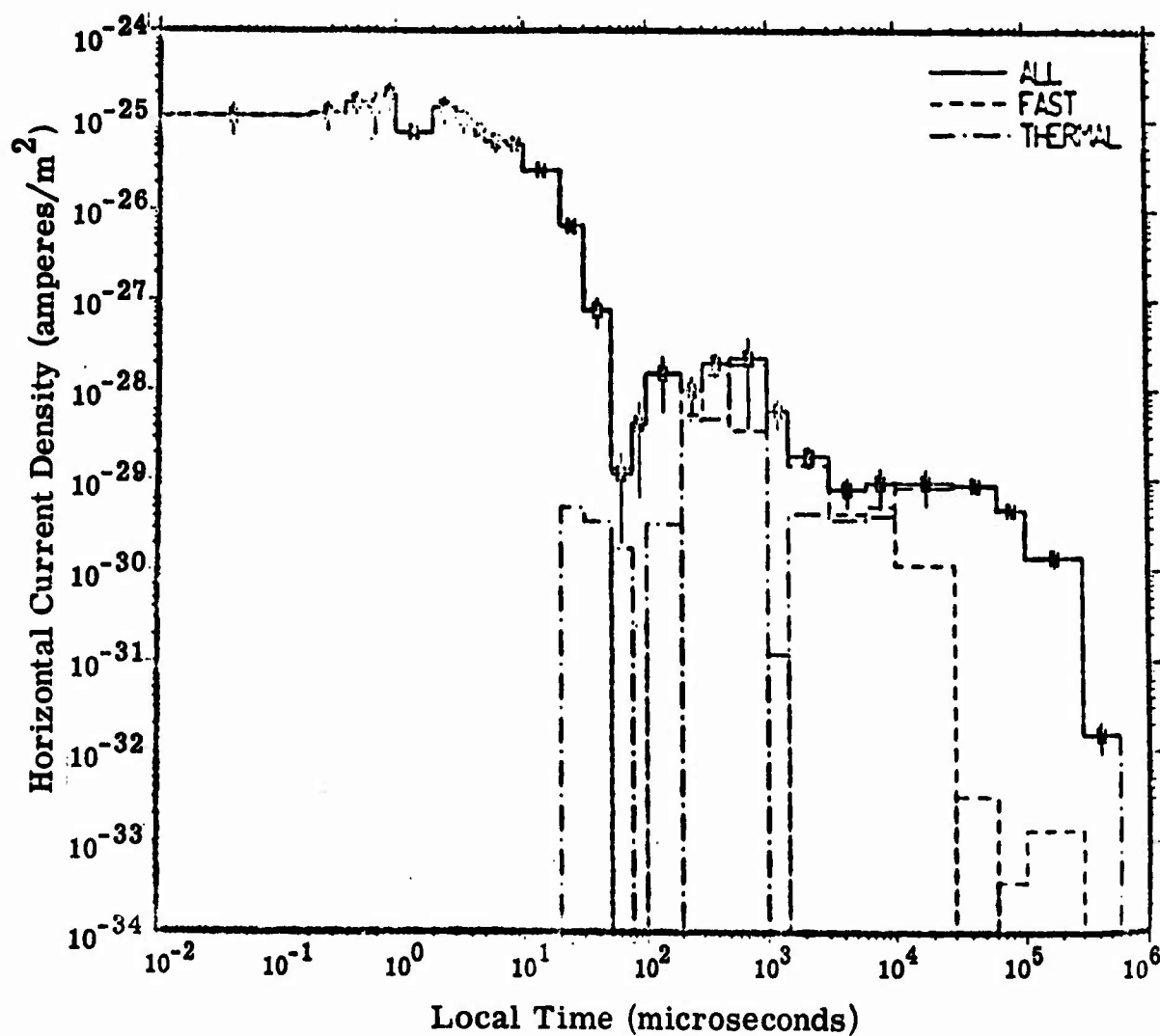


Figure 2. 68. Horizontal current density vs. time at radius = 850 - 1050 m, elevation = 0 - 50 m, due to thermo-nuclear source at HoB = 500 m.

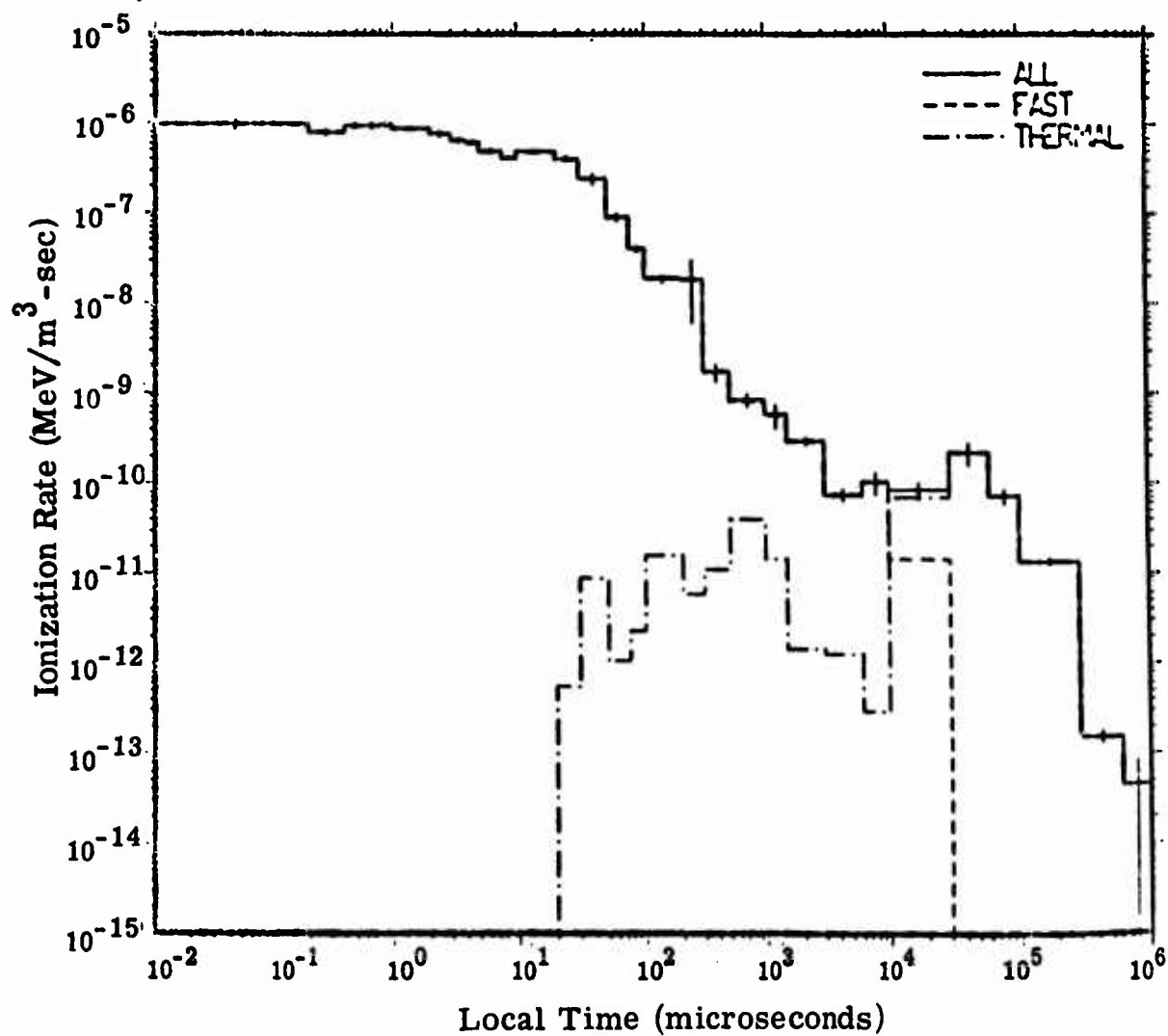


Figure 2. 69. Ionization rate vs. time at radius = 850 - 1050 m,  $\cos \theta = 0.5 - 1.0$ , due to thermonuclear source at HoB = 500 m.

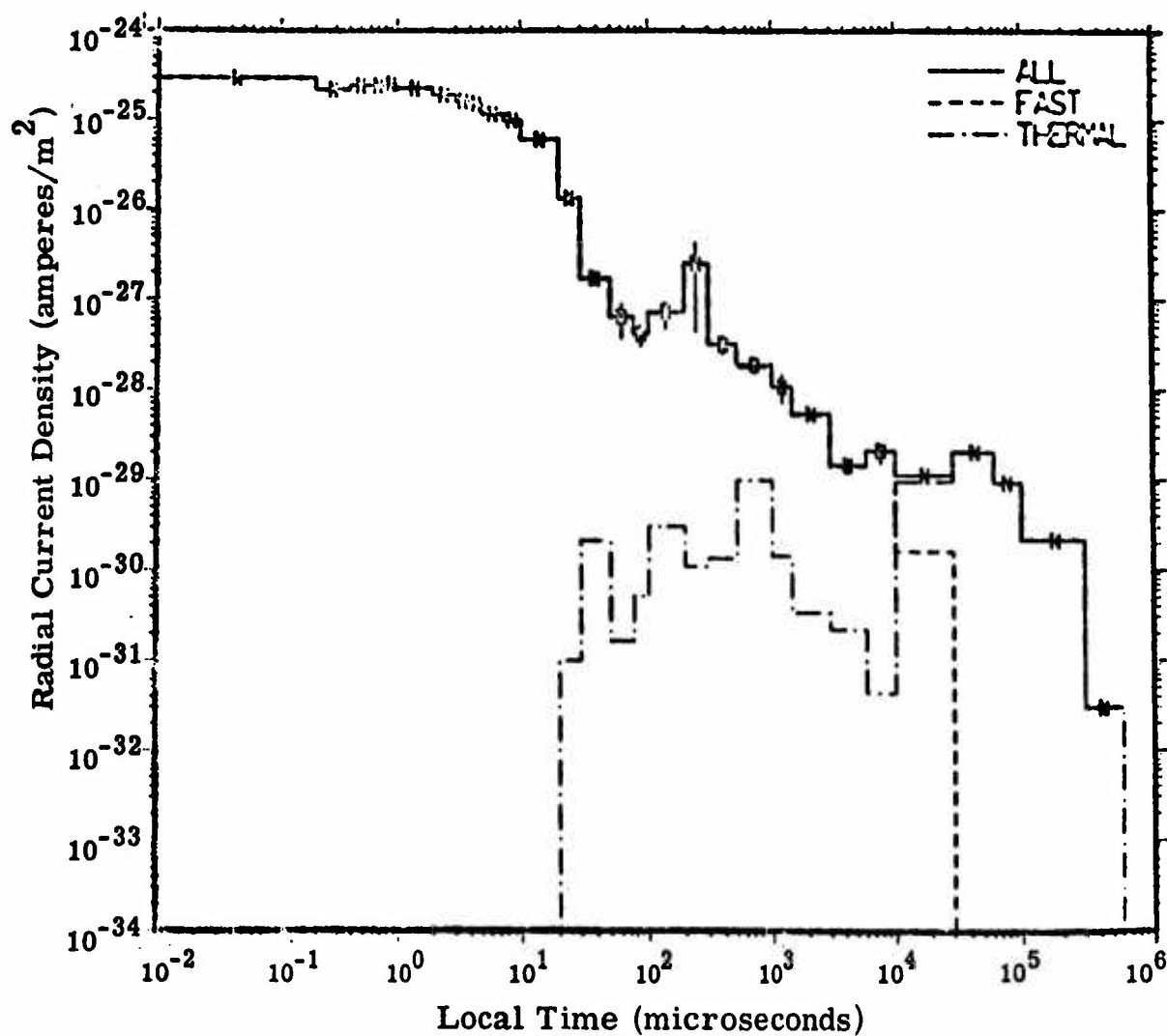


Figure 2.70. Radial current density vs. time at radius = 850 - 1050 m,  $\cos \theta = 0.5 - 1.0$ , due to thermo-nuclear source at HoB = 500 m.

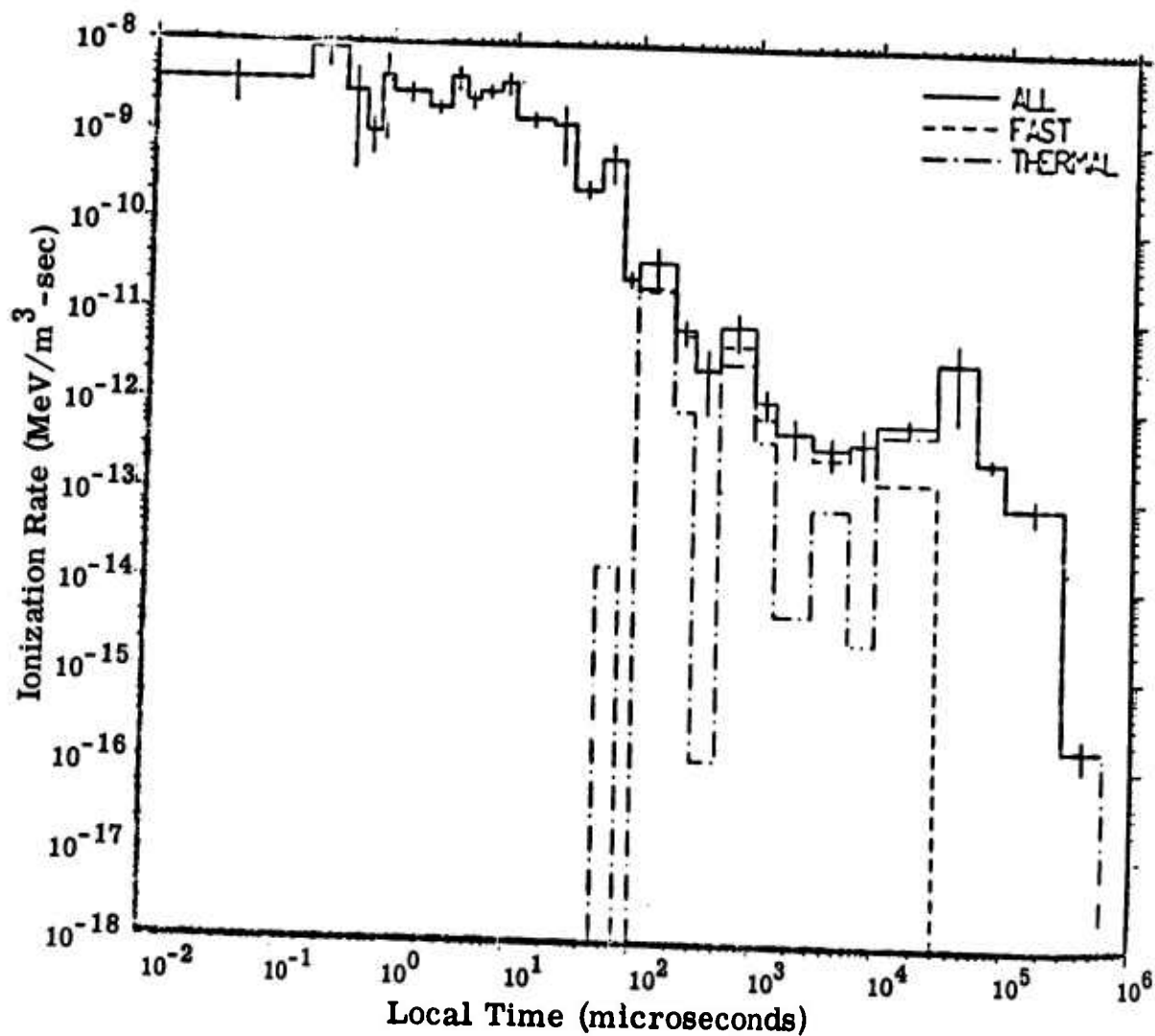


Figure 2.71. Ionization rate vs. time at radius = 1900 - 2100 m, elevation = 0 - 50 m, due to thermo-nuclear source at HoB = 500 m.

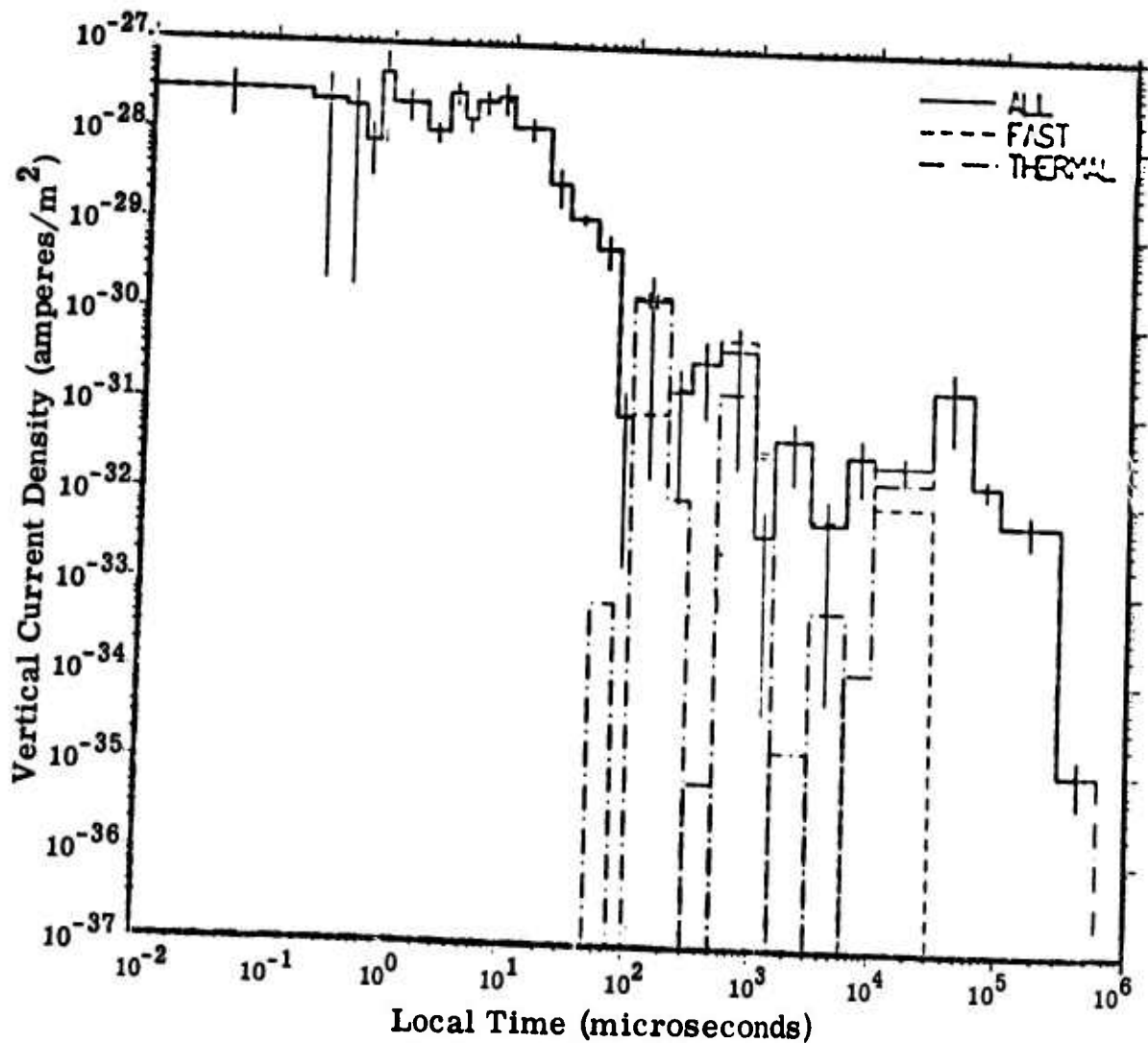


Figure 2.72. Vertical current density vs. time at radius = 1900 - 2100 m, elevation = 0 - 50 m, due to thermonuclear source at HoB = 500 m.

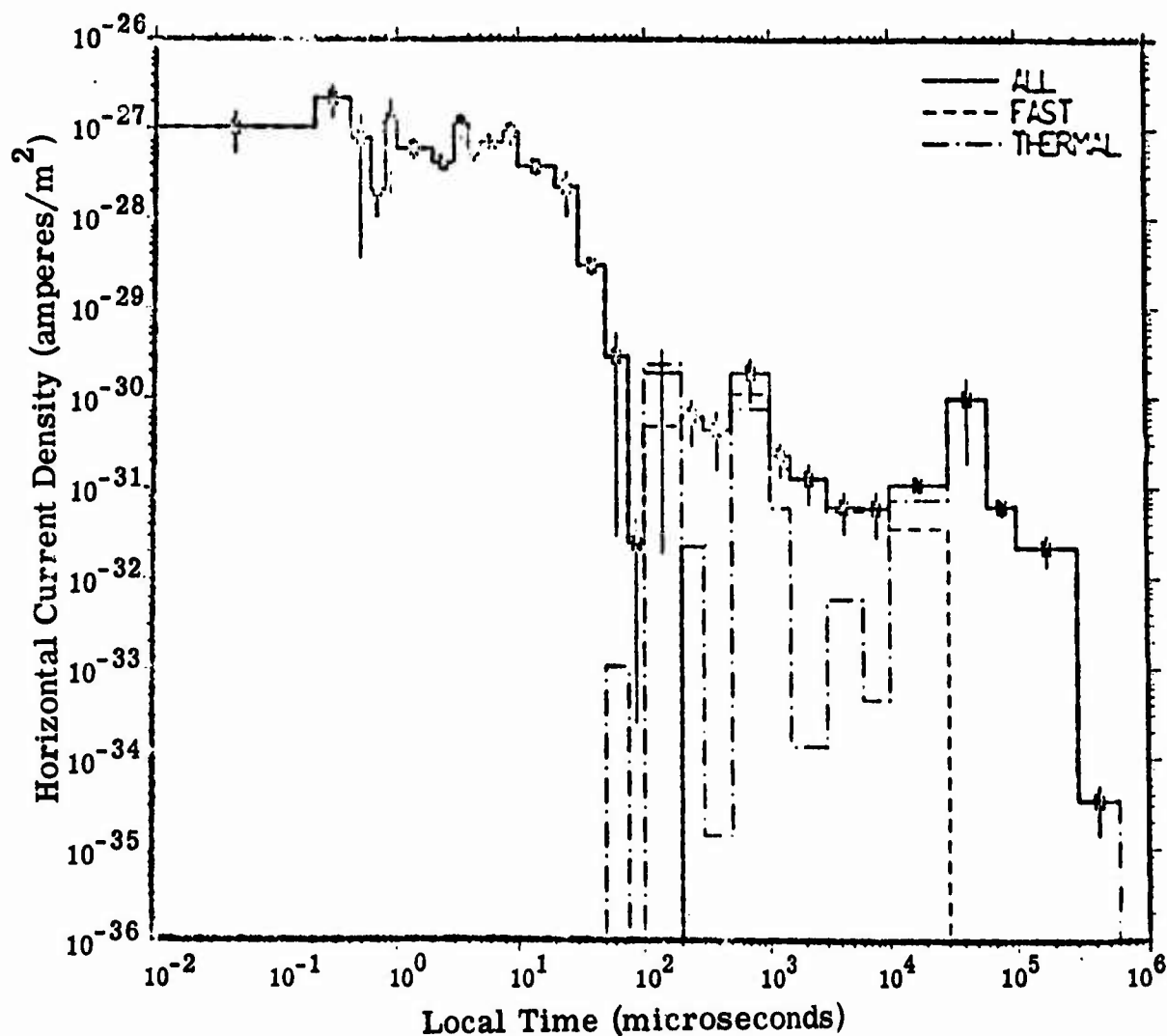


Figure 2.73. Horizontal current density vs. time at radius = 1900 - 2100 m, elevation = 0 - 50 m, due to thermonuclear source at HoB = 500 m.

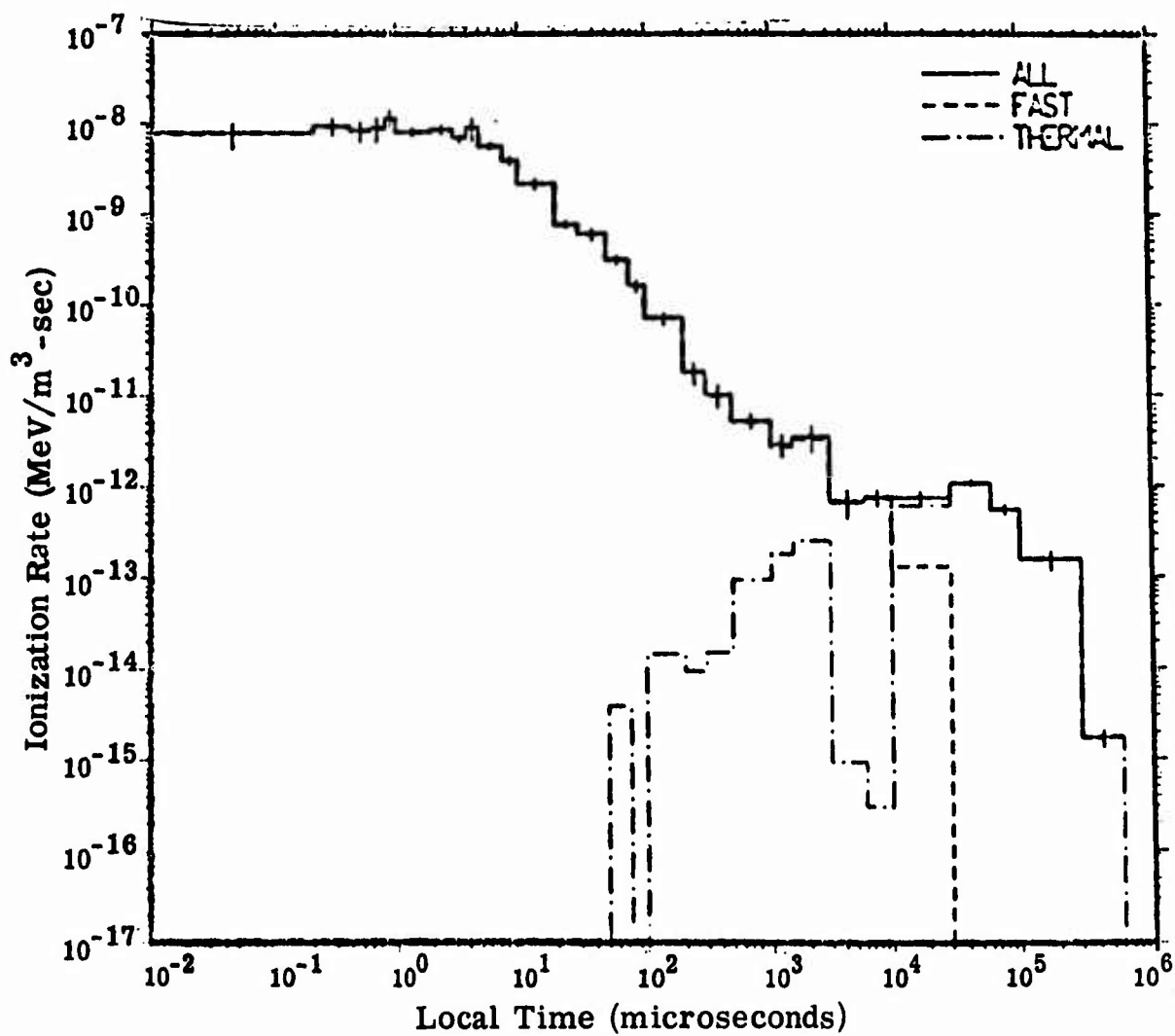


Figure 2.74. Ionization rate vs. time at radius = 1900 - 2100 m,  $\cos \theta = 0.5 - 1.0$ , due to thermonuclear source at HoB = 500 m.

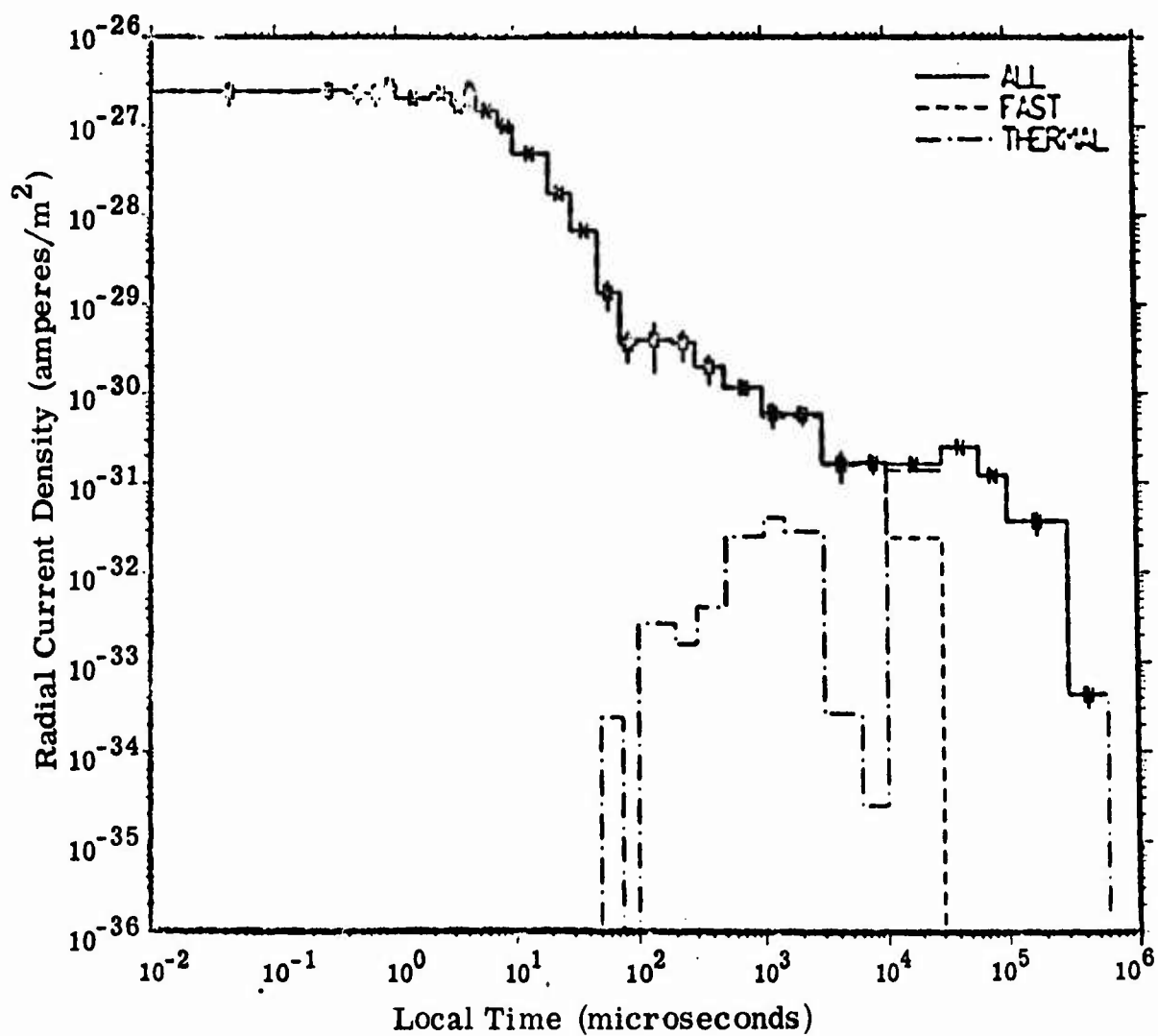


Figure 2.75. Radial current density vs. time at radius = 1900 - 2100 m,  $\cos \theta = 0.5 - 1.0$ , due to thermonuclear source at HoB = 500 m.



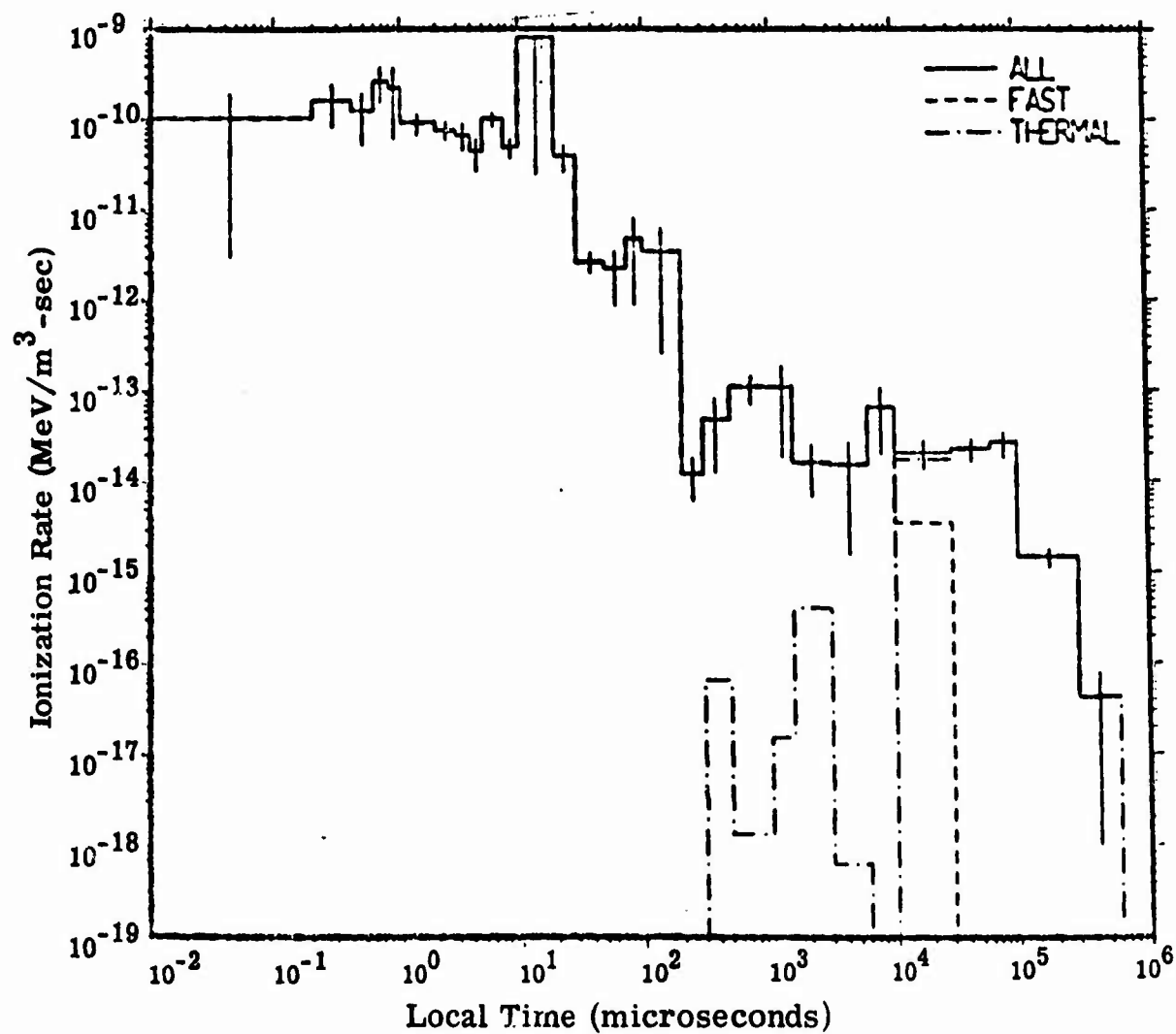


Figure 2.76. Ionization rate vs. time at radius = 2700 - 3100 m, elevation 0 - 50 m, due to thermonuclear source at HoB = 500 m.

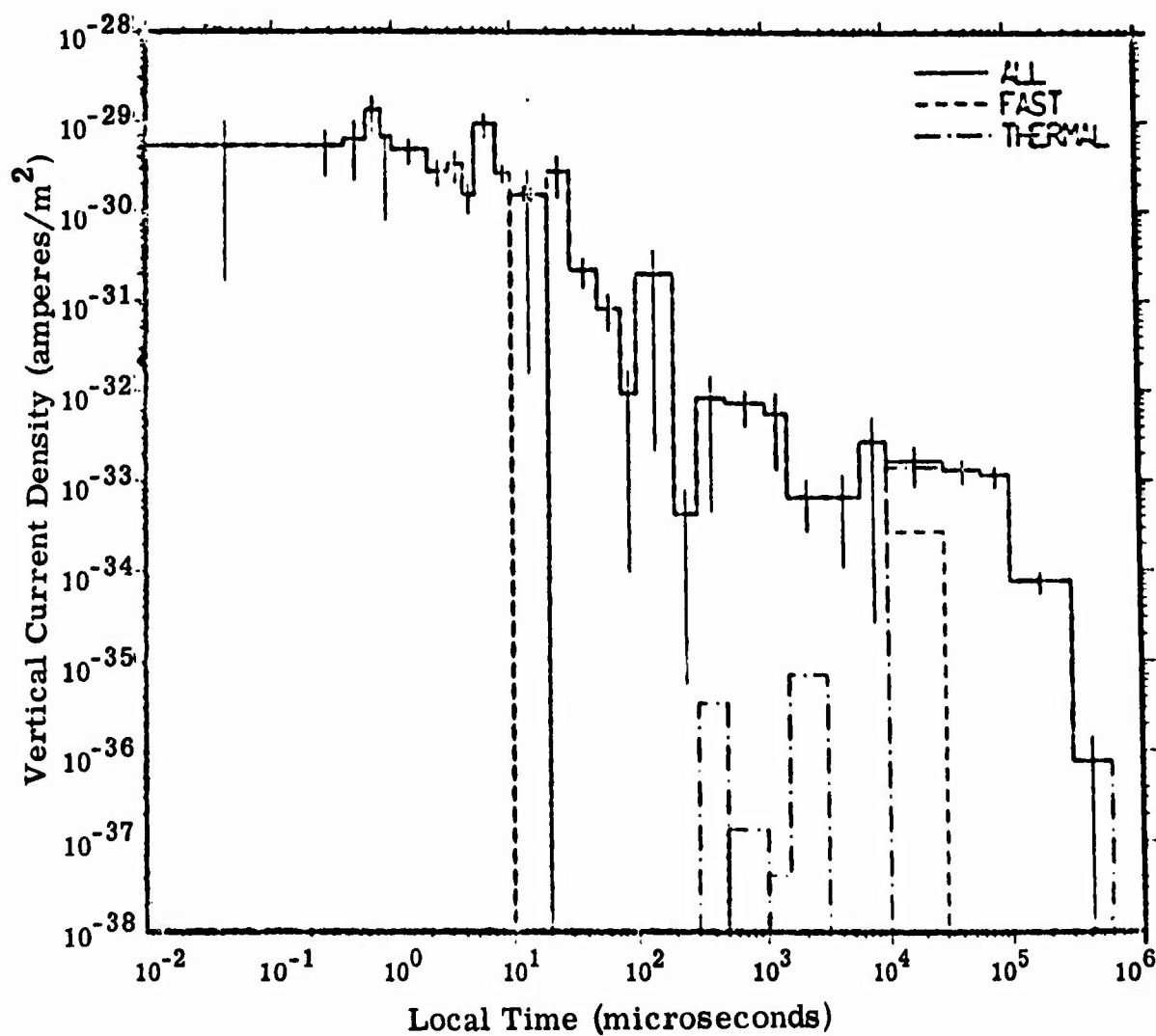


Figure 2.77. Vertical current density vs. time at radius 2700 - 3100 m, elevation = 0 - 50 m, due to thermonuclear source at HoB = 500 m.

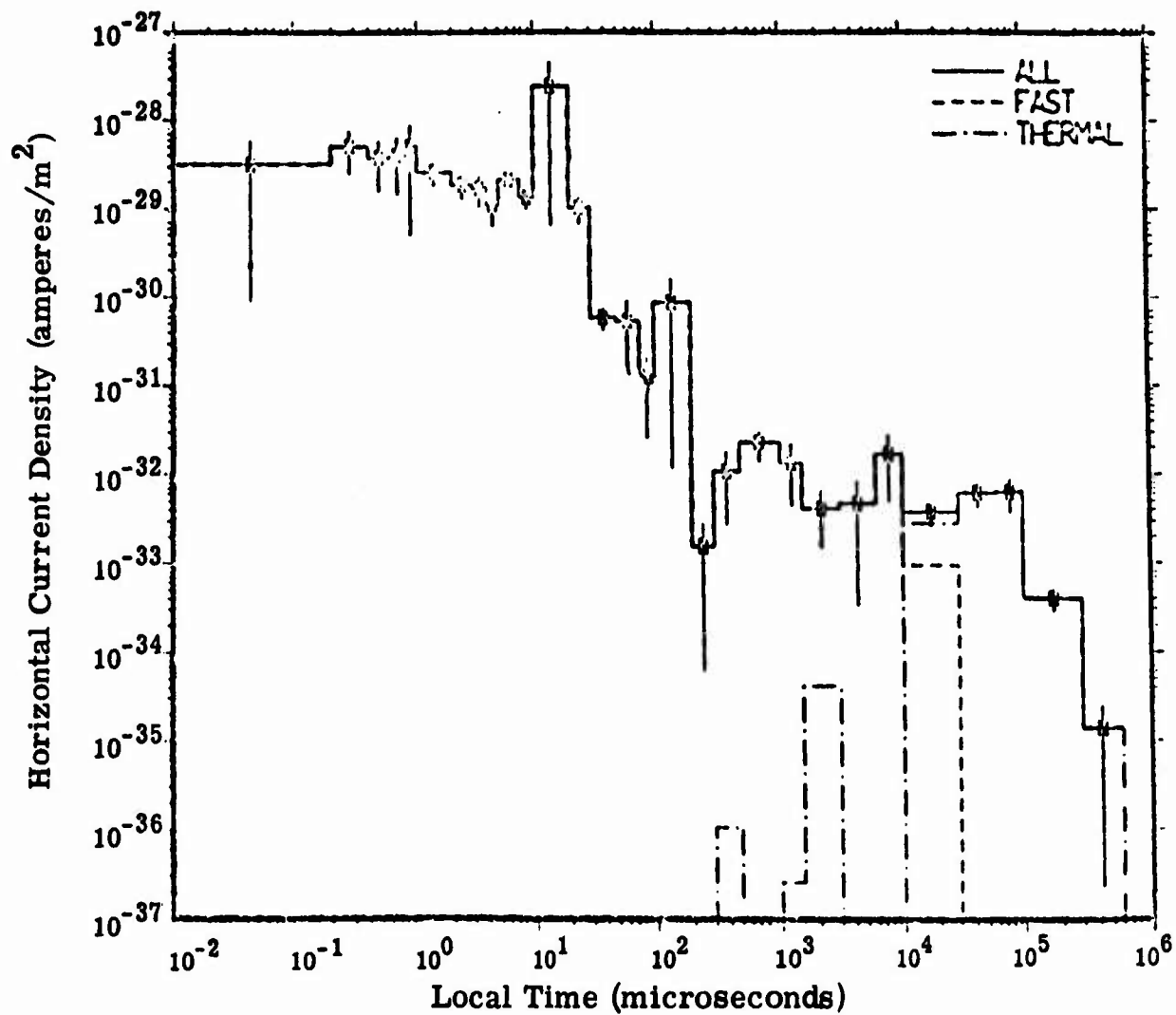


Figure 2. 78. Horizontal current density vs. time at radius = 2700 - 3100 m, elevation = 0 - 50 m, due to thermo-nuclear source at HoB = 500 m.

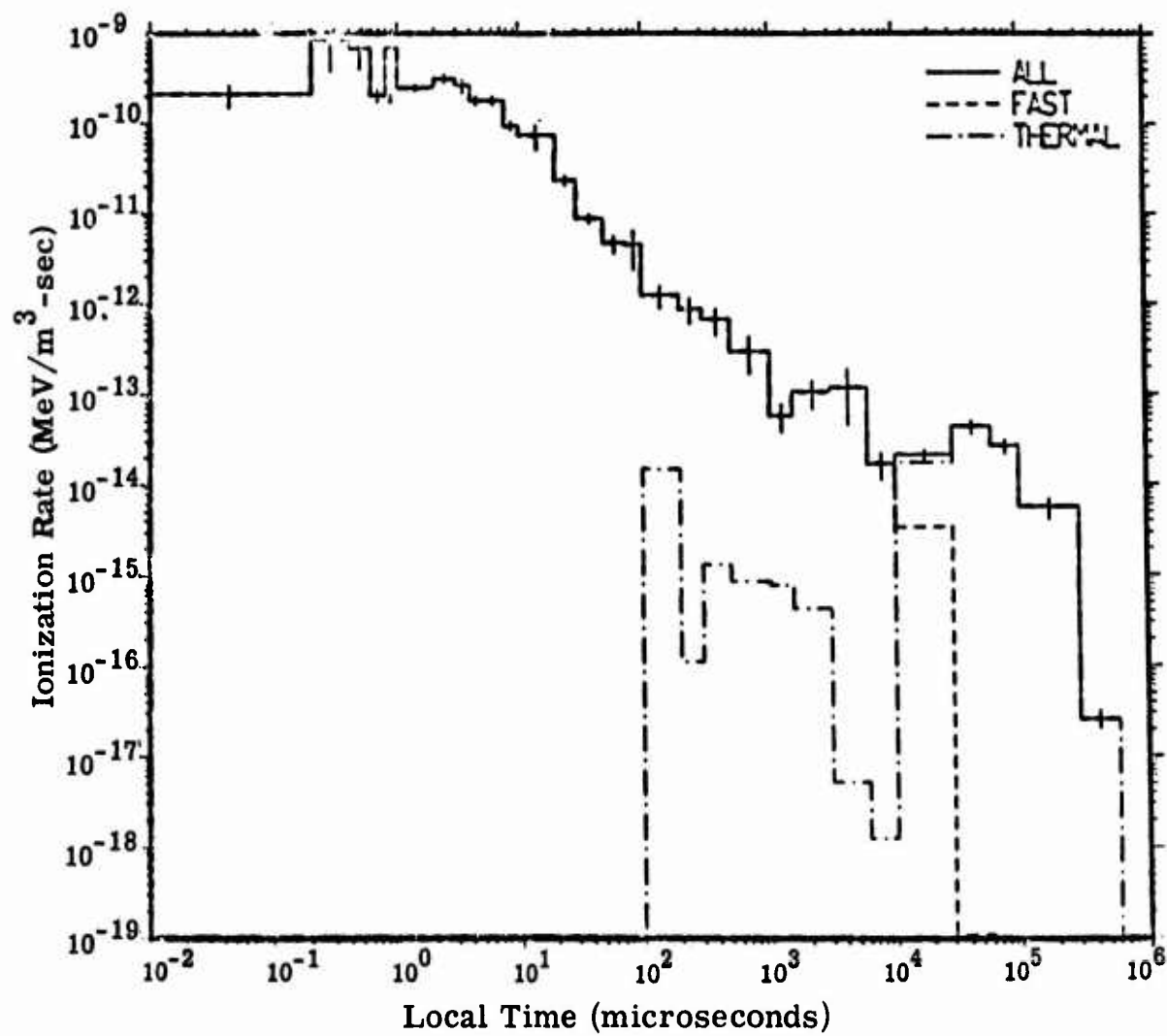


Figure 2.79. Ionization rate vs. time at radius = 2700 - 3100 m,  $\cos \theta = 0.5 - 1.0$ , due to thermonuclear source at HoB = 500 m.

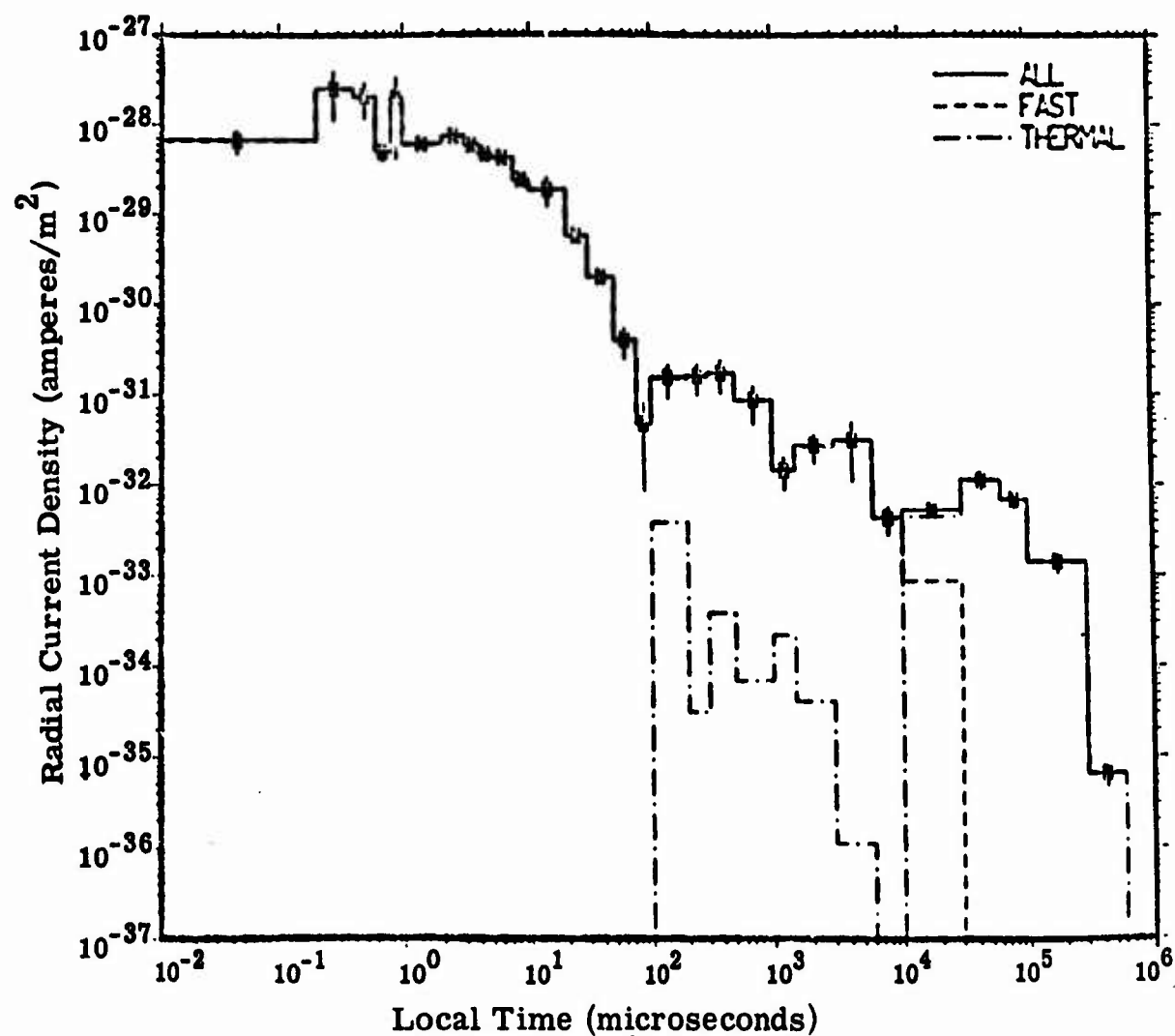


Figure 2.80. Radial current density vs. time at radius = 2700 - 3100 m,  $\cos = 0.5 - 1.0$ , due to thermo-nuclear source at HoB = 500 m.

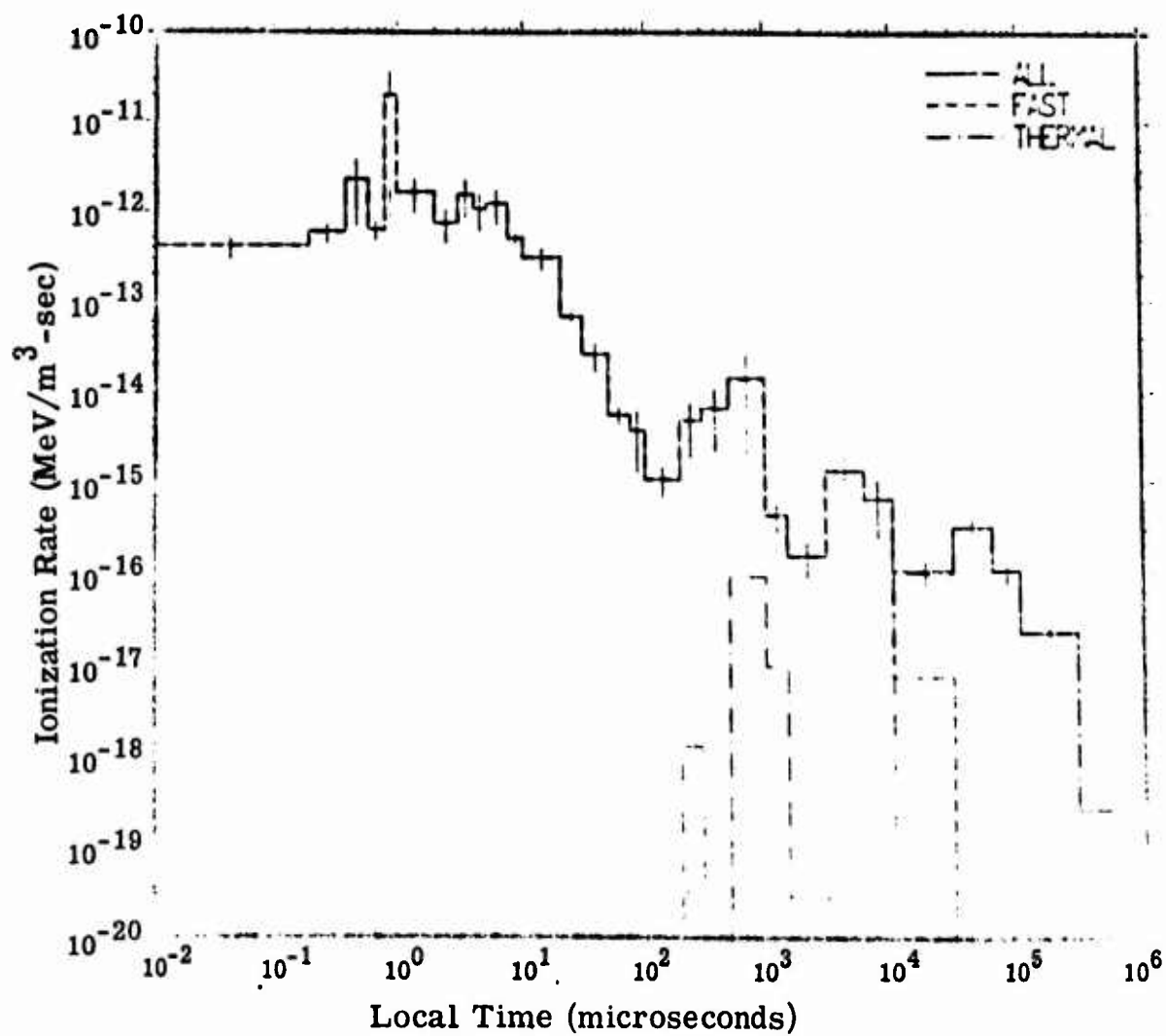
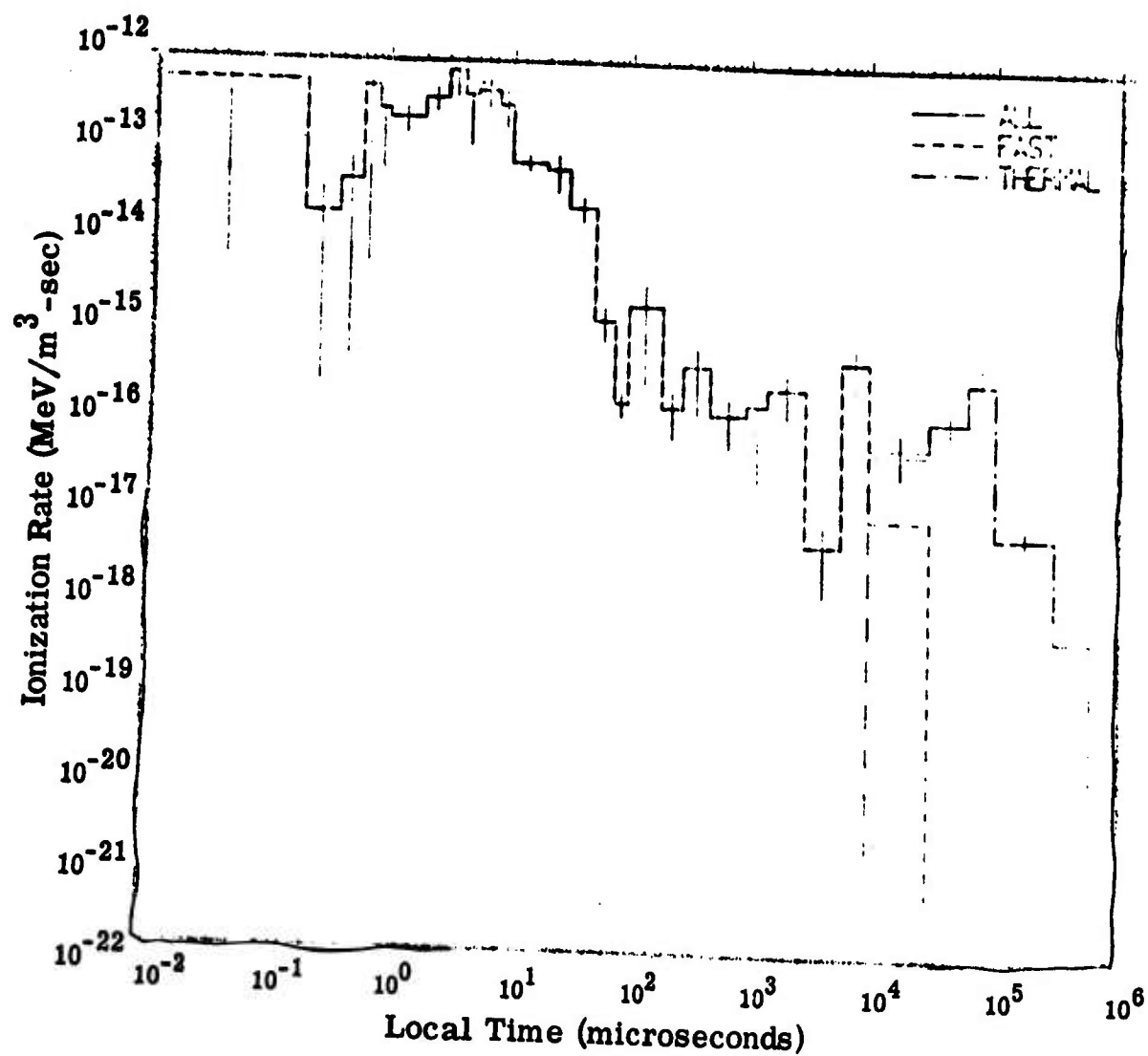


Figure 2.81. Ionization rate vs. time at radius = 4000 - 5000 m,  $\cos \theta = 0.5 - 1.0$ , due to thermonuclear source at HoB = 500 m.



Reproduced from  
best available copy.

Figure 2.82. Ionization rate vs. time at radius = 4000 - 5000 m, elevation = 0 - 50 m, due to thermonuclear source at HoB = 500 m.

### 3. CURVE FIT REPRESENTATION OF TRANSPORT RESULTS

#### 3.1 GENERAL REMARKS

The transport calculations for EMP sources result in a very large set of numbers. In addition, EMP environment prediction codes require sources at various ranges, angles and times many of which are not directly available in the transport calculation data. Therefore, it is necessary to provide some sort of curve fit representation to reduce the quantity of data in the transport results and allow sources to be generated at arbitrary times, ranges and angles.

This section describes the curve fitting of transport data from a previous EMP neutron-induced source calculation<sup>(3)</sup>. This calculation was for the typical thermonuclear spectrum<sup>(4)</sup>, but used an older set of the ENDF/B data and did not include any air capture effects. The transport bin structure is presented in Table 5. While this previous calculation lacks many of the desirable features of the calculation described elsewhere in this report, it still makes available a good two dimensional representation of neutron induced EMP sources.

The curve fitting effort was mainly directed toward the implementation of new sources in the AFWL code SC. The new sources will enhance the reliability of the code in extended regions of space and time as well as adding ground capture effects, angular dependence of sources and transverse currents which were not previously considered. While the fits were produced with SC in mind they should be readily usable with any other EMP ground burst code. They are already a part of the AFWL code NEW1 and work is proceeding to implement them in SC.



Table 5

## BIN STRUCTURES FOR TRANSPORT PROBLEMS

Radial Intervals (meters)	Depth Intervals (cm)	Polar Angle Intervals ( $\cos \theta$ )	Local Time Intervals ( $\mu\text{sec}$ )	Height Intervals (meters) (Applicable only to HoB = 200 meter problem)
0 - 150	0 - 2	0 - 0.1	0 -	0.2
150 - 250	2 - 6	0.1 - 0.2	0.2 -	0.4
250 - 350	6 - 14	0.2 - 0.4	0.4 -	0.6
350 - 450	14 - 30	0.4 - 0.7	0.6 -	0.8
450 - 550	30 - 50	0.7 - 1.0	0.8 -	1.0
550 - 650	50 - 90		1 -	2
650 - 750	90 - 120		2 -	3
750 - 850	120 - 180		3 -	4
850 - 950			4 -	5
950 - 1050			5 -	7.5
1050 - 1300			7.5 -	10
1300 - 1500			10 -	15
1500 - 1700			15 -	20
1700 - 1900			20 -	25
1900 - 2100			25 -	30
2100 - 2300			30 -	40
2300 - 2500			40 -	50
2500 - 2700			50 -	75
2700 - 2900			75 -	100
2900 - 3100			100 -	200
			200 -	350
			350 -	500
			500 -	1000
			1000 -	1500
			1500 -	3000
			3000 -	6000
			6000 -	10,000

### 3.2 THE TRANSPORT DATA

The fitting effort considered only the transport data in the air for the ground burst. Ground sources have been neglected as has the data for the 200 meter height of burst. Aside from time considerations, the 200 meter burst data was not fit because there is at present no available two dimensional code which could use the data. One dimensional codes such as NEW1 at AFWL can use the data but do not seem to require an elaborate set of fits in angle, range and time. If a two dimensional code is developed for above ground bursts, it would be desirable to base its sources on the improved source calculation described in the other sections of this report. Some studies with NEW1 have indicated that the ground sources associated with a ground burst do not change EMP fields drastically for close in problems.<sup>(5)</sup> Their effect should be small for ranges farther out and outside the source region. Thus, since it seemed that ground sources should not be installed in SC they were not fit. It does seem, however, that the fitting procedure discussed here could easily be made to handle the data for the ground sources or the 200 meter burst with minor modifications.

Data are available out to a range of 3000 meters and a time of 10 milliseconds. However, statistics associated with the transport results become steadily worse as one goes to far ranges or later times. The fitting only considered times out to 1 millisecond. This is appropriate because air capture effects ( which were not considered) are important beyond this time. The statistics associated with the transverse (theta) currents are particularly bad at the far ranges. Thus, fits to the transverse currents only go out to 1000 meters.

### 3.3 THE FITTING PROCEDURE

The desirable result of a fitting effort is a short FORTRAN subroutine which can be included in the EMP prediction codes. The subroutine must provide the neutron induced source information for arbitrary points in range, angle and time and should be reasonably efficient and easy to use.

It was decided that it would be exceedingly difficult to find functional forms which would adequately fit the data in the three variables of interest. Therefore, with the source subroutine in mind, the following approach was followed. First, the data were fit as well as possible in the time domain for each point in range and angle. Then with these time domain fits as data for the subroutine, an interpolation scheme is used to generate values at any point in range and angle. Each time domain fit involves 10 parameters and there are 285 curves (5 angle bins x 19 range bins x 3 source quantities = 285 curves to be fit). Thus, the subroutine stores 2850 parameters but still can occupy less than 6000 octal memory locations. This is easily compatible with the space available in the EMP prediction codes at AFWL. It should be noted that the first range bin is deleted because of poor statistics and that parameters are carried for transverse current beyond 1000 meters though it is recommended they not be used.

### 3.4 THE TIME DOMAIN FITS

In the time domain each source curve is divided into three regions: (1) times before neutron arrival (based on a 15 MeV neutron); (2) late times arbitrarily defined to the times greater than 3 times the neutron arrival time; and (3) the remaining region from arrival time  $t_a$  to time  $3 t_a$ .

In the region of time  $t < t_a$  the logarithms of the source values are fit as a linear function of time by a least square polynomial fitting routine (for the transverse current the logarithm of 1 plus the value is fit). In the late-time region  $t > 3t_a$  a cubic function is fit to the logarithm of the source values as a logarithmic function of time by the same routine. In the remaining region  $t_a < t < 3t_a$  a similar cubic function is used which provides continuity between the other two fits and satisfies other conditions which vary with the different source quantities. Thus, ten parameters A1, ----, A10 represent each curve as follows:

$$\text{Source } (t) = \begin{cases} \exp (A1 + A2 t), & t \leq t_a \\ \exp (A3 + A4 (\ln t) + A5 (\ln t)^2 + A6 (\ln t)^3), & t_a < t < 3 t_a \\ \exp (A7 + A8 (\ln t) + A9 (\ln t)^2 + A10 (\ln t)^3), & t \geq 3 t_a . \end{cases}$$

The parameters A1, A2, A7, A8, A9 and A10 are calculated by the least polynomial fitting routine POLY<sup>(6)</sup> using the transport statistics as fitting weight factors. The cubic function in the middle represented by parameters A3, A4, A5 and A6 is determined by the following requirements:

1. For dose rate the function must
  - (a) connect with the first fit at  $t_a$  and the second fit at  $3t_a$ ,
  - (b) match the slope of the second fit at  $3t_a$ , and
  - (c) pass through the transport data point in the first time bin past  $t_a$ .

2. For radial current the function must
  - (a) connect with first fit at  $t_a$  and the second fit at  $3t_a$ , and
  - (b) match the slopes of the first fit at  $t_a$  and the second fit at  $3t_a$ .
  - (c) In addition, if the resulting function crosses over between  $t_a$  and  $3t_a$ , it is replaced by a quadratic function which satisfies (a) and (b) except for matching the slope at  $3t_a$  (in this case  $A6 = 0$ ).
3. For transverse current the function must
  - (a) connect with first fit at  $t_a$  and second fit at  $3t_a$  and
  - (b) match the slopes of the first fit at  $t_a$  and the second fit at  $3t_a$ .

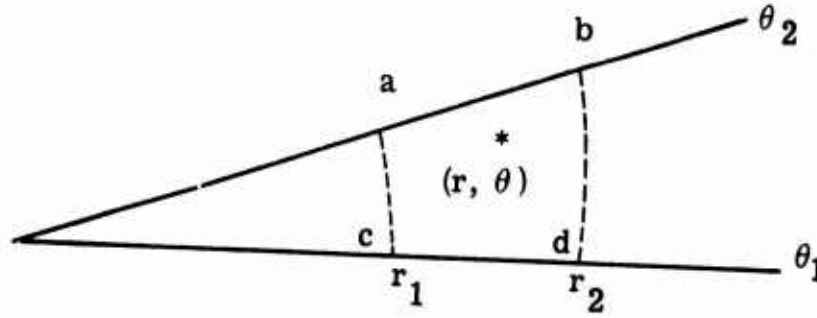
Examples of fits obtained in this way are shown overlayed with the transport data in Figs. 3.1 through 3.26. It can be seen that the transverse current fits (JTHETA) have some undesirable features but the error bars from the transport are rather large. The fits beyond one millisecond should be ignored for JTHETA. There are some additional difficulties at far ranges with the fits for dose rate and radial current. Some of them might have been eliminated with additional effort but it is felt errors that are not too drastic at far ranges will not severely affect EMP field calculations.

### 3.5 THE INTERPOLATION PROCEDURE

To calculate source information for use in the EMP codes, interpolation is done between the time domain fits. For dose rate and radial current the range interpolation is done linearly for the logarithm

of the square of the range times the source quantity. For the transverse current, the range interpolation is linear for the square of the range times the value. In all cases the angle interpolation is linear for the cosine of the angle.

For an arbitrary point in time, range and angle  $(t, r, \theta)$  sources are calculated as follows. If the point lies within the transport data space grid, it will be located between 4 points where time domain fits exist.



In the above figure the four points are labeled a, b, c, and d. Let  $V_a, V_b, V_c, V_d$  be the values of any one of the source quantities at the four points calculated from the time domain fits at time  $t$ . For dose rate or radial current, obtain the intermediate quantities  $V_l$  and  $V_u$  by range interpolation:

$$V_l = \frac{1}{r^2} \exp \left\{ \ln(r_1^2 V_c) + \frac{r - r_1}{r_2 - r_1} (\ln(r_2^2 V_d) - \ln(r_1^2 V_c)) \right\}$$

$$V_u = \frac{1}{r^2} \exp \left\{ \ln(r_1^2 V_a) + \frac{r - r_1}{r_2 - r_1} (\ln(r_2^2 V_b) - \ln(r_1^2 V_a)) \right\}$$

For transverse current (which crosses over in time):

$$V_l = \frac{1}{r^2} \left\{ (r_1^2 V_c) + \frac{r - r_1}{r_2 - r_1} ((r_2^2 V_b) - (r_1^2 V_l)) \right\}$$

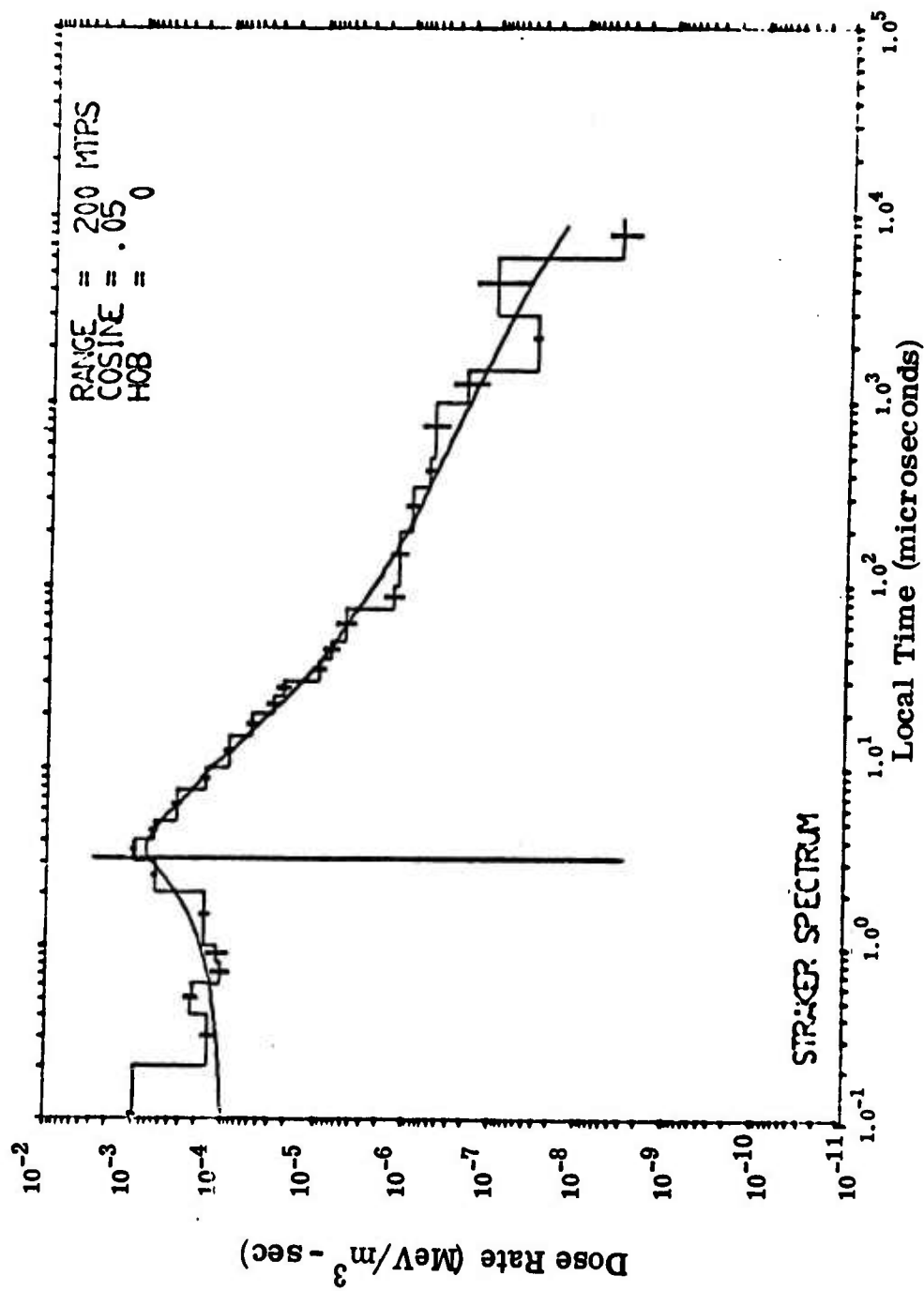


Figure 3.1. Curve fits for dose rates for typical thermonuclear source on ground, range = 200 meters,  $\cos \theta = 0.05$ .

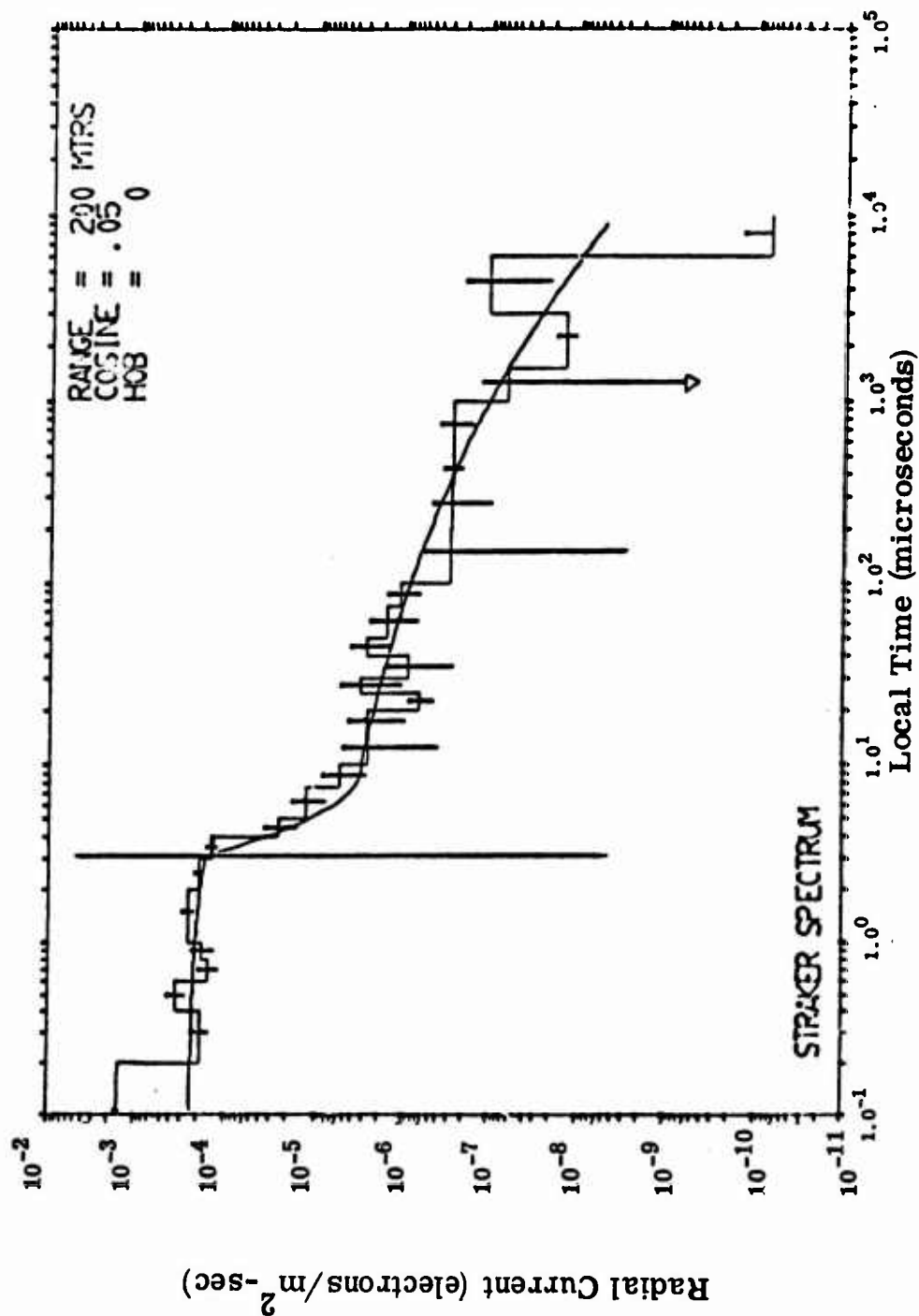


Figure 3.2. Curve fits for radial current densities for typical thermo-nuclear source on ground, range = 200 meters,  $\cos \theta = 0.05$ .



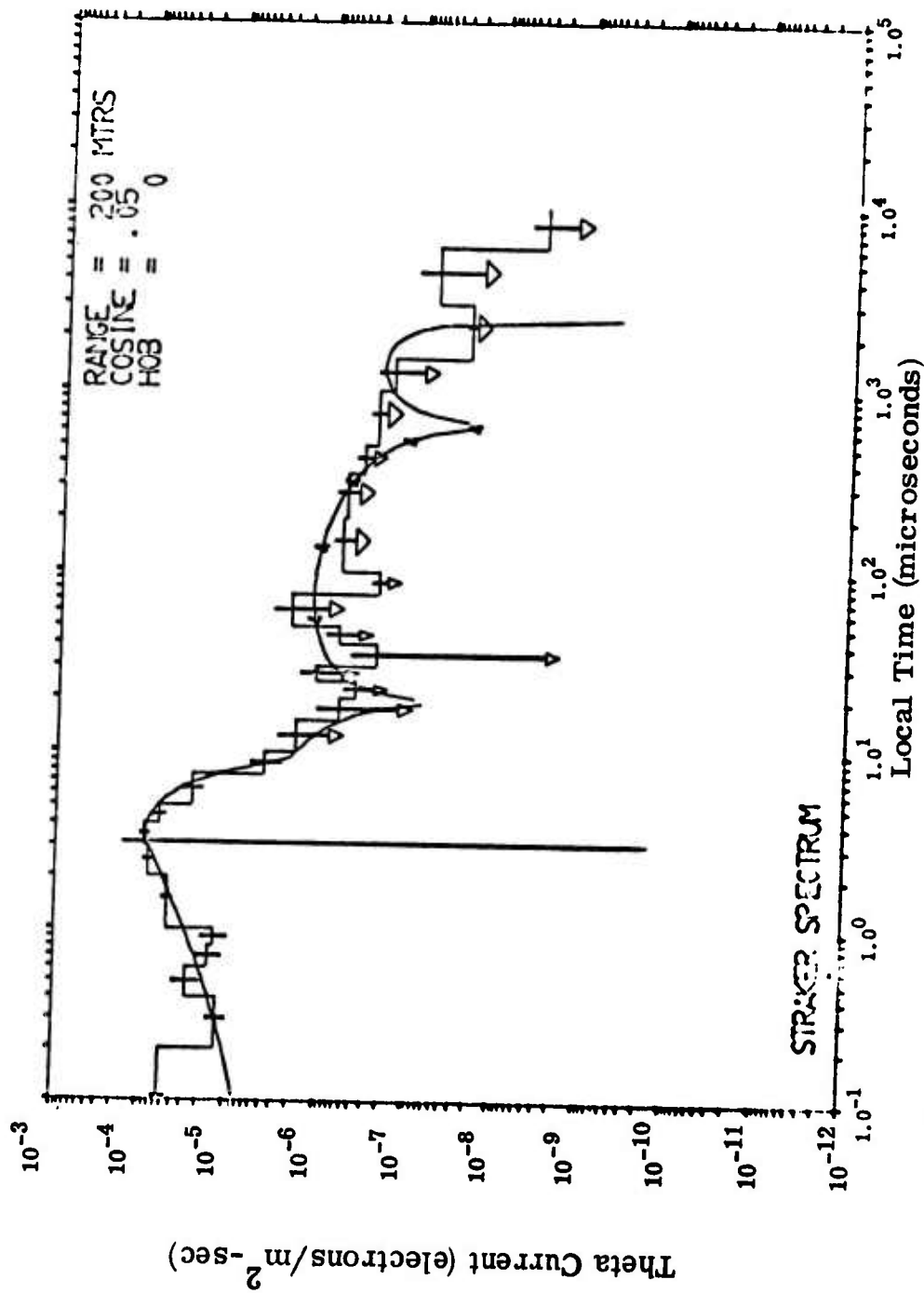


Figure 3.3. Curve fits for theta current densities for typical thermo-nuclear source on ground, range = 200 meters,  $\cos \theta = 0.05$ .

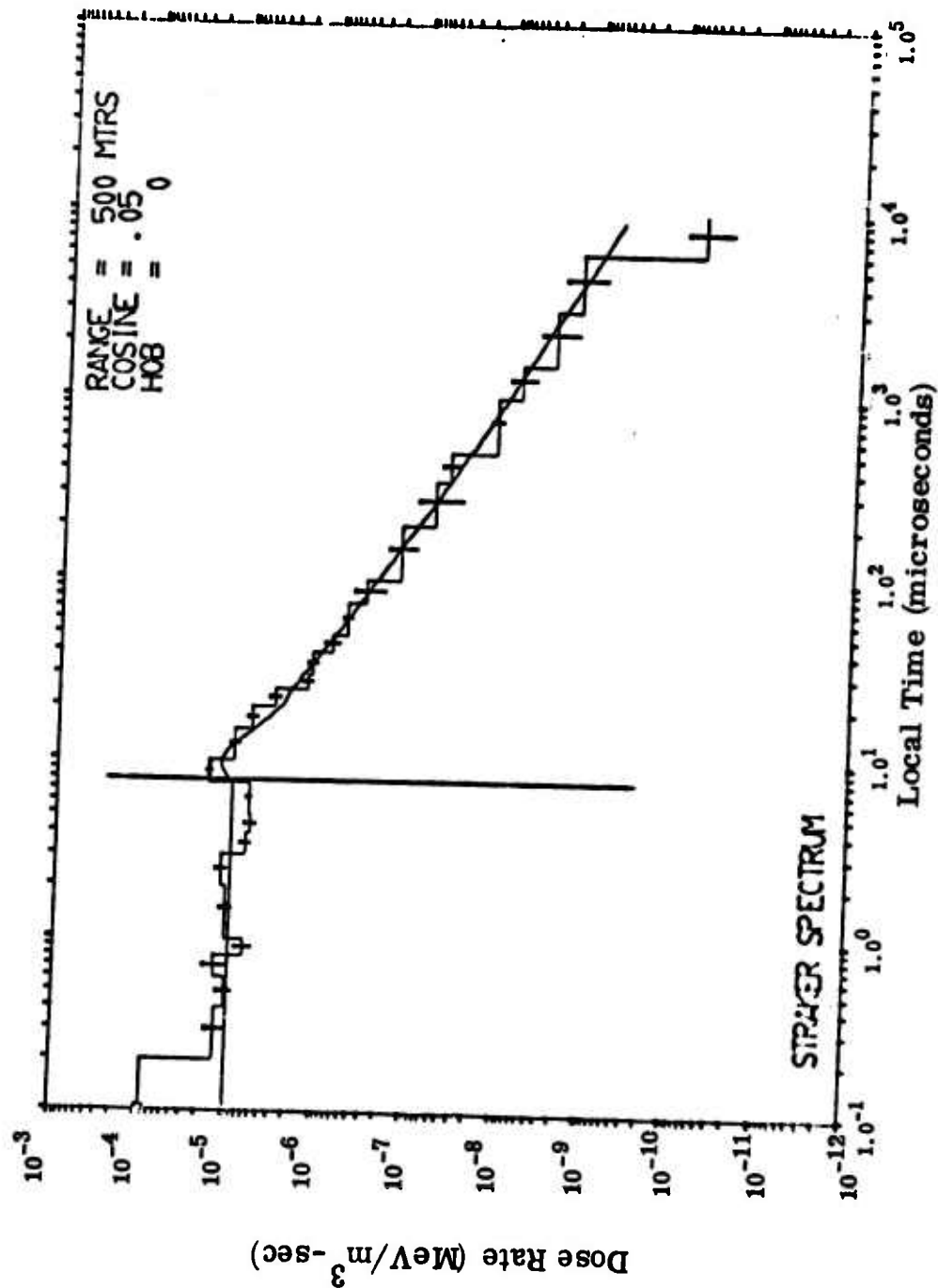


Figure 3.4. Curve fits for dose rates for typical thermonuclear source on ground, range = 500 meters,  $\cos \theta = 0.05$ .

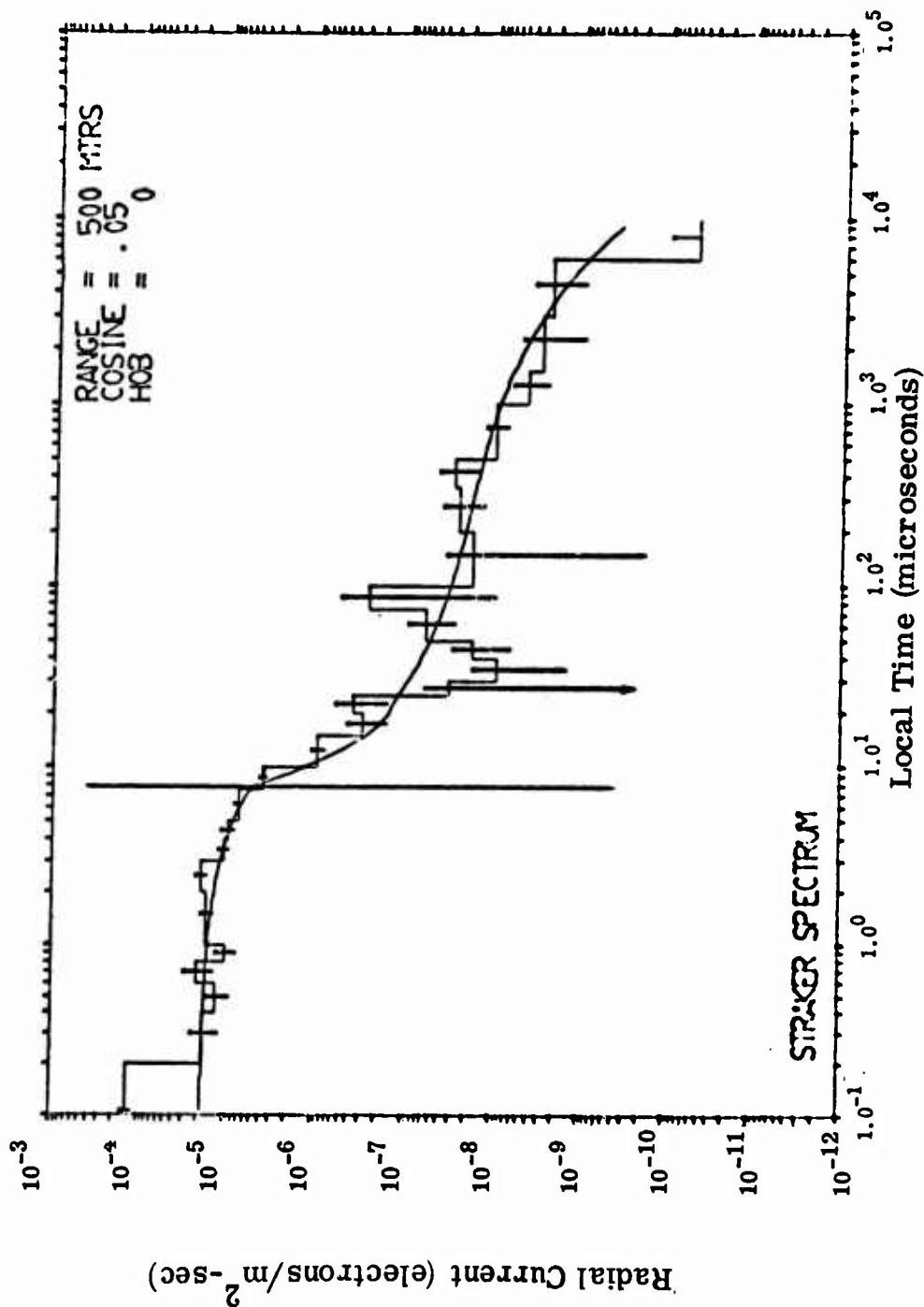


Figure 3.5. Curve fits for radial current densities for typical thermo-nuclear source on ground, range = 500 meters,  $\cos \theta = 0.05$ .

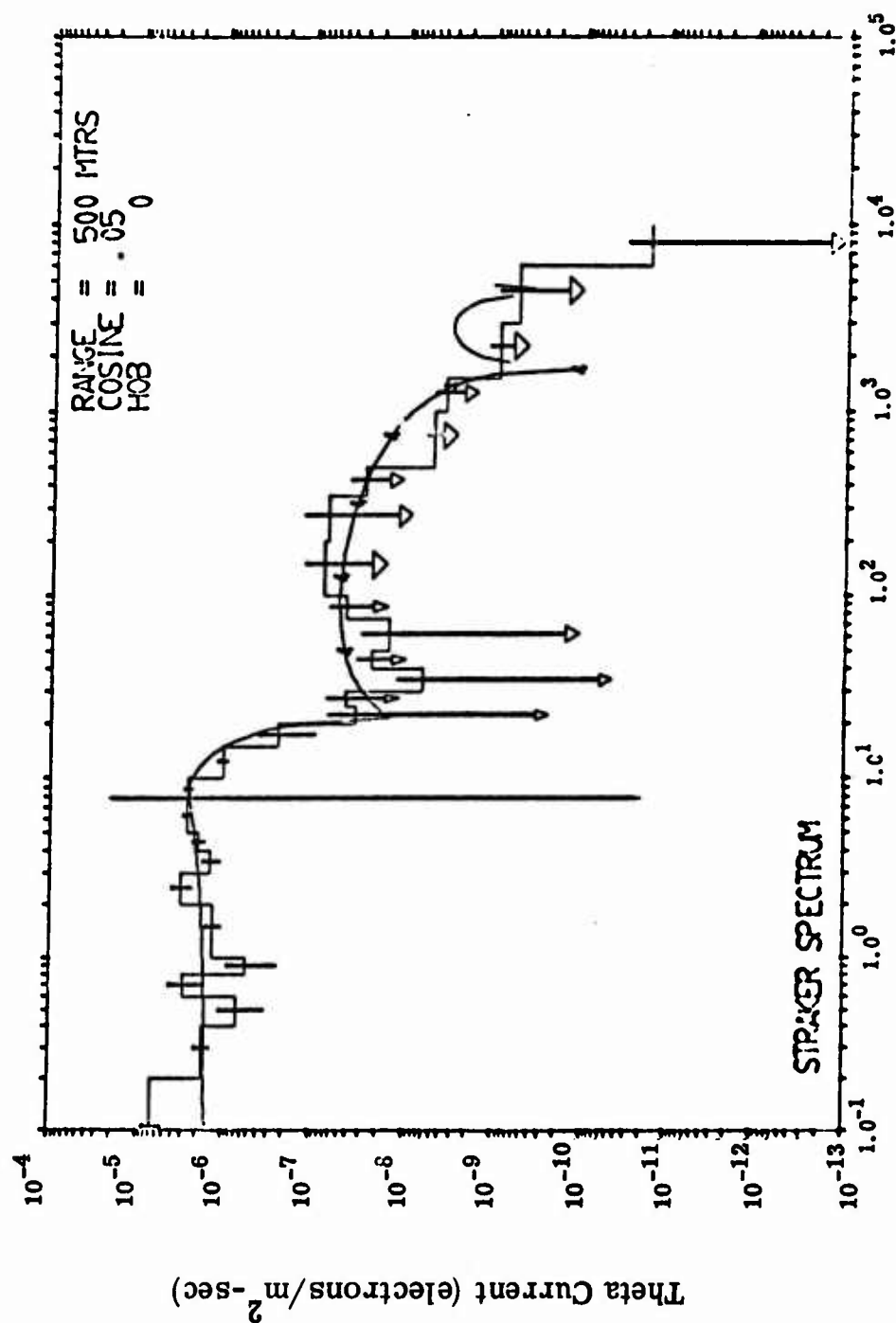


Figure 3.6. Curve fits for theta current densities for typical thermo-nuclear source on ground, range = 500 meters,  $\cos \theta = 0.05$ .

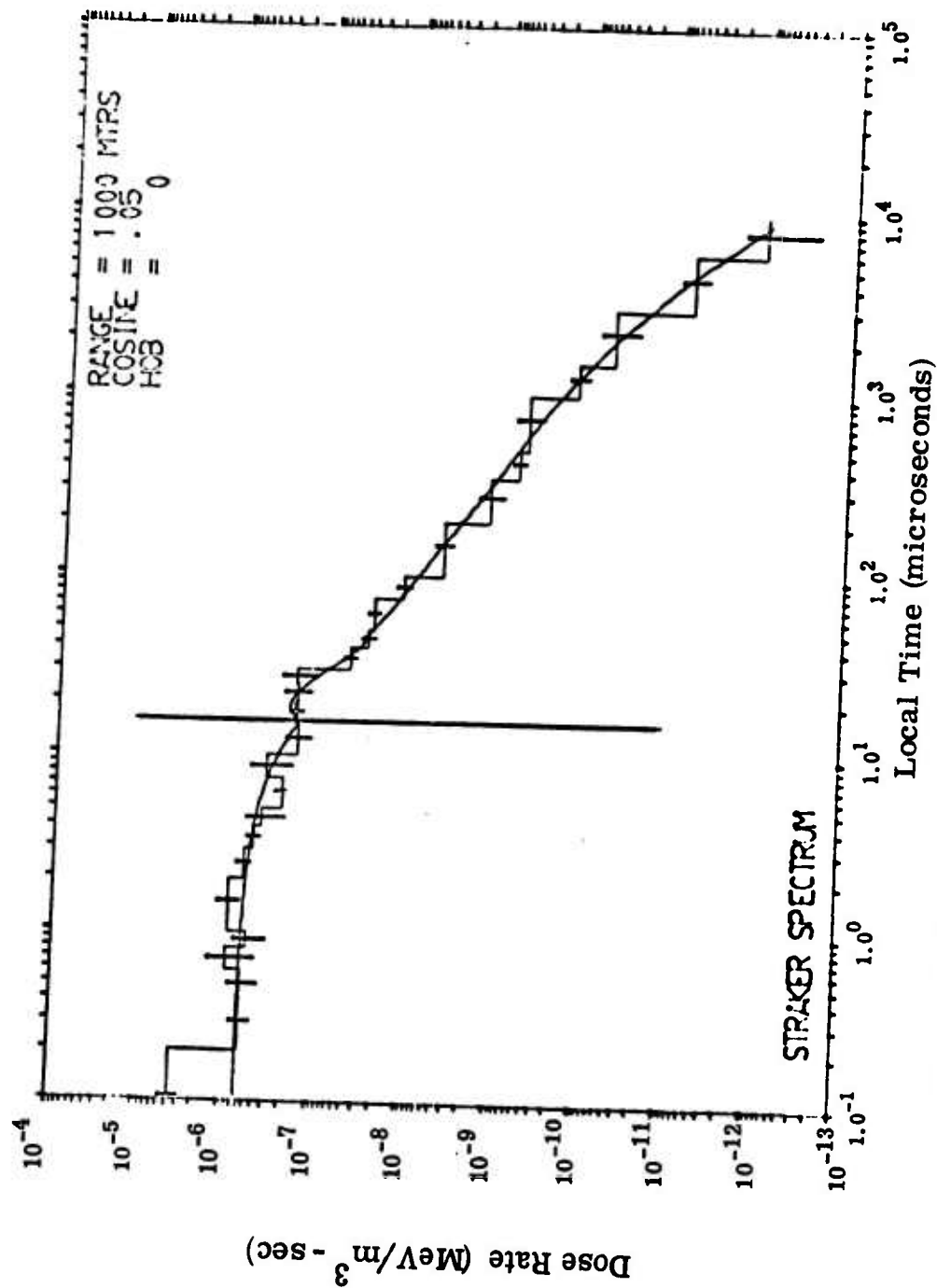


Figure 3.7. Curve fits for dose rates for typical thermonuclear source on ground, range = 1000 meters,  $\cos \theta = 0.05$ .

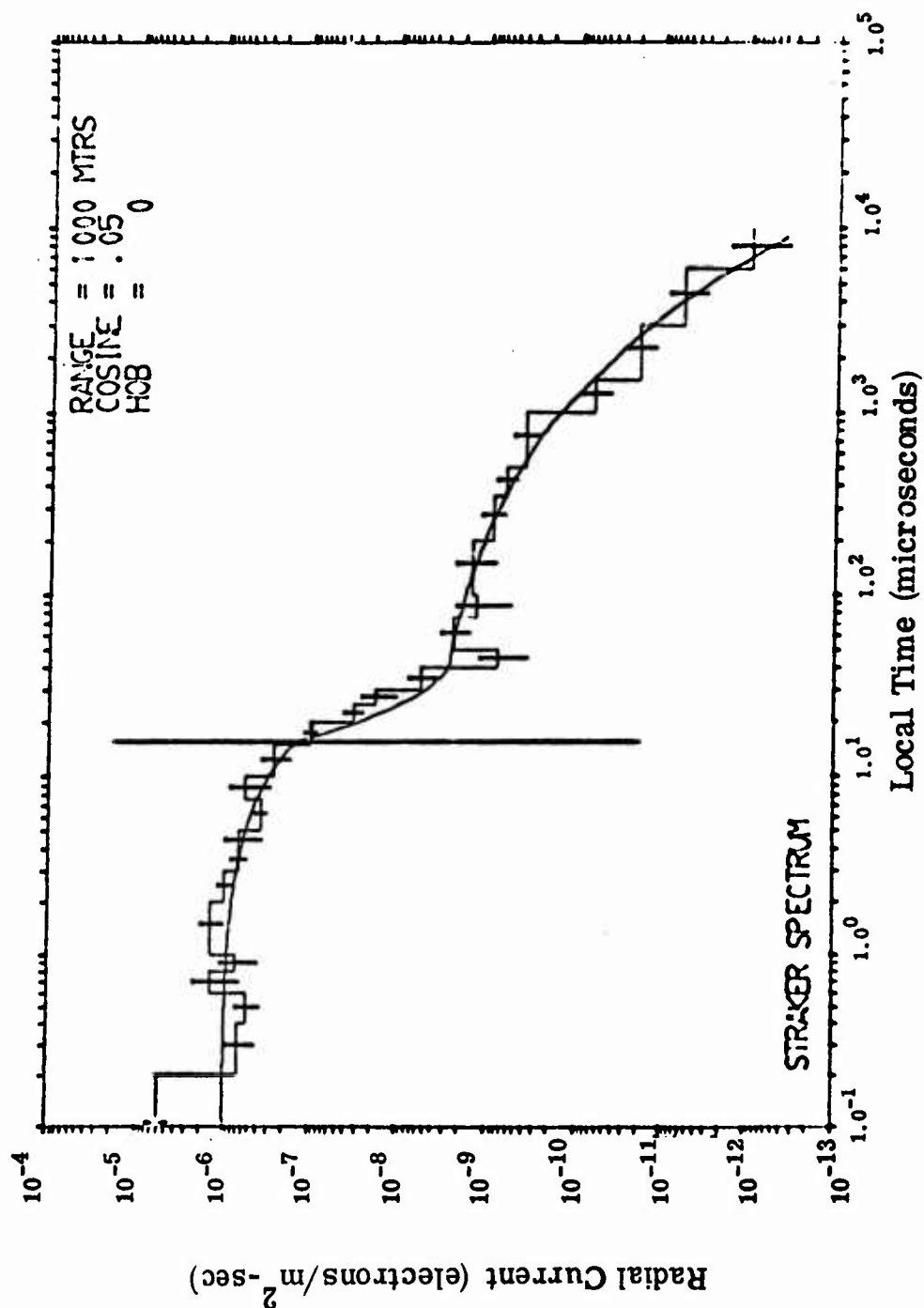


Figure 3.8. Curve fits for radial current densities for typical thermo-nuclear source on ground, range = 1000 meters,  $\cos \theta = 0.05$ .

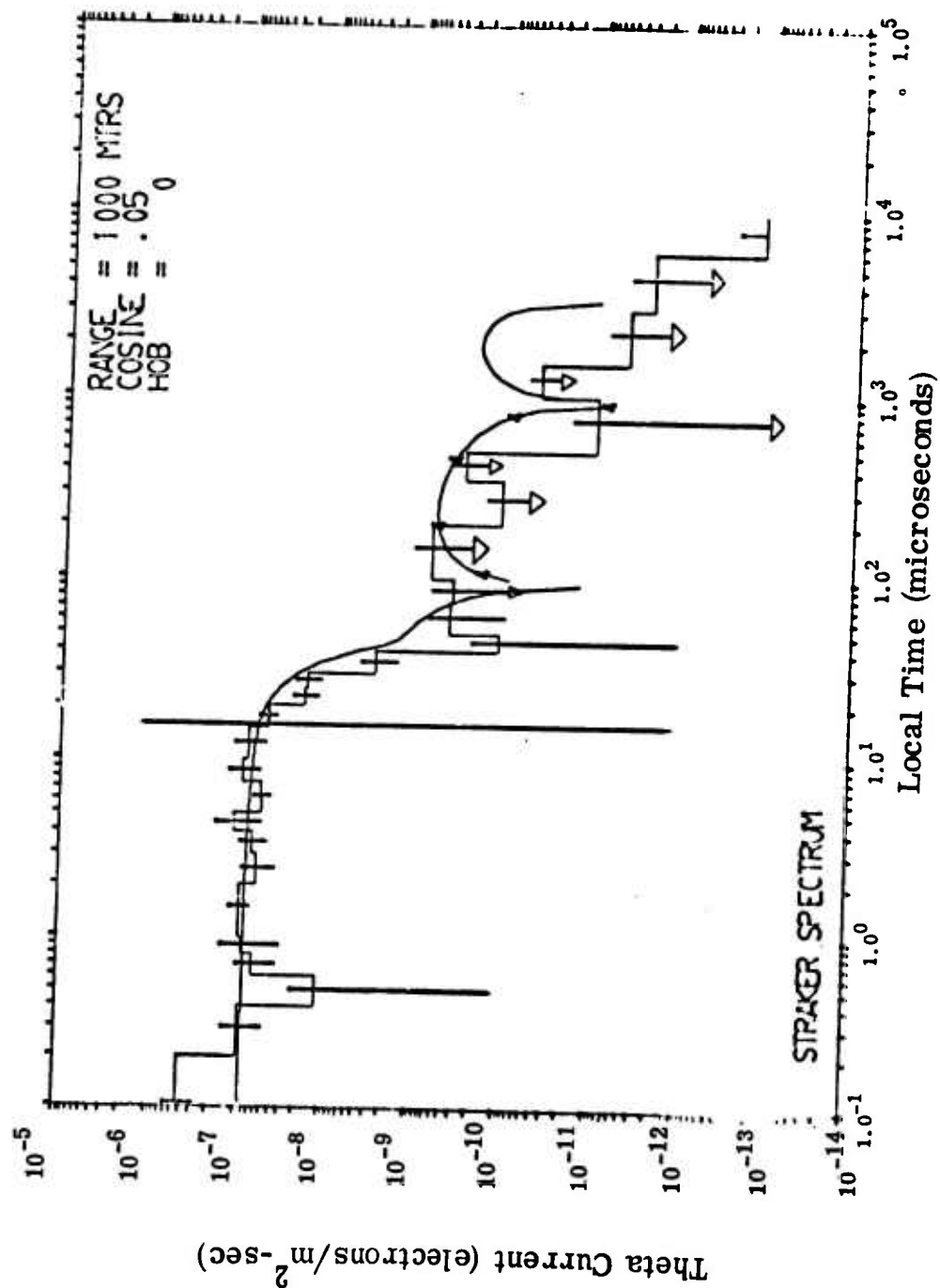


Figure 3.9. Curve fits for theta current densities for typical thermo-nuclear source on ground, range = 1000 meters,  $\cos \theta = 0.05$ .

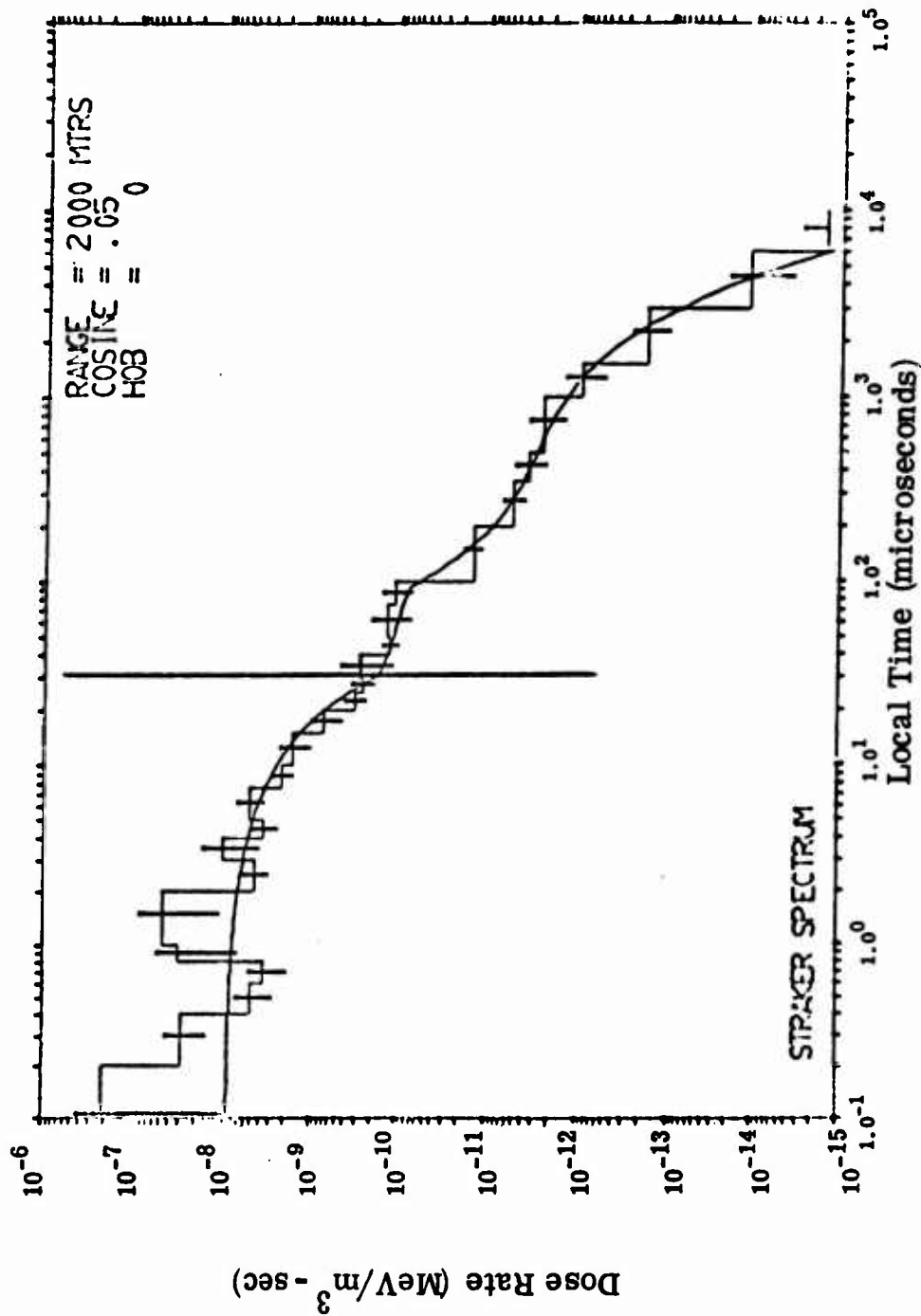


Figure 3.10. Curve fits for dose rates for typical thermonuclear source on ground, range = 2000 meters,  $\cos \theta = 0.05$ .



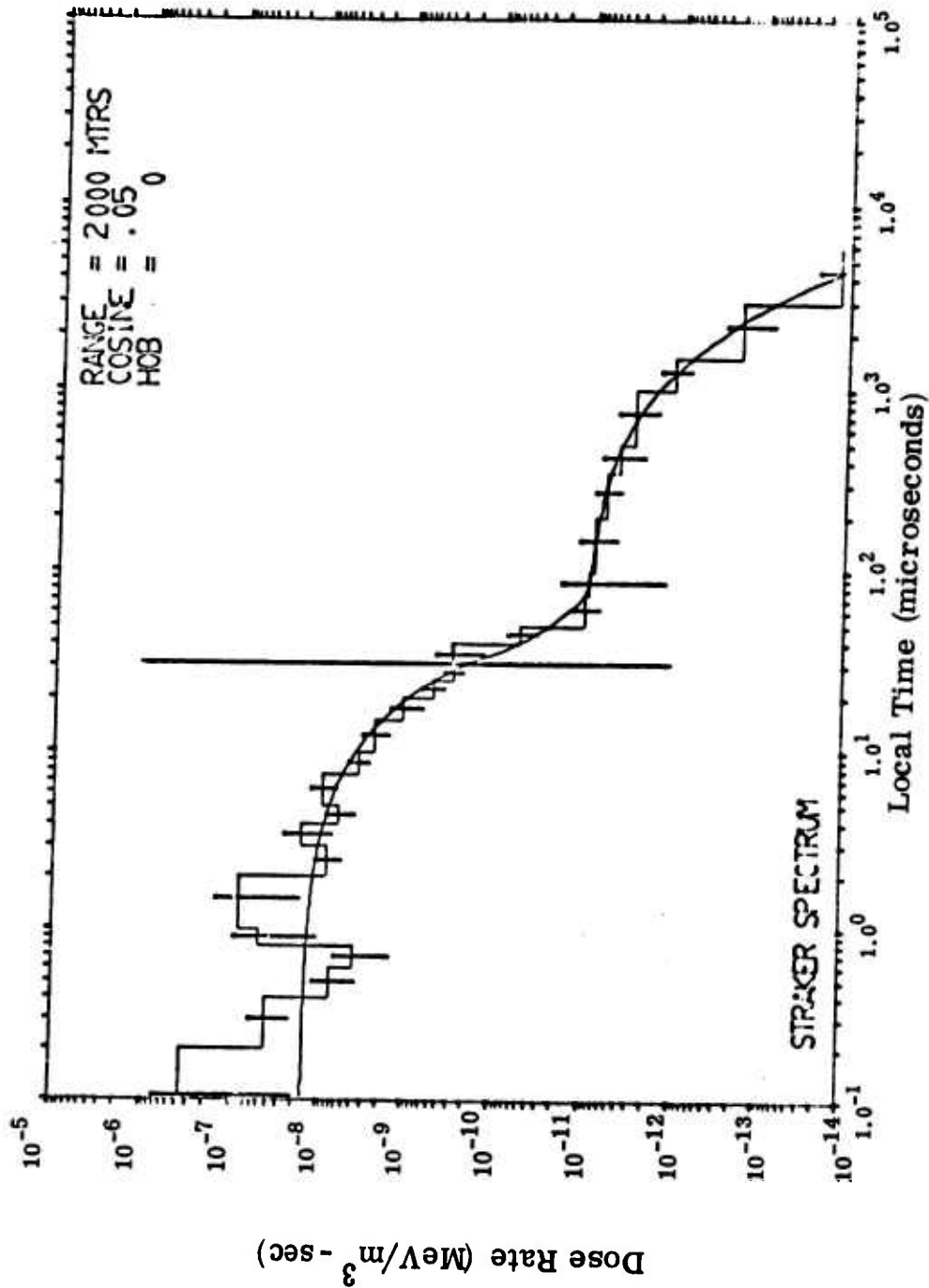


Figure 3.11. Curve fits for radial current densities for typical thermo-nuclear source on ground, range = 2000 meters,  $\cos \theta = 0.05$ .

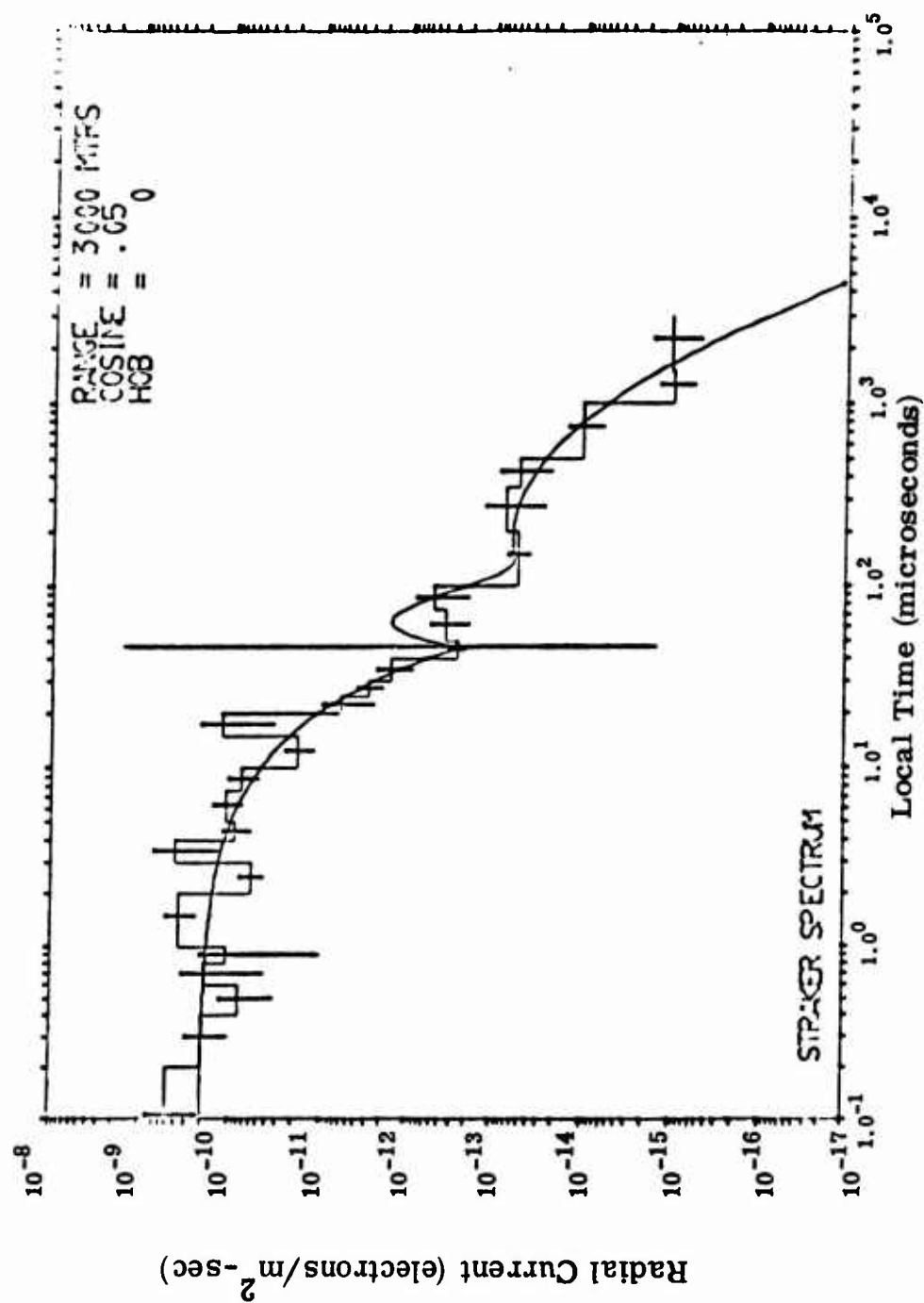


Figure 3.12. Curve fits for dose rates for typical thermonuclear source on ground, range = 3000 meters,  $\cos \theta = 0.05$ .

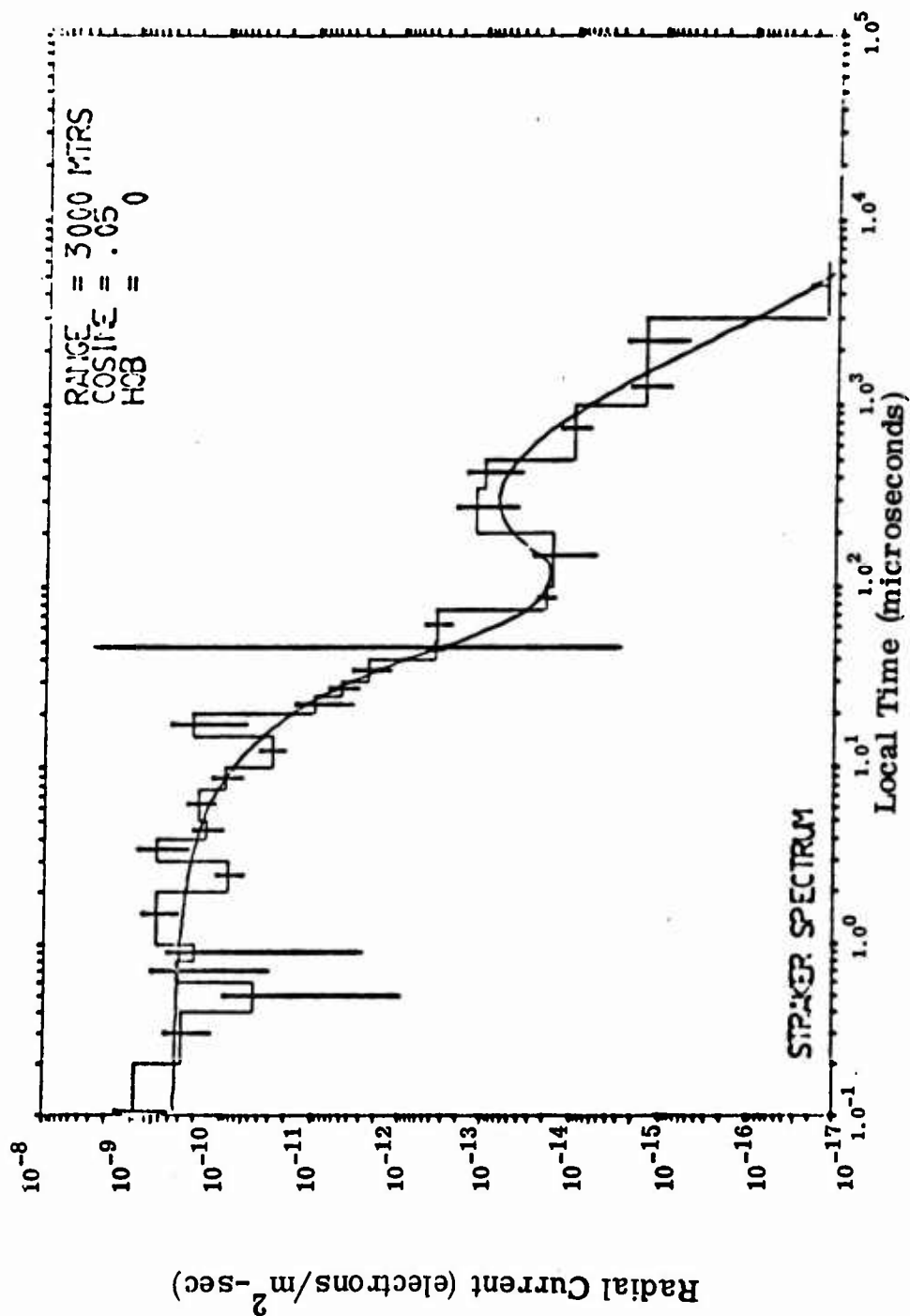


Figure 3.13. Curve fits for radial current densities for typical thermo-nuclear source on ground, range = 3000 meters,  $\cos \theta = 0.05$ .

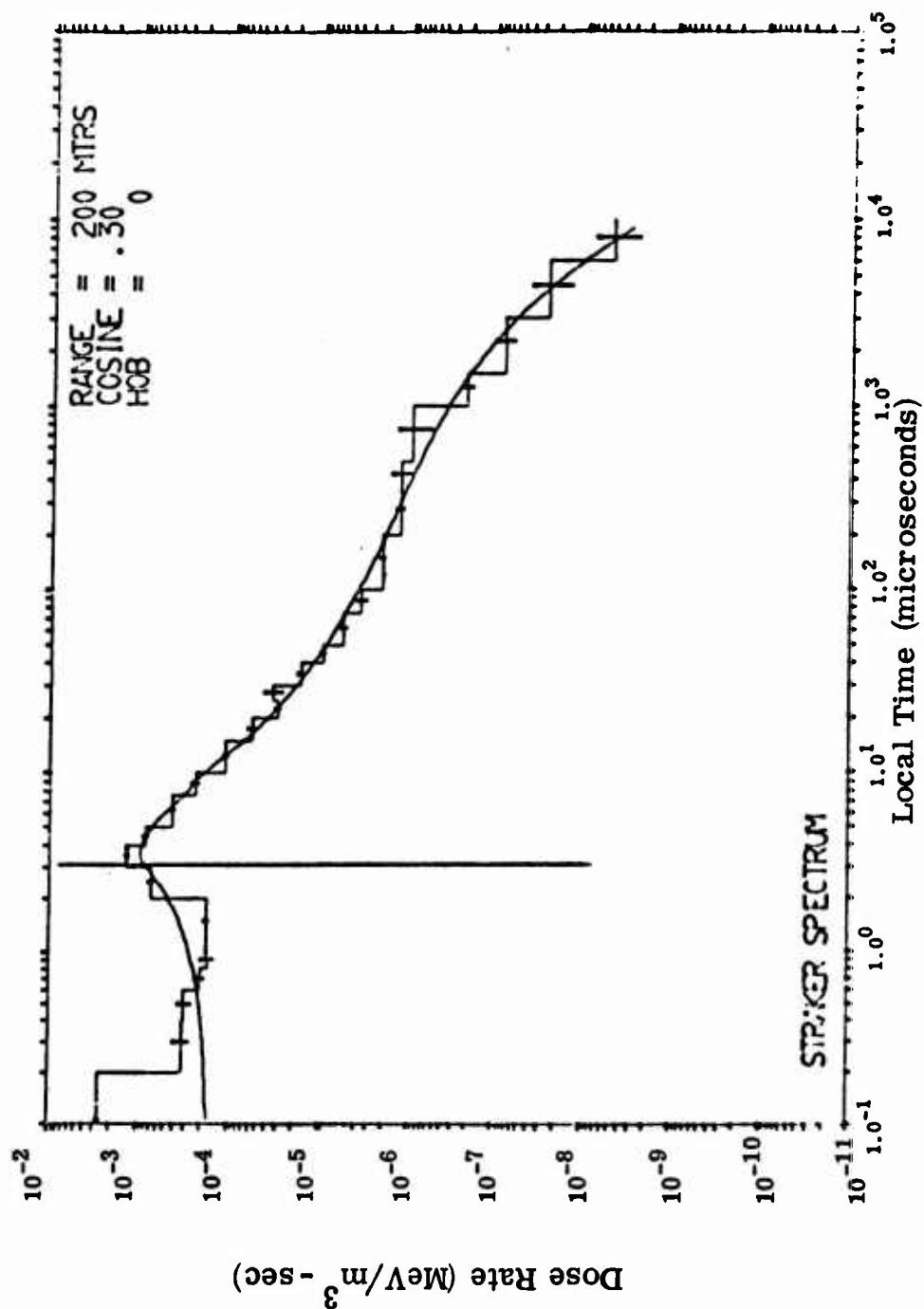


Figure 3.14. Curve fits for dose rates for typical thermonuclear source on ground, range = 200 meters,  $\cos \theta = 0.30$ .

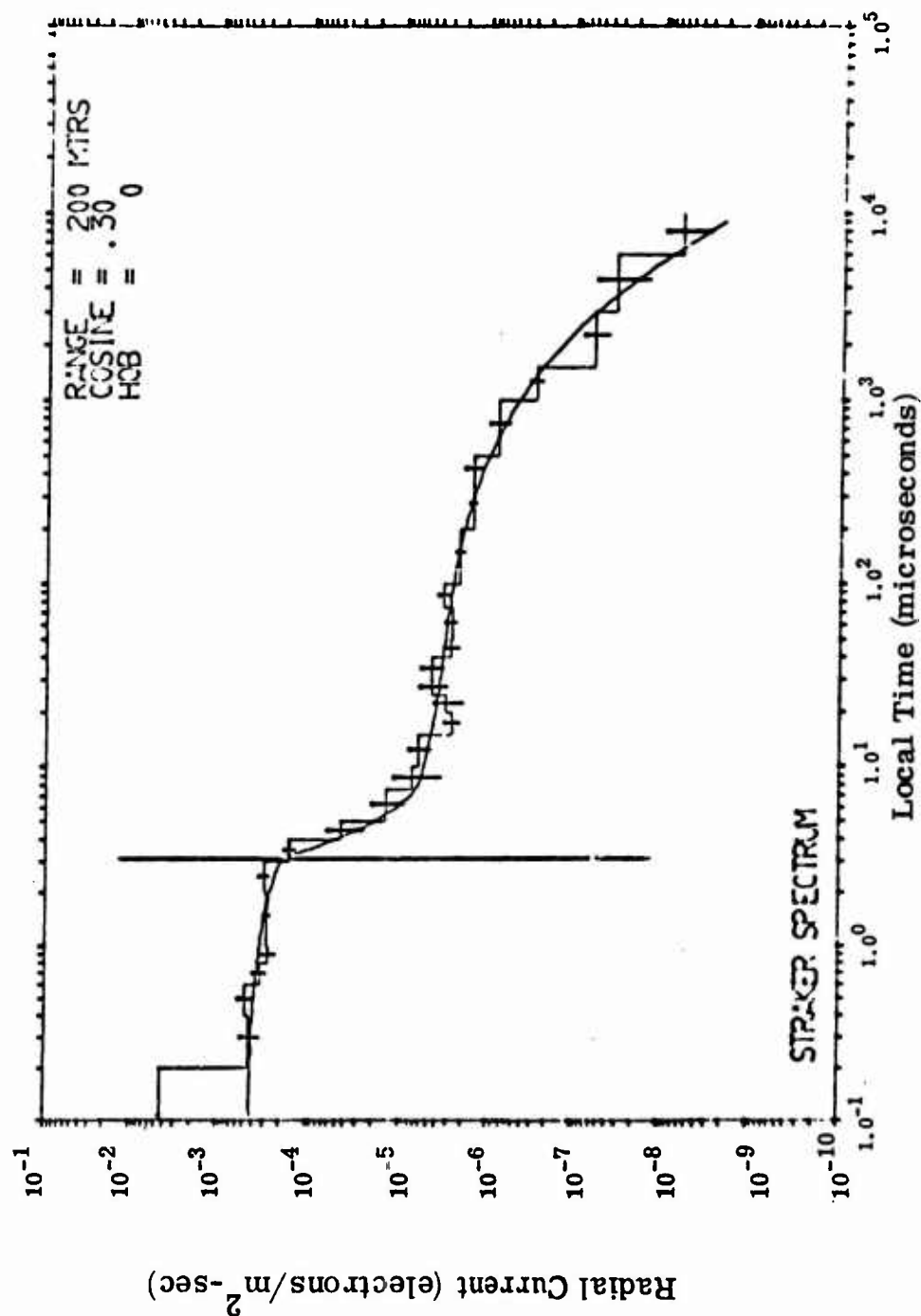


Figure 3.15. Curve fits for radial current densities for typical thermo-nuclear source on ground, range = 200 meters,  $\cos \theta = 0.30$ .

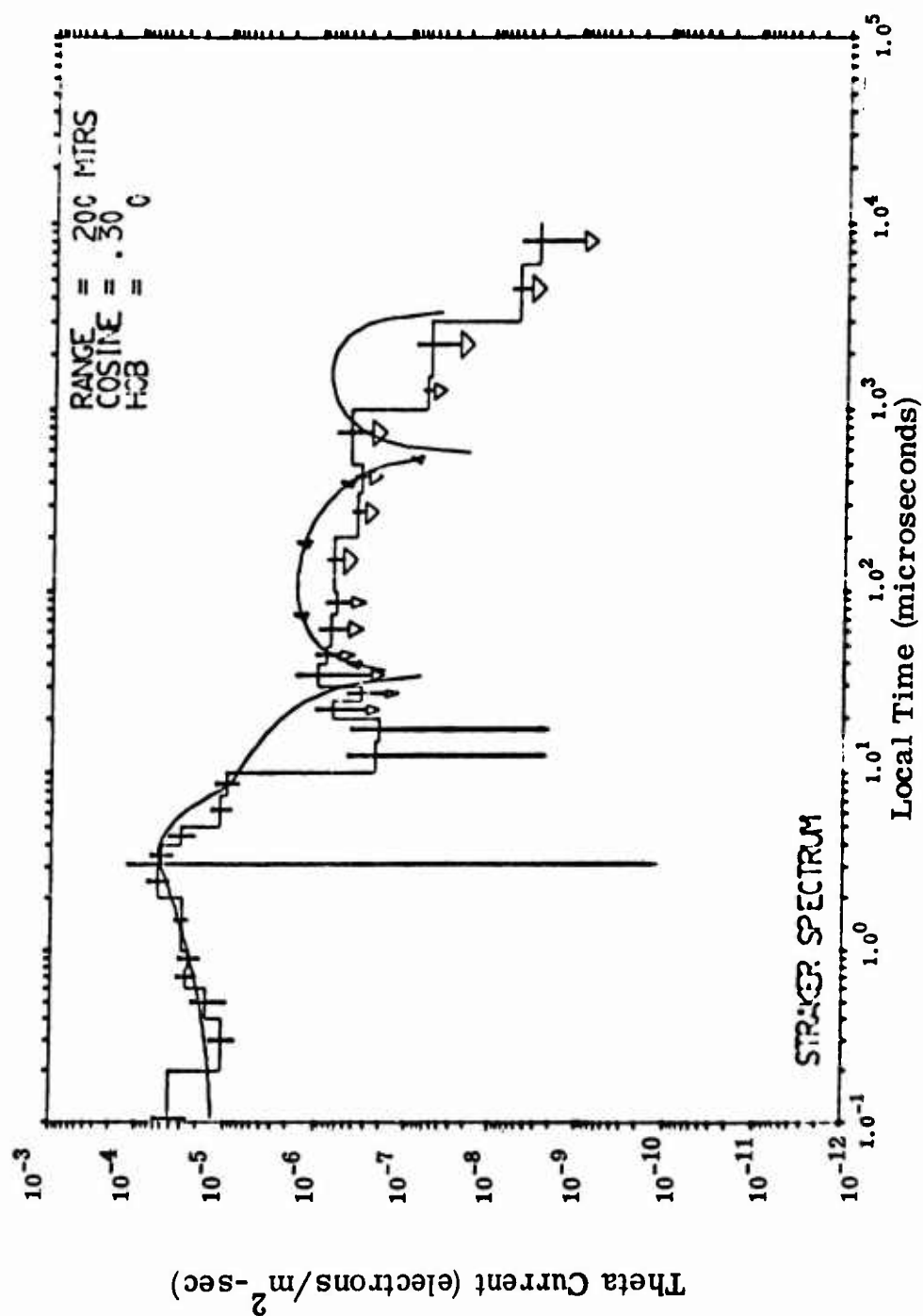


Figure 3.16. Curve fits for theta current densities for typical thermodynamic nuclear source on ground, range = 200 meters,  $\cos \theta = 0.30$ .

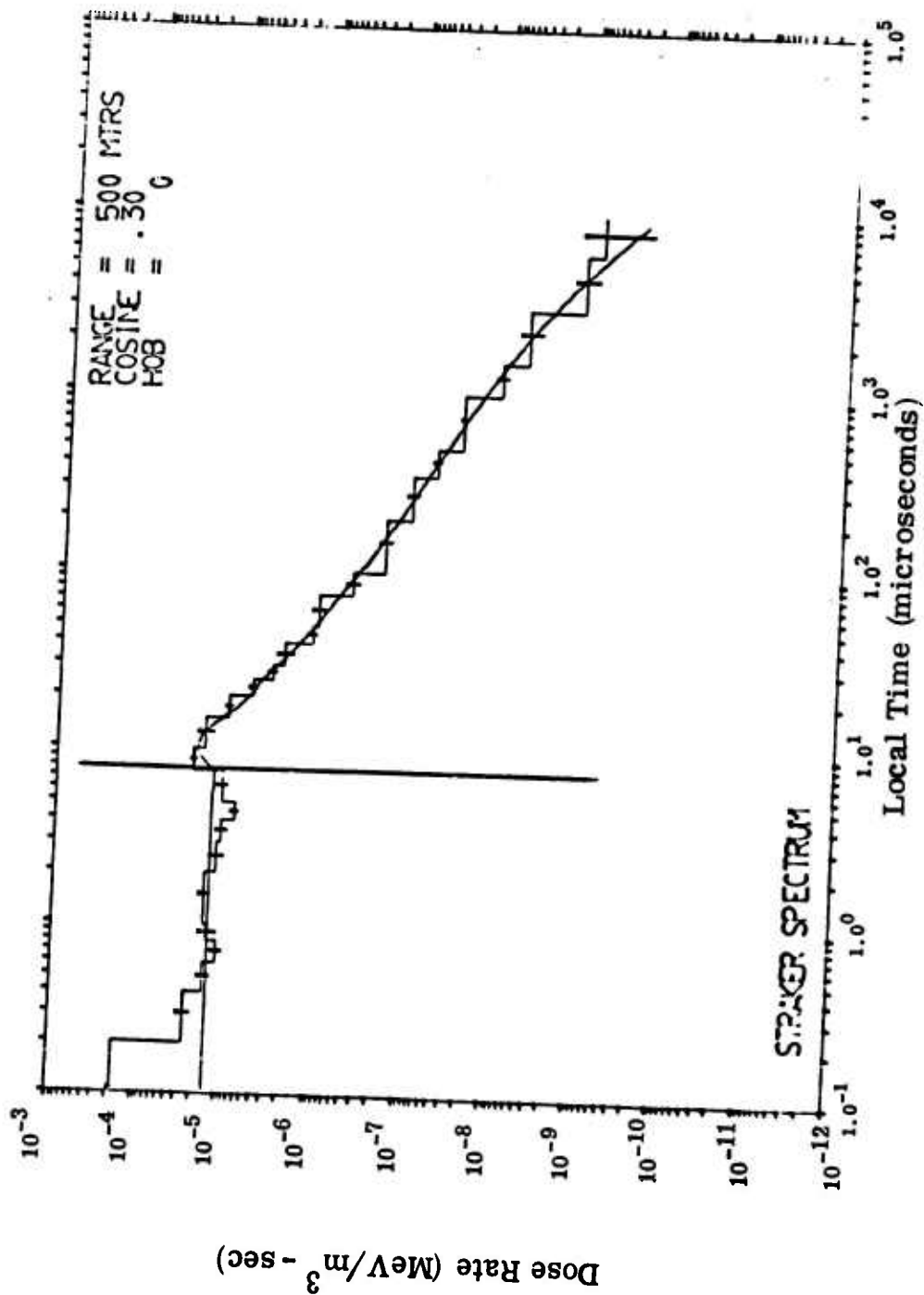


Figure 3.17. Curve fits for dose rates for typical thermonuclear source on ground, range = 500 meters,  $\cos \theta = 0.30$ .

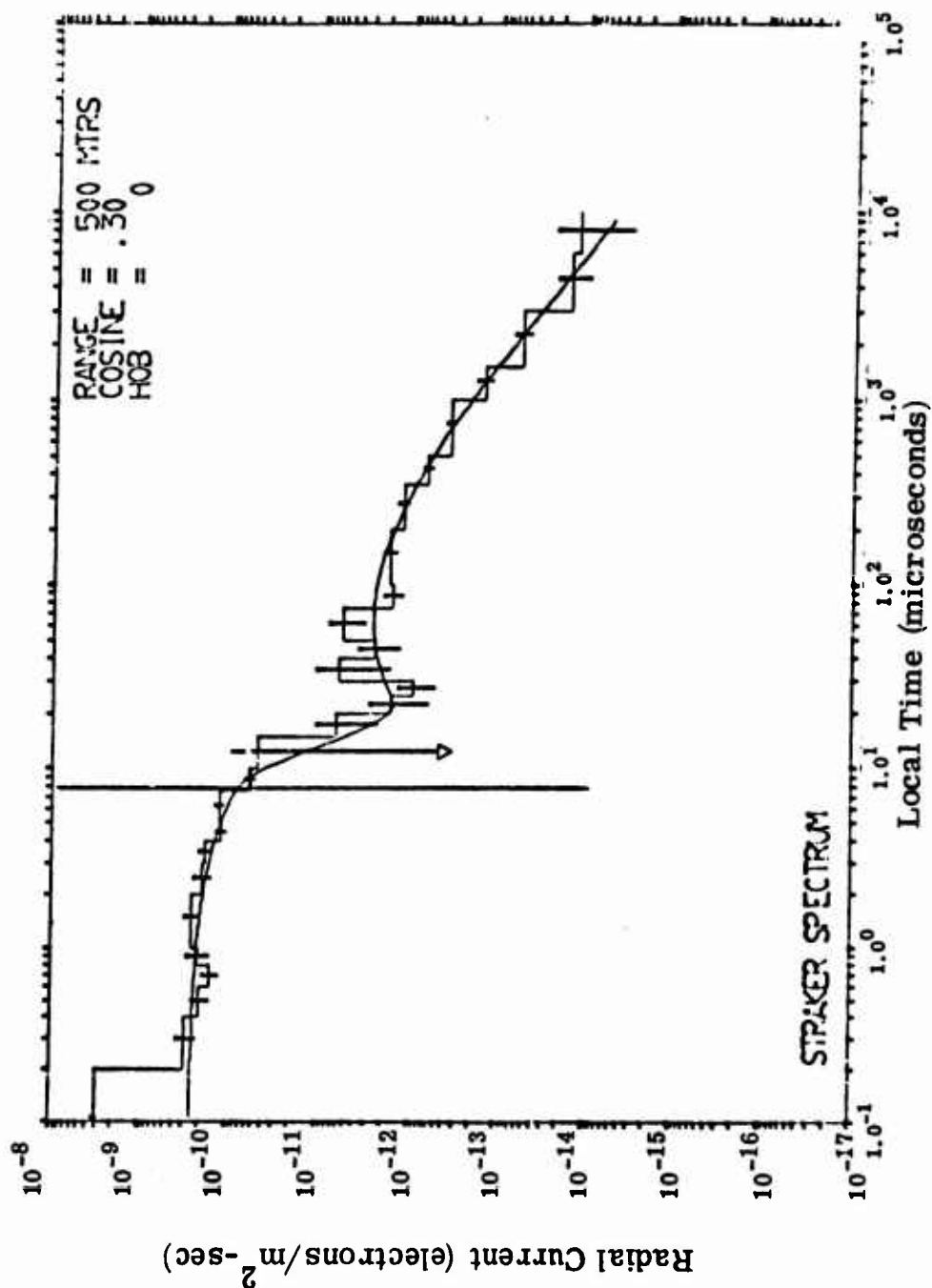


Figure 3.18. Curve fits for radial current densities for typical thermo-nuclear source on ground, range = 500 meters,  $\cos \theta = 0.30$ .



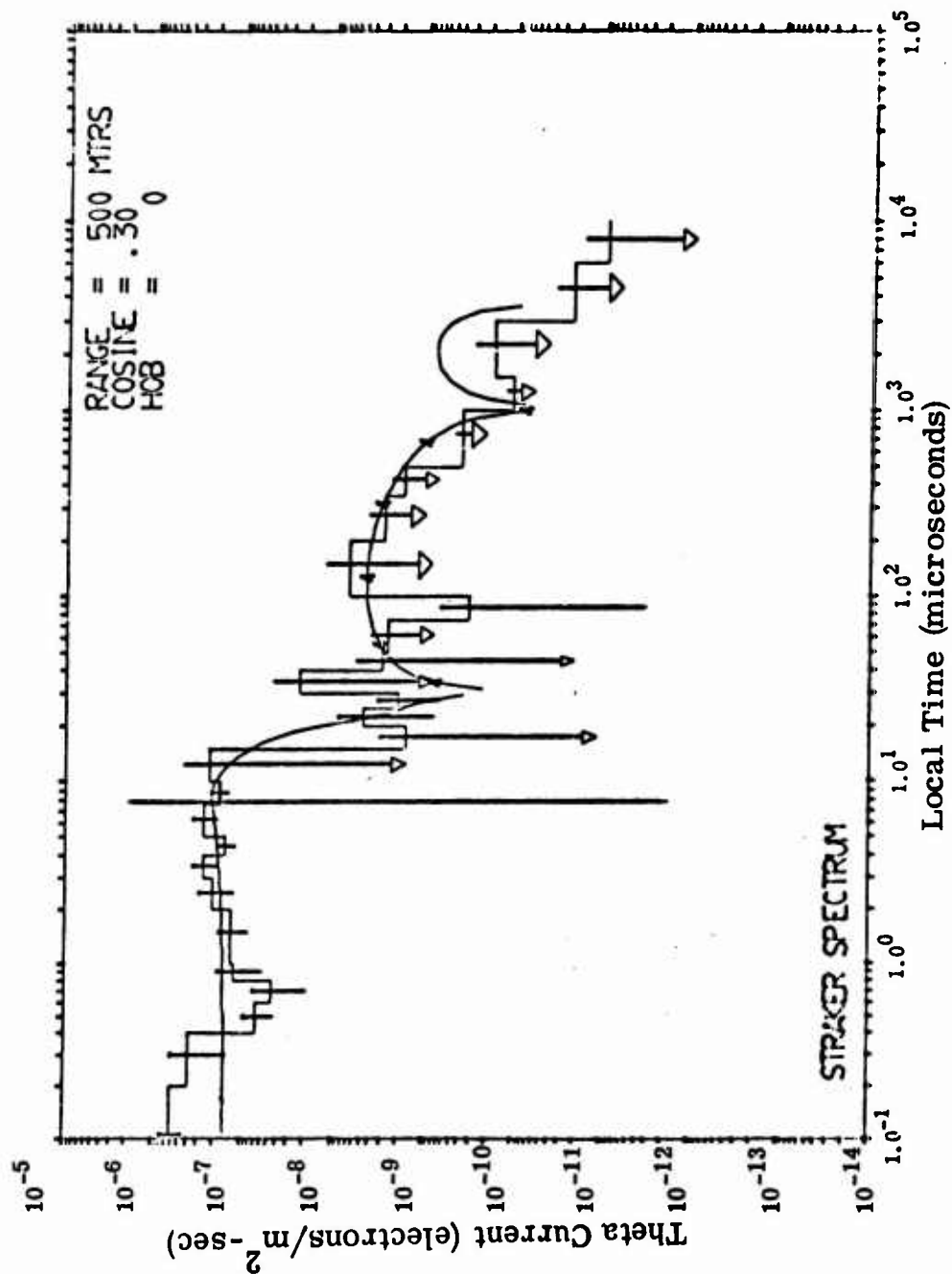


Figure 3.19. Curve fits for theta current densities for typical thermo-nuclear source on ground, range = 500 meters,  $\cos \theta = 0.30$ .

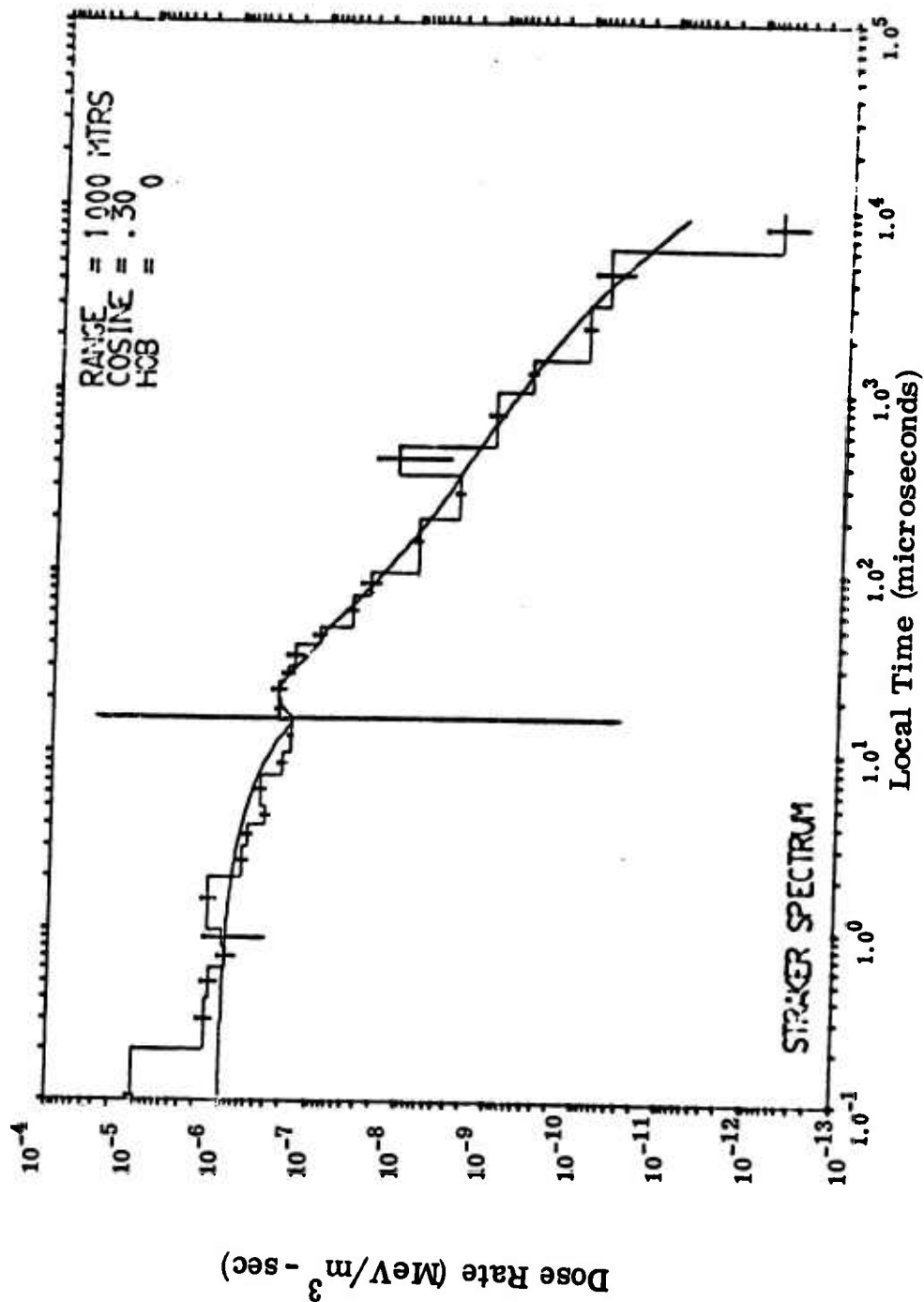


Figure 3.20. Curve fits for dose rates for typical thermonuclear source on ground, range = 1000 meters,  $\cos \theta = 0.30$ .

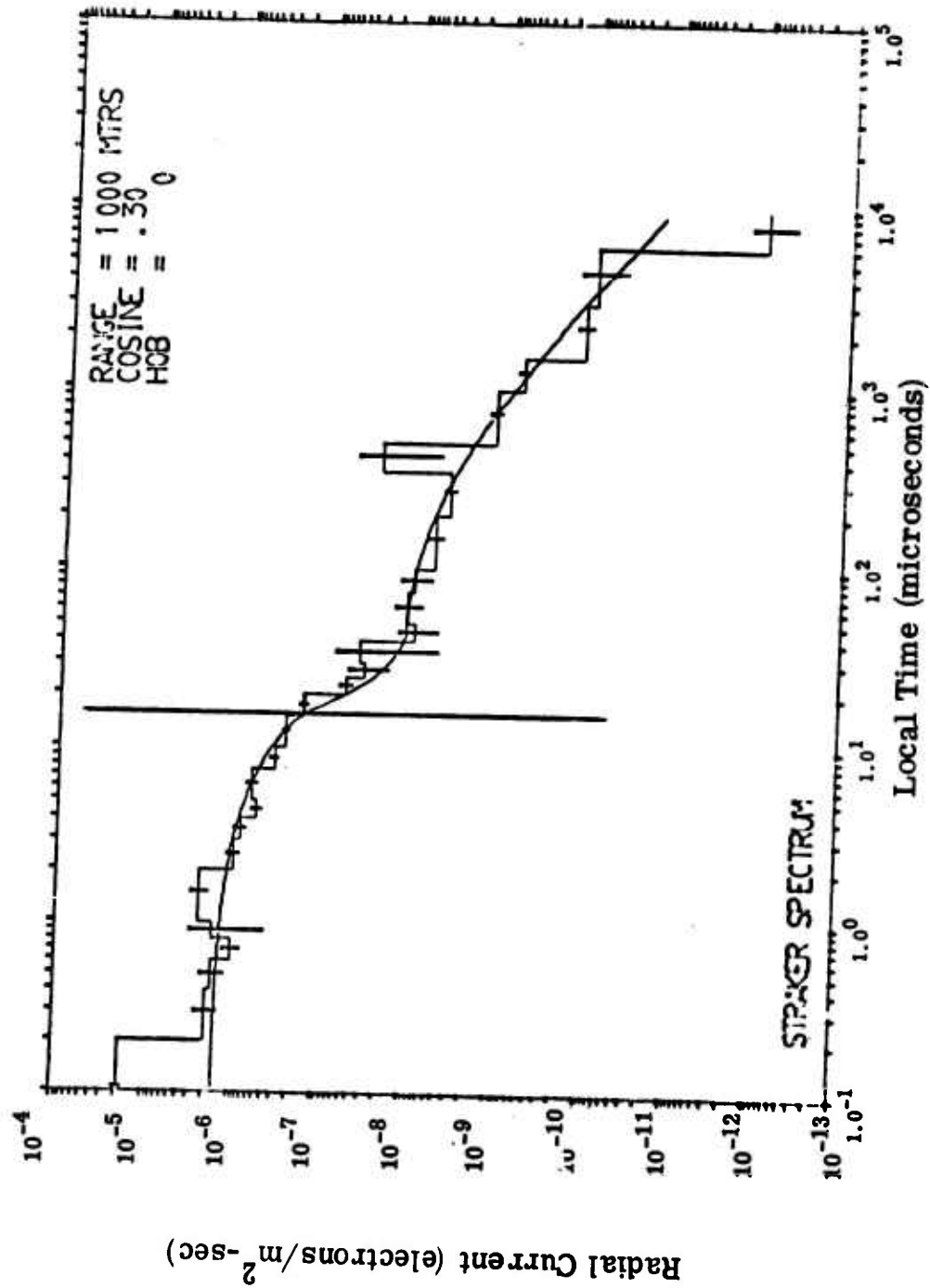


Figure 3.21. Curve fits for radial current densities for typical thermodynamic nuclear source on ground, range = 1000 meters,  $\cos \theta = 0.30$ .

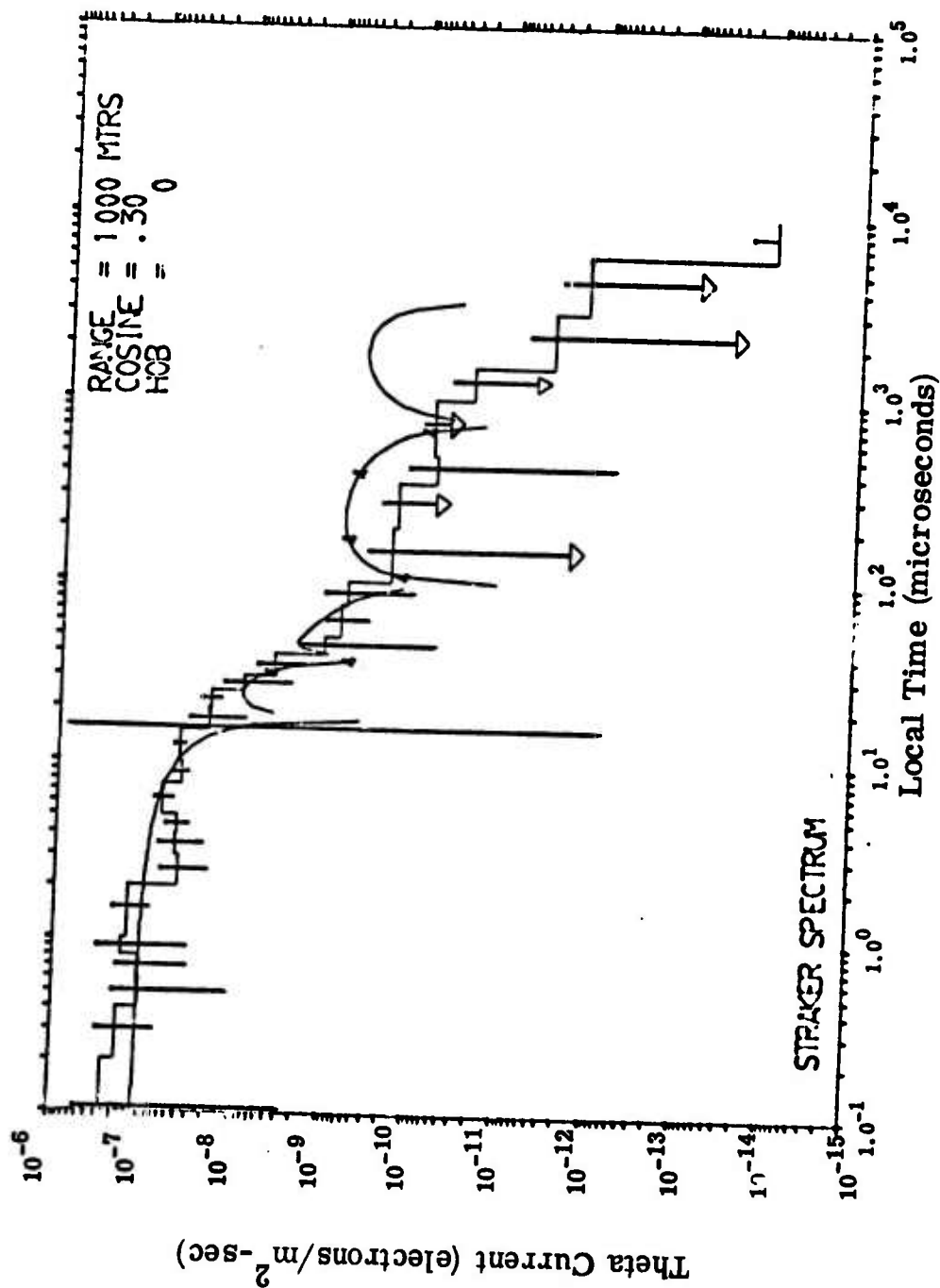


Figure 3.22. Curve fits for theta current densities for typical thermo-nuclear source on ground, range = 1000 meters,  $\cos \theta = 0.30$ .

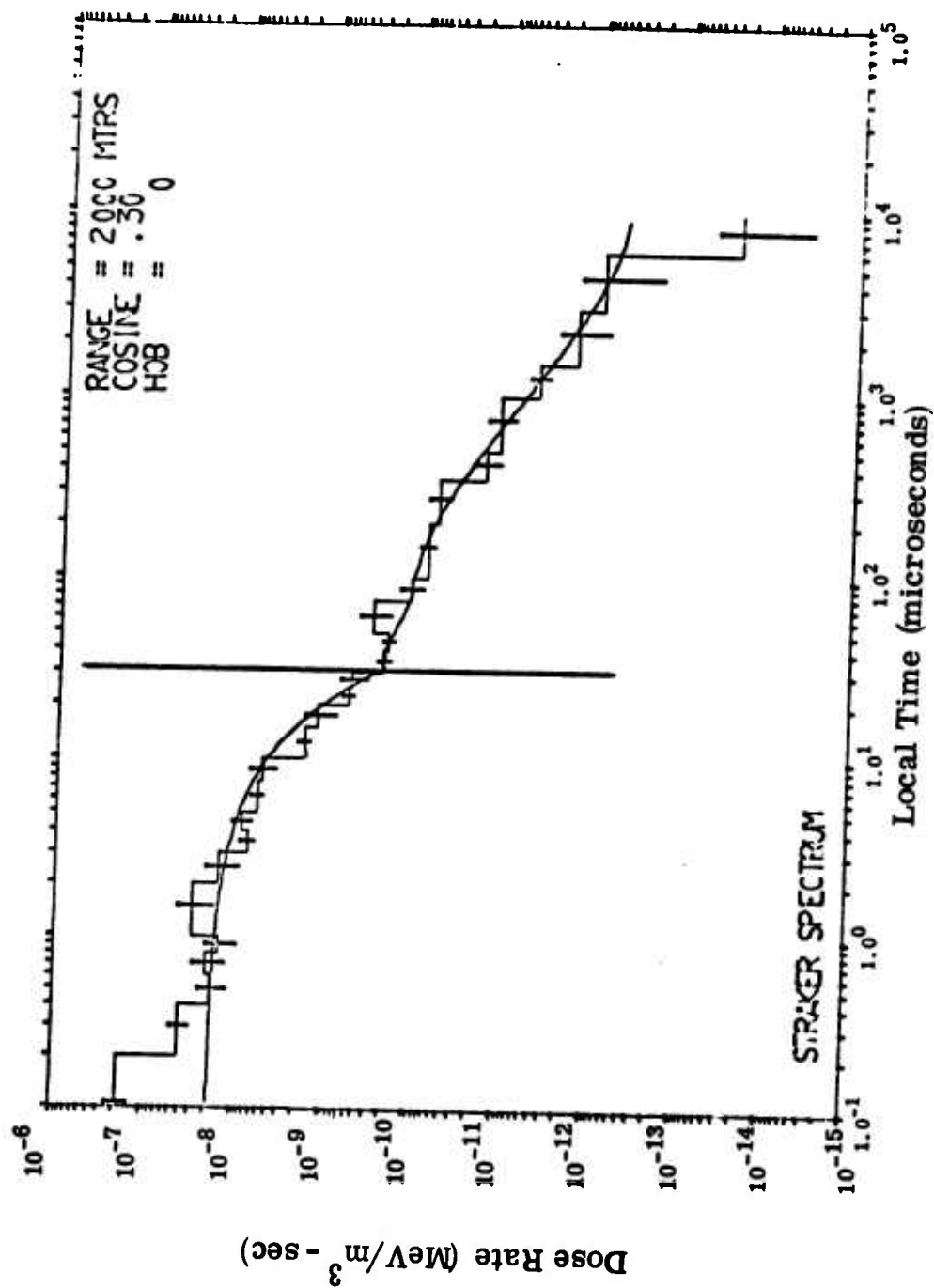


Figure 3.23. Curve fits for dose rates for typical thermonuclear source on ground, range = 2000 meters,  $\cos \theta = 0.30$ .

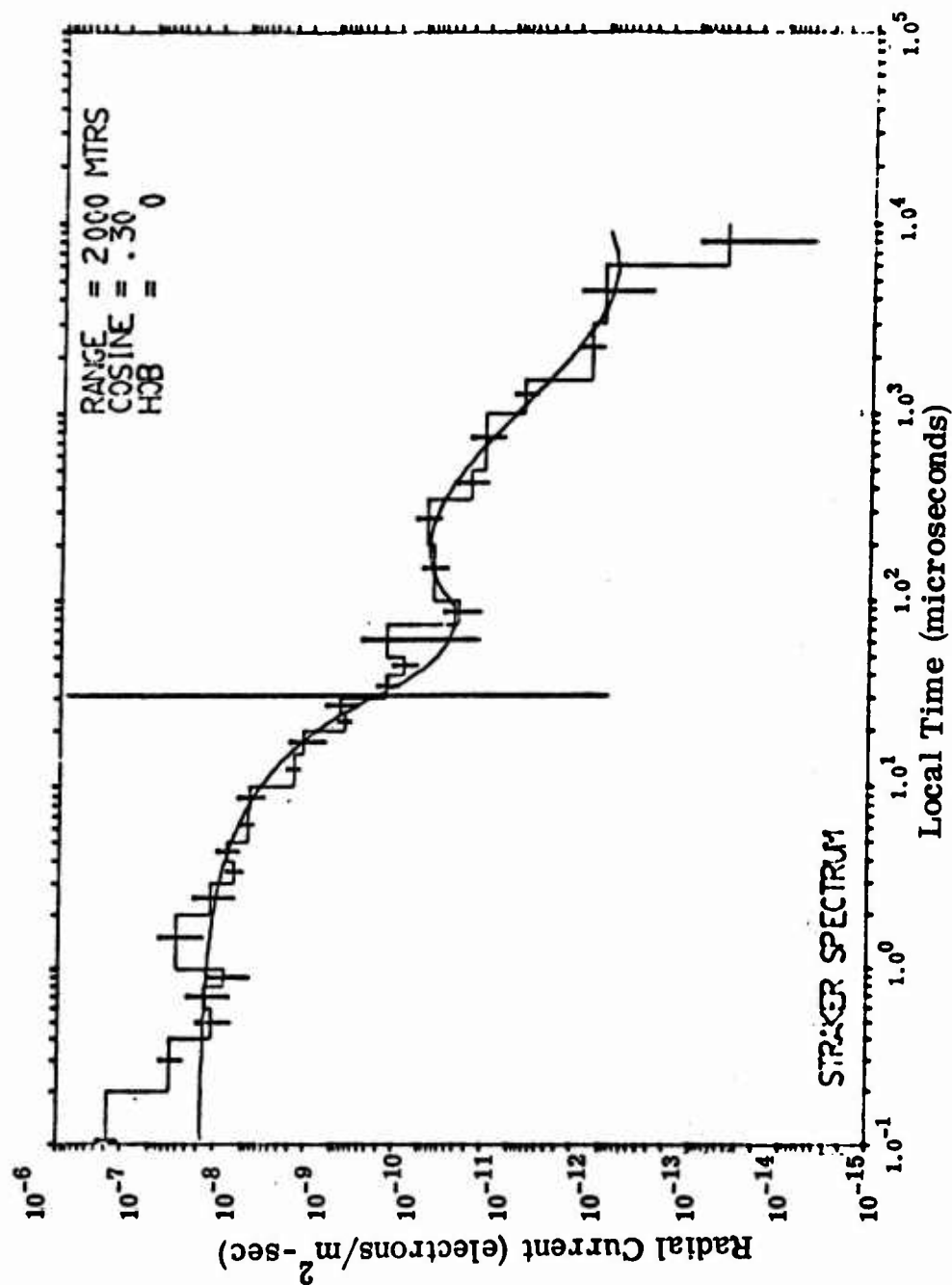


Figure 3.24. Curve fits for radial current densities for typical thermo-nuclear source on ground, range = 2000 meters,  $\cos \theta = 0.30$ .

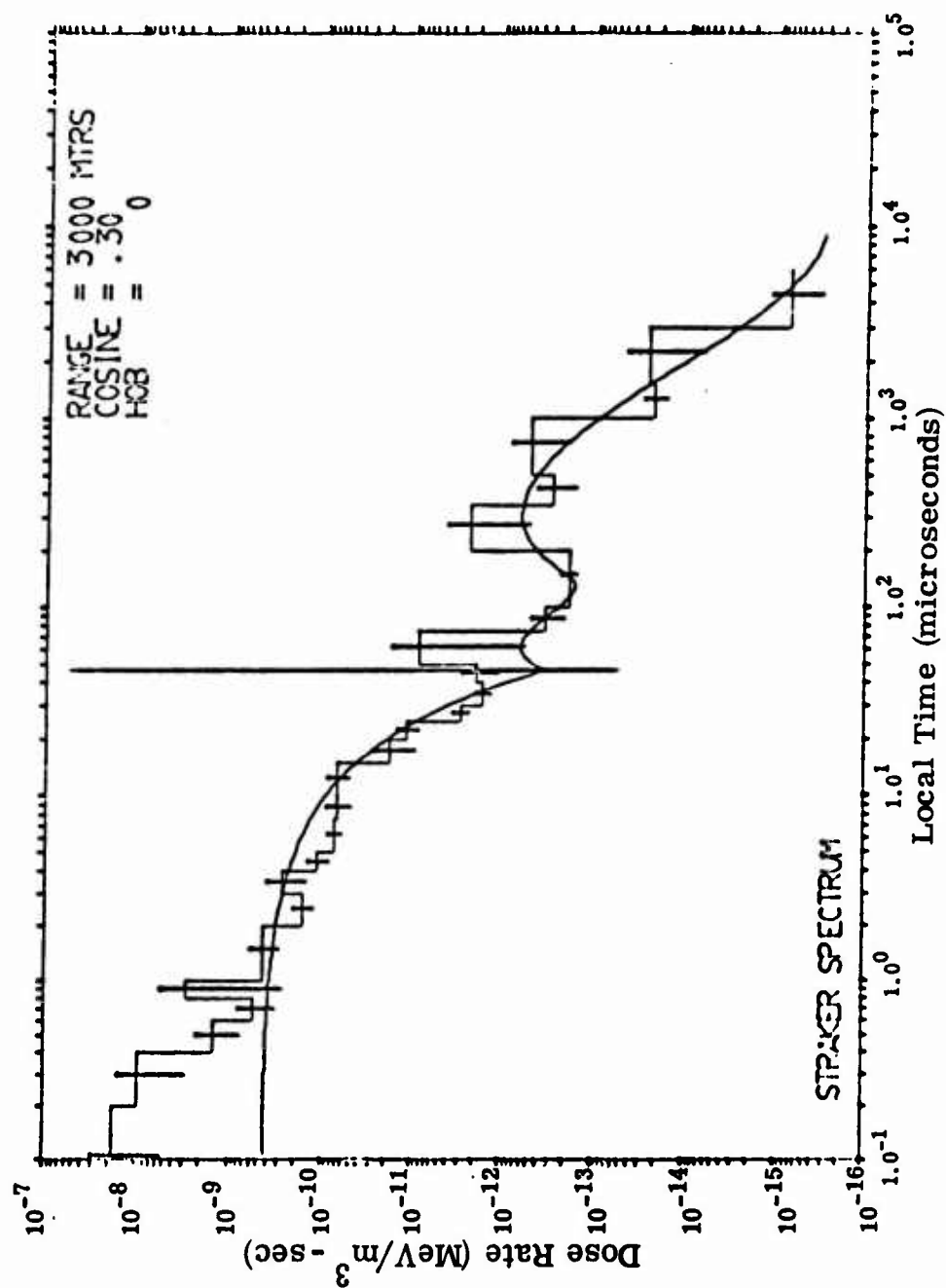


Figure 3.25. Curve fits for dose rates for typical thermonuclear source on ground, range = 3000 meters,  $\cos \theta = 0.30$ .

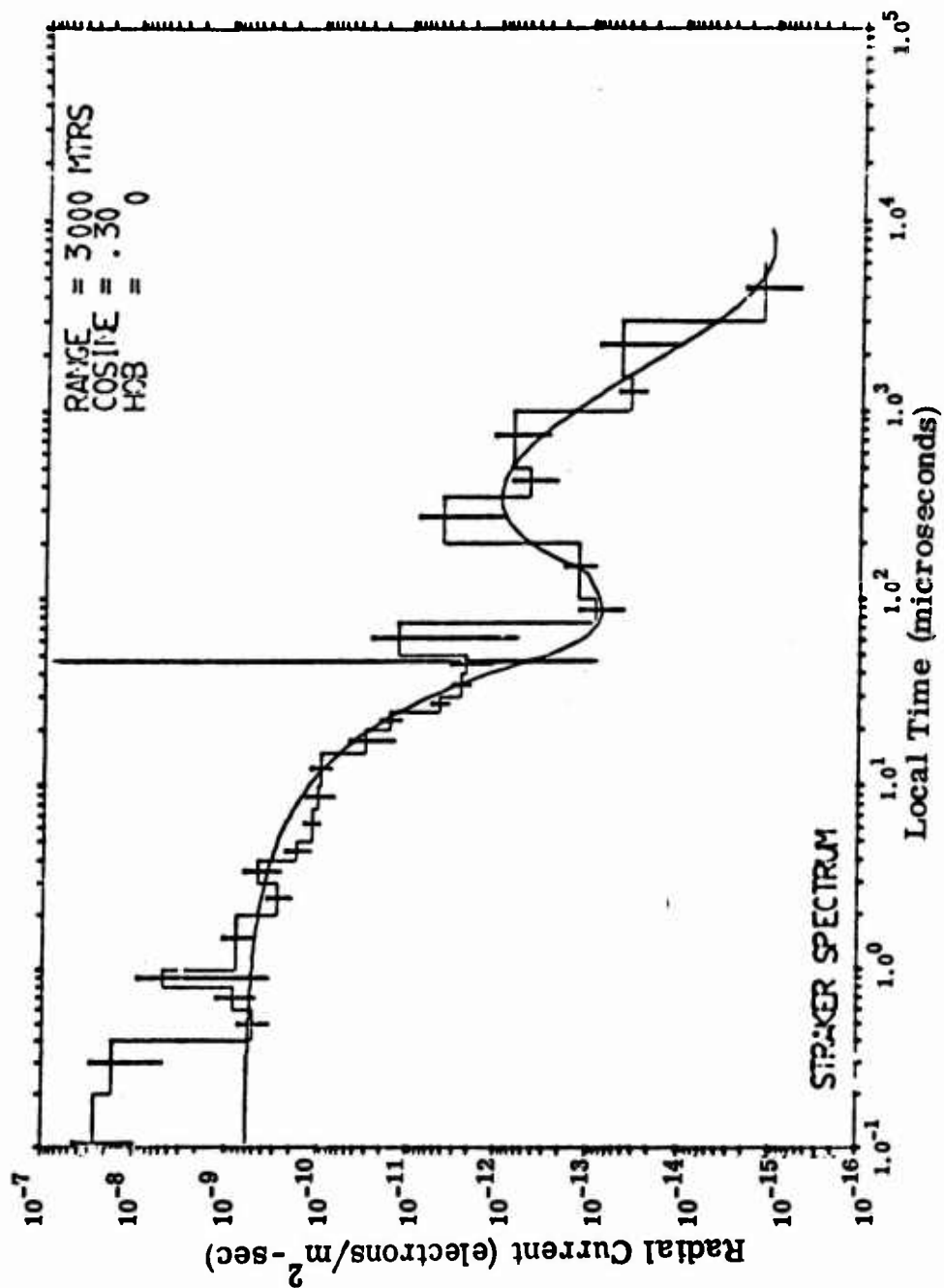


Figure 3.26. Curve fits for radial current densities for typical thermo-nuclear source on ground, range = 3000 meters,  $\cos \theta = 0.30$ .



$$V_u = \frac{1}{r^2} \left\{ (r_1^2 V_a) + \frac{r - r_1}{r_2 - r_1} ((r_2^2 V_b) - (r_1^2 V_a)) \right\}$$

Then the value of the source quantity is calculated:

$$V = V_1 + \left( \frac{\cos \theta - \cos \theta_1}{\cos \theta_2 - \cos \theta_1} \right) (V_u - V_1)$$

This calculation is carried out in FORTRAN routines which are described in Section 3.7.

### 3.6 THE CURVE FITTING CODE NF

NF is a program which reads a tape containing transport data, performs the curve fits to the data and produces punched cards with the curve fit parameters for use in subroutine NSOURCE. NSOURCE and its associated routines may be used in EMP source calculations. It performs the interpolations based on the time domain fits and is described in the next section.

At this time NF is a somewhat inefficient and poorly organized code. However, no apology is made for this situation. NF is an assembly of many routines which worked quite well in the fitting effort. Also, because it has not been made efficient or well organized for the effort described here, it should be quite easy to modify it for use with other data or to perform other fitting tasks.

A typical run of NF takes only about 2 minutes of computer time (on the CDC 6600). It requires the one input tape with the transport data and requires about 60000 octal memory locations.

A brief description of NF follows.

### 3.7 THE NEUTRON INDUCED SOURCE SUBROUTINE NSOURCE

NSOURCE has been designed to calculate neutron induced source response functions in a reasonably efficient manner while being very easy to use. In its present form NSOURCE requires one special call which causes it to read a set of data cards. It would be straightforward for any user to change this situation to a tape read if desired.

To use the routine there must be a one time call:

CALL NSOURCE (-1.).

At this time NSOURCE will read data cards and fill an array of arrival times for its use. Thereafter one may obtain the source quantities with the following call:

CALL NSOURCE (R, C, T, S)

where

R is the range in meters where sources are desired,

C is the cosine of the angle from the vertical,

T is the time in microseconds,

S(1) is the returned dose rate value,

S(2) is the radial current value and

S(3) is the transverse current value.

A brief description of NSOURCE and its associated routines follows.

**Main Routine:** NF

**Function:** Organizes input data and calls routines for fitting and display of results.

**Subroutines called:** AVG, ARRIVAL, F, HISTPLT

**Flow:**

1. Call AVG to fill arrays of transport bin midpoints.
2. Read transport data from TAPE 1.
3. Scale data if desired.
4. Call ARRIVAL to calculate neutron arrival times associated with ranges in the transport data.
5. Call F for fitting of each of the three source quantities.
6. Call HISTPLT to display transport data and fits on microfilm plots.
7. Punch cards with fit parameters.

●

Subroutine Name:     ARRIVAL (R, E, T)

Function:            Calculates neutron arrival time based on  
                      a range and energy.

Called by:            NF

Parameters:           R - range in meters  
                      E - neutron energy in MeV  
                      T - neutron arrival time returned  
                      in microseconds

Subroutine Name: F(XX, YY, S, KA, N, AB, AA, NB, NA, NV)

Function: Calls least squares polynomial fitting routine to fit two parts of a single source curve and calculates and prints errors associated with the fits.

Called by: NF

Subroutines called: POLY, POLYF

Parameters:

- XX - array of times
- YY - array of source values
- S - array of statistics
- KA - XX(KA) closest point to neutron arrival time
- N - name of quantity being fit e.g., 9 H DOSE RATE
- AB - Array of parameters for fit before arrival
- AA - Array of parameters for fit after arrival
- NB - number of parameters in AB
- NA - number of parameters in AA
- NV - variable flag

**Subroutine Name:**     N(X, F, A)

**Function:**            Calculates parameters for a cubic function passing through three points (X(1), F(1)), (X(2), F(2)), (X(3), F(3)) with slope specified at a fourth (X(4), F(4)).

**Called by:**           PEV

**Parameters:**        X, F   - see above  
                      A       - cubic parameters

Subroutine Name: POLY (X, Y, Z, NXYZ, A, NA)  
(written by Harry M. Murphy, Jr. of AFWL)

Function: Least squares polynomial fit

Called by: F

Parameters:

- X - array of abscissa values
- Y - array of ordinate values
- Z - array of fitting weight values
- NXYZ - number of values in X, Y or Z
- A - array of polynomial fit parameters returned
- NA - number of parameters in A

**Function Name:** POLYF (X, A, NA)  
POLYD (X, A, NA)

**Function:** Evaluate a polynomial (POLYF) or its derivative (POLYD) at a specified point.

**Called by:** PEV, F

**Parameters:** X - abscissa value  
A - Array of polynomial coefficients  
NA - number of values in A



Subroutine Name: PEV(NT, T, FT, TA, AB, AA, NB, NA, NE, QS,  
TS)

Function: Evaluate a fit to a source curve

Called by: HISTPLT

Parameters

- NT - number of times where values are desired
- T - time array
- FT - array of fit values returned
- TA - neutron arrival time
- AB - array of polynomial fit parameters for curve  
curve after arrival
- NB - number of parameters in AB
- NA - number of parameters in AA
- NE - source quantity flag
  - 1 - dose rate
  - 2 - transverse current
  - 3 - radial current
- (TS, QS) point which the dose rate fit is required to  
pass through

Subroutine Name:    AVG(T, TM, NT, R, RM, TYPE, NR, Z,  
                          ZM, NA, ND, NH)

Function:            Fill arrays with transport bin midpoint values

Called by:           NF

Parameters:

T	-	time bin boundaries
TM	-	time bin midpoints returned
NT	-	number of elements in TM
R	-	range bin boundaries
RM	-	range bin midpoints
TYPE	-	array of flags for angle or depth
NR	-	number of elements in RM
Z	-	cosine $\theta$ or depth bin boundaries
ZM	-	cosine $\theta$ or depth bin midpoints
NA	-	number of angles
ND	-	number of depths
NH	-	200 meter burst flag

Subroutine Name: HISPLT (Q, SQ, CR, SCR, CT, SCT, NHORZ, NVERT, NTIMES, RANGE, CANG, HOB, TNEUT, TT, IAN)

Function Overlay fits on the transport data for microfilm plots

Called by: NF

Subroutines called: GRAPH, SYMBOL, NUMBER, PEV  
(GRAPH, SYMBOL AND NUMBER are parts of a standard plot package of AFWL)

Parameters:

Q	transport dose rate values
SQ	statistics associated with dose rate values
CR	transport radial current values
SCR	statistics associated with radial current values
CT	transport transverse current values
SCT	statistics associated with transverse current values
NHORZ	number of decades horizontally in plot
NVERT	number of decades vertically in plot
NTIMES	number of elements in Q, SQ, etc.
RANGE	range
CANG	value of cosine $\theta$
HOB	height of burst
TNEUT	neutron arrival time
TT	transport time bin mid points
IAN	number of the angle bin

**Subroutine Name:** QUAD (Y1, T1, Y2, T2, YPZ, A, B, C)

**Function:** Calculates parameters for a quadratic function passing through two points with slope specified at the third.

**Called by:** PEV

**Parameters**

- (T1, Y1)
- (T2, Y2) - Two specified points
- YP2 - specified slope at T2
- A, B, C - quadratic parameters

**Subroutine Name:** SPLINE (Y1, YP1, T1, Y2, YP2, T2, A, B, C, D, IDRIV)

**Function:** Calculates parameters for a cubic function passing through two points with slope specified at each.

**Called by:** PEV

**Parameters:**

- (T1, Y1) Two specified points
- (T2, Ye)
- YP1, YP2 slopes at T1 and T2
- A, B, C, D-cubic parameters
- IDRIV -flag which indicates whether or not calculated cubic crosses over between T1 and T2.

**Subroutine Name:** NSOURCE (RX, CX, TX, SX)

**Function:** To calculate neutron induced EMP source terms at any range angle and time covered by the transport data.

**Subprograms called:** NSET, VAL, XINT, XINTL

**Flow:**

1. Check to see if RX is negative.  
If so, call NSET and return.
2. Locate (RX, CX) in mesh of points where time domain fits are available
3. Call VAL, XINT and XINTL to interpolate for source term values.

Function Name: XINTL (R, C, RA, RB, CA, CB, VA, VB, VC, VD)  
XINT (R, C, RA, RB, CA, CB, VA, VB, VC, VD)

Function: Perform the linear interpolation for transverse current value (XINTL) of the log interpolation for dose rate or radial current (XINT)

Called by: NSOURCE

Parameters

R	-	r	(See Section 3.4)
C	-	c	
RA	-	$r_1$	
RB	-	$r_2$	
CA	-	$c_1$	
CB	-	$c_2$	
VA	-	$V^a$	
VB	-	$V^b$	
VC	-	$V^c$	
VD	-	$V^d$	

**Subroutine Name:** NSET (NR, R, TA, DD, DR, DT)

**Function:** To read time domain fit parameters and fill arrival time array for later use in NSOURCE

**Called by:** NSOURCE

**Parameters**

- NR - number of ranges where time domain fits are available
- R - array of ranges
- TA - array of arrival times
- DD - array of time domain fit parameters for dose rate
- DR - array of time domain fit parameters for radial current
- DT - array of time domain fit parameters for transverse current



**Function name:** VAL (T, N, A)  
**Function:** to evaluate a time domain fit  
**Called by:** NSOURCE  
**Parameters:**

- T - time for evaluation
- N - = 1 use fit for  $t \leq t_a$   
       = 2 use fit for  $t_a < t < 3t_a$   
       = 3 use fit for  $t \geq 3t_a$
- A - array of fit parameters

## 4. THE 05RNIES PROGRAM

### 4.1 GENERAL REMARKS

The 05RNIES program is a versatile Monte Carlo code for solving the time-dependent neutron and gamma ray transport equations in two space dimensions. From these solutions, the Compton currents and ionization rates in air and ground due to a specified neutron source are obtained. Late-time electromagnetic fields may then be computed by solving Maxwell's equations together with the relevant air and ground chemistry equations. A brief discussion of these equations was presented in a previous report and will not be repeated here.<sup>(3)</sup> The 05RNIES program described in this section has been substantially revised from the version of last year. We will attempt to emphasize those areas of the code which have been altered to any significant extent. We concentrate here on the newer portions of the code and include some of the revised subroutines of last year.

The new version of 05RNIES has been programmed with a band source energy concept to facilitate folding in arbitrary neutron spectra at a later time. In addition, new air capture techniques have been introduced which extend the time scale out to the one second region. Neutrons in the lower energy ranges are now tracked from one medium to another so that capture gamma rays in both air and ground are accurately taken into account. Thermal neutron energy deposition in the air is also considered for the first time. New gamma ray analytical methods have also been introduced for transporting gamma rays at

positions distant from the air-ground interface. Individual contributions to ionization and Compton currents by neutrons and gamma rays, as well as by fast and thermal reaction processes, are now displayed to assist in fitting of the vast amount of data generated.

The latest ENDF/B neutron transport and gamma ray production cross sections have been processed and incorporated into data files for use in these calculations. Ionization rates and Compton currents are stored on magnetic tapes at AFWL as these data are produced so that they may be retrieved for later calculations. 05RNIES also has restart capabilities which enable the user to finish a calculation which was aborted for any reason.

## 4.2 SOURCE ENERGY BAND VERSION

### 4.2.1 Selection of Bands

Full production calculations using 05RNIES may typically require 20 hours of time on the CDC 6600 to generate 200,000 neutron histories. In the past, a new 05RNIES calculation was needed for each input neutron source spectrum. Since there are many neutron spectra of interest in EMP studies, it became clear that a new computational scheme, which would not require rerunning full production calculations for each new neutron source, was needed. The source energy band version of 05RNIES was designed to fulfill this requirement.

The present version of the code has a total of 13 fixed energy bands. The number 13 was chosen as a compromise between the many groups actually required to accurately fit arbitrary nuclear weapon neutron output spectra and only a few groups which would reduce the computer execution times. The new code is run until a sufficient number of neutron histories are generated for each source band. Various

quantities of interest are then stored on data tapes as a function of neutron source group. The auxiliary folding code O5NPT is then used to generate EMP drivers for any desired input neutron source spectrum. In this way, only a few minutes of computer time are required to generate EMP sources for a new neutron source rather than the 20-hour calculations of previous years.

In Table 6 the 13 energy bands used in these calculations are displayed. The probability distribution of source neutrons for the typical thermonuclear spectrum of Table 1 is also shown in the new 13-group structure. In Fig. 4.1 a comparison of the new 13-band source distribution and the original 17-group thermonuclear distribution is made. It is apparent that the new band structure is very satisfactory for the thermonuclear spectrum. Corroboration of the adequacy of the band structure for several other devices has also been made.

#### 4.2.2 Statistical Analysis

Estimates for the mean and variance of computed quantities using the new band version of O5RNIES are obtained in a straightforward fashion. Assume that there are  $M$  energy bands of source neutrons, and for each band there are  $n$  neutron histories followed in each batch or run. There are then  $N$  batches or runs performed to generate production results for a given HoB. Furthermore, let  $f_k$  be the fraction of source neutrons in the  $k$ -th energy band. Then if  $X_{ijk}$  represents the  $i$ -th batch sample, for history index  $j$  and band  $k$ , we easily find for the  $i$ -th sample,

$$X_i = \sum_{k=1}^M \frac{1}{n} \sum_{j=1}^n f_k X_{ijk},$$

where

$$\sum_{k=1}^M f_k \equiv 1.0.$$

Table 6

COMPARISON OF THE TYPICAL THERMONUCLEAR  
NEUTRON SOURCE SPECTRUM IN THE  
ORIGINAL 17-GROUP STRUCTURE AND IN THE  
NEW 13-BAND SOURCE VERSION.

17-Group Thermonuclear Neutron Distribution			13-Band Energy Version		
Group No.	Upper Energy (MeV)	Probability	Band No.	Upper Energy (MeV)	Probability
1	15.000000	.07060	1	16.500000	.00000
2	12.200000	.02560	2	15.000000	.03782
3	10.000000	.01410	3	13.500000	.06578
4	8.190000	.01470	4	9.050000	.03959
5	6.360000	.01800	5	4.960000	.06681
6	4.970000	.01700	6	2.350000	.09152
7	4.070000	.02600	7	1.100000	.08348
8	3.010000	.01900	8	.550000	.07186
9	2.460000	.00500	9	.240000	.03014
10	2.350000	.02800	10	.110000	.26832
11	1.830000	.06200	11	.031600	.04210
12	1.110000	.08500	12	.019300	.05455
13	.550000	.10200	13	.003360	.14803
14	.110000	.36500		.000023	
15	.003350	.12200			
16	.000583	.02400			
17	.000101	.00200			
	.000029				

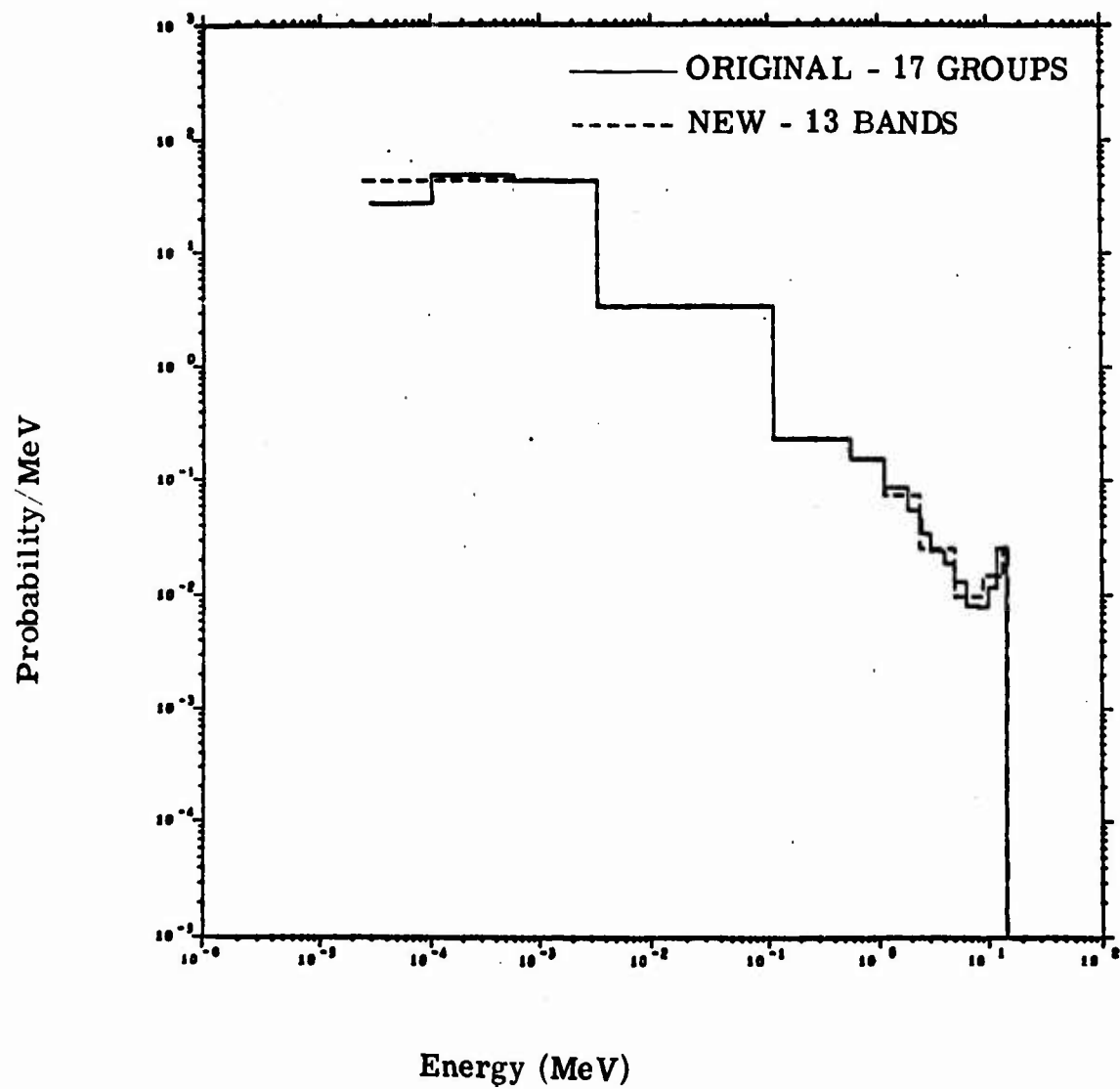


Figure 4. 1. Comparison of the typical thermonuclear spectrum in the original 17-group structure and in the new 13-band version.

Then we also have

$$x_i^2 = \left[ \sum_{k=1}^M \frac{f_k}{n} \sum_{j=1}^n x_{ijk} \right]^2$$

The estimates for the mean and variance are then found from

$$\mu = \frac{1}{N} \sum_{i=1}^N x_i$$

and

$$\sigma^2 = \frac{1}{N(N-1)} \left[ \sum_{i=1}^N x_i^2 - \frac{\left( \sum_{i=1}^N x_i \right)^2}{N} \right].$$

In our sampling we perform  $N$  runs or batches, each run consisting of  $M \times n$  neutron histories. The unit sample is the run and not an individual neutron history. The principal advantage to this method of grouping is the reduction in the number of samples and sample squares which must be computed and stored for the statistical analysis. In our calculations at each of three HoB's, we have performed a total of  $N = 15$  runs, with  $M = 13$  energy bands, and  $n = 1000$  neutron histories for each band. Thus, each production run is comprised of a total of 195,000 neutron histories.

### 4.3 LATE-TIME EMP DRIVERS

#### 4.3.1 Air Capture Computational Models

In earlier versions of O5RNIES<sup>(1-2)</sup> there were limitations on the validity of results of late times because contributions from thermal neutron capture in the ground were not considered. Last year a significant improvement in the O5RNIES late-time physics calculations was made by introducing a time-dependent one-velocity<sup>(3)</sup> diffusion model to treat thermal neutron capture events in the ground. The model, although approximate, enabled calculations out to times as late as  $10^4 \mu\text{sec}$ . The diffusion model replaced the air, in the two-region, air-ground problem, by a vacuum, so that thermal neutrons leaving the ground and entering the air never returned to the ground. This approximation is valid for the time range discussed above. However, when air capture events are considered, local times as late as  $10^6 \mu\text{sec}$  are of interest and a new computational model which correctly tracks low energy neutrons from one medium to another is required. The air capture models described below are applicable to both air and ground regions and enable accurate calculations to times of 1 second.

The two-region, time-dependent, air capture gamma problem has been one of the largely unresolved radiation transport problems of importance to EMP studies at late times (beyond about  $10 \mu\text{sec}$ ). A direct brute force Monte Carlo analysis of this problem was not computationally efficient because of the extremely long computer times required. The difficulty stems mainly from the fact that air capture events take place predominantly at low neutron energies and many neutron collisions are required before thermalization in air is achieved. For example, a



neutron in air suffers approximately five times as many collisions in downscattering from 0.1 MeV to thermal energies as it does in slowing down from a typical source energy of 2.0 MeV to 0.1 MeV. Therefore, direct Monte Carlo calculations in the epithermal range (0.1 MeV to 2.38 eV) as well as in the thermal group (below 2.38 eV) could conceivably take several times as long to perform as the previous 25-hour runs required for fast neutron EMP studies.<sup>(3)</sup> Biasing of the Monte Carlo calculations to emphasize air capture events would be one way to lower computer execution times for this particular problem. Some efforts along these lines were pursued, but eventually abandoned in favor of new analytical approaches which show great promise.

In the calculations discussed here the neutron transport is carried out by different methods in each of three separate energy ranges. In the highest energy range, above an input quantity  $E_c$ , usually about 0.111 MeV, the neutron transport is analyzed by the standard Monte Carlo approach. In the epithermal range between  $E_c$  and the thermal group cutoff energy,  $E_t = 2.38$  eV, an analytical age diffusion method is coupled with the conventional Monte Carlo technique. The analytical model is based on the premise that a neutron which is sufficiently high above the air-ground interface can be accurately treated by infinite medium Fermi age theory. Similarly, neutrons which are in the ground and sufficiently below the air-ground interface can also be treated by age theory. The analytical scheme is used for spatial positions distant from the air-ground interface, whereas the Monte Carlo approach is used for particles near the two-region interface.

For thermal neutrons,  $E < E_t$ , a one-group, time-dependent, diffusion model is coupled with a one-velocity Monte Carlo technique. The diffusion theory approach can be employed whenever thermal neutrons are located at spatial positions distant from the air-ground interface, while the Monte Carlo method is used near the interface. When a thermal neutron capture gamma ray is produced, a new analytical gamma ray transport model is also introduced to track those photons, in both air and ground, which are initially distant from the air-ground interface.

By coupling of the Monte Carlo and the analytical methods, the approximate analytical techniques are applied, where appropriate in the epithermal and thermal groups, to greatly improve computer execution times. On the other hand, the Monte Carlo method is retained to treat particles in spatial or energy regimes in which the analytical methods are not valid. The coupled techniques therefore enable accurate extension of previous transport calculations to later time regions with good computational efficiency.

In the next three sections we describe in more detail how epithermal and thermal neutron transport, as well as gamma ray transport, are dealt with in the new code.

#### 4.3.2 Epithermal Neutron Transport

Since a brute force approach to solving the late-time air capture problem was not deemed satisfactory, an alternative analytical procedure was developed. The new model basically determines whether or not a neutron in the air is sufficiently distant from the ground so that simpler transport approximations can be incorporated. For neutrons far from the air-ground interface, the new approximations assume that complexities introduced by the ground can essentially be

ignored and air transport calculations can be performed with an infinite medium Fermi age model. Similarly, for neutrons deeply imbedded in the ground, infinite medium ground transport calculations are assumed to be appropriate with the air being ignored. In this section we describe the coupled Monte Carlo-age theory calculations which are used in treating neutrons in the epithermal energy region  $E_c \geq E \geq E_t$ . When neutrons are downscattered to energies below  $E_t$ , one velocity Monte Carlo calculations are combined with time-dependent thermal diffusion theory calculations as described in the next section.

For a given neutron of energy  $E$  and altitude  $Z$  above the air-ground interface, it is possible from age theory and solid angle arguments to compute the probability,  $P(Z, E \rightarrow E_t)$ , that the neutron in slowing down to the thermal energy group cutoff,  $E_t$ , will strike the ground. If  $P(Z, E \rightarrow E_t)$  is smaller than some small predetermined lower probability limit,  $P_{MAX}$ , then the two-region, air-ground problem can be effectively uncoupled, and the neutron can be treated by infinite-air Fermi age theory. If  $P(Z, E \rightarrow E_t)$  is not smaller than  $P_{MAX}$ , a new lower energy  $E_1$  may be selected, where  $E_1 > E_t$ , so that  $P(Z, E \rightarrow E_1)$  is smaller than  $P_{MAX}$ . Age theory infinite medium calculations can then again be applied.

Eventually, there is an altitude,  $Z_c$ , below which it is not appropriate to employ infinite medium age theory since there is an intolerably high probability for a neutron to cross from the air to the ground for this altitude. Note that this is not the case if we chose to only degrade the neutron an infinitesimal amount in energy,  $E_j \rightarrow E_j - \Delta$  where  $\Delta \rightarrow 0$ . However, this would not be efficient computationally and could also introduce a bias into the calculations. Therefore, in our calculations for distances in air below  $Z_c = 75$  meters, we have used the Monte Carlo method exclusively.

The Monte Carlo technique is used to follow the neutron until its altitude has either increased above 75 meters or until it has reached the thermal neutron group,  $E \leq E_t$ . As the neutron moves away from the air-ground interface it is monitored and analytical methods are used as soon as appropriate. A neutron may be effectively followed by an alternating succession of Monte Carlo and analytical routines if the neutron travels back and forth between the narrow Monte Carlo region and regions away from the air-ground interface. The combined Monte Carlo-age theory tracking of the neutron is continued until the neutron energy falls within the thermal energy group.

An entirely similar process is used to analytically treat neutrons in the epithermal range which are in the ground. In this case the analytical method is used for depths greater than 5 cm and the Monte Carlo technique is used to follow neutrons which are close to the air-ground interface.

The neutron flux in the epithermal energy range, at spatial positions distant from the air-ground interface, is determined by solving the age-diffusion equation. For a monoenergetic spherically symmetric point source at the origin the age equation may be written as

$$\frac{1}{v} \frac{\partial \phi}{\partial t} = D \left\{ \frac{\partial^2 \phi}{\partial r^2} + \frac{2}{r} \frac{\partial \phi}{\partial r} \right\} - \xi \Sigma_s \frac{\partial \phi}{\partial u} - \Sigma_a \phi + Q_0 \frac{\delta(r)}{4\pi r^2} \delta(t) \delta(u), \quad (4.1)$$

where

$$\phi \equiv \phi(r, u, t) \quad (4.2)$$

and the lethargy  $u$  is related to the neutron speed  $v$  by

$$v = v_0 e^{-u/2}, \quad (4.3)$$

where  $v_0$  is the neutron source speed. The other notation in Eq. (4.1) is standard.

For an infinite medium, Eq. (4.1) is solved by applying successively Fourier spatial and Laplace time transforms and then inverting. The solution is found to be

$$\phi(r, u, t) = \frac{Q_0}{\xi \Sigma_s(0)} e^{-\Sigma_a(u)vt} \frac{e^{-(r^2/4r)}}{(4\pi r)^{3/2}} \delta(t - t_{SD}(v_0 \rightarrow v)), \quad (4.4)$$

where the slowing down time  $t_{SD}$  is defined by

$$t_{SD}(v_0 \rightarrow v) \equiv \int_v^{v_0} \frac{2}{\xi \Sigma_s(v')} \frac{dv'}{v'^2} \quad (4.5)$$

and the Fermi age  $r$  is given by

$$r(0 \rightarrow u) \equiv r(E_0 \rightarrow E) = \int_0^u \frac{D(u') du'}{\xi \Sigma_s(u')} = \int_E^{E_0} \frac{D(E')}{\xi \Sigma_s(E')} \frac{dE'}{E'} \quad (4.6)$$

To be able to use the neutron probability distribution functions of Eq. (4.4), an expression must be derived which relates the validity of the infinite medium age equation to the altitude, or depth,  $Z$ , and the incident energy  $E$  of the neutron.

We concern ourselves henceforth with the case of a neutron in the air; the problem of a neutron in the ground is treated by very similar methods. We have found numerically that the air and ground can be effectively uncoupled and age theory can be introduced if the altitude of the neutron is greater than

$$Z = C \sqrt{\tau(E_b \rightarrow E_a)} \quad (4.7)$$

Here  $Z$  is the neutron altitude above the air-ground interface and  $C$  is a constant. Values of  $C$  between 2.5 and 3.5 have been found to give satisfactory numerical results in our calculations. And finally,  $\tau(E_b \rightarrow E_a)$  is the Fermi age for downscattering from initial energy  $E_b$  to final energy  $E_a$

$$\tau(E_b \rightarrow E_a) \equiv \int_{E_a}^{E_b} \frac{D(E')}{\xi \Sigma_s(E')} \frac{dE'}{E'} \quad (4.8)$$

An expression equivalent to Eq. (4.7) holds for a neutron in the ground where  $Z$  in that case refers to the depth below the interface.

Physically  $\tau(E_b \rightarrow E_a)$  of Eq. (4.8) is a measure of the mean square distance traveled by a neutron as it downscatters from energy  $E_b$  to energy  $E_a$ . Hence, as  $E_a$  is reduced,  $\tau(E_b \rightarrow E_a)$  and the distance traveled by the neutron increases, and the altitude  $Z$  of Eq. (4.7) must also increase if the infinite medium theory is to be valid.

We are given an epithermal neutron of energy  $E_b$  and altitude  $Z$  above the ground. The problem is to determine the final energy  $E_a$  in order that age theory hold. It is apparent that as  $E_a$  approaches  $E_b$ ,  $r(E_b \rightarrow E_a)$  of Eq. (4.8) tends to zero and a very low altitude  $Z \rightarrow 0$  will satisfy Eq. (4.7). Values of  $E_a$  very close to  $E_b$  are not satisfactory from a computational standpoint since bias can be introduced into the results. Therefore, we only allow age theory calculations to take place if a non-negligible energy decrement,  $\Delta E$ , of the order of 10% is available. We furthermore only permit age theory calculations in the air above 75 meters and in the ground at depths below 5 centimeters. In this way Monte Carlo is used to treat the important region near the air-ground interface without introducing a bias due to overextension of the age theory models.

We use Eqs. (4.7) and (4.8) in the following manner for an epithermal neutron in air. An initial test is made to see if the neutron is above the 75-meter Monte Carlo cutoff plane. The final energy  $E_a$  of the neutron, after downscattering through a number of scattering collisions, is then determined by an iterative scheme. We would like  $E_a$  to be as small an energy as possible, preferably  $E_t$ , so that the normally time consuming Monte Carlo downscattering process in the epithermal range is replaced by the efficient analytical age theory models. It is clear that if the neutron is very high above the ground, it should be possible to downscatter the neutron to the thermal group cutoff,  $E_a = E_t$ , analytically. For example, if a neutron of energy 0.111 MeV is located 700 meters above the ground, the probability of analytically thermalizing the particle is very high. In this case, the probability of the neutron reaching  $E_t$  by age theory calculations, without striking the ground, is greater than 0.99. On the other hand, a 0.111 MeV neutron at an altitude of 100 meters has a much higher probability of striking the ground if it is

allowed to downscatter to thermal energies. Therefore, for the lower altitude particle, smaller energy decrements are allowed and new spatial positions are computed by age theory. If the new altitudes which are computed for the particle increase over the initial 100-meter height, the probability of eventually thermalizing the neutron by age theory calculations is also increased. However, if the particle drops below the 75-meter cutoff plane, the conventional Monte Carlo method is again instituted until the particle either is scattered above 75 meters, or until it is downscattered and reaches thermal energies. Another possibility is for a Monte Carlo neutron in the air to be tracked deep into the ground and eventually to reach such a depth that a ground age theory calculation may be used.

The calculation of the final allowable energy  $E_a$  is derived from squaring of Eq. (4.7),

$$Z^2 = C^2 \int_{E_a}^{E_b} \frac{D(E')}{\xi \Sigma_s(E')} \frac{dE'}{E'} = C^2 \left( \overline{\frac{D}{\xi \Sigma_s}} \right) \ln (E_b/E_a) \quad (4.9)$$

or on inverting Eq. (4.9),

$$E_a = E_b \times \exp \left\{ - \frac{(Z/C)^2}{(D/\xi \Sigma_s)} \right\}, \quad (4.10)$$



where  $(D/\xi\Sigma_s)$  is a weakly varying function of energy and is averaged over the energy range between  $E_b$  and  $E_a$ . From Eq. (4.10) it is apparent that once the altitude  $Z$  and incident energy  $E_b$  are known, it is possible to iteratively determine the final energy  $E_a$  after energy averaging the  $(D/\xi\Sigma_s)$  cross section terms which depend on  $E_b$  and  $E_a$ .

Once  $E_a$  is found, the age  $\tau(E_b \rightarrow E_a)$  can also be computed from Eqs. (4.8) and (4.9). This age then represents the largest age decrement which a neutron, at altitude  $Z$  with initial energy  $E_b$ , can undergo without accepting an intolerably high probability of striking the ground. The actual spatial position of the neutron following this aging process is found by sampling a distance  $r$  from a time-integrated and normalized solution of the age equation of Eq. (4.4). This solution or probability density function is given by

$$\psi(r, u) = \psi(r, \tau) = \frac{e^{-r^2/4\tau}}{(4\pi\tau)^{3/2}} 4\pi r^2, \quad (4.11)$$

where the  $\tau$  in Eq. (4.11) is the  $\tau(E_b \rightarrow E_a)$  as determined by Eqs. (4.8) and (4.9). The distance  $r$  traveled by a neutron in aging from  $E_b$  to  $E_a$  is found by sampling from Eq. (4.11) by a rejection technique. The initial spatial coordinates  $(x_1, y_1, z_1)$  as well as the initial time  $t_1$  are known. To find the final space coordinates, we generate an isotropic unit vector  $\vec{\Omega}$  with components  $\alpha, \beta$ , and  $\gamma$  in the  $x, y$ , and  $z$  directions. The final spatial position is then  $(x_2, y_2, z_2)$  where

$$\begin{aligned} x_2 &= x_1 + r \cdot \alpha \\ y_2 &= y_1 + r \cdot \beta \\ z_2 &= z_1 + r \cdot \gamma \end{aligned} \quad (4.12)$$

where  $r$  is sampled from Eq. (4.11).

In the relatively rare case where the isotropic vector  $\vec{\Omega}$  points straight downwards, it is possible for a neutron in the air to cross over into the ground. In these exceptional cases, a new isotropic vector is selected so that the particle does not move from one media to another. These selection processes have been carefully verified so that essentially no bias is introduced into the calculations.

The time required for the neutron to age from energy  $E_b$  to energy  $E_a$  is given by the slowing down time  $t_{SD}(v_b \rightarrow v_a)$  of Eq. (4.5). The total time, from birth as a source neutron to energy  $E_a$  is given by

$$t_2 = t_1 + t_{SD}(v_b \rightarrow v_a), \quad (4.13)$$

where  $t_1$  is the net time to the particles appearance at energy  $E_b$  and  $t_{SD}$  is the slowing down time to energy  $E_a$ .

We then have the final particle position  $(x_2, y_2, z_2)$  and time  $t_2$  which become the initial coordinates for the next downscattering or thermal diffusion calculations.

In Eq. (4.11) it is apparent that neutron absorption is not properly considered. The probability of neutron absorption during the aging process,  $E_b \rightarrow E_a$ , is included by using the concept of a resonance escape probability  $p(E_b \rightarrow E_a)$ , where

$$p(E_b \rightarrow E_a) = \exp \left\{ - \Sigma_a(v) v t_{SD}(E_b \rightarrow E_a) \right\} \quad (4.14)$$

The neutron weight before collision,  $W_b$ , is multiplied by  $p(E_b \rightarrow E_a)$  to obtain the weight after aging,  $W_a$ ,

$$W_a = W_b p(E_b \rightarrow E_a). \quad (4.15)$$

This is analagous to the usual Monte Carlo treatment of absorption where the neutron weight is multiplied by the nonabsorption probability,  $(\Sigma_s/\Sigma_t)$ , to determine the final weight.

To determine a spatial position and time for depositing energy due to neutron absorption and elastic scattering in the epithermal energy range, we first generate a new age for deposition,  $\tau_{\text{dep}}$ ,

$$\tau_{\text{dep}} = \tau(E_b \rightarrow E_a) \times \rho \quad (4.16)$$

where  $\rho$  is a random number uniformly distributed on the interval (0, 1) and  $\tau(E_b \rightarrow E_a)$  is the total age decrement as used in Eq. (4.11). Corresponding to this  $\tau_{\text{dep}}$  age decrement is a slowing down time  $t_{\text{dr}}$  so that we may determine the total time for energy deposition

$$t_2 = t_1 + t_{\text{dep}} \quad (4.17)$$

Furthermore, the spatial position for energy deposition is determined by sampling a distance  $r$  from Eq. (4.11) with  $\tau = \tau_{\text{dep}}$  and using Eq. (4.12) to find the final spatial coordinates.

The amount of energy deposited varies depending on whether the neutron is in the air or in the ground: In the air, energy is deposited from neutron absorption and elastic scattering processes. The neutron absorption is due primarily to the (n, p) reaction in nitrogen with the proton energy deposited locally at the absorption site. The (n,  $\gamma$ ) reaction is also considered but the gamma ray energy is transported away from the absorption site as will be discussed later. The energy deposited in the air due to absorption is scored in the analytical routines as

$$E_{\text{dep}} = (E_b + Q) \times \text{FRNP} \times W_b (1 - p(E_b \rightarrow E_a)) \quad (4.18)$$

where  $E_b$  is the neutron energy before collision,  $Q$  is the energy released during the (n, p) reaction in nitrogen (.6264 MeV), FRNP is the fraction

of the absorption cross section which results in proton emission ( $\sim .96$ ).  $W_b$  is the neutron weight before collision, and  $p(E_b \rightarrow E_a)$  is the resonance escape probability for the neutron in aging from  $E_b$  to  $E_a$ .

There is also energy deposited in the air due to elastic scattering reactions. In this case, we have determined empirically that approximately half of the neutron energy is transmitted to electrons in this energy range. Therefore, elastic energy deposition in the air is scored in the analytical routines as

$$E_{\text{dep}} = (E_b - E_a) \times W_b \times p(E_b \rightarrow E_a) \times FE \quad (4.19)$$

where  $E_b$  and  $E_a$  are the neutron energies before and after aging,  $W_b$  is the neutron weight before collision,  $p(E_b \rightarrow E_a)$  is the resonance escape probability, and FE represents the fraction of energy converted to electrons or .50 in this case.

In the ground, the only neutron energy deposited is due to elastic scattering reactions with absorption being neglected in this energy range. For ground, we assume full conversion of the neutron energy to electrons, so that Eq. (4.19) is valid with  $FE = 1.0$ .

#### 4.3.3 Thermal Neutron Transport

When a neutron has reached energies below the thermal group cutoff energy,  $E_t$ , a new time-dependent one-group diffusion model is utilized whenever infinite medium diffusion theory is valid. The new model is applied at spatial positions which are distant from the air-ground interface. At altitudes or depths which are closer to the interface, a one-velocity Monte Carlo calculation is invoked so that the two-region geometrical complications can be accurately treated. The new coupled Monte Carlo-diffusion theory scheme does enable tracking of thermal neutrons back and forth from ground to air. In this manner, the new model is a significant improvement over the ground thermal

capture treatment of last year in which neutrons leaving the ground were assumed lost from the system and were no longer followed.

The validity of the analytical model can be determined on the basis of solid angle and thermal diffusion theory arguments. We have found that thermal neutrons located at altitudes in air, or at ground depths, more than three diffusion lengths from the air-ground interface can be treated by infinite medium diffusion theory. Only a small percentage of those neutrons located three or more diffusion lengths from the air-ground interface will eventually cross the interface and enter the other medium. Therefore, only in rare instances do we need to reject the direction chosen for a particle which is analyzed by diffusion theory. The bias introduced into the calculations by this direction selection process should be negligible.

Those neutrons which are less than three diffusion lengths from the interface are followed with one velocity Monte Carlo and may travel from one medium to the other. The Monte Carlo treatment is continued until the particle is either killed on the basis of weight criteria or until it moves to a position more than three diffusion lengths from the interface where the analytical model may be applied. The Monte Carlo calculations are generally much slower than the analytic routines, especially in the ground where several hundred collisions may be required before the neutron can be disposed of on weight criteria. Fortunately, however, the neutrons do migrate on each Monte Carlo collision so that they may diffuse out to distances where the more efficient analytic routines may be employed.

The infinite medium thermal neutron flux distribution, away from the air-ground interface, is obtained by solving the time dependent

diffusion equation for a spherically symmetric point source  $Q_0$  at time  $t = 0$ ,

$$\frac{1}{v} \frac{\partial \phi}{\partial t} = D \left\{ \frac{\partial^2 \phi}{\partial r^2} + \frac{2}{r} \frac{\partial \phi}{\partial r} \right\} - \Sigma_a \phi + Q_0 \frac{\delta(r)}{4\pi r^2} \delta(t) \quad (4.20)$$

where  $\phi \equiv \phi(r, t)$  is the thermal neutron flux and the cross sections and speed  $v$  in Eq.(4.20) are thermal values.

The solution to Eq. (4.20) is given by

$$\phi(r, t) = \frac{Q_0 e^{-\Sigma_a v t} e^{-(r^2/4 D v t)}}{(4\pi D v t)^{3/2}} \quad (4.21)$$

where  $r$  is the distance from the source point.

The coupled thermal diffusion theory-Monte Carlo method is employed in the following manner. A test is made initially to determine whether a thermal neutron is within three diffusion lengths of the air-ground interface. If the particle is within three diffusion lengths, the one velocity Monte Carlo method is used to track the neutron which may be either in the air or in the ground. The Monte Carlo method is used until the particle is either killed by weight criteria or until the neutron is transported far enough from the interface so that the analytical treatment can be employed. Once the neutron is in the diffusion theory region, the time and distance traveled before its absorption and removal from the system are computed by sampling from Eq. (4.21).

Before performing the sampling, the neutron flux is first normalized so that it becomes a true probability density function. This is accomplished by setting

$$f(r, t) = \frac{4\pi r^2}{Q_0} \Sigma_a \phi(r, t) \quad (4.22)$$

where  $\phi(r, t)$  is given by Eq. (4.21). We then have

$$\int_0^\infty dt \int_0^\infty dr f(r, t) = 1.0 \quad (4.23)$$

Since there are two variables,  $r$  and  $t$ , which are to be sampled from Eq. (4.22), we first form a marginal density  $f_1(t)$  and a marginal distribution  $F_1(t)$ , from which we sample a time  $t$ . These functions are defined as,

$$f_1(t) \equiv \int_0^\infty f(r, t) dr = \Sigma_a v e^{-\Sigma_a v t}, \quad (4.24)$$

and

$$F_1(t) \equiv \int_0^t f_1(t') dt' = 1 - e^{-\Sigma_a v t}, \quad (4.25)$$

After we have sampled a time  $t$  from Eq. (4.25) we form the conditional distribution  $F_2(r|t)$ , where

$$F_2(r|t) = \int_0^r \frac{f(r', t)}{f_1(t)} dr' = \int_0^r \frac{4\pi r'^2 e^{-r'^2/4Dvt} dr'}{(4Dvt)^{3/2}} \quad (4.26)$$

We then sample a distance  $r$  from the distribution of Eq. (4. 26) for a given time  $t$ . The sampling of the distance  $r$  is accomplished by the rejection method<sup>(7)</sup> which is very fast and has an efficiency of about 40% for this particular distribution function.

The distance  $r$  then represents the total distance traveled by the neutron from its initial coordinates in the diffusion theory region. If these initial coordinates are  $(x_3, y_3, z_3)$ , then the final location of the neutron, or its absorption coordinates, are given by  $(x_4, y_4, z_4)$ , where

$$\begin{aligned}x_4 &= x_3 + \alpha' \cdot r \\y_4 &= y_3 + \beta' \cdot r \\z_4 &= z_3 + \gamma' \cdot r\end{aligned}\tag{4. 27}$$

and  $\alpha'$ ,  $\beta'$ , and  $\gamma'$  are the components of an isotropically generated unit vector, and  $r$  is the distance sampled above. In the unusual event that the particle crosses the air-ground interface, a new isotropic vector is chosen and the coordinates  $(x_4, y_4, z_4)$  are recalculated.

In a similar fashion, the initial time of appearance of the neutron,  $t_3$ , in the analytical region is added to the time  $t$  which is sampled from Eq. (4. 25) to obtain the total diffusion time,  $t_4$ , before the particle is absorbed,

$$t_4 = t_3 + t\tag{4. 28}$$



When the neutron is being transported in the one-velocity Monte Carlo region, its weight is reduced on each collision by the factor  $p = \Sigma_g / \Sigma$ . The fraction of weight lost on each collision is incorporated into gamma ray weight. Upon absorption of the neutron in the diffusion region, part of the neutron weight remaining is carried off by gamma rays. As in the case of the epithermal energy region, neutron energy is deposited in the thermal group in air due to the (n, p) reaction in nitrogen. Elastic scattering energy deposition is neglected for the thermal group since it is extremely small. The thermal neutron energy deposited in air is given by

$$E_{\text{dep}} = Q \times \text{FRNP} \times W_b \times (1 - p) \quad (4.29)$$

where  $Q$  is energy released due to the (n, p) reaction, FRNP is the fraction of the absorption cross section in air which results in proton emission,  $W_b$  is the neutron weight before collision, and  $p$  is the non-absorption probability. Equation (4.29) is valid for the Monte Carlo region and is also true for the diffusion region if it is understood that in the analytic region  $p \rightarrow 0$ .

For the ground, the neutron energy deposition is neglected for the thermal group since it is very small. Gamma ray energy deposition for both ground and air is discussed in the next section.

#### 4.3.4 Gamma Ray Transport

In this section we discuss briefly the new analytical techniques used to treat gamma ray transport following thermal neutron absorption. There are, of course, also gamma rays produced by fast neutron reactions such as inelastic scattering, charged particle processes, etc. These gamma rays are dealt with using the techniques described in earlier reports<sup>(1-3)</sup> and will not be discussed further here. We will concern ourselves only with gamma rays which are produced by neutron absorptions in the thermal group. Gamma rays which are produced by epithermal neutron absorptions are tracked by Monte Carlo routines for convenience. The analytical model described below could in principle be extended to treat these photons in a straightforward manner.

The method used to treat gamma rays produced by thermal neutron absorptions is based on combining an analytical buildup factor model with the conventional Monte Carlo method used in the past. The buildup factor model can be applied to gamma rays which originate at absorption sites which are distant from the air-ground interface. For gamma rays which are born at positions closer to the interface, the previous Monte Carlo techniques are employed. In this regard, the gamma ray transport from thermal neutron reactions is treated in a fashion similar to the epithermal and thermal neutron transport, i. e. , analytical models are used away from the air-ground interface, and Monte Carlo methods are applied near the interface.

Buildup factor approximations have been applied successfully to many gamma ray transport problems. These approximations are based on the observation that the calculation of the unscattered gamma ray flux is usually a simple matter and involves only an exponential kernel. A buildup factor is then introduced as a multiplicative factor

to incorporate the effects of scattered photons. In a uniform medium the gamma ray flux at radial position  $r$  due to a unit point source at the origin of gamma rays of energy  $E$  is then given by

$$\phi(r, E) = B_{\phi}(r, E) \frac{e^{-\Sigma(E)r}}{4\pi r^2} \quad (4.30)$$

where  $\Sigma(E)$  is the macroscopic absorption coefficient for gamma rays of energy  $E$ .  $B_{\phi}(r, E)$  is the flux buildup factor for the gamma rays of energy  $E$ , and also depends on the distance  $r$  from the source of photons.

In a similar manner we may write the photon current at  $r$  due to gamma rays of energy  $E$  as

$$J(r, E) = B_J(r, E) \frac{e^{-\Sigma(E)r}}{4\pi r^2} \quad (4.31)$$

where  $B_J(r, E)$  is now the photon current buildup factor for gamma rays of energy  $E$ .

We are ultimately interested in determining the gamma ray ionization rate as well as the various Compton currents. The ionization rate is obtained from Eq. (4.30) by introducing the fluence to ionization conversion factor,  $K_{\gamma}(E)$ ,

$$K_{\gamma}(E) = E \sigma_{ca} + E \sigma_{PE} + (E-1.02) \sigma_{pp}. \quad (4.32)$$

where  $K_{\gamma}(E)$  is discussed in detail in Refs. 1 and 3.

Using Eq. (4. 32) in Eq. (4. 30) we obtain the gamma ionization rate

$$D(r) = \int K_{\gamma}(E) \phi(r, E) dE \quad (4. 33)$$

where it is, of course, also implied that  $\phi(r, E)$  and  $D(r)$  are time dependent quantities.

The radial, or horizontal, Compton currents can be obtained from Eq. (4. 31) by introducing the mean forward electron range  $R_f(E)$  and integrating over energy<sup>( 3)</sup>

$$J_c(r) = e \int \frac{R_f(E)}{\lambda_c(E)} J(r, E) dE \quad (4. 34)$$

where  $\lambda_c(E)$  is the Compton mean free path length.

The currents as determined by Eq. (4. 34) are defined with respect to the birth site of the photon. To determine the true radial or horizontal components, we must translate these results back to the origin of the coordinate system. When this is done the true radial or horizontal, as well as the theta or vertical, components are easily determined.

Before Eqs. (4. 30) and (4. 31) can be used for the photon flux and current, expressions must be derived for the flux and current buildup factors,  $B_{\phi}(r, E)$  and  $B_J(r, E)$ . We have derived polynomial expressions for  $B_{\phi}(r, E)$  and  $B_J(r, E)$  which should give reasonably good results. In both cases we have assumed that the buildup factors can be developed in a series of the form,

$$B(r, E) = 1 + a(E) \cdot (\Sigma(E) \cdot r) + b(E) \cdot (\Sigma(E) \cdot r)^2 \quad (4. 35)$$

where  $a(E)$  and  $b(E)$  are coefficients to be determined for each photon energy of interest, and  $(\Sigma(E) \cdot r)$  is the photon distance from the source in units of the mean free path.

We have determined the coefficients  $a(E)$  and  $b(E)$  for both the flux and current buildup factors for a number of photon energies. These coefficients were obtained by performing least squares fits to Monte Carlo gamma transport data in air supplied by V. W. Pine of AFWL. The AFWL data span the energy range from 0.5 MeV to 8.0 MeV. We have extrapolated coefficients obtained from these results to higher energies since photons in air at energies as high as 11.0 MeV are of interest.

We have compared our polynomial expressions for the buildup factors with some other derived results<sup>(8)</sup> to ensure accuracy. The buildup factor expressions derived from the air transport calculations have also been used for the ground transport calculations. The buildup factor calculations are influenced primarily by the atomic number of the transport medium so that differences between air and ground should be small.

After a neutron absorption site has been determined from the epithermal and thermal neutron transport routines, a photon energy is selected from the appropriate capture gamma spectrum. Capture gamma spectra for both air and ground are taken from the latest ENDF/B tabulations. Epithermal capture gamma spectra are assumed to have the same shape as the thermal spectra.

Tests are then made to decide whether the analytical or Monte Carlo gamma ray transport routines should be used. In our calculations

we have used the analytical buildup factor models for gamma rays which are born more than three mean free paths from the air-ground interface. Photons closer to the interface are treated using the previous Monte Carlo CHARGE routine. All gamma rays which are formed from epithermal neutron absorption are also followed using the CHARGE routine.

For photons which are distant from the interface we can sample the distance  $r$  traveled by the photon before its demise from normalized probability density functions of the form

$$\psi(r, E) = 4\pi r^2 B(r, E) \frac{e^{-\Sigma r}}{4\pi r^2} \cdot N \quad (4.36)$$

where  $N$  is a normalization factor, and  $B(r, E)$  is either a flux or current buildup factor as given by Eq. (4.35). In actual calculations, we have chosen to sample  $r$  from the exponential distribution  $e^{-\Sigma r}$  and then modify the weight by  $N \times B(r, E)$  for both flux and current. In this way the ionization and Compton currents are both scored at the same spatial position, but the magnitudes differ because of the different weight modifications.

After the distance  $r$  is sampled, we obtain the final coordinates  $(x_5, y_5, z_5)$  from the initial coordinates  $(x_4, y_4, z_4)$  by generating a unit isotropic vector with components  $(a'', \beta'', \gamma'')$  and forming

$$\begin{aligned} x_5 &= x_4 + a'' \cdot r \\ y_5 &= y_4 + \beta'' \cdot r \\ z_5 &= z_4 + \gamma'' \cdot r \end{aligned} \quad (4.37)$$

Particles which cross the interface are again not allowed, but these events are very rare.

The current coordinates at  $(x_5, y_5, z_5)$  are relative to the photon birth site at  $(x_4, y_4, z_4)$ . By translating these coordinates to the origin of coordinates for the system, we easily can obtain the true Compton currents.

It is also possible for us to generate  $K$  photons per neutron absorption and modify the weight of each by dividing by  $K$ . We have found that  $K = 10$  gamma rays per thermal absorption to be a reasonable number which improves our statistical results for the analytical photon transport calculations without undue computational effort.

It has been assumed that the photon travels from its birth position to its final position instantaneously. This is a good approximation since the time required for neutron absorption is orders of magnitude longer than the photon transit time.

#### 4.4 BIASING TECHNIQUES

There are several Monte Carlo biasing techniques utilized in O5RNIES to reduce computer running times and to obtain results which would otherwise be difficult to attain using conventional methods. The amount of biasing used in the present version of the code has been reduced somewhat from earlier versions and has been replaced in part by analytical routines.

However, to obtain reasonable statistical results at great distances from the source, path length stretching is still required. For neutrons in air, stretching is used for particles of energy greater than an epithermal cutoff energy,  $E \approx 0.111$  MeV. Path length stretching is also used for gamma rays in the air to attain distant results. A more complete discussion of these techniques is given in Ref. 2.

The angle of scattering biasing discussed in last year's work <sup>(3)</sup> has been eliminated since we are now interested in neutrons moving back and forth from the ground to the air. In the earlier calculations

the scattering angle biasing eliminated many of the then unwanted neutrons which were traveling away from the ground. Source direction biasing, as discussed previously, has been retained, but the source energy biasing has been eliminated with the new energy band version of the code.

The previous limited scoring and capture gamma ray production biasing schemes have also largely been eliminated and replaced with new techniques. For neutrons in the epithermal range,  $E_c \geq E \geq E_t$ , neutron absorption is simulated by multiplying the neutron weight by the nonabsorption probability at each collision. It is not efficient, however, to produce and track capture gamma rays at each of these numerous collisions. Therefore, an input quantity, RREPI, is used as the probability of producing capture gamma rays in both the air and in the ground. These photons which are produced then have their weights adjusted to reflect the modified production rate.

For neutrons in the thermal group,  $E \leq E_t$ , limited capture gamma production is again utilized, with another input quantity, RRTHM, reflecting the fraction of times a gamma ray is produced per thermal neutron collision. The energy deposited by thermal neutrons is also only scored a fraction RRTHM of the time to avoid wasting large amounts of computer time on tallying small quantities. The weights of both the capture gamma rays and the neutrons are, of course, modified to reflect the limited photon production and neutron scattering.

It should be noted that the limited photon production and scoring is used for particles which are being tracked with the time consuming Monte Carlo techniques. The analytical methods do not include biasing routines used at present since they are substantially



more efficient than the Monte Carlo approach. We also mention that it is possible to vary the number of photons produced per collision in the epithermal and thermal ranges, through RREPI and RRTHM, as well as in the fast range through NPHOT. In this way we may adjust the average weight carried off by photons in each of the three ranges so as to obtain lower statistical variance.

## 4. 5      NUCLEAR CROSS SECTIONS

### 4. 5. 1    Introduction

In these calculations we have assumed that the air was composed of nitrogen and oxygen with atom percentages of 79 and 21 percent, respectively. The air density was taken to be 1.29 mg/cc. The ground was assumed to be composed of hydrogen (16%), oxygen (57%), aluminum (8%), and silicon (19%), with a density of 1.7 g/cc.

The data utilized in our present work are based entirely on the most recent ENDF/B tabulations for both neutron and gamma ray production cross sections. Gamma ray interaction cross sections are those used in our previous studies and are sufficiently well known for EMP applications. Since the neutron and gamma ray production data for previous EMP source calculations were based on earlier data sets, we discuss below some of the differences in the new and old cross section tabulations. Furthermore, some estimates of the sensitivity of EMP source calculations to changes in nuclear cross sections are also presented.

Preparation of new cross section sets for use with O5RNIES is a fairly time consuming task requiring several man-weeks of effort. A number of processing codes must be employed before ENDF/B Library data can be placed in formats useable by O5RNIES. Initially the RIGEL code was used to convert the ENDF/B data tapes from BCD modes to binary modes. RIGEL was also used for combining data from several data tapes onto a single tape. The SAD code was used to convert data

from tabulated angular scattering probability distributions to Legendre polynomials for hydrogen. Code 678 was used to create neutron scattering cross section tapes and the PHI angular distribution tapes, as well as preparing the master cross section data tapes. The QDE and AVKER codes were used to create energy deposition data for air and ground collisions, respectively. Several other codes were also used for creating gamma production probability distributions for discrete and continuum gamma cross sections.

#### 4.5.2 Specific Nuclear Cross Sections

##### 4.5.2.1 Hydrogen

The new data for hydrogen comes from Modification 1 of the ENDF/B-III Library (February 1972). The new hydrogen cross sections should be very similar to those employed in previous EMP studies<sup>(3)</sup>. The new data differ primarily in format changes made to enable the new results to conform with ENDF/B-III library specifications, and in modifications to add photon interaction data. The photon production data for hydrogen are simple, consisting of only a single neutron capture gamma ray emitted at approximately 2.23 MeV.

##### 4.5.2.2 Nitrogen

The nitrogen neutron and gamma production cross sections were taken from Modification 3 of the ENDF/B-III tabulation. The latest modification again was made to enable the current DNA library to conform with ENDF/B-III Library specifications. The new cross sections for nitrogen differ primarily in the inelastic scattering data. The total cross sections for the new tabulation are in reasonably good agreement with the older results. The inelastic cross sections, however, are generally a factor of two or so lower than the older data. The new gamma production cross sections, which include the effects of inelastic

neutron cross section changes, also differ markedly from the earlier ENDF-UNC data. <sup>(9)</sup>

The new tabulation also includes detailed listings of inelastic scattering level and charged particle decay schemes. For nitrogen we are considering some 26 discrete inelastic scattering levels and no inelastic continuum. The first 12 inelastic levels decay by conventional means with emission of gamma rays. The 14 higher levels, above 9 MeV, decay by emission of protons in addition to gamma rays. For the standard inelastic scattering processes the energy deposited by the recoiling nitrogen atom is given by

$$E_{\text{dep}} = E_{\text{in}} - E_{\text{out}}(Q) - Q, \quad (4.38)$$

where  $E_{\text{in}}$  is the neutron energy before collision and  $E_{\text{out}}(Q)$  is the energy after collision and is dependent on the level excitation energy  $Q$ .

For the cases of inelastic scattering followed by charged particle emission,  ${}^7\text{N}^{14}(n, n'p){}_6\text{C}^{13}$ , the total energy deposited locally, by the recoiling  ${}^7\text{N}^{14}$  atom and the proton, is given by

$$E_{\text{dep}} = E_{\text{in}} - E_{\text{out}}(Q) - BE, \quad (4.39)$$

where BE here is the binding energy of  ${}^7\text{N}^{14}$  relative to  ${}_6\text{C}^{13} + {}_1\text{p}^1$ . It is assumed that the final carbon state is the ground state since no gamma rays from excited carbon-13 states are in the inelastic ENDF/B tabulation.

In addition to the inelastic neutron scattering levels which decay by charged particle emission, a number of conventional absorption and charged particle emission reactions are also considered in

the new cross section set. For  ${}^7\text{N}^{14}(\text{n}, \text{p}){}^6\text{C}^{14}$  processes, cross sections are given for one final  ${}^6\text{C}^{14}$  ground state process and for four transitions to excited carbon levels with eventual gamma ray decay. For deuteron emission processes,  ${}^7\text{N}^{14}(\text{n}, \text{d}){}^6\text{C}^{13}$ , one final  ${}^6\text{C}^{13}$  ground state and three excited carbon-13 states are considered. The excited states again decay by gamma emission. For triton decay processes,  ${}^7\text{N}^{14}(\text{n}, \text{t}){}^6\text{C}^{12}$ , one ground state and one excited  ${}^6\text{C}^{12}$  state are treated.  $(\text{n}, \alpha)$  reactions are considered with a final ground and also ten excited  ${}^5\text{B}^{11}$  states which then decay by gamma emission.

Thermal neutron  $(\text{n}, \gamma)$  capture processes in nitrogen are also being considered in our EMP calculations for the first time. These cross sections are also available from the ENDF/B file. The multiplicity is found to be 2.166 and the average gamma emission energy is about 5 MeV. This results in a total gamma source energy of 10.83 MeV which agrees with the binding energy available due to neutron absorption in  ${}^7\text{N}^{14}$ . It is assumed that the thermal capture gamma spectrum can be applied to higher energy ranges also since spectral data at higher energies are sparse. This should not introduce any appreciable error since the thermal group is most important for  $(\text{n}, \gamma)$  reactions and furthermore the total gamma energy available of 10.83 MeV remains approximately constant at epithermal neutron energies.

#### 4.5.2.3 Oxygen

The oxygen data were taken from the ENDF/B tabulation of August 1971. The new oxygen data include recent gamma production cross sections which differ from the older UNC data <sup>(9)</sup> used in our previous EMP studies. The new neutron inelastic scattering cross sections are also generally lower than the earlier ENDF/B results used in EMP calculations.

The new ENDF/B tabulation includes considerably more detailed charged particle and inelastic scattering decay schemes. In our present calculations we have considered some 28 discrete neutron inelastic scattering levels with level excitations up to 15.25 MeV. No inelastic continuum is required for the new tabulation. Of the 28 inelastic levels, only 6 are conventional (n, n'γ) levels, while the other 22 levels decay by either proton, alpha particle, or alpha plus gamma emission. As in the case of nitrogen, it becomes important to correctly treat the charged particle emissions from neutron inelastic scattering levels since the charged particles deposit essentially all of their energies locally, whereas gamma rays may deposit their energies over much greater distances.

For the six conventional inelastic scattering levels, the energy deposition of the recoiling oxygen atom is again determined from 4.38.

$$E_{\text{dep}} = E_{\text{in}} - E_{\text{out}}(Q) - Q, \quad (4.38)$$

where  $E_{\text{in}}$  is the neutron energy before the inelastic scattering collision,  $E_{\text{out}}(Q)$  is the energy after collision and is dependent on the level excitation energy  $Q$ .

The energy deposition for the eight inelastic levels which decay by alpha emission to the ground state of carbon-12 is given by

$$E_{\text{dep}} = E_{\text{in}} - E_{\text{out}}(Q) - \text{BE}({}_6\text{C}^{12}), \quad (4.40)$$

where BE is the binding energy of oxygen-16 relative to breakup into carbon-12 plus an alpha particle.

There are also eight inelastic levels which are assumed to decay first by alpha emission to the first excited state of carbon-12 and then decay by emission of 4.439 MeV gamma rays to the  ${}_6\text{C}^{12}$  ground state. The local energy deposition for these levels is computed from

$$E_{\text{dep}} = E_{\text{in}} - E_{\text{out}}(Q) - BE, \quad (4.41)$$

where  $E_{\text{in}}$  is again the incident neutron energy,  $E_{\text{out}}$  is the neutron energy after the inelastic scattering event for level  $Q$ , and  $BE$  is the binding energy for oxygen breakup into an alpha particle plus carbon-12 plus a 4.439 MeV gamma ray.

In addition, four inelastic levels are assumed to decay by proton emission to the ground state of nitrogen-15. No neutrons are energetic enough in our calculations to result in inelastic scattering events which decay by proton emission to the excited states of nitrogen-15 with subsequent gamma ray decay. The local energy deposition for proton emission to the nitrogen-15 ground state is determined from

$$E_{\text{dep}} = E_{\text{in}} - E_{\text{out}}(Q) - BE({}_7\text{N}^{15}), \quad (4.42)$$

where  $E_{\text{in}}$  and  $E_{\text{out}}(Q)$  are the neutron energies before and after scattering for level  $Q$ , and  $BE({}_7\text{N}^{15})$  is the binding energy for oxygen-16 breakup into nitrogen-15 plus a proton.

In addition to the gamma rays produced by inelastic neutron scattering, gamma rays along with charged particles are also emitted in absorption processes. Both  $(n, p\gamma)$  and  $(n, \alpha\gamma)$  processes are considered in our calculations. The  $(n, \gamma)$  capture reaction in oxygen is very small and has been neglected in our studies.

#### 4.5.2.4 Aluminum

The new aluminum data were taken from the ENDF/B-II Modification 1 tabulation of July 1971. There were 35 discrete inelastic levels considered in the latest calculations. No inelastic continuum was used, but the  $(n, 2n)$  reaction was considered. Local energy deposition through charged particle reactions was treated by using tabulated kerma values as was done last year.

A gamma ray continuum was included in the new calculations as well as gamma ray production cross sections due to neutron inelastic scattering and capture reactions.

#### 4.5.2.5 Silicon

The new silicon data were taken from a recent ENDF/B tabulation and include revisions by R. Q. Wright (2-05-71) and R. R. Kinsey (1-15-72). The new neutron and gamma ray production data are based on the M. K. Drake evaluation.<sup>(10)</sup> Since our previous EMP silicon data were also based on this evaluation, we anticipate little change in the silicon cross section set. We have compared our latest silicon data with earlier data to attempt to confirm this suspicion. We have found that the new and old total cross sections differ generally by less than about 10% from 18.0 MeV down to thermal energies. The elastic cross sections also are in good agreement and the inelastic data are also within about 10% down to about 6 MeV.

For silicon we consider 21 discrete neutron inelastic scattering levels plus a continuum. In addition,  $(n, 2n)$  and  $(n, n'p)$  reactions and a gamma ray continuum are treated in these calculations. Local energy deposition for silicon, as for all ground materials, is handled using the AVKER code which calculates neutron kerma factors which are then used to compute dose rates.



#### 4.5.3 Cross Section Sensitivity Studies

Since there were significant cross section changes between the new ENDF/B data and older cross section sets used in EMP studies, a simple set of cross section sensitivity calculations was performed. The changes in nitrogen and oxygen neutron inelastic scattering and gamma ray production cross sections were generally the most substantial, and the sensitivity studies were therefore concentrated on these materials.

Neutron and secondary gamma ray transport calculations were performed in infinite air using the latest ENDF/B neutron and gamma ray production cross sections for nitrogen and oxygen. A second set of calculations was also performed using the earlier data sets utilized in previous EMP studies<sup>(3)</sup> in order to assess the sensitivity of neutron and gamma ray transport to cross section perturbations. The calculations were carried out using the one dimensional, time-dependent discrete ordinates code TDA.<sup>(11)</sup> The TDA code was used because it required less computer time for a one-dimensional problem than the Monte Carlo method. More detailed two-dimensional Monte Carlo calculations could then be performed if the TDA results indicated further more detailed studies were warranted.

A point source of neutrons with a typical thermonuclear source energy distribution was used and scalar fluxes, ionization rates and radial currents were computed using the two sets of cross sections. Results were obtained out to distances of 3100 meters in air and to times of approximately 100  $\mu$ sec. Thermal neutron capture reactions were not considered.

Detailed plots at 480, 1000, 2000, and 3100 meters of radial Compton currents, neutron and gamma ray ionization rates, and total

ionization rates were made to compare the new ENDF/B data results with the older cross section data. In Figs. 4.2-4.5, these time-dependent ionization rates and Compton currents for the two data sets are shown at a distance of 480 meters from the source. Similar results were obtained at the other spatial positions.

In Fig. 4.2 the neutron ionization rate for the new data appears to be substantially higher than the older data results, particularly at early times, and again at later times. This reflects in part the lower neutron inelastic scattering cross sections used in the new data sets which result in less spectral degradation of neutrons and larger neutron ionization rates. The gamma ray production cross sections in the new data sets are substantially lower than the earlier data, and these changes are exemplified in factor of two reductions in gamma ray ionization rates at early times as illustrated in Fig. 4.3. Figure 4.4 shows the total ionization rate as a function of real time. The total ionization rate as computed using the older data is substantially higher at early times when only gamma rays are contributing. However, with the arrival of the neutron wave front, the ENDF/B data calculations become higher than the older results. The radial Compton current results shown in Fig. 4.5 generally follow the shapes of the gamma ionization rates with the older data results being substantially higher at early times.

The cross section sensitivity studies imply that factor of two differences in quantities such as radial Compton currents and total ionization rates may be introduced by using the latest ENDF/B data for oxygen and nitrogen. Changes in EMP field calculations due to cross section changes should be somewhat smaller.

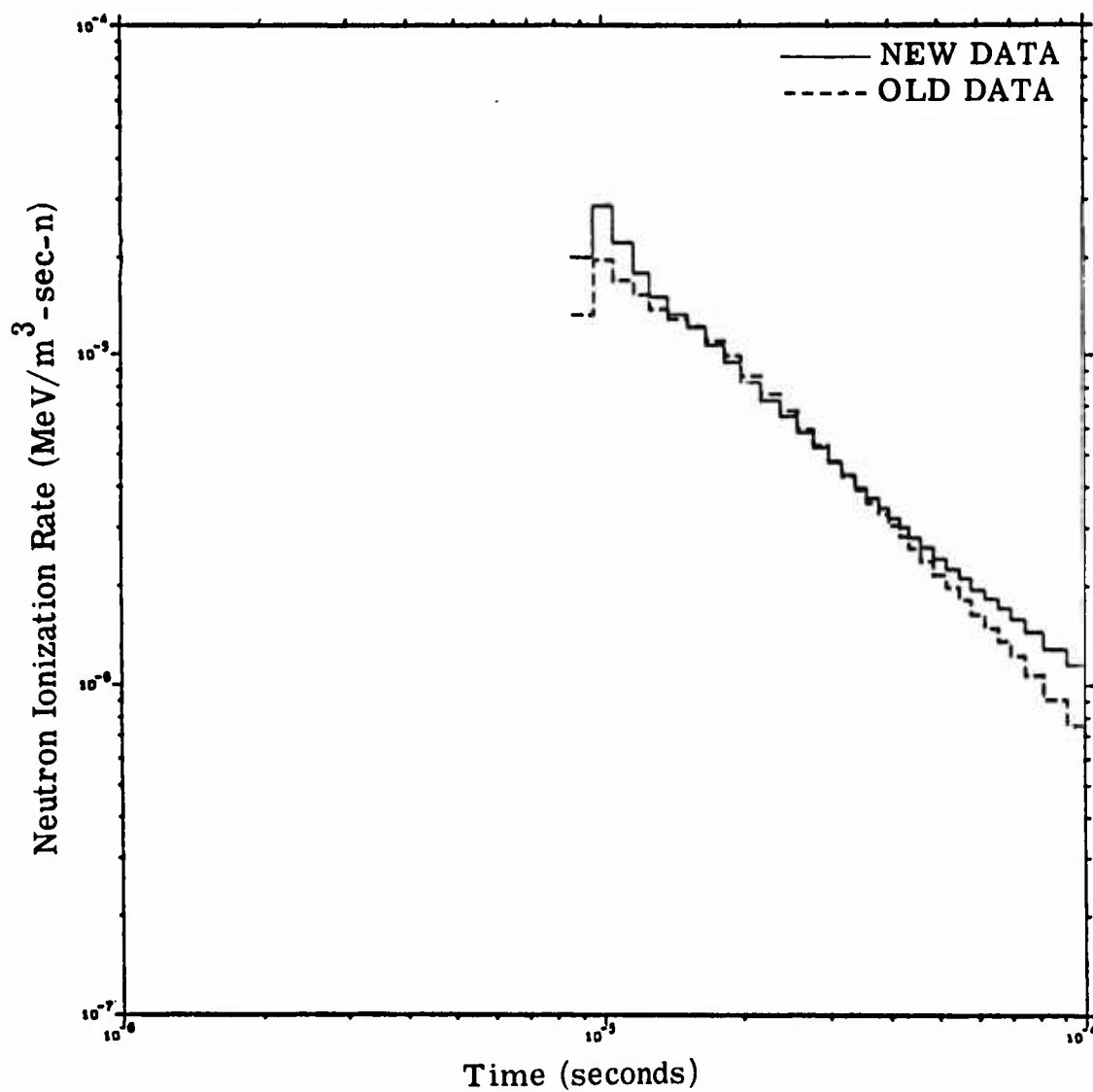


Figure 4. 2. Comparison of neutron ionization rate calculations using ENDF/B and older data at 480 meters.

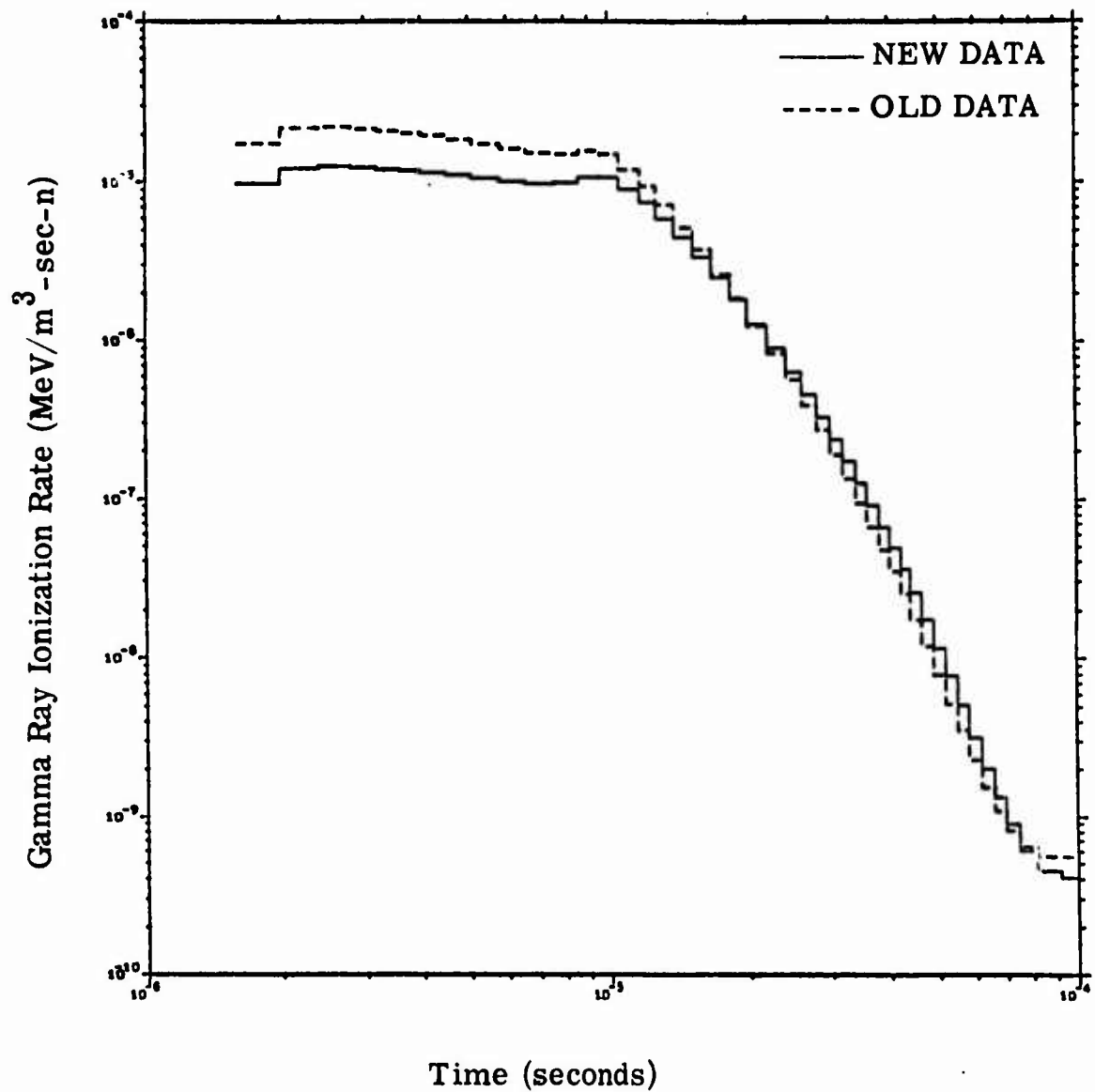


Figure 4. 3. Comparison of gamma ray ionization rate calculations using ENDF/B and older data at 480 meters.

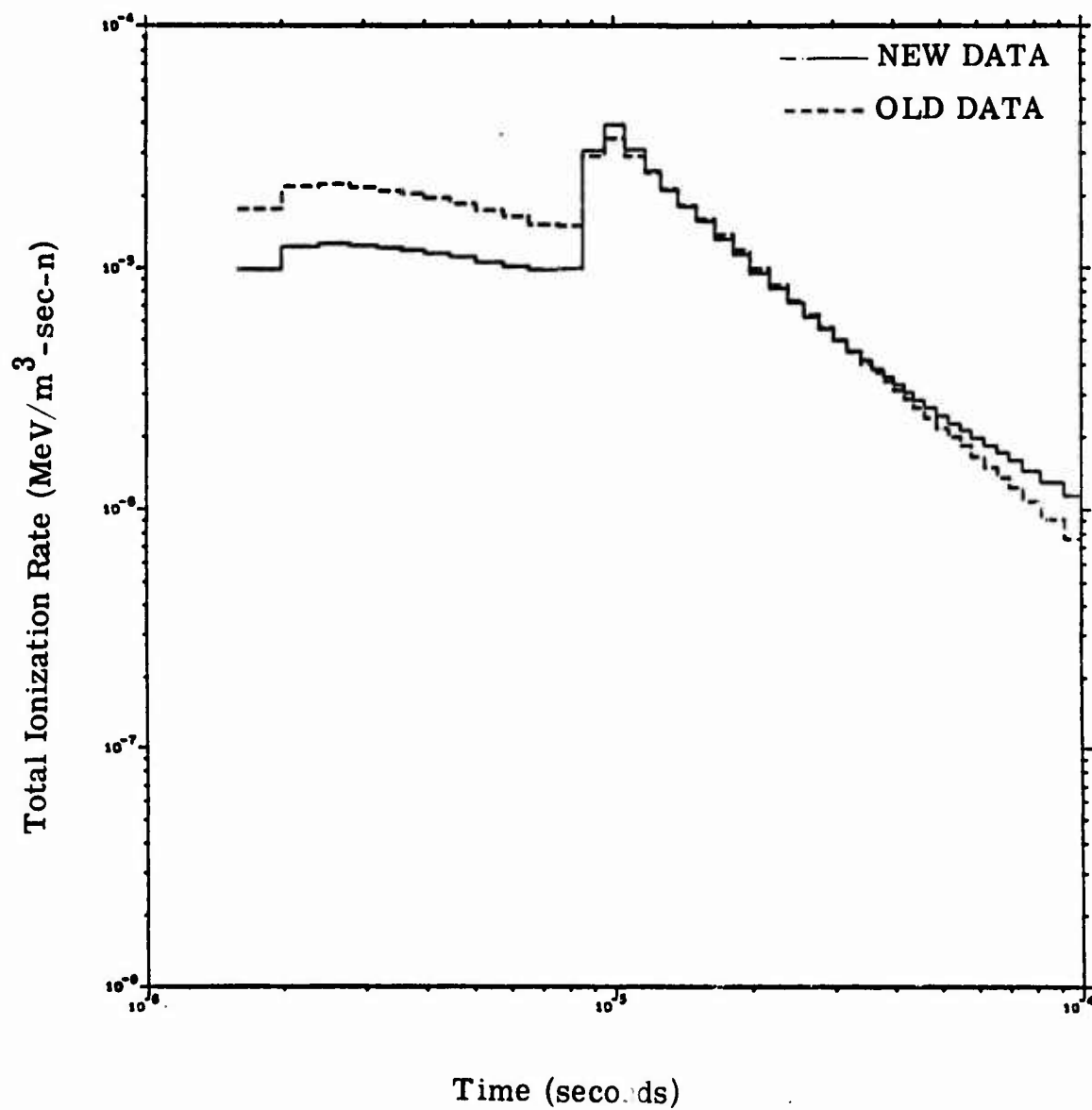


Figure 4. 4. Comparison of total ionization rate calculations using ENDF/B and older data at 480 meters.

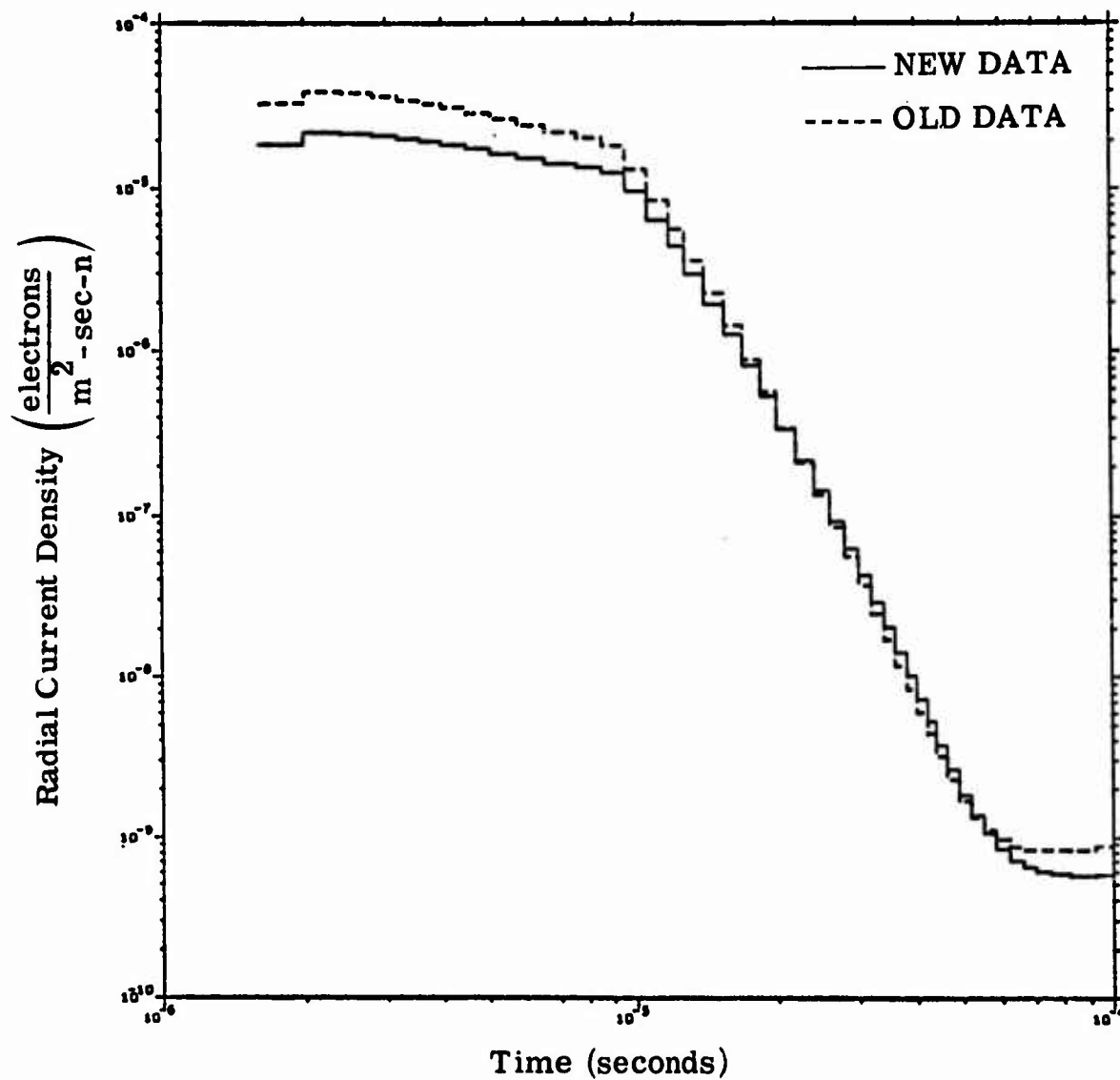


Figure 4. 5. Comparison of radial Compton current calculations using ENDF/B and older data at 480 meters.

Brief consideration of the effect of cross section changes on the EMP drivers in the ground was also made. The ground used in these studies was composed of hydrogen (16%), oxygen (57%), silicon (19%), and aluminum (8%). The new ENDF/B data for hydrogen should not differ from the data used in earlier EMP calculations. The oxygen data are considerably different and the TDA numerical calculations in air discussed above imply that factor of two maximum changes in ionization rates and compton currents may result with the new data. Differences in ground induced fields due to changes in oxygen data should be similar to those found in the infinite air calculations. The silicon and aluminum components of the ground have new ENDF/B neutron and gamma ray production cross section sets. In order to determine the effects of these cross section changes on EMP drivers, complicated and time consuming two-dimensional transport calculations would be required. Therefore, we decided to simply compare the old and new data for silicon to see if further transport calculations would be needed. The aluminum data were not compared in detail since Al is only an 8% constituent and should not affect the EMP drivers to any great extent.

For Si both the older EMP gamma production data and the new ENDF/B data are based on M.K. Drake's evaluation.<sup>(10)</sup> Therefore, gamma ray production data should not be altered with the new ENDF/B data. The new ENDF/B neutron data are also based on Drake's evaluation, whereas the EMP data were drawn from various sources. We have compared the total cross sections, as well as the total elastic and nonelastic cross sections for the two sets of data. It appears that differences between new ENDF/B neutron data and the EMP data are not large. For example, the total cross sections for the two sets generally

deviate from one another by  $\sim \pm 10\%$ . There are a few points where the disagreement is somewhat larger. The total elastic cross sections also seem to be within  $\sim 10\%$  of one another, while the nonelastic cross sections down to about 6 MeV are also in good agreement. Below 6 MeV there are larger discrepancies for the nonelastic cross sections.

In summary, it appears that the new ENDF/B and older EMP neutron and gamma ray production data are in good agreement for silicon. The  $\sim 10\%$  discrepancies between these data sets are relatively insignificant when compared to the deviations in the oxygen data sets. Therefore, it appears that a full transport calculation to accurately compute changes in EMP drivers due to changes in ground cross section data is not warranted at this time.



## 4. 6        INSTRUCTIONS FOR USING O5RNIES

### 4. 6. 1     O5RNIES Input Instructions

The input information required to run O5RNIES is discussed in this section. The subroutines which actually read the input data are also included to increase the user's familiarity with the O5RNIES code. Rather than explain in detail all of the possible options for O5R subroutines, the instructions herein describe the input as these subroutines are used in O5RNIES. The input subroutines used here include INPUT, INELIN, GATR, XINT, SOURCE, and SSTART. Input instructions for the auxiliary folding and plotting code O5NPT are presented in Section 4. 7. 1. In addition to the input cards, which are discussed in this section, tape units must be mounted for each run. These are discussed in Section 4. 6. 3.

The input cards for O5RNIES are as follows:

#### SUBROUTINE INPUT

CARD A: TITLE

FORMAT (20A4)

TITLE (dimensioned 20): Hollerith identification of the printed output.

CARD B: NSTRT, NMOST, NITS, NQUIT, EBOT, NTHRML, THPEED

FORMAT (4I5, E10.5, I5, E10.5)

NSTRT: The number of neutrons with which to start off each energy band.

NMOST: = NSTRT

NITS: = 1

NQUIT: = The number of batches to be run.

EBOT: The energy, in eV, below which neutrons are considered to be in the thermal group.

NTHRML: = 1, One-velocity thermal group

CARD C: MEDIA, NCONT1, NCONT2, NSTAPE

FORMAT (4I5)

MEDIA: = 2, The total number of media appearing in the system

NCONT1: = 3, The logical number of the system data tape (neutron collision cross section data).

NCONT2: = NCONT1

NSTAPE: = 0

A set of the cards whose descriptions follow D, E, and F must be furnished for each medium. They are to be loaded in the order:  $D_1$ ,  $E_1$ ,  $F_1$ ,  $D_2$ ,  $E_2$ ,  $F_2$ , with the media 1 (air), 2 (ground) in the same order as they are listed on the system data tape.

CARD D: (LF1 (LM, M), LM = 1, L), where M = media, and L = number of scatterers in media M

FORMAT (8I5)

LF1 = 0: Pick from isotropic scattering distribution  
 = N: Pick from the distribution function

$$f^*(\mu) = \sum_{K=0}^n \phi_K \delta(\nu_K - \mu)$$

and use the Nth scatterer appearing on the phi tape.

= +N: Pick from the anisotropic distribution  
 $P(\mu) = (1 + 3f_1 \mu)/2$  and use the Nth set of  $f_1$ 's on the system data tape.

CARD E: (ASSES (LM, M), LM = 1, L), where M and L are as defined above for Card D

FORMAT (7E10.5)

This card (or cards) carries the atomic masses, in amu, of each scatterer of a given medium. An inelastic scatterer is represented by a negative mass.

CARD F: SLOTH(M), SLOPS(M), SLOFS(M)

FORMAT (3E10.5)

SLOTH(M): The thermal mean free path for the medium M, in cm.

SLOPS(M): The thermal nonabsorption probability for the medium M.

SLOFS(M): 0.0

CARD G: ESOUR, UINP, VINP, WINP, WTSTRT

FORMAT (5E10.4)

ESOUR: = 0.)  
 UINP: = 0.)  
 VINP: = 0.)  
 WINP: = 0.)

Not used since subroutine SOURCE specifies initial neutron energy and direction.

WTSTRT: = 1., The statistical weight to be assigned to each source neutron.

CARD H: XSTRT, YSTRT, ZSTRT, NMED, NREG

FORMAT (3E10.4, 2I5)

XSTRT: = 0. }  
YSTRT: = 0. } The coordinates of the initial position  
ZSTRT: = 0. } of all neutrons

NMED: = 0

NREG: = 0

CARD I: DUMMY

FORMAT (O20)

DUMMY: The octal representation of the initial random multiplier. If equal to zero, the random number function starts with an initial random multiplier.

CARD J: NSPLT, NKILL, MXREG, MAXGP

FORMAT (4I5)

NSPLT: 0, no neutron splitting

NKILL: =1, neutrons subjected to Russian roulette  
(when thermal)

MAXREG: =1

MAXGP: The number of energy groups for the application of weight standards.

CARD K: (WTS (I), I = 2, MAXGP)

FORMAT (7E10.5)

WTS: Energy values, in eV, used to divide the energy range of the problem into groups for the application of weight standards. There will be a total of (MAXGP-1) values of WTS, listed in descending order. The first group weight standards then will apply to neutrons having energies greater than WTS(1). The second group of standards will apply to neutrons with energies between WTS(1) and WTS(2), and so on. The last group of weight standards will apply to all neutrons having energies below WTS(MAXGP-1). Card L is omitted if the number of energy groups is one or zero or if NSPLT and NKILL are both equal to zero.

CARD L:        NGP1, NDG, NGP2, NRG1, NDRG, NRG2, WTHIH1,  
                 WTLOW1, WTAVE1

FORMAT (I5, I5, I5, I5, I5, I5, E10.5, E10.5, E10.5)

- |           |   |   |
|-----------|---|---|
| a. NGP1   | } | These parameters designate particular groups and regions within which the weight standards given by g, h, and i, below, are to be applied. From energy group NGP1 to energy group NGP2, inclusive, in steps of NDG, and from region NRG1 to region NRG2, inclusive, in steps of NDRG the weight standards to be applied are the values given by g, h, and i. If NGP1 is set to zero, all groups will be given the weights specified by g, h, and i, and if NRG1 is set to zero all regions will be given the weights specified by g, h, and i. As many cards "M" as are required may be used. The end of the loading of all weight standards is signaled by a separate card "M" with NGP1 = -1. |
| b. NDG    |   |   |
| c. NGP2   |   |   |
| d. NRG1   |   |   |
| e. NDRG   |   |   |
| f. NRG2   |   |   |
| g. WTHIH: |   | Neutrons having weights above this value in the groups and regions indicated will be split.   |
| h. WTLOW: |   | Neutrons having weights below this value in the groups and regions indicated will be subjected to Russian roulette.   |
| i. WTAVE: |   | If a neutron is not killed by Russian roulette it will be assigned a new weight equal to WTAVE.   |

The operation of these parameters may be clarified by a glance at the following FORTRAN DO-loop:

```
DO 1 I = NGP1, NGP2, NDG
DO 1 J = NRG1, NRG2, NDRG
WTHIH(I,J) = WTHIH
WTLOW(I,J) = WTLOW
WTAVE(I,J) = WTAVE
1 CONTINUE
```

If neither splitting nor Russian roulette are permitted, card "M" is omitted.

CARD M: NSOUR, MFISTP

FORMAT (2I5)

NSOUR: = 0

MFISTP: = 0

CARD N: NPTAPE, NTYPE

FORMAT (2I5)

NPTAPE: = 4, The logical number of the phi tape

NTYPE: = 0

#### SUBROUTINE JOMIN

CARD As: MED, Z

FORMAT (I5, E10.5)

MED: Medium with lower bound of Z.

Z: Z-axis boundary value, in cm. The Z value on the MED = 0 card specifies the maximum Z value.

CARD B: Blank (no region geometry)

CARD C: XL, XU, YL, YU

FORMAT (4E10.5)

XL: Lower X boundary, in cm.

XU: Upper X boundary, in cm.

YL: Lower Y boundary, in cm.

YU: Upper Y boundary, in cm.

#### SUBROUTINE INELIN

In O5RNIES, , each scattering reaction that an element may undergo is counted as a separate "scatterer." Thus, for example, an element with 5 discrete levels, elastic scattering, continuum inelastic scattering, and an (n, 2n) reaction contributes 8 separate scatterers.

CARDS B through F, below, are required for each nonelastic scatterer (I).  
The order is  $B_1, \dots, G_1, B_2, \dots, G_2, \dots, B_{NINLS}, \dots, G_{NINLS}$ .

**CARD C:** (NMEDE (J, I), NELE (J, I), J = 1, NAPP (I))  
**FORMAT (4I5)**  
**NMEDE:** Medium that this scatterer is in  
**NELE:** Scatterer number in that medium

**CARD D:**        **Q(1, I)**  
                  **FORMAT (E10.4)**  
                  **Q:     Energy level of this scatterer (in CMCS).**

**CARD E:**        **None**

**CARD F:**        **None**

CARD G:       None

If NU = 1, then

CARD D:       ELAW (1, 1), NLAW (1, 1)  
              FORMAT (E10.4, 110)

This card describes the distribution for secondary neutrons.

ELAW: Energy threshold for this scatterer (in eV).

NLAW: Indicates distribution for secondary neutron.  
      Usually NLAW = 3 to indicate that sampling is  
      to be made from Maxwellian distribution.

If NLAW = 1

CARD E:       FM (1, 1), NENG (1), NAE (1)  
              FORMAT (E10.4, 2110)

FM:           Multiplicity for secondary emission. (Example:  
              FM = 1. for inelastic scattering; FM = 2. for  
              (n, 2n); FM = 3. for (n, 3n). )

NENG:         Number of energy groups for this scatterer.

NAE:         Index specifying array location where secondary  
              energy probability distributions are stored for  
              this scatterer.

There are NENG sets of F and G cards (one F card and as  
many G cards as necessary for each set).

CARD F:       ENG (K, NAE(I)), NETAB1 (K, NAE(I))  
              FORMAT (E10.4, 110)

ENG:         Upper energy boundary for following secondary  
              energy probability distribution, in eV.

NETAB1:       Number of secondary energy values for following  
              probability distribution.

CARD G:       (ETAB1 (L, K, NAE(I)), PTAB1 (L, K, NAE(I)), L = 1,  
              NETAB1)

ETAB1:       Secondary energy (eV)

PTAB1:       Cumulative probabilities.



If NLAW = 3

CARD E: FM (I, I)

FORMAT (E10.4)

FM: Multiplicity for secondary emission.

CARD F: TA (I), TB (I), TC (I)

FORMAT (3E10.4)

Nuclear temperature (MeV) for Maxwellian is expressed as  $T = TA + TB * \sqrt{E} + TC * E$ , where E is the incident neutron energy (eV).

#### SUBROUTINE GATR

DO 55 I = 1, 2

READ (5, 1) (A(J, I), J = 1, 11)

READ (5, 1) (B(J, I), J = 1, 11)

READ (5, 1) (AA(J, I), J = 1, 11)

READ (5, 1) (BB(J, I), J = 1, 11)

1 FORMAT (6E12.5)

55 CONTINUE

A and B are the coefficients for the buildup factor for energy deposition.

AA and BB are the coefficients for the buildup factor for current.

I = 1 is air

I = 2 is ground

The energy group boundaries for the above data are set in the data statements in GATR (arrays EA and EG). For further details see Section 4.3.4.

## SUBROUTINE XINIT

CARD A: TIMMAX, EPICUT, RREPI, RRTHM

FORMAT (4E10.5)

TIMMAX: The maximum time limit after which neutrons are no longer followed, in sec

EPICUT: Upper limit of epithermal range, in eV.

RREPI: Probability specifying how often a gamma particle will be produced while tracking epithermal neutrons.

RRTHM: Probability specifying how often a gamma particle will be produced while tracking thermal neutrons.

CARD B: NXTAP, NHIS

FORMAT (2I6)

NXTAP: = 14, Gamma production,  $\bar{Q}$ , and  $\Delta E$  data file

NHIS: Number of neutron histories per energy band

CARD C: NTIMA, NRADA, NCOSA, NZMA, IWANT

FORMAT (5I6)

NTIMA: Number of time bins

NRADA: Number of radial bins

NCOSA: Number of angular bins

NZMA: Number of horizontal bins

IWANT: = 1, Energy is not deposited for first neutron collision  
= 0, Normal condition  
> 1, Computes energy deposition from first neutron collision only.

CARD D: (TIMC (I), I = 1, NTIMA + 1)

FORMAT (6E12.5)

As many card D's as necessary

TIMC: Time bin boundaries in increasing value, in microsecs.

**CARD E:** (RADC (I), I = 1, NRADA + 1)  
 FORMAT (6E12.5)  
 As many card E's as necessary  
 RADC: Radial bin boundaries in increasing value, in meters.

**CARD F:** (ZADC (I), I = 1, NZMA + 1)  
 FORMAT (6E12.5)  
 As many card F's as necessary  
 ZADC: Horizontal bin boundaries in increasing value, in cm. The ground-air interface has value 0.0.

**CARD G:** (ANGC (I), I = 1, NCOSA + 1)  
 FORMAT (6E12.5)  
 As many card G's as necessary  
 ANGC: Angular bin boundaries ( $\cos \theta$ ) in increasing value, with 0 being horizontal to the ground and 1.0 in a vertical direction.

**CARD H:** NPHOT, WTLIM, A, NTHERM  
 FORMAT (I12, 2E12.5, I12)  
 NPHOT: Number of photons produced at each photon producing collision by high energy neutrons.  
 WTLIM: Weight below which Russian roulette is played in ROUTIN to determine if photon is followed.  
 A: Height (cm) of the neutron source above the ground.  
 NTHERM: Number of capture  $\gamma$ 's produced for each thermal neutron at its history termination.

## SUBROUTINE SOURCE

CARD A: NEB

FORMAT (I5)

NEB: Number of energy groups

CARD B: (E (I), I = 1, NEB +1)

FORMAT (7E10. 4)

As many card B's as necessary

E: Energy group boundaries, in MeV, in decreasing magnitude

CARD C: NUMA

FORMAT (I5)

NUMA: Number of source angular distribution bins

CARD D: (RMU (I), I = 1, NUMA +1)

FORMAT (7E10. 4)

As many card D's as necessary

RMU: Angular bin boundaries ( $\cos \theta$ ), in increasing numerical order. RMU (1) = -1.0 (straight down) and RMU (NUMA + 1) = 1.0 (straight up)

CARD E: (ASTAR (I), I = 1, NUMA)

FORMAT (7E10. 4)

As many card E's as necessary.

ASTAR: The biased source intensities for the angular bins. The assumed true source angular distribution is isotropic.

# **SUBROUTINE SSTART**

**CARD A:      IRESLT, NRPT, NEBC, NBAC, IDR**

**FORMAT (5I5)**

**IRESLT:    O5RNIES results tape. .**

**NRPT:      Number of batches per results tape reel.**

**NEBC:      Number of energy groups completed for batch  
            presently working on.**

**NBAC:      Number of batches already completed.**

**IDR:        Run identification number.**

Typical input information for an O5RNIES production run is shown in Table 7. Some of the information comes from external data files.

### TYPICAL INPUT FOR AN O5RNIES PRODUCTION RUN

215

Table 7 (Continued)

H08=000M

H08=000M

2 = 250.  
 1 = 0.  
 0 5000.E2

-5000.E2 5000.F2 -5000.E2 5000.E2  
 INELASTIC INPUT = ENDF/B CROSS SECTION DATA = 2/72  
 NITROGEN (N,2N) 0 1 1

115

1.13130E7	1		
2.	5	1	
1.1406E7	2		
6.25000+04	5.00000-01	1.87500+05	1.00000+00
1.1750E7	3		
6.25000+04	2.37159-01	1.87500+05	7.11539-01 3.26000+05 1.00000+00
1.3000E7	6		
6.25000+04	1.00691-01	1.87500+05	3.38073-01 3.26000+05 6.15861-01
5.13500+05	8.67301-01	7.50000+05	9.87680-01 9.45000+05 1.00000+00
1.5000E7	15		
6.25000+04	1.52501-02	1.87500+05	5.10004-02 3.26000+05 1.06937-01
5.13500+05	2.05322-01	7.50000+05	3.29393-01 9.45000+05 4.02474-01
1.19500+06	5.89675-01	1.50000+06	7.10928-01 1.75000+06 8.12302-01
2.00000+06	8.88427-01	2.25000+06	9.43053-01 2.50000+06 9.77178-01
2.75000+06	9.94553-01	3.00000+06	9.94928-01 3.14900+06 1.00000+00
1.7000E7	24		
6.25000+04	6.62473-03	1.87500+05	2.25616-02 3.26000+05 4.77166-02
5.13500+05	9.27607-02	7.50000+05	1.52303-01 9.45000+05 1.88922-01
1.19500+06	2.89538-01	1.50000+06	3.63785-01 1.75000+06 4.39782-01
2.00000+06	5.16279-01	2.25000+06	5.92026-01 2.50000+06 6.65648-01
2.75000+06	7.35020-01	3.00000+06	7.97392-01 3.14900+06 8.08432-01
3.39900+06	8.95890-01	3.75000+06	9.31389-01 4.00000+06 9.58388-01
4.25000+06	9.77762-01	4.50000+06	9.90386-01 4.75000+06 9.97386-01
5.00000+06	9.99886-01	5.18200+06	1.00000+00
1ST LEVEL NITROGEN	1	0	1
1 4			
2.283E6			
2ND LEVEL NITROGEN	1	0	1
1 5			
3.917E6			
3RD LEVEL NITROGEN	1	0	1
1 6			
4.848E6			
4TH LEVEL NITROGEN	1	0	1
1 7			
5.059E6			
5TH LEVEL NITROGEN	1	0	1
1 8			
5.621E6			
6TH LEVEL NITROGEN	1	0	1
1 9			
5.796E6			
7TH LEVEL NITROGEN	1	0	1
1 10			
6.148E6			
8TH LEVEL NITROGEN	1	0	1
1 11			
6.394E6			
9TH LEVEL NITROGEN	1	0	1
1 12			
6.991E6			

Table 7 (Continued)

10TH LEVEL NITROGEN	1	0	1
1 13			
7.904F6			
11TH LEVEL NITROGEN	1	0	1
1 14			
8.010E6			
12TH LEVEL NITROGEN	1	0	1
1 15			
8.431E6			
13TH LEVEL NITROGEN	1	0	1
1 16			
8.712E6			
14TH LEVEL NITROGEN	1	0	1
1 17			
9.134F6			
15TH LEVEL NITROGEN	1	0	1
1 18			
9.626E6			
16TH LEVEL NITROGEN	1	0	1
1 19			
10.118E6			
17TH LEVEL NITROGEN	1	0	1
1 20			
10.680F6			
18TH LEVEL NITROGEN	1	0	1
1 21			
11.172E6			
19TH LEVEL NITROGEN	1	0	1
1 22			
11.663E6			
20TH LEVEL NITROGEN	1	0	1
1 23			
12.155F6			
21ST LEVEL NITROGEN	1	0	1
1 24			
12.647E6			
22TH LEVEL NITROGEN	1	0	1
1 25			
13.139E6			
23TH LEVEL NITROGEN	1	0	1
1 26			
13.631F6			
24TH LEVEL NITROGEN	1	0	1
1 27			
14.123E6			
25TH LEVEL NITROGEN	1	0	1
1 28			
14.615E6			
26TH LEVEL NITROGEN	1	0	1
1 29			
15.177E6			
1ST LEVEL OXYGEN	1	0	2
1 30 2 5			
5.987E6			
2ND LEVEL OXYGEN	1	0	2
1 31 2 6			
6.093E6			
3RD LEVEL OXYGEN	1	0	2
1 32 2 7			



Table 7 (Continued)

6.873E6					
4TH LEVEL OXYGEN	1	0	2		
1 33 2 8					
7.050E6					
5TH LEVEL OXYGEN	1	0	2		
1 34 2 9					
8.821E6					
6TH LEVEL OXYGEN	1	0	2		
1 37 2 10					
9.494E6					
7TH LEVEL OXYGEN	1	0	2		
1 38 2 11					
9.707E6					
8TH LEVEL OXYGEN	1	0	2		
1 39 2 12					
10.274E6					
9TH LEVEL OXYGEN	1	0	2		
1 35 2 13					
10.841E6					
10TH LEVEL OXYGEN	1	0	2		
1 36 2 14					
10.983E6					
11TH LEVEL OXYGEN	1	0	2		
1 40 2 15					
10.983E6					
12TH LEVEL OXYGEN	1	0	2		
1 41 2 16					
11.118E6					
13TH LEVEL OXYGEN	1	0	2		
1 42 2 17					
11.337E6					
14TH LEVEL OXYGEN	1	0	2		
1 43 2 18					
11.407E6					
15TH LEVEL OXYGEN	1	0	2		
1 44 2 19					
11.549E6					
16TH LEVEL OXYGEN	1	0	2		
1 45 2 20					
11.974E6					
17TH LEVEL OXYGEN	1	0	2		
1 54 2 21					
12.329E6					
18TH LEVEL OXYGEN	1	0	2		
1 46 2 22					
12.400E6					
19TH LEVEL OXYGEN	1	0	2		
1 47 2 23					
12.683E6					
20TH LEVEL OXYGEN	1	0	2		
1 48 2 24					
12.896E6					
21ST LEVEL OXYGEN	1	0	2		
1 55 2 25					
13.037E6					
22ND LEVEL OXYGEN	1	0	2		
1 49 2 26					
13.321E6					
23RD LEVEL OXYGEN	1	0	2		
1 50 2 27					

Table 7 (Continued)

13.675E6						
24TH LEVEL OXYGEN	1	0	2			
1 56 2 28						
13.95AE6						
25TH LEVEL OXYGEN	1	0	2			
1 51 2 29						
14.242E6						
26TH LEVEL OXYGEN	1	0	2			
1 57 2 30						
14.575E6						
27TH LEVEL OXYGEN	1	0	2			
1 52 2 31						
14.809E6						
28TH LEVEL OXYGEN	1	0	2			
1 53 2 32						
15.163E6						
ALUMINUM (N+2N)	0	1	1			
2 33						
1.35450E7	1					
2. 4 2						
1.3772E7	2					
5.00000+04 5.00000-01 1.50000+05 1.00000+00						
1.4500E7 4						
5.00000+04 1.65200-01 1.50000+05 5.02000-01 2.50000+05 8.36800-01						
3.50000+05 1.00000+00						
1.5500E7 14						
5.00000+04 3.24500-02 1.50000+05 1.03750-01 2.50000+05 1.85150-01						
3.50000+05 2.73150-01 4.50000+05 5.63800-01 5.50000+05 4.53600-01						
6.50000+05 5.41800-01 7.50000+05 6.27150-01 8.50000+05 7.08100-01						
9.50000+05 7.83300-01 1.05000+06 8.52850-01 1.15000+06 9.16550-01						
1.25000+06 9.73350-01 1.35000+06 1.00000+00						
1.6500E7 23						
5.00000+04 1.53500-02 1.50000+05 5.02000-02 2.50000+05 9.22500-02						
3.50000+05 1.39650-01 4.50000+05 1.90250-01 5.50000+05 2.42650-01						
6.50000+05 2.96700-01 7.50000+05 3.52000-01 8.50000+05 4.08050-01						
9.50000+05 4.64350-01 1.05000+06 5.20350-01 1.15000+06 5.75350-01						
1.25000+06 6.29050-01 1.35000+06 6.81300-01 1.45000+06 7.31550-01						
1.55000+06 7.79250-01 1.65000+06 8.23900-01 1.75000+06 8.64900-01						
1.85000+06 9.01600-01 1.95000+06 9.34250-01 2.05000+06 9.63300-01						
2.15000+06 9.88450-01 2.25000+06 1.00000+00						
1ST LEVEL ALUMINUM	1	0	1			
2 34						
.835E6						
2ND LEVEL ALUMINUM	1	0	1			
2 35						
1.007E6						
3RD LEVEL ALUMINUM	1	0	1			
2 36						
2.196E6						
4TH LEVEL ALUMINUM	1	0	1			
2 37						
2.704E6						
5TH LEVEL ALUMINUM	1	0	1			
2 38						
2.958E6						
6TH LEVEL ALUMINUM	1	0	1			
2 39						
2.977E6						

Table 7 (Continued)

7TH LEVEL ALUMINUM	1	0	1
2 40			
3.648E6			
8TH LEVEL ALUMINUM	1	0	1
2 41			
3.920E6			
9TH LEVEL ALUMINUM	1	0	1
2 42			
4.029E6			
10TH LEVEL ALUMINUM	1	0	1
2 43			
4.374E6			
11TH LEVEL ALUMINUM	1	0	1
2 44			
4.483E6			
12TH LEVEL ALUMINUM	1	0	1
2 45			
4.556E6			
13TH LEVEL ALUMINUM	1	0	1
2 46			
4.756E6			
14TH LEVEL ALUMINUM	1	0	1
2 47			
5.191E6			
15TH LEVEL ALUMINUM	1	0	1
2 48			
5.699E6			
16TH LEVEL ALUMINUM	1	0	1
2 49			
6.208E6			
17TH LEVEL ALUMINUM	1	0	1
2 50			
6.680E6			
18TH LEVEL ALUMINUM	1	0	1
2 51			
7.188E6			
19TH LEVEL ALUMINUM	1	0	1
2 52			
7.696E6			
20TH LEVEL ALUMINUM	1	0	1
2 53			
8.205E6			
21ST LEVEL ALUMINUM	1	0	1
2 54			
8.713E6			
22ND LEVEL ALUMINUM	1	0	1
2 55			
9.185E6			
23RD LEVEL ALUMINUM	1	0	1
2 56			
9.656E6			
24TH LEVEL ALUMINUM	1	0	1
2 57			
10.165E6			
25TH LEVEL ALUMINUM	1	0	1
2 58			
10.673E6			
26TH LEVEL ALUMINUM	1	0	1
2 59			

Table 7 (Continued)

11.109E6 27TH LEVEL ALUMINUM 2 60	1	0	1
11.617E6 28TH LEVEL ALUMINUM 2 61	1	0	1
12.125E6 29TH LEVEL ALUMINUM 2 62	1	0	1
12.634E6 30TH LEVEL ALUMINUM 2 63	1	0	1
13.142E6 31TH LEVEL ALUMINUM 2 64	1	0	1
13.650E6 32TH LEVEL ALUMINUM 2 65	1	0	1
14.159E6 33TH LEVEL ALUMINUM 2 66	1	0	1
14.667E6 34TH LEVEL ALUMINUM 2 67	1	0	1
15.175E6 35TH LEVEL ALUMINUM 2 68	1	0	1
15.611E6 SILICON (N,2N) 2 69	0	1	1
16.700E6 2. -0.69227E5 .21560E3-.42488E-2 SILICON (N,NPRIME)P 2 70	0	1	1
1.2000E7 1. -0.23807E6 .29357E3-.13242E-1 1ST LEVEL SILICON 2 71	1	0	1
1.254E6 2ND LEVEL SILICON 2 72	1	0	1
1.763E6 3RD LEVEL SILICON 2 73	1	0	1
2.017E6 4TH LEVEL SILICON 2 74	1	0	1
2.217E6 5TH LEVEL SILICON 2 75	1	0	1
2.399E6 6TH LEVEL SILICON 2 76	1	0	1
3.035E6 7TH LEVEL SILICON 2 77	1	0	1
3.362E6			

Table 7 (Continued)

8TH LEVEL SILICON	1	0	1
2 78			
3.599E6			
9TH LEVEL SILICON	1	0	1
2 79			
3.726E6			
10TH LEVEL SILICON	1	0	1
2 80			
3.744E6			
11TH LEVEL SILICON	1	0	1
2 81			
4.580E6			
12TH LEVEL SILICON	1	0	1
2 82			
4.908E6			
13TH LEVEL SILICON	1	0	1
2 83			
6.217E6			
14TH LEVEL SILICON	1	0	1
2 84			
6.453E6			
15TH LEVEL SILICON	1	0	1
2 85			
6.835E6			
16TH LEVEL SILICON	1	0	1
2 86			
6.835E6			
17TH LEVEL SILICON	1	0	1
2 87			
7.344E6			
18TH LEVEL SILICON	1	0	1
2 88			

7.344E6			
19TH LEVEL SILICON	1	0	1
2 89			
7.743E6			
20TH LEVEL SILICON	1	0	1
2 90			
7.889E6			
21ST LEVEL SILICON	1	0	1
2 91			
8.216E6			
CONTINUUM SILICON	0	1	1
2 92			

4.0000E6 3

23272F3	.17802F3	.68193E-3			
.38415	1.08346	.8645	.7048	.58017	.517
.4544	.41	.36615	.34	.31348	
.68507	.15638	.02877	.00605	1.382 -03-	.0012
- 3.7702-03-	4.04	-03- 4.3134-03-	4.32 -03-	4.330-03	
.734	.499	.462	.399	.384	.369 AA 1
.355	.340	.326	.326	.326	AA 2
.0431	.0365	.00881	.00638	.004	.0016 BA 1
-8.84 -04	-2.07	-03 -0.00236	-0.00236	-0.00236	882
.38415	1.08346	.8645	.7048	.58017	.517
.4544	.41	.36615	.34	.31348	
.68507	.15638	.02877	.00605	1.382 -03-	.0012
- 3.7702-03-	4.04	-03- 4.3134-03-	4.32 -03-	4.330-03	

Table 7 (Continued)

.734	.499	.462	.399	.384	.369	AA 1
.355	.340	.326	.326	.326		AA 2
.0431	.0365	.00881	.00638	.004	.0016	HB 1
-8.84 -04	-2.07 -03	-.00236	-.00236	-.00236		BB2
1.0	.111E6	.1	.1			
14 1000						
39 19	5 9	0				
.000	.015	.020	.030	.040		HOB=000M
.080	.100	.140	.200	.300		.060HOB=000M
.600	.800	1.00	2.00	3.00		.400HOB=000M
5.00	7.50	10.0	20.0	30.0		4.00HOB=000M
75.0	100.	200.	300.	500.		50.0HOB=000M
1500.	3000.	6000.	1.E4	3.E4		1000.HOB=000M
1.E5	3.E5	6.E5	1.E6			6.E4HOB=000M
00.0	150.	250.	350.	450.		HOB=000M
650.	850.	1050.	1300.	1500.		550.HOB=000M
1900.	2100.	2300.	2700.	3100.		1700.HOB=000M
4000.	5000.					3500.HOB=000M
-250.	-180.	-120.	-90.	-50.		HOB=000M
-14.	-6.0	-2.0	0.00			-30.HOB=000M
.0	.05	.10	.20	.50		HOB=000M
20	1.E-10	0.0	10			1.0HOB=000M
						HOB=000M
13						
16.5	15.0	13.5	9.05	4.96	2.35	1.10
.55	.24	.11	.0316	.0193	.00336	.000023
6						
-1.0	0.00	.05	.10	.20	.50	1.0
5.0	1.0	1.0	1.0	1.0	1.0	
16 3	0 12	0				

HOB=000M  
HOB=000M  
HOB=000M  
HOB=000M

\*\*

#### 4. 6. 2    O5RNIES Output

During each run a small amount of printed output of a general nature is produced. In addition, detailed ionization rate and Compton current information is tabulated and plotted on microfilm. The information printed during each run is used to indicate how well certain input parameters and biasing techniques were chosen. Restart information is also printed to enable the user to restart calculations which were aborted for any reason.

Figure 4. 6 shows the normal output produced by O5RNIES. The tracking part of the output consists of the total weight and the weighted average position for all neutrons in a given energy band, along with the last random multiplier, after all neutrons have become thermal, and all neutron histories have been terminated. Also, the computer time required for non-thermal and thermal tracking and subsequent energy deposition is noted. At the end of each energy band the integer (ICOUNT) and floating point (PCOUNT) counter values are printed. At the end of a batch the counter values summed over all energy bands in that batch are printed as KCOUNT and ZCOUNT arrays with the floating point counters being normalized.

The KCOUNT array is used to record the number of particles produced, and number of neutrons whose histories are terminated in specific ways, and the number of collisions of a given type. The ZCOUNT array records total energy deposited by neutrons and gammas, the weight and weighted energies of neutrons and gamma rays and various other important integral quantities.

Definitions of the quantities contained in the KCOUNT and ZCOUNT arrays are listed in Tables 8 and 9.

<b>BAND 11</b>									
<b>BATCH 15</b>									
WEIGHT	X AVERAGE	Y AVERAGE	Z AVERAGE	RANDOM	MEM				
0.0000000E+00	0.0000000E+00	0.0000000E+00	0.0000000E+00	2000165712137030731	1000				
0.0000000E+00	0.0000000E+00	0.0000000E+00	0.0000000E+00	2000070633470707743	1000				
NON THERMAL TRACKING TOOK 87.9926 SECS.									
1.0000000E+15	0.0000000E+00	0.0000000E+00	0.0000000E+00	20001760602355202463	1000				
THERMAL TRACKING TOOK 180.7460 SECS.									
ENERGY BAND NO. 11 BATCH NO. 15									
ICOUNT									
1000	0 5159 7610 0 303	0 11243 0 1876	0 2799 0 9007	1091 21998	18128	0			
PCOUNT	38 582 607 906	613 0 0.000	0.000 0.000	0 0 0	0	0			
0.0000000E+00	0.28772E+03 0.000	0.000 0.000	0.000 0.000	0.98250E+03 0.25102E+02	0.19351E+04	0.43158E+02			
0.19522E+04 0.000	0.000 0.000	0.000 0.000	0.000 0.000	0.33866E+02 0.22943E+03	0.17351E+04	0.46640E+03			
0.02322E+02 0.16681E+02 0.000	0.000 0.000	0.000 0.000	0.000 0.000	0.000 0.000	0.000	0.000			
<b>BAND 12</b>									
<b>BATCH 15</b>									
WEIGHT	X AVERAGE	Y AVERAGE	Z AVERAGE	RANDOM	MEM				
0.0000000E+00	0.0000000E+00	0.0000000E+00	0.0000000E+00	20005073364373645423	1000				
0.0000000E+00	0.0000000E+00	0.0000000E+00	0.0000000E+00	20000715315355421751	1000				
NON THERMAL TRACKING TOOK 63.6660 SECS.									
1.0000000E+15	0.0000000E+00	0.0000000E+00	0.0000000E+00	20004560043366731161	1000				
THERMAL TRACKING TOOK 190.8270 SECS.									
ENERGY BAND NO. 12 BATCH NO. 15									
ICOUNT									
1000	0 4812 6896 0 285	0 12125 0 1785	0 2462 0 9535	1085 22232	17516	0			
PCOUNT	23 559 715 911	590 0 0.000	0.000 0.000	0 0 0	0	0			
0.0000000E+00	0.27859E+03 0.000	0.000 0.000	0.000 0.000	0.98700E+03 0.11520E+02	0.19771E+04	0.42158E+02			
0.19967E+04 0.000	0.000 0.000	0.000 0.000	0.000 0.000	0.59792E+02 0.25491E+03	0.17756E+04	0.46640E+03			
0.55871E+02 0.74727E+01 0.000	0.000 0.000	0.000 0.000	0.000 0.000	0.000 0.000	0.000	0.000			
<b>BAND 13</b>									
<b>BATCH 15</b>									
WEIGHT	X AVERAGE	Y AVERAGE	Z AVERAGE	RANDOM	MEM				
0.0000000E+00	0.0000000E+00	0.0000000E+00	0.0000000E+00	20004784740574575471	1000				
0.0000000E+00	0.0000000E+00	0.0000000E+00	0.0000000E+00	20000616123761211223	1000				
NON THERMAL TRACKING TOOK 52.2550 SECS.									
1.0000000E+15	0.0000000E+00	0.0000000E+00	0.0000000E+00	20001410234155362441	1000				
THERMAL TRACKING TOOK 190.6080 SECS.									
ENERGY BAND NO. 13 BATCH NO. 15									
ICOUNT									
1000	0 5124 5977 0 269	0 12419 0 1465	0 1665 0 9232	884 20998	15053	0			
PCOUNT	53 525 731 881	544 0 0.000	0.000 0.000	0 0 0	0	0			
0.0000000E+00	0.27355E+03 0.000	0.000 0.000	0.000 0.000	0.98675E+03 0.16292E+01	0.19645E+04	0.40101E+02			
0.19509E+04 0.000	0.000 0.000	0.000 0.000	0.000 0.000	0.31532E+02 0.20998E+03	0.17524E+04	0.47714E+03			
0.41023E+02 0.11997E+01 0.000	0.000 0.000	0.000 0.000	0.000 0.000	0.000 0.000	0.000	0.000			
13900 23 47571 120077 0 4318	274 1152	0 16 118303	26514 212728	266318 476063					
4863 414 11410 8662 14930 9672	6114 103753	13935 33900	0 0	0 0					
<b>Totals</b>									
<b>BATCH 15</b>									
0.49627E-12	0.27065E+00	0.25792E+01	0.87305E+00	0.42436E+00					
0.17229E+01 0.000	0.13680E+01	0.44209E+00	0.000 0.000	0.42708E+01	0.17127E+01	0.51393E+01			
0.98059E-01 0.45056E-01 0.000	0.000 0.000	0.000 0.000	0.000 0.000	0.23158E+00	0.15623E+01	0.50873E+01			

Figure 4.6. Typical O5RNIES output.



Table 8  
KCOUNT Array

Number	Set in Routine	Quantity
1	BANKR	Number of source neutrons
2	BANKR	Number of neutrons escaping from system
3	BANKR	Number of boundary crossings
4	DOSEN	Number of collisions in the ground analyzed by DOSEN
5	BANKR	Number of neutrons whose local time exceeds TMAX
6	O5RNIES	Number of neutrons reaching thermal in air
7	DOSEN	Number of oxygen inelastic collisions in the air analyzed
8	DOSEN	Number of nitrogen inelastic collisions in the air analyzed
9	DOSEN	Number of continuum (n, n <sup>1</sup> ) nitrogen collisions in the air analyzed
10	DOSEN	Number of (n, 2n) nitrogen collisions in the air analyzed
11	DOSEN	Number of elastic nitrogen collisions in the air analyzed
12	DOSEN	Number of elastic oxygen collisions in the air analyzed
13	GATR	Total number of gammas produced by epithermal and thermal neutron reactions
14	NIES	Number of collisions analyzed
15	ROUTIN	Number of inelastic gammas produced
16	BANKR	Number of neutrons killed in O5R by Russian Roulette

Table 8 (Continued)

Number	Set in Routine	Quantity
17	BANKR	Number of neutrons surviving Russian Roulette in O5R
18	GATR	Number of gammas followed by GATR for neutrons terminated by RDIFF
19	O5RNIES	Number of neutrons reaching thermal in ground
20	GATR	Total number of gammas followed by GATR
21	BANKR	Number of neutrons taken to thermal energy analytically
22	BANKR	Number of neutrons terminated by analytic techniques in RDIFF
23	BANKR	Number of gammas generated by thermal neutrons
24	BANKR	Number of epithermal collisions (also number of non-analytic epithermal gammas)
25	BANKR	Number of gammas produced by analytic epithermal neutron reactions
26 thru 30		Not used

KCOUNTChecks

$$\text{KCOUNT (1)} = \text{KCOUNT (2 + 5 + 16 + 22)}$$

$$\text{KCOUNT (14)} = \text{KCOUNT (4 + 7 + 8 + 9 + 10 + 11 + 12)}$$

$$\text{KCOUNT (1)} \cong \text{KCOUNT (6 + 19)}$$

$$\text{KCOUNT (13)} = \text{KCOUNT (24 + 25)} + \text{KCOUNT (23)} + \text{N THERM} * \text{KCOUNT (22)}$$

NOTE: For conciseness,  $\text{KCOUNT (6 + 19)} = \text{KCOUNT (6)} + \text{KCOUNT (19)}$ , etc.

Table 9  
ZCOUNT Array

Number	Set in Routine	Quantity
1	BANKR DOSEN	Energy of neutrons outside spatial bins
2	DEP	Energy deposited by thermal neutron reactions
3	DOSEN	Energy deposited by fast neutron reactions, $E > E_c$
4	CHARGE	Energy deposited by gammas produced by fast neutron reactions, $E > E_c$
5	ROUTIN	Weight of inelastic gammas
6	ROUTIN	Energy of inelastic gammas
7	BANKR	Weight of source neutrons
8	BANKR	Energy of source neutrons
9	CHARGE GATR	Energy deposited by gammas produced by thermal neutron reactions, $E < E_t$
10	GATR	Energy of gammas created by epithermal neutrons, $E_c \leq E \leq E_t$
11	GATR	Energy of gammas created by thermal neutrons, $E_t \leq E$
12	DEP	Part of 2 deposited in the ground
13	DOSEN	Part of 3 deposited in the ground
14	CHARGE	Part of 4 deposited in the ground
15	BANKR	Energy of neutrons whose elapsed local times exceed TMAX
16	CHARGE	Energy deposited by gammas produced by epithermal neutron reactions, $E_c \leq E \leq E_t$
17	CHARGE	Part of 16 deposited in ground

Table 9 (Continued)

Number	Set in Routine	Quantity
18	O5RNIES	Weight of neutrons in air which reach thermal energies
19	CHARGE GATR	Part of 9 deposited in ground
20	O5RNIES	Weight of neutrons in ground which reach thermal energies
21	DOSEN	Energy deposited by epithermal neutron reactions
22	DOSEN	Part of 21 deposited in ground
23 thru 30		Not used

ZCOUNTChecksZCOUNT (7)  $\approx 1$ .ZCOUNT (8)/ZCOUNT (7)  $\approx$  expected energy of source neutronsZCOUNT (4)  $\approx$  ZCOUNT (6)ZCOUNT (9)  $\approx$  ZCOUNT (11)  $\approx .04 * 10.67 * \text{ZCOUNT (18)} + 4.923 * \text{ZCOUNT (20)}$ ZCOUNT (16)  $\approx$  ZCOUNT (10)ZCOUNT (2)  $\approx .624 * \text{ZCOUNT (18)} * .96$ 

ZCOUNT (12) = 0.

ZCOUNT (3) + ZCOUNT (6)  $\approx$  ZCOUNT (8)

### 4. 6. 3 Structure of the O5RNIES Code

#### 4. 6. 3. 1 Flowcharts

Figures 4. 7 - 4. 25 show flowcharts of the various subroutines in the analysis section of O5RNIES. Most subroutines in the O5R section are not included, as they have been documented elsewhere. <sup>(12)</sup> However, a few O5R subroutines either are not included in Reference 12 or have been substantially modified, and we include flowcharts for these. Among these are BANKR, SOURCE, KINNY, and INELIN.

Figure 4. 7 shows a block diagram of what we refer to as the O5R section of O5RNIES. This section of the program generates the neutron histories. Figure 4. 8 shows a block diagram of the analysis section of O5RNIES; it performs the analysis of the neutron histories. Although it is not shown, several of the routines in the O5R section are also used by the analysis section. For example, CHARGE which performs a complete gamma ray transport calculation calls the subroutine GTISO, which is also called by several routines in the O5R section. The remaining pages of this subsection contain flowcharts of the individual analysis subroutines and selected O5R subroutines. Each subroutine flowchart is accompanied by descriptive material about the subroutine.

Except for BANKR, the O5R subroutines are almost identical to those described in Reference 12. We have made some minor changes in some of the routines, however. These routines are:

RWCON	-	Same as before, except it now rewinds NXTAP and sets the initial values of ETOPI and EBOTI.
-------	---	---

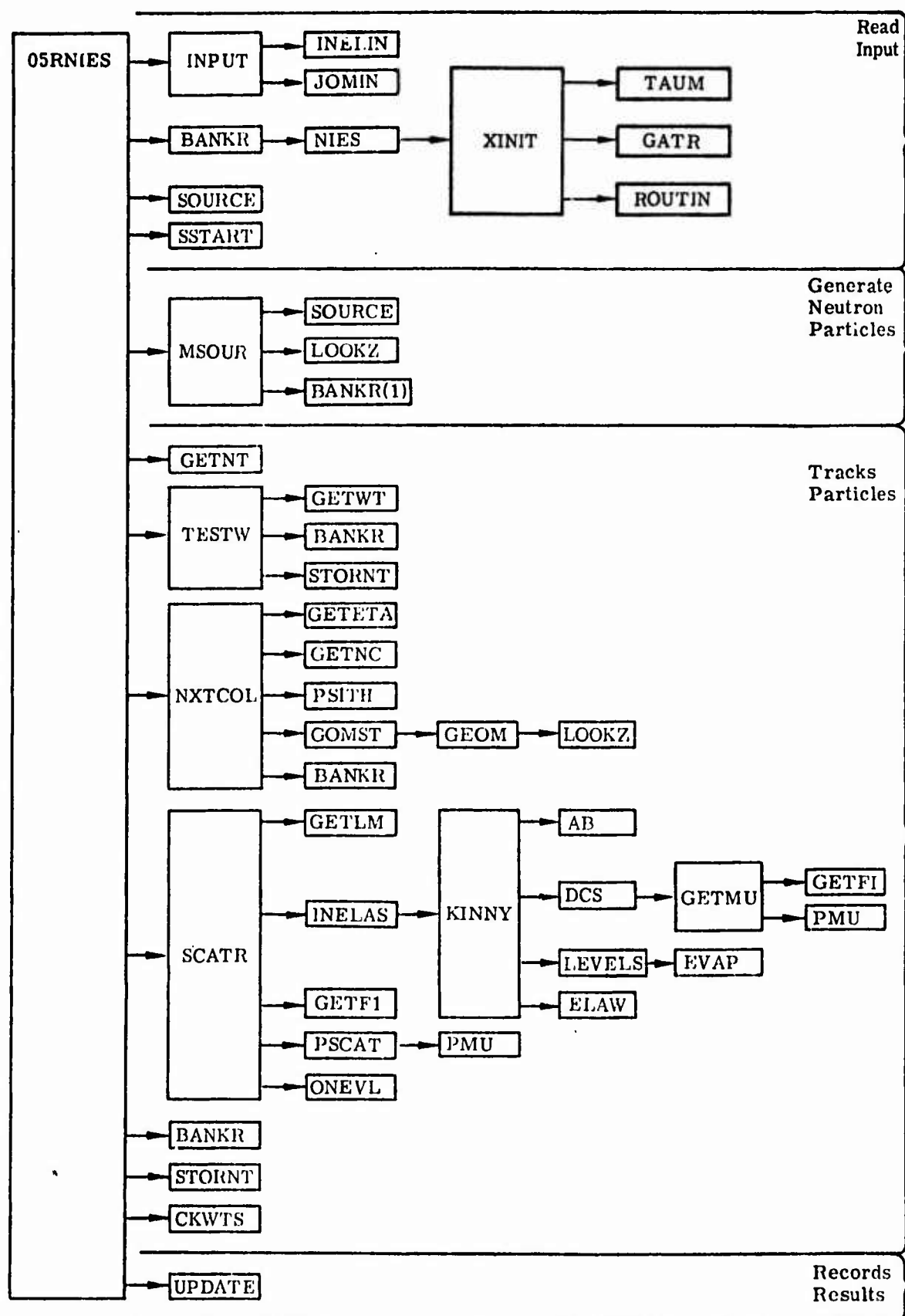


Figure 4.7. Block diagram of history-generating subroutines in O5RNIES.

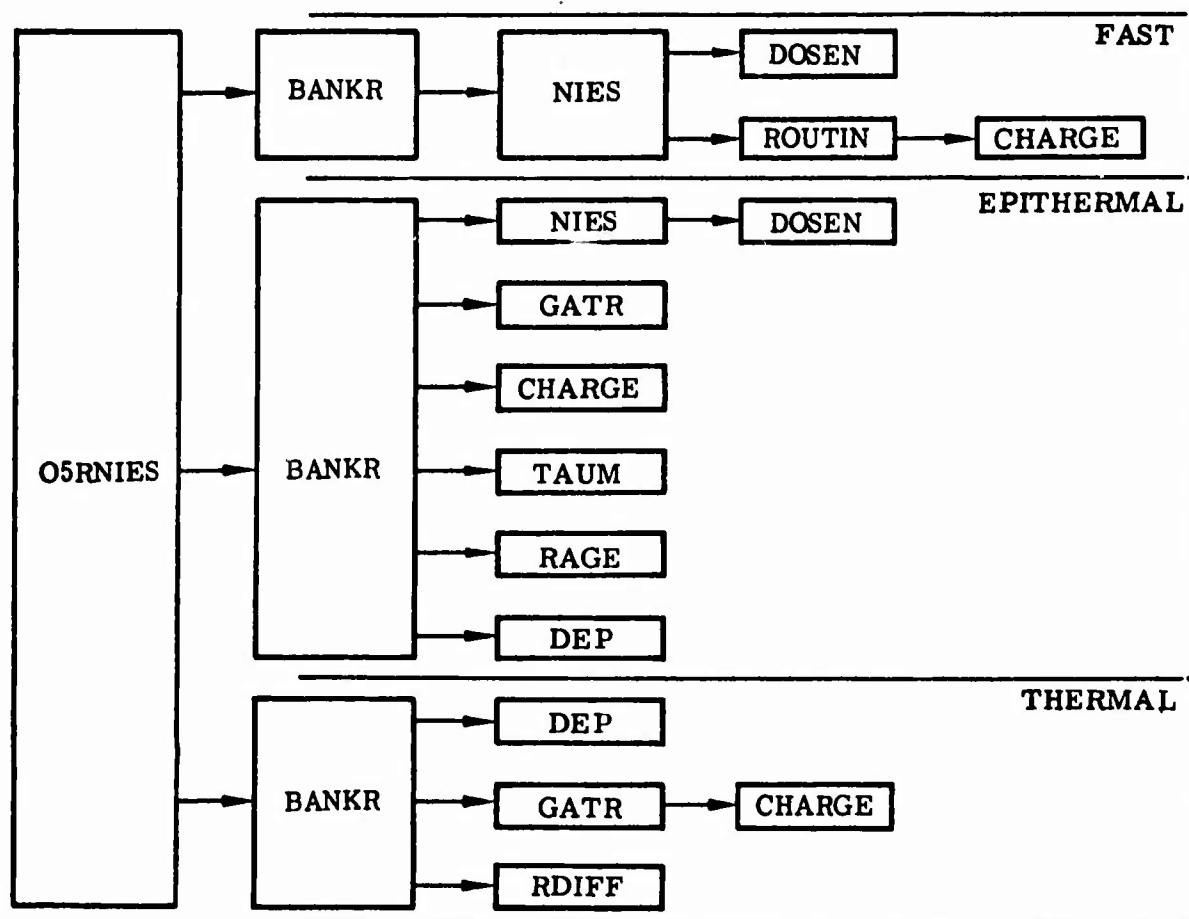


Figure 4.8. Analysis routines in O5RNIES

- READR - Same as before, except it now reads  
NXTAP and sets ETOPI and EBOTI.
- NXTCOL - Neutrons in the air with energies above  
AIRCUT have their path lengths stretched.

A number of subroutines and functions are called only by sub-routine KINNY. We do not include flowcharts for each of these, but below is a brief description of the role played by each of these subroutines and functions:

AB - Obtains ALPHA and BETA for a given target nuclide.

$\text{ALPHA} = M_N / (M_N + M_T)$  and  $\text{BETA} = M_T / (M_N + M_T)$ , where  $M_N$  is the mass of the incident neutron and  $M_T$  is the mass of the target nuclide.

CHOS - Linear interpolating function. Given the arrays P and Q (of size NPQ), where Q is a function of P, and P is in decreasing numerical order. Then, for a given R within the range P(1) to P(NPQ), CHOS will determine the corresponding Q by linear interpolation.

DCS - Computes the new direction cosines for the neutron.

ELAWS - Determines the speed of neutron after the non-elastic collision exciting continuum levels.

EVAP - Determines the neutron energy after inelastic scattering by evaporation model.

LEVELS - Determines a speed used in calculating the new velocity components of a neutron after collision with an inelastic discrete level target nuclide.



The analysis section of O5RNIES contains several additional subroutines, for which we do not include flowcharts. A brief description of the role played by these subroutines is as follows:

**KLEIN** – Routine used to select scattering angle and resulting energy from Compton scattering using Klein-Nishina cross section.

**MOWER** – Determines the smallest power of 2 greater than or equal to a given number.

**NINCS** – Determines which value in the NIES cross section data array is to be used.

**XION** – Computes fraction of energy deposition in N and O which causes ionization. (From fits to calculations of Lindhard, et al.)<sup>(13)</sup>

**Subroutine Name:** BANKR (NBNKID) (Fig. 4.9)

**Function:** Calls subroutine NIES to process collision information or update accumulative results arrays. It also sets certain ICOUNT and PCOUNT values.

**Calling Program:** O5R, MSOUR, NTXCOL, TESTW

**Subroutines Called:** CHARGE, DEP, GATR, NIES, RAGE, RDIFF, ROUTIN, TAUM

**Input Parameter:** NBNKID: Specifies what action BANKR is to take. See Ref. 12 for details.

**Labeled COMMON:** CALLE , CBANK , CFRNP, CTHERM, CTHPED, MAXMIN, NUTRON, RD, RECAL, SNGLES , XTT

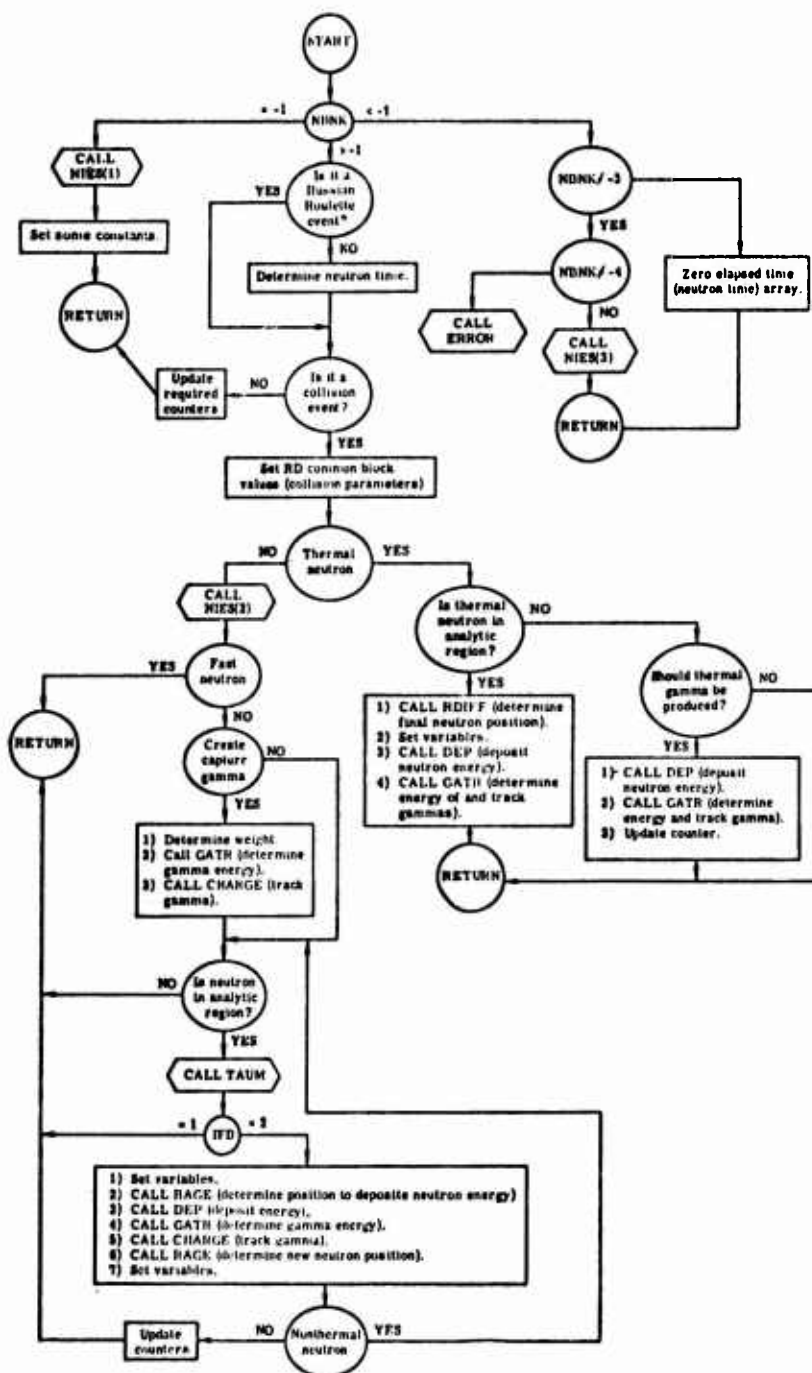


Figure 4. 9. Flowchart for subroutine BANKR.

**Subroutine Name:** CHARGE (Fig. 4. 10)

**Function:** Performs photon transport calculations in air-over-ground geometry. Computes and scores energy deposition and Compton current at photon collision sites. Similar to TIGRE program used at AFWL for prompt gamma EMP drivers.

**Calling Program:** BANKR, GATR, ROUTIN

**Subroutines Called:** AZIRN, GTISO, KLEIN, SEARCH

**Labeled COMMON:** CTHPED, ENDXX, MAXMIN, RD, RECAL, XTT, ZSTOR

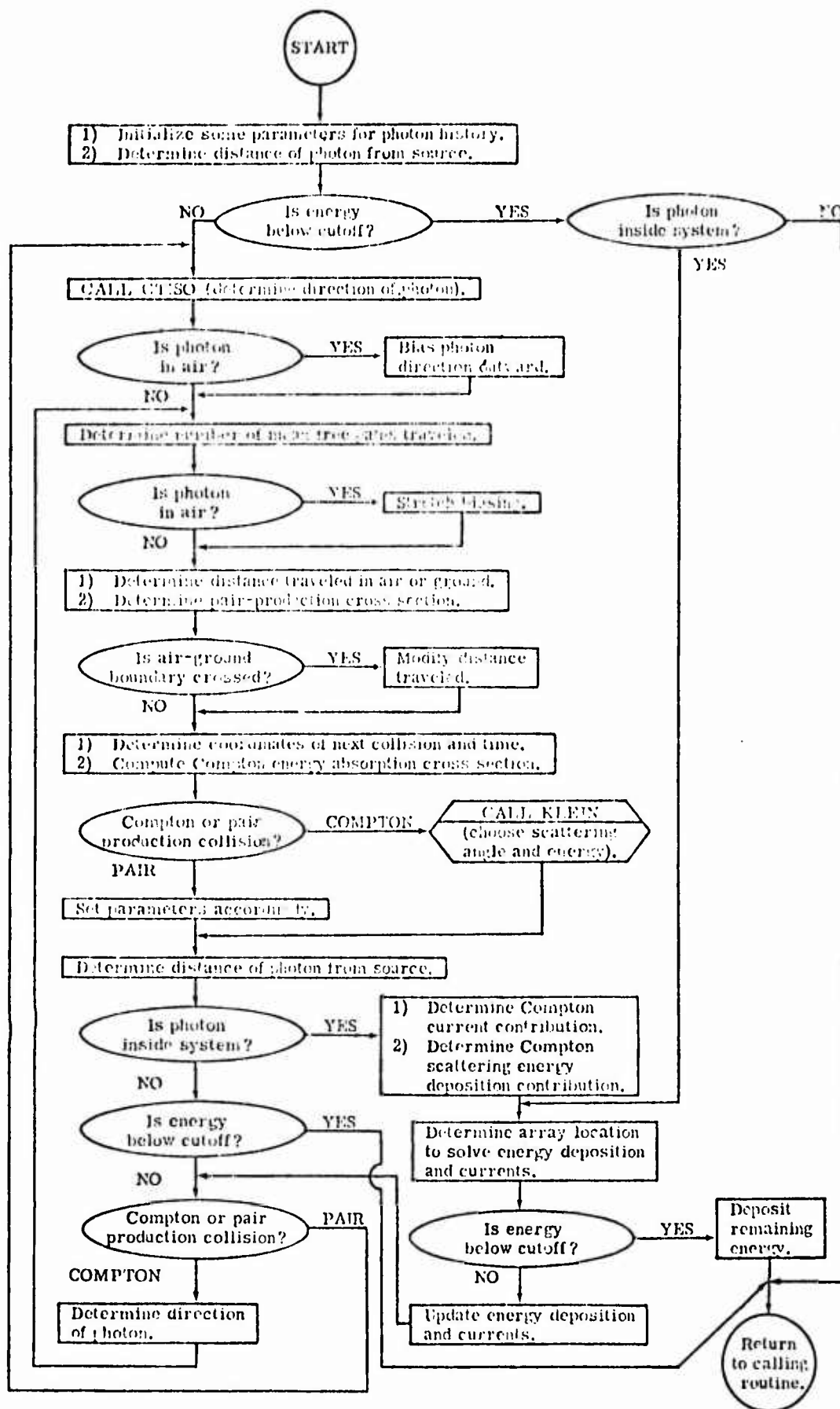


Figure 4. 10. Flowchart for subroutine CHARGE.

**Subroutine Name:** DEP (VOUTD, WT, PP, TSD, X2, Y2, Z2, T2, VO) (Fig. 4. 11)

**Function:** Computes and scores energy deposition due to thermal neutron collisions and nonthermal neutrons treated analytically.

**Calling Program:** BANKR

**Subroutine Called:** SEARCH

**Input Parameters:** VOUTD: Velocity of neutron after energy deposition.  
 WT: Weight of neutron.  
 TSD: Slowing down time for neutron  
 X2, Y2, Z2: Coordinates of the neutron energy deposition position.  
 T2: Neutron time at energy deposition.  
 VO: Velocity of neutron before energy deposition.

**Output Parameters:** WT: Neutron weight after energy deposition.  
 PP: Gamma weight.

**Labeled COMMON:** CFRNP, CROSS, CTHPED, ENDXX, MAXMIN, RD, RECAL, ZSTOR

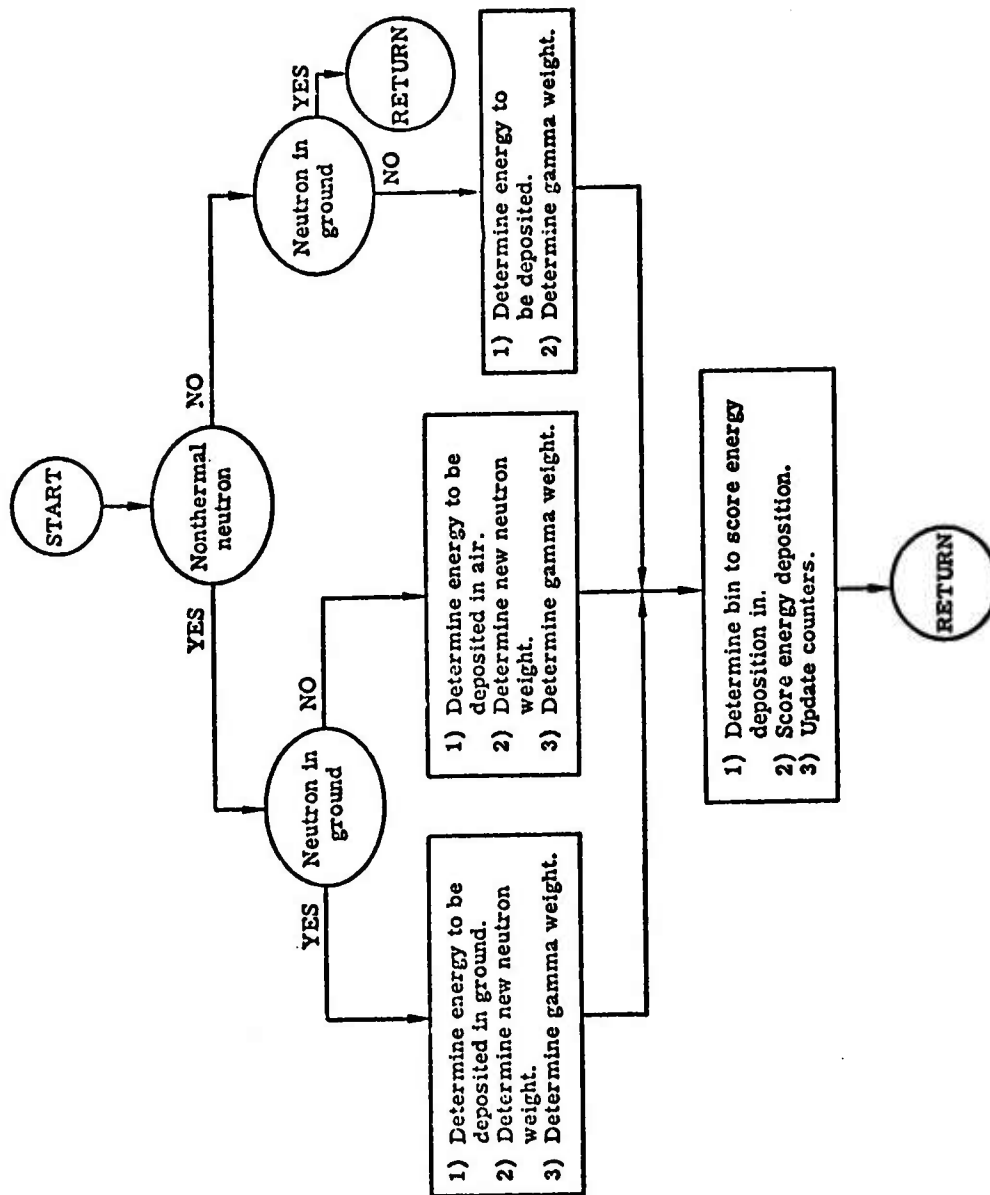


Figure 4. 11. Flowchart for subroutine DEP .

**Subroutine Name:** DOSEN (Fig. 4. 12)

**Function:** Computes and scores ionization due to fast  
Monte Carlo neutron collisions.

**Calling Program:** NIES

**Subroutines Called:** NINCS, SEARCH, XION

**Labeled COMMON:** CNXTAP, ENDXX, ENGNOS, GROSS, MAXMIN,  
PILL, RD, RECAL, XTT, ZSTOR



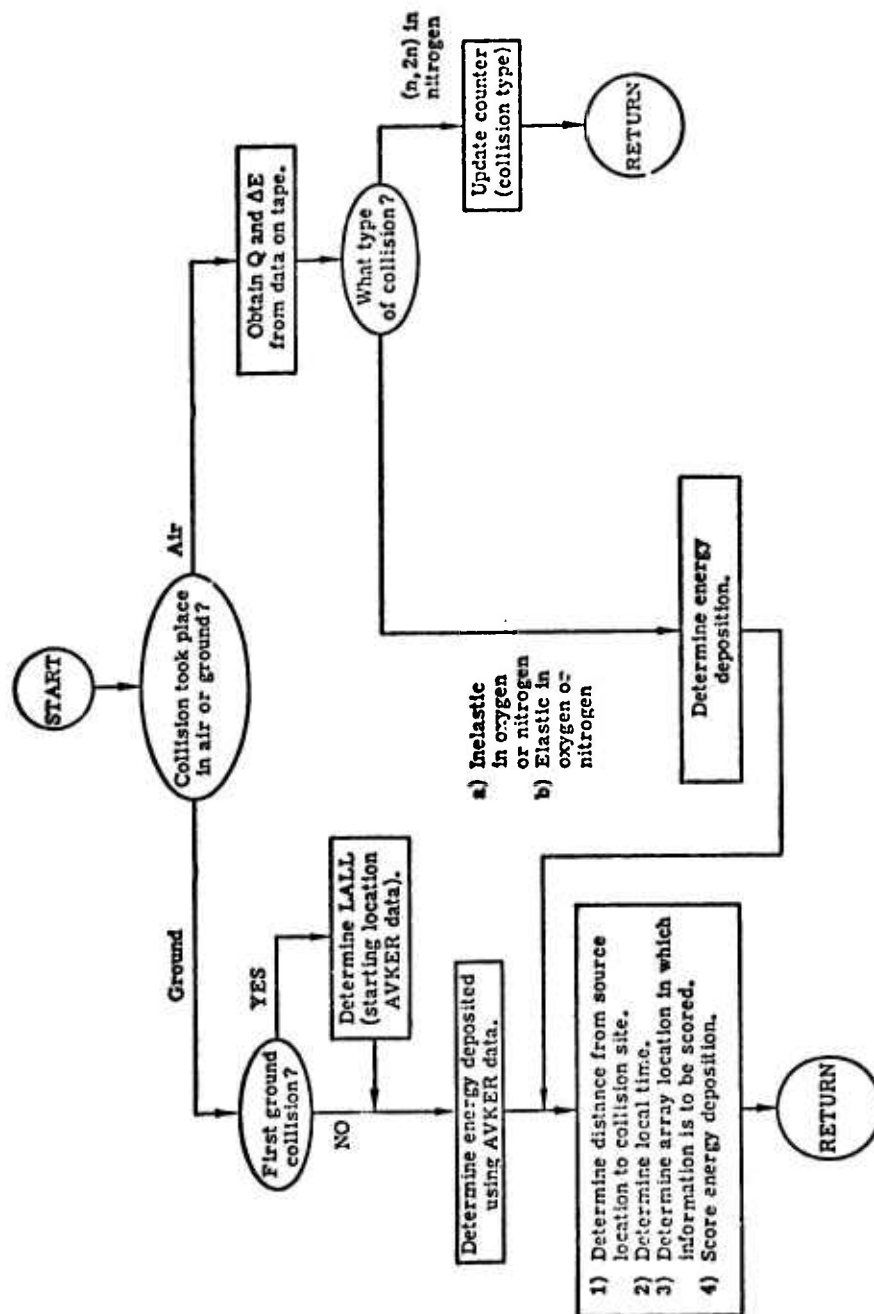


Figure 4.12. Flowchart for subroutine DOSEN.

**Subroutine Name:** GATR (NTIMES, IFA) (Fig. 4.13)

**Function:** Determine energy of capture gammas. Tracks analytic thermal gammas.

**Calling Program:** BANKR, XINIT

**Subroutines Called:** CHARGE, GTISO, SEARCH

**Input Parameters:** NTIMES: Number of gammas to be produced.  
IFA  $\neq$  0: Determine only gamma energy.

**Labeled COMMON:** CROSS, CTHERM, CTHPED, ENDXX, MAXMIN, RD, RECAL, XTT, ZSTOR

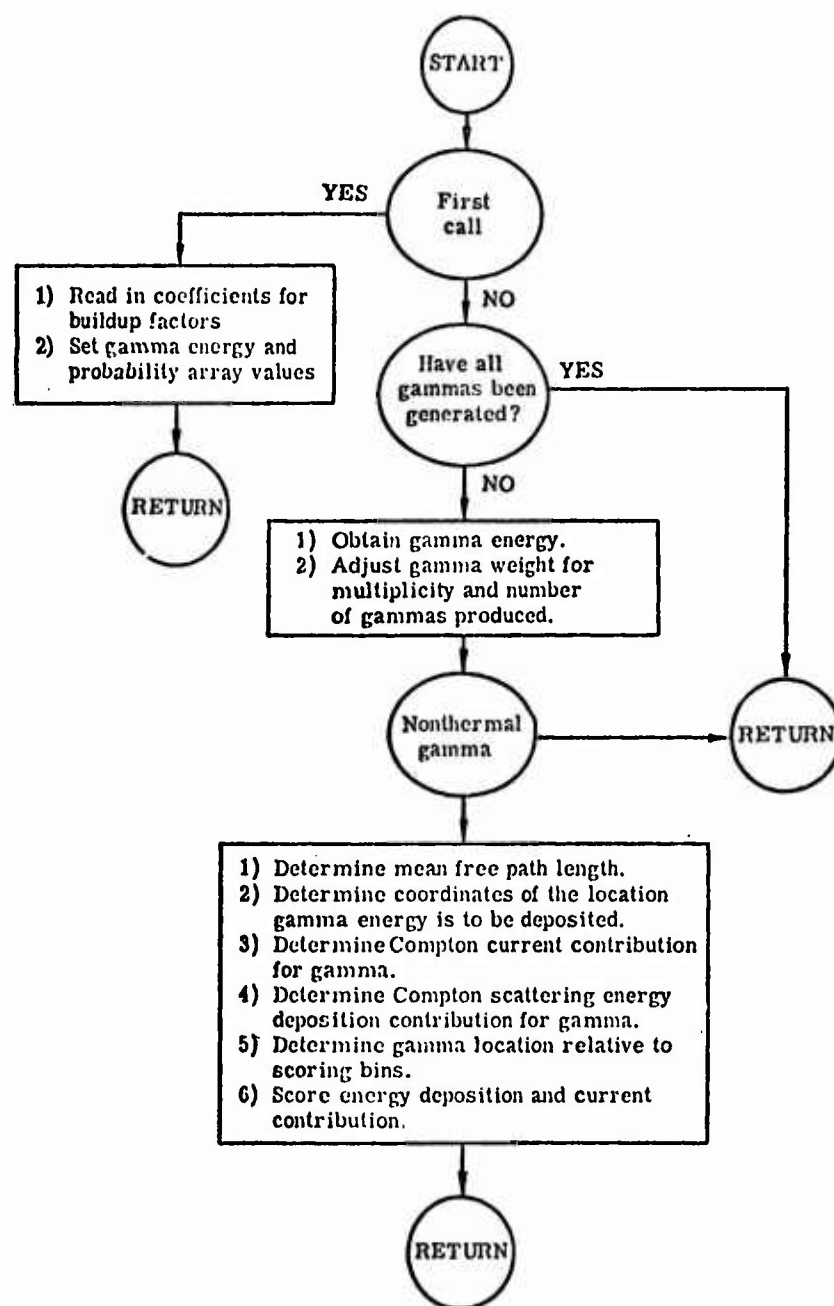


Figure 4. 13. Flowchart for subroutine GATR .

( )

**Subroutine Name:** INELIN (Fig. 4.14)

**Function:** Read input data cards related to inelastic scattering.

**Calling Program:** INPUT

**Labeled COMMON:** INELC

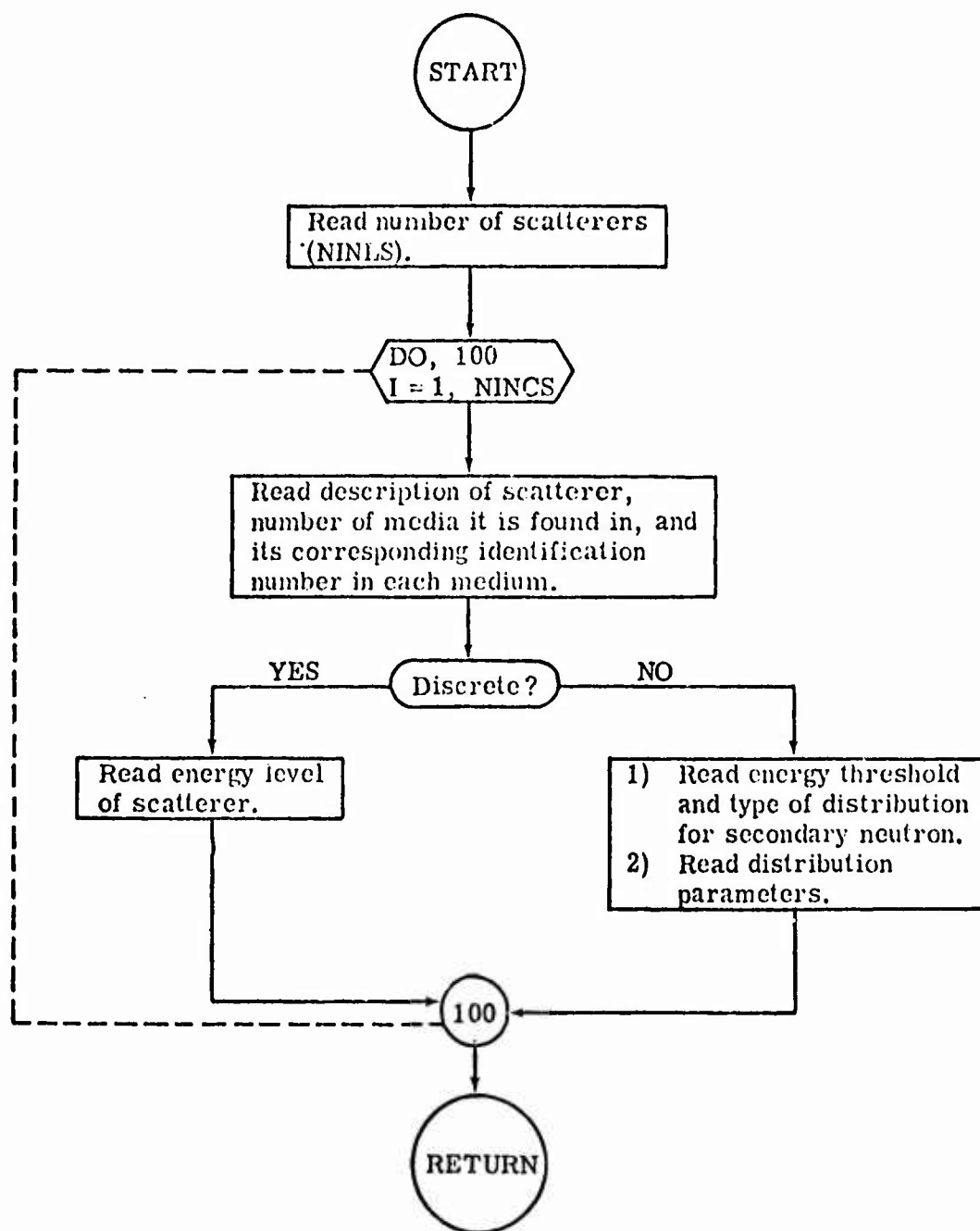


Figure 4. 14. Flowchart for subroutine INELIN.

**Subroutine Name:** KINNY (SPDSQ, U, V, W, WATE, NMED, LELEM) (Fig. 4.15)

**Function:** Treats the inelastic collisions, determining final speed of neutron after collision. It also determines the velocity components, U, V, and W.

**Calling Program:** INELAS which is called by SCATR.

**Subroutines Called:** AB, DCS, ELAW, LEVELS

**Input Parameters:** SPDSQ: Neutron speed squared.  
 U, V, W: Velocity components.  
 WATE: Weight before collision.  
 NMED: Medium collision took place in.  
 LELEM: Nuclide collided with.

**Output Parameters:** SPDSQ: Neutron speed square after collision.  
 U, V, W: Velocity components.

**Labeled COMMON:** INELC

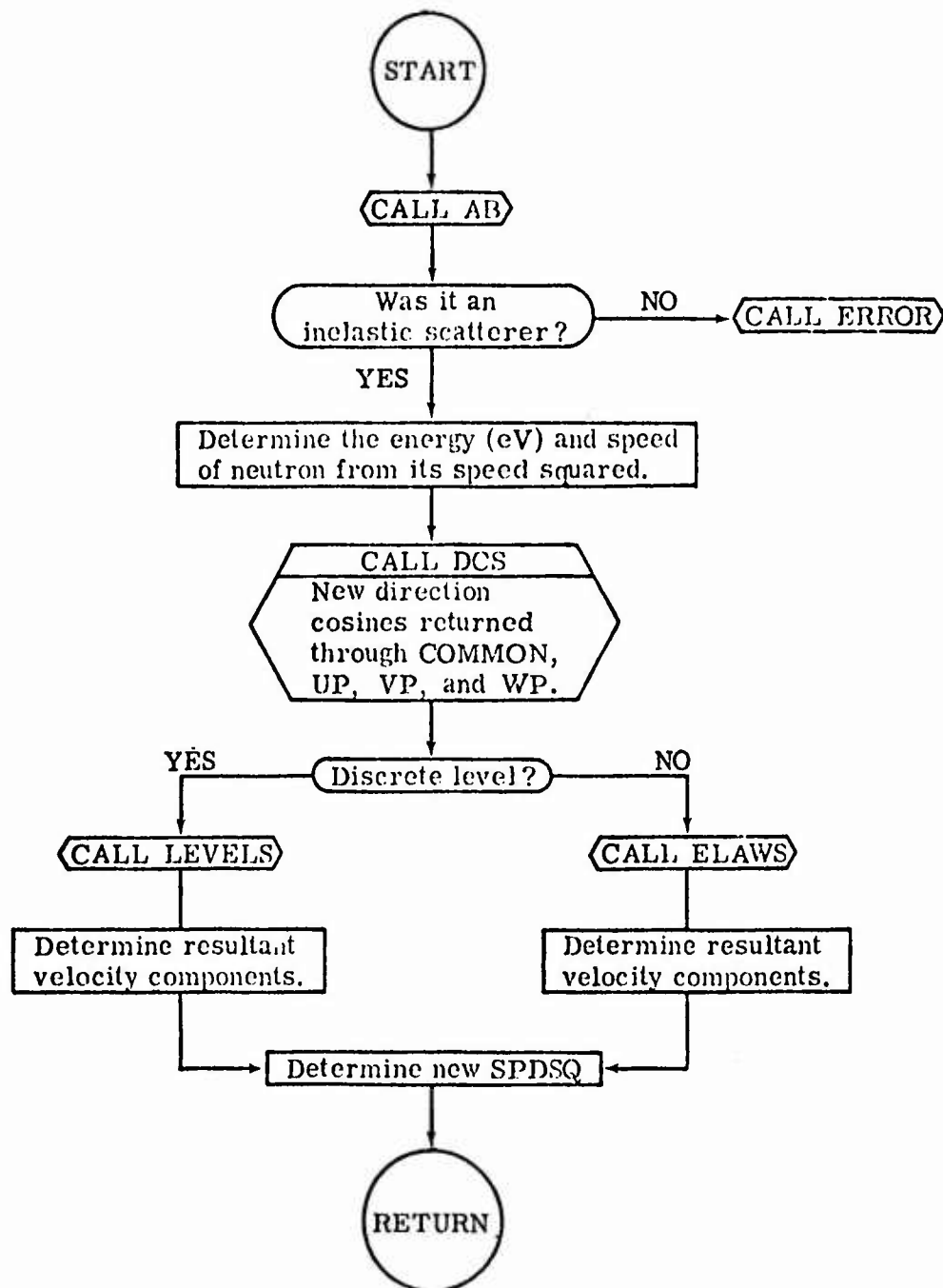


Figure 4. 15. Flowchart for subroutine KINNY.

**Subroutine Name:** NIES (NROUTE) (Fig. 4.16)

**Function:** Zeros scoring arrays, calls XINIT, ROUTIN, and DOSEN.

**Calling Program:** BANKR

**Subroutines Called:** DOSEN, ROUTIN, XINIT

**Input Parameter:** NROUTE: Specifies what action is to be taken by NIES. NROUTE - 1 implies start of program execution, read XINIT input, initialize certain arrays and variables. NROUTE = 2 implies collision information is to be analyzed. NROUTE = 3 implies end of an energy group.

**Labeled COMMON:** CALLE, CBANK, CNXTAP, ENDXX, MAXMIN, ONETWO, PILL, RD, RECAL, XTT, XUNITS.



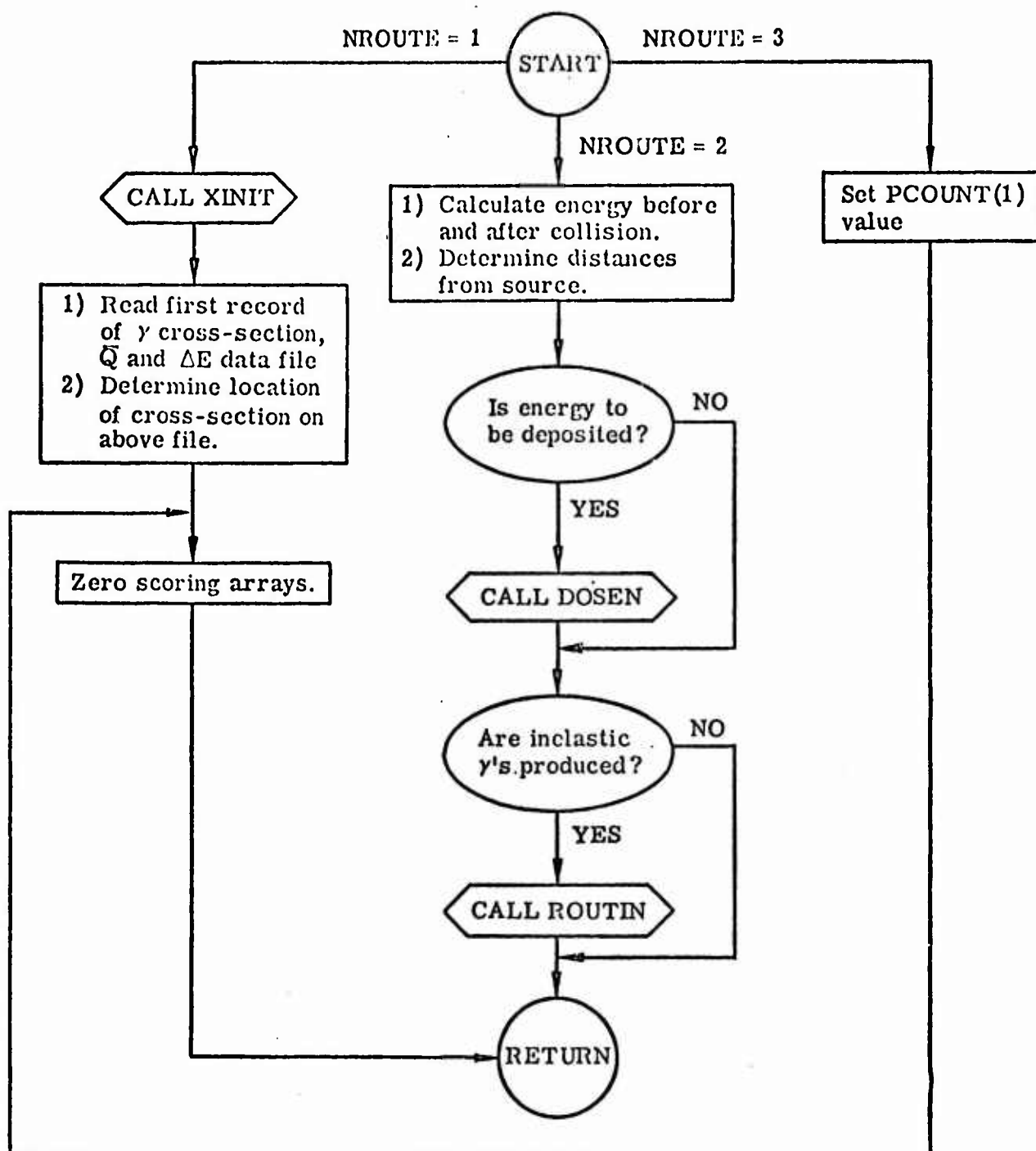


Figure 4. 16. Flowchart for subroutine NIES.

**Subroutine Name:** RAGE (AX, AY, Z, T, TAU, C1, C2, C3, TS) (Fig. 4. 17)

**Function:** Determine new epithermal neutron position and time, for analytically treated neutrons.

**Calling Program:** BANKR

**Subroutines Called:** GTISO

**Input Parameters:** AX, AY, Z: Old neutron position coordinates.  
T: Old neutron time.  
TS: Slowing down time.  
TAU: Fermi age.

**Output Parameters:** AX, AY, Z: New neutron position coordinates.  
T: New neutron time.  
C1, C2, C3: Components of an isotropic unit vector.

**Labeled COMMON:** CROSS

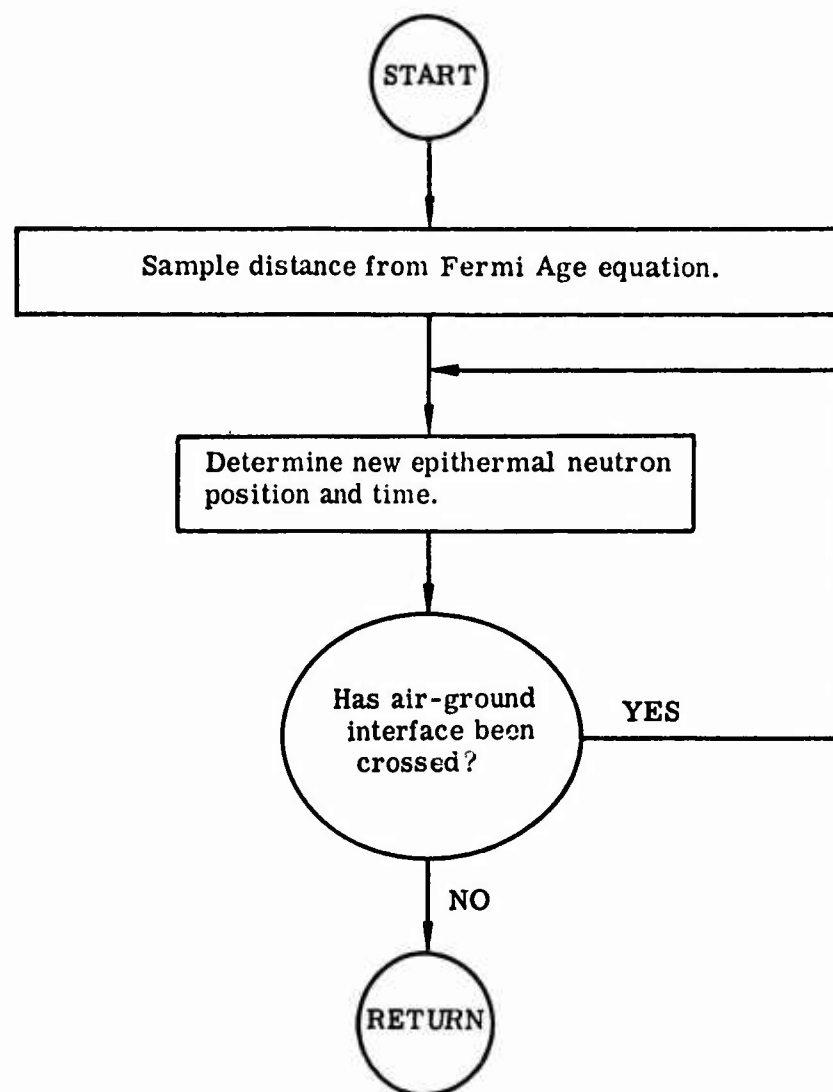


Figure 4. 17. Flowchart for subroutine RAGE.

Subroutine Name: RDIFF (XO, YO, ZO, TO, NMED, X1, Y1, Z1, T1) (Fig.4. 18)

Function: Determine final thermal neutron position and time.

Calling Program: BANKR

Subroutines Called: GTISO

Input Parameters: XO, YO, ZO: Old neutron position  
TO: Old neutron time  
NMED: Medium neutron is in

Output Parameters: X1, Y1, Z1: Final neutron position  
T1: Final neutron time

Labeled COMMON: CROSS, CTHPED

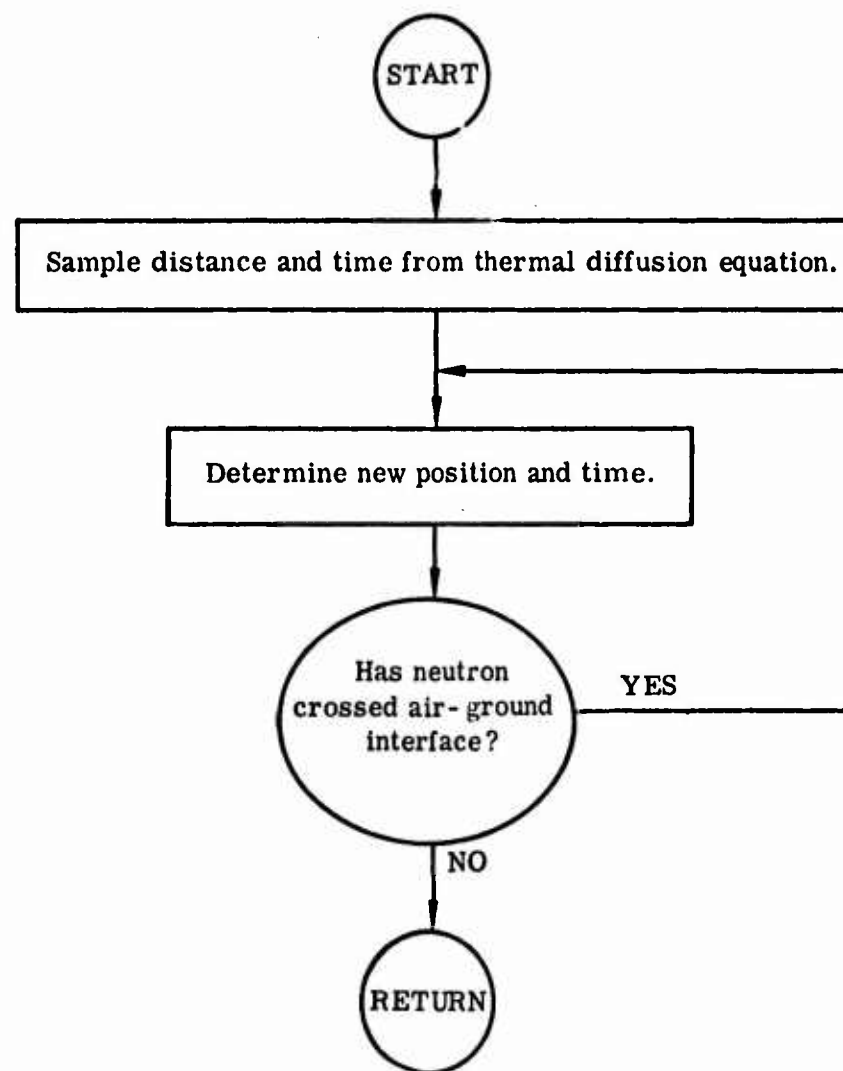


Figure 4. 18. Flowchart for subroutine RDIFF.

**Subroutine Name:** ROUTIN (Fig. 4.19)

**Function:** Creates photons resulting from high-energy neutron collisions, giving their energies and weights.

**Calling Program:** NIES, XINIT

**Subroutines Called:** CHARGE, NINCS

**Labeled COMMON:** CNXTAP, CROUT, GROSS, RD, RECAL, XTT

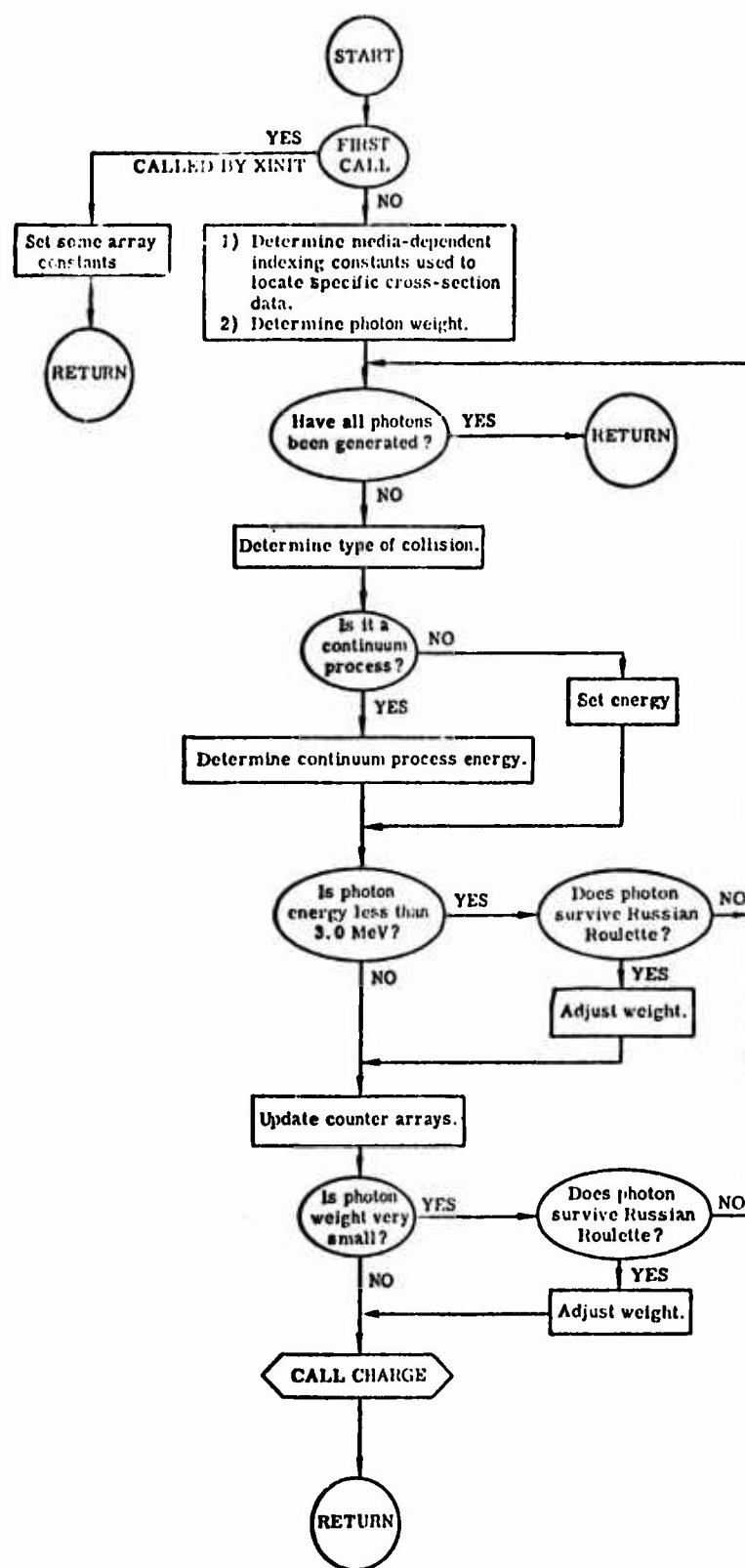


Figure 4. 19. Flowchart for subroutine ROUTIN.

**Subroutine Name:** SEARCH (T, TT, N, M, K) (Fig. 4.20)

**Function:** SEARCH is used to determine the indexing values which specify the particular array locations in which information is to be stored.

**Calling Program:** CHARGE, DOSEN

**Input Parameters:**

- T: A value within the range TT(1) to TT(N).
- TT: An array of size N of boundary values in increasing numerical order.
- N: Size of TT array.
- M: Smallest power of 2 greater than or equal to N.

**Output Parameter:** K: The index value.



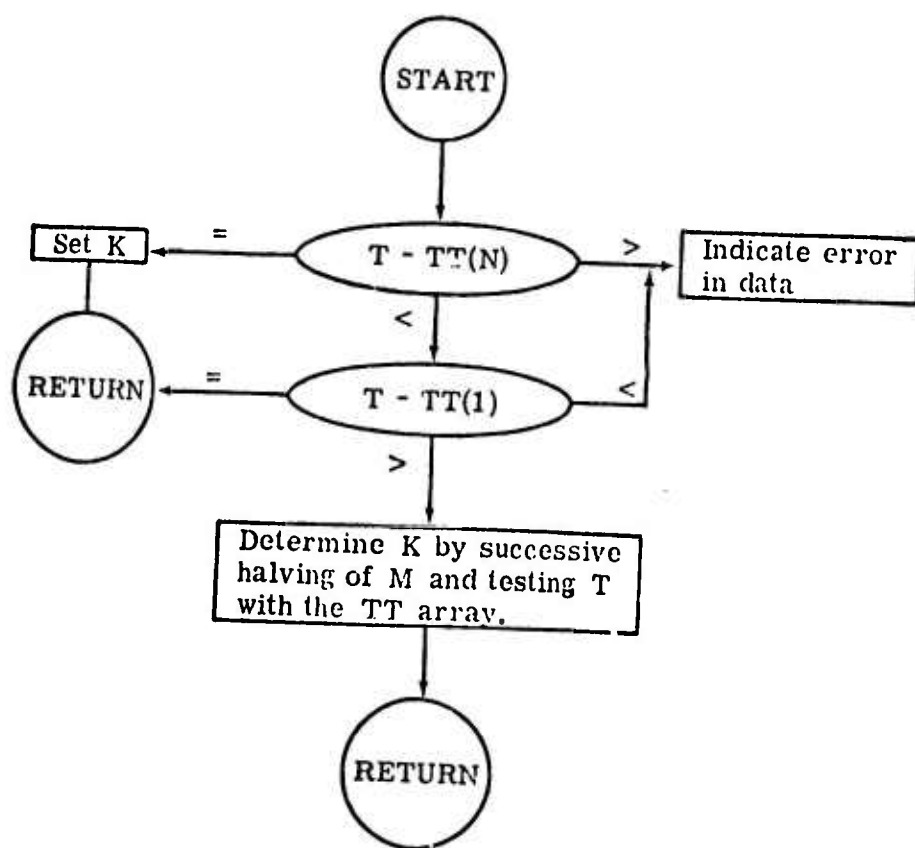


Figure 4. 20. Flowchart for subroutine SEARCH.

<b>Subroutine Name:</b>	<b>SOURCE</b> (SPDSQ, U, V, W, X, Y, Z, WATE, N, NMEN, NMED, NREG) (Fig. 4. 21)
<b>Function:</b>	Specifies the initial parameters of a neutron. These parameters are: neutron energy, direction of its first flight, and its statistical weight. The starting coordinates are (0. , 0. , 0. ), set by a data card.
<b>Calling Program:</b>	MSOUR, O5RNIES
<b>Output Parameters:</b>	<p>SPDSQ:     The neutron speed squared.</p> <p>U, V, W:    The direction cosines of the source neutron.</p> <p>WATE:       The starting weight to be assigned to the source neutron.</p>
<b>Parameters Not Set or Used:</b>	<p>X, Y, Z:    The starting coordinates of the source neutron.</p> <p>N:           Integer associated with a particular neutron.</p> <p>NMEN:       Total number of neutrons to be given source data.</p> <p>NMED:       The medium in which X, Y, and Z lie.</p> <p>NREG:       The region in which X, Y, and Z lie.</p>
<b>Labeled COMMON:</b>	CSOURC, XUNITS

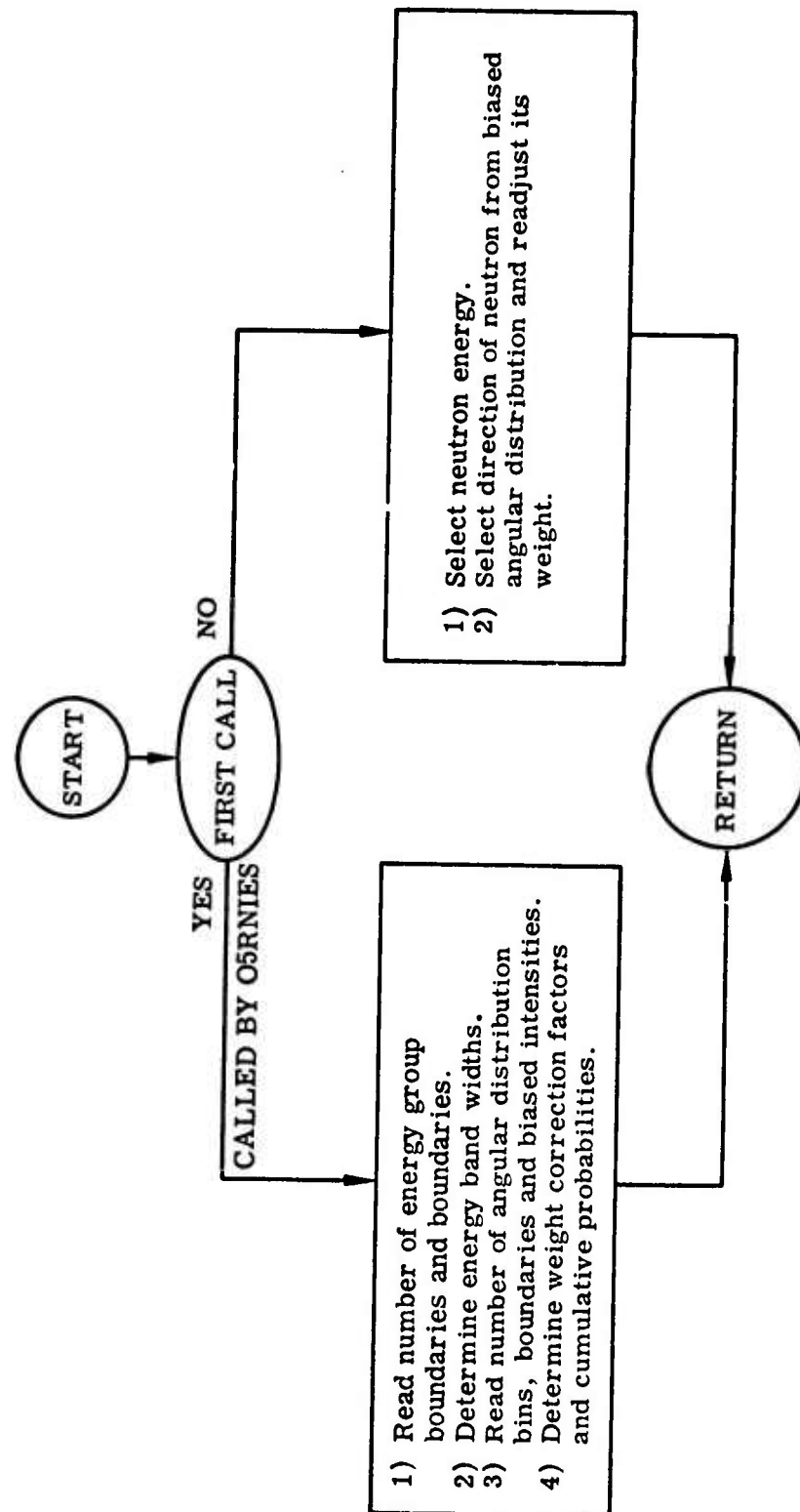


Figure 4.21. Flowchart for subroutine SOURCE.

**Subroutine Name:** SSTART (NQST) (Fig. 4. 22)

**Function:** Checks to see that correct results tape is mounted and positions the desired tape.

**Calling Program:** O5RNIES

**Input Parameter:** NQST: Counter used to indicate how many energy bands remain to be processed for current RUN.

**Labeled COMMON:** CSOURC, CSTOR, ENDXX, RECAL, XUNITS

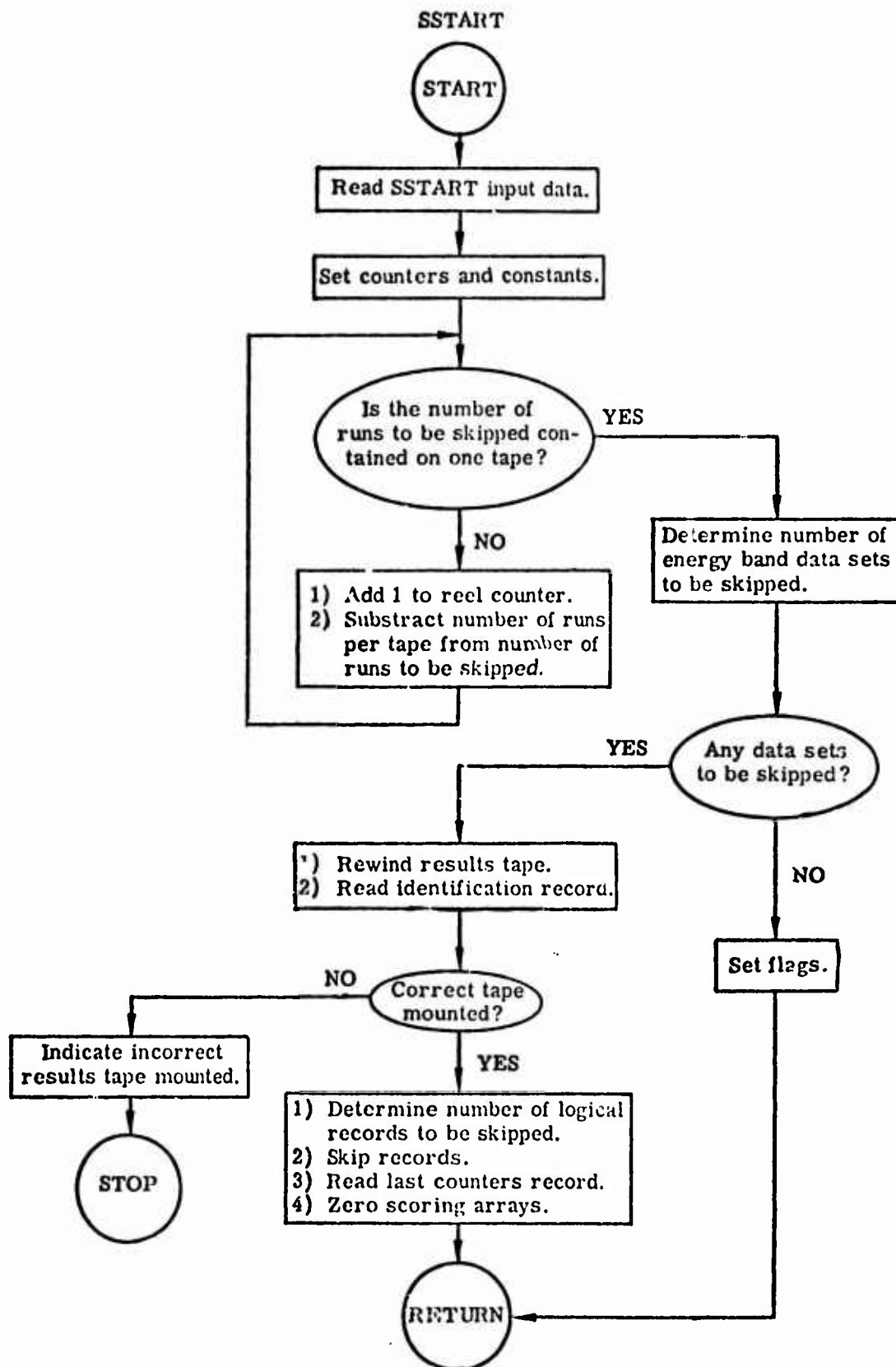


Figure 4. 22. Flowchart for subroutine SSTART.

**Subroutine Name:** TAUM (AZ, VIN, NMED, TAU, VOUT, TS, TAUD TSD, IFB) (Fig. 4. 23)

**Function:** Determine Fermi ages, slowing down times and energy for analytically treated neutrons.

**Calling Program:** BANKR

**Subroutines Called:** SEARCH

**Input Parameters:** AZ: Distance above or below air-ground interface  
VIN: Neutron speed at start of Fermi age process  
NMED: Medium neutron is in

**Output Parameters:** TAU: Maximum Fermi age decrement  
VOUT: Neutron speed at end of Fermi age process  
TS: Slowing down time corresponding to maximum Fermi age decrement  
TAUD: Fermi age decrement used for energy deposition calculations  
VOUTD: Neutron speed used for energy deposition calculations  
TSD: Slowing down time used for energy deposition calculations  
IFB: = 1: Cannot treat epithermal neutron analytically  
      = 2: Can treat epithermal neutron analytically

**Labeled COMMON:** CTHPED

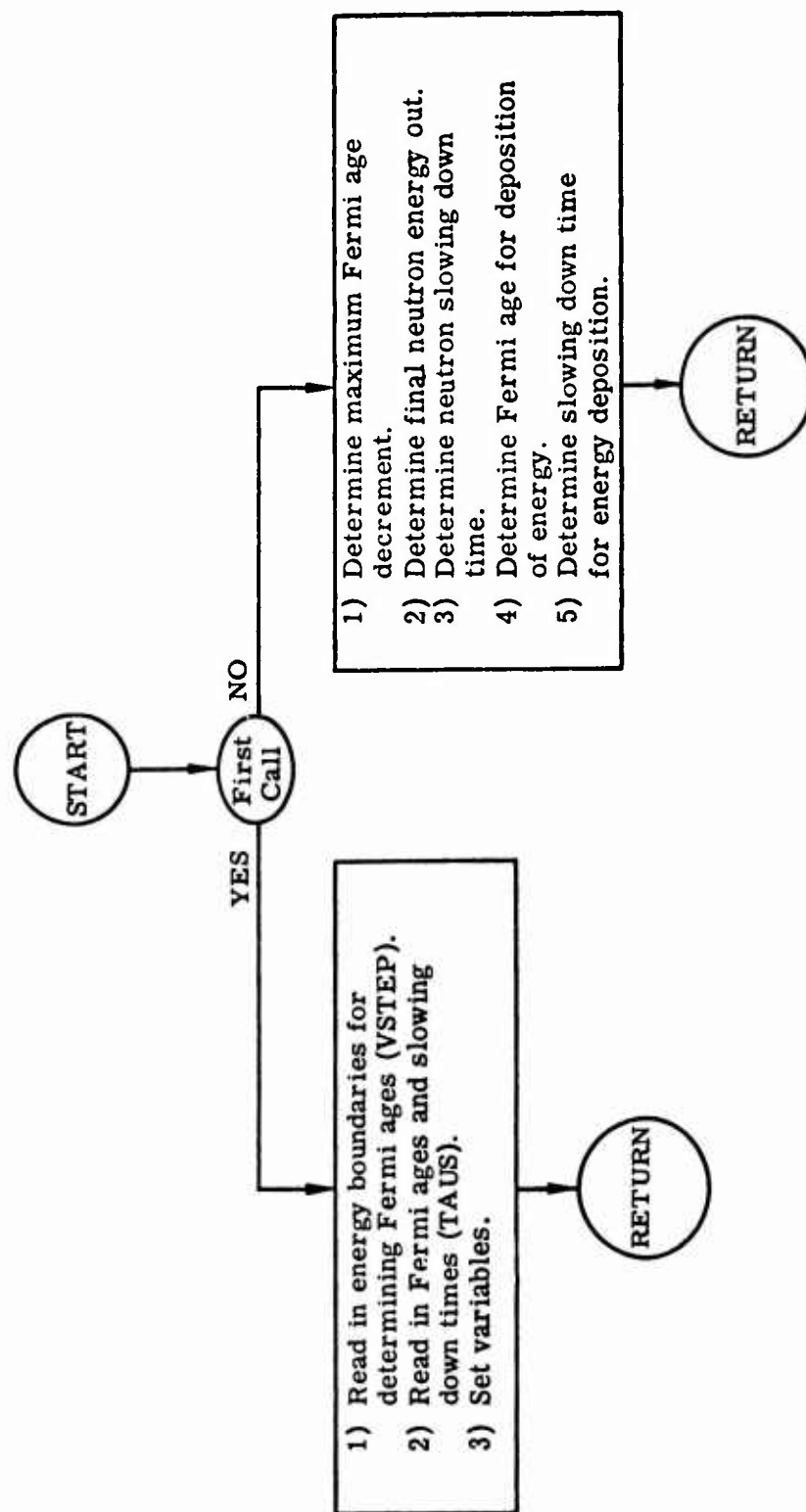


Figure 4. 23. Flowchart for subroutine TAUM.

**Subroutine Name:** UPDATE (IFA) (Fig. 4.24)

**Function:** Writes energy band data and other information on results tape. Determines when new results tape should be mounted. Prints out counter arrays.

**Calling Program:** O5RNIES

**Input Parameters:** IFA = 1, fast results  
2, thermal results

**Labeled COMMON:** COECS, CSOURC, CSTOR, CVOL, ENDXX, RECAL, VTTX, XUNITS, ZSTOR



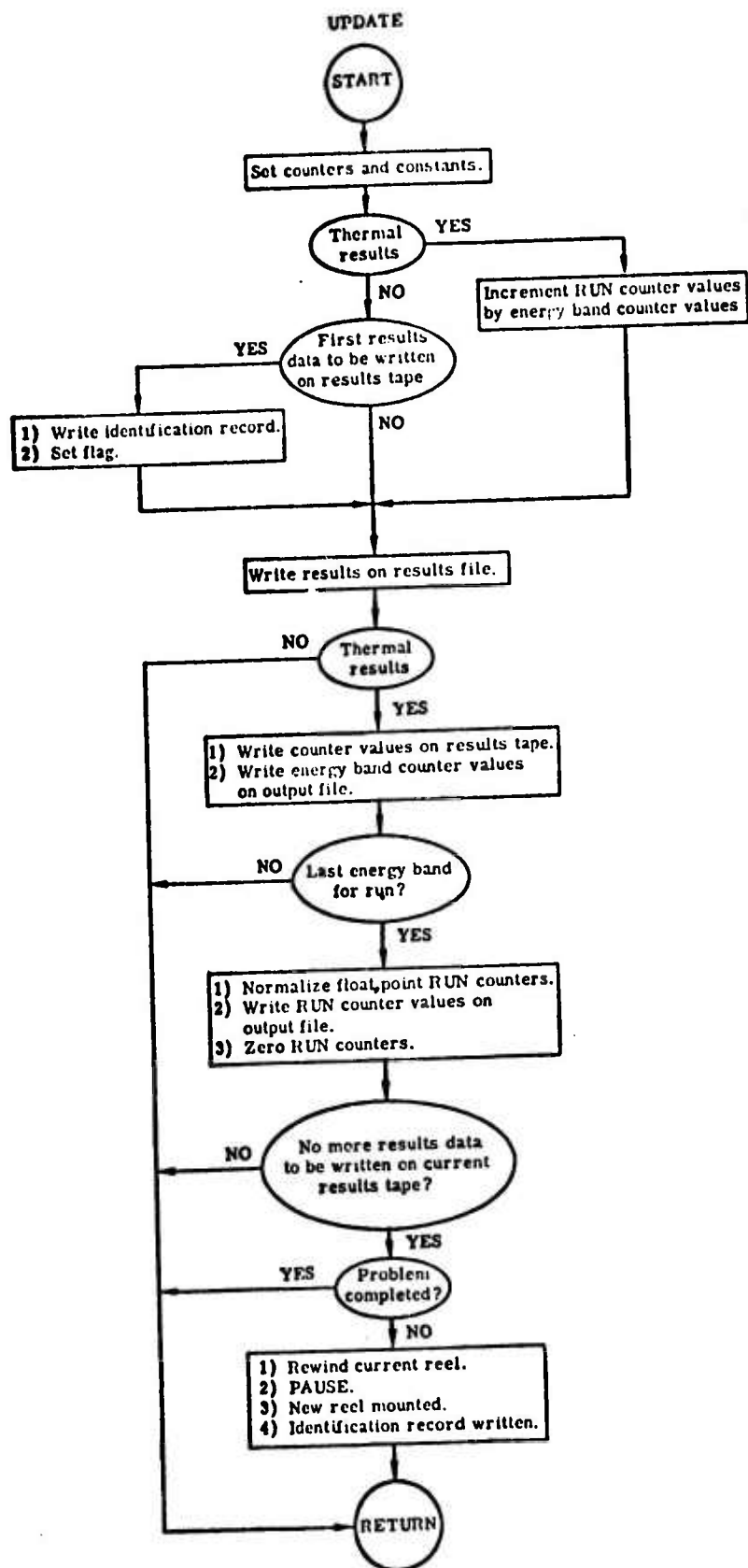


Figure 4. 24. Flowchart for subroutine UPDATE.

**Subroutine Name:** XINIT (NIST) (Fig. 4. 25)

**Function:** Reads and prints analysis input. It also determines constants used in the analysis routines based on input values.

**Calling Program:** NIES

**Subroutine Called:** TAUM, GATR, ROUTIN

**Output Parameter:** NIST: dummy

**Labeled COMMON:** CBANK, CNXTAP, COECS, CROUT, C THERM, CVOL, ENDXX, MAXMIN, ONETWO, RECAL, VTTX, XUNITS, ZSTOR

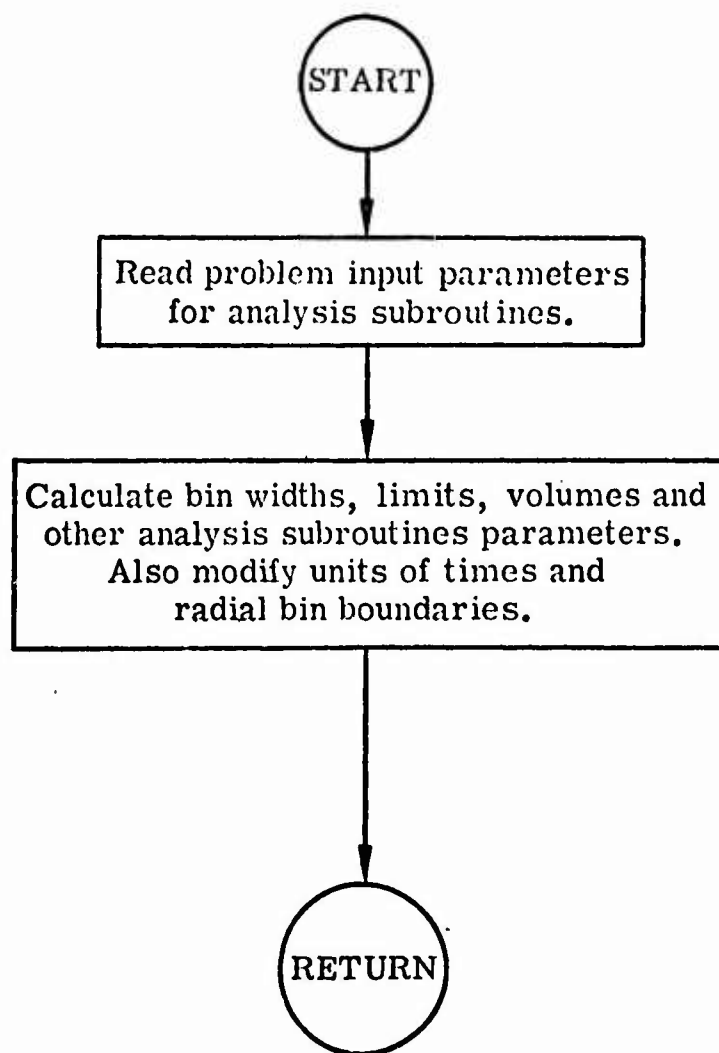


Figure 4. 25. Flowchart for subroutine XINIT.

#### 4. 6. 3. 2 Labeled Common Blocks

In this subsection we define, briefly, all of the variables which are to be found in labeled common blocks of the analysis section of OSRNIES.

##### 1. COMMON/CALLE/ALLE

ALLE - Energy lost due to neutrons escaping from the system

##### 2. COMMON/CBANK/TIMMAX, EPICUT, ICOLL (1000), RREPI, RRTHM

TIMMAX - Local time past which neutrons no longer followed

EPICUT - Epithermal cutoff in  $(\text{cm/sec})^2$

ICOLL - Array containing the number of collisions undergone by the given neutrons

RREPI - Russian roulette probability to determine if a gamma ray should be produced from an epithermal neutron collision

RRTHM - Russian roulette probability to determine if a gamma ray should be produced from a thermal neutron collision

##### 3. COMMON/CFRNP/FRNP

FRNP - Fraction of the absorption cross section for air which results in photon emission for epithermal and thermal neutron collisions

##### 4. COMMON/CNXTAP/NXTAP, SIG (1700), NPQ, ISTRT (40), EBOTI, ETOPI, NPT (40)

NXTAP - Gamma production cross section,  $\bar{Q}$ , and energy deposition, data file number

SIG - Array into which gamma production cross section  $\bar{Q}$ , and energy deposition, data are stored

4. (Cont.)

- NPQ - Record length of the above (SIG) data
- ISTRIT - Array containing the starting locations of the individual cross section in the SIG array
- EBOTI - Lower energy (cm/sec)<sup>2</sup> boundary of the SIG data
- ETOPIT - Upper energy (cm/sec)<sup>2</sup> boundary of the SIG data
- NPT - Array containing the size of the individual cross sections in the SIG array

5. COMMON/COECS/I1, I2, I3, N2

- I1 - Maximum number of spatial bins
- I2 - Maximum number of time-spatial bins
- I3 -  $2 * (I1 + I2)$
- N2 - Number of items to be stored. Possible items are: ionization due to neutrons, ionization due to gammas, horizontal (or radial) currents, and vertical (or theta) currents.

6. COMMON/CROSS/GSIGA, GD, RTPI, PI, EPS, ASIGA, ADXX

- GSIGA - Thermal absorption cross section in ground
- GD - Thermal diffusion coefficient in ground
- RTPI -  $\sqrt{\pi}$
- PI -  $\pi$
- EPS -  $e = 2.718282$
- ASIGA - Thermal absorption cross section in air
- ADXX - Thermal diffusion coefficient in air

7. COMMON/CROUT/NPHOT, WPHOT, WTLIM, TENWTL

- NPHOT - Number of photons produced by each inelastic neutron collision
- WPHOT - Floating point representation of NPHOT
- WTLIM - Weight below which Russian Roulette is played in ROUTIN to determine if photon is followed
- TENWTL -  $10 * WTLIM$ , used in determining survival probability of photon in ROUTIN

8. COMMON/CSOURC/IFAG, INBA, IRESLT, NBA, NEB, NEBL, NRPT, NOREEL, NQUIS

- IFAG -  $\neq 1$ , start new results tape
- INBA - Energy band currently processing
- IRESLT - Unit number of results tape
- NBA - Number of runs (batches)
- NEB - Number of energy bands
- NEBL - Number of energy bands left to be processed for current runs
- NRPT - Number of runs per results tape
- NOREEL - Reel number of current results tape
- NQUIS - Number of runs left to be processed
- E - Energy band boundaries (monotonically decreasing)

9. COMMON/CSTOR/ID

- ID - Run ID number

10. COMMON/CTHERM/NTHERM, TMULT(2), A3(2)

- NTHERM - Number of gammas produced by thermal neutrons on the terminating collisions
- TMULT - Neutron capture gamma multiplicities: TMULT(1)-air, TMULT(2)-ground
- A3 - Boundary value (cm) to determine whether Monte Carlo or analytic method should be used to track thermal neutrons A3(1)-air (elevation), A3(2)-ground (depth)

11. COMMON/CTHPED/THPEED, THPSQ

- THPEED - Velocity of thermal neutrons (cm/sec)
- THPSQ -  $\text{THPEED}^2$  (cm/sec)<sup>2</sup>

12. COMMON/CVOL/DELT (41), VOLB (360)

- DELT - Time bin widths (sec)
- VOLB - Volumes of the spatial bins (m<sup>3</sup>)

13. COMMON/ENDXX/ENDEP (10400), GENDEP (10400), XCR (10400), XCT (10400), IMAX, JMAX, KMAX

- ENDEP - Array in which energy deposition due directly to neutrons is stored
- GENDEP - Array in which energy deposition due to gammas created by neutron collisions is stored
- XCR - Array in which radial or horizontal current component is stored
- XCT - Array in which theta or vertical current component is stored

14. COMMON/ENGNOs/wo(28), WN(26)

- WO - Energy levels (Q's) of the discrete inelastic oxygen scatterers
- WN - Energy levels (Q's) of the discrete inelastic nitrogen scatterers

15. COMMON/GROSS/NDISC(2), NCONT(2), GAMENG(2,30)

- NDISC(I) - Number of discrete photon energy cross sections for medium I
- NCONT(I) - Number of continuum photon energy cross sections for medium I
- GAMENG  
(I, J) - Energy (MeV) of photon resulting from cross section J in medium I

16. COMMON/INELC/SP, UP, VP, WP, E, S, NINLS, IN, NR(120), Q(1,120), NE(1,120), EL(1,1,1), SIGL(1,1,1), NU(120), ELAW(1,120), NLAW(1,120), NENG(120), ENG(5,2), NETAB1(5,2), ETAB1(23,5,2), PTAB1(23,5,2), NETAB2(1), ETAB2(1,1), PTAB2(1,1), FM(1,120), EA(1), EB(1), TA(120), TB(120), TC(120), NAPP(120), NMEDE(2,120), NELE(2,120), NAE(120)

- SP - Velocity of resultant neutron (cm/sec)
- UP - X axis unit component of SP
- VP - Y axis unit component of SP
- WP - Z axis unit component of SP
- E - Energy of incident neutron (eV)
- S - Velocity of incident neutron (cm/sec)
- NINLS - Number of inelastic scatterers
- IN - Scatterer involved in neutron collision



16. (Cont.)

NR	-	Scatterer flag, =1 for discrete levels
Q	-	Q value for scatterer
NE	-	dummy
E	-	dummy
SIGL	-	dummy
NU	-	Scatterer flag, =1 non-discrete scatterer
ELAW	-	Energy threshold for non-discrete scatterers
NLAW	-	Indicates distribution to be used for selecting resultant neutron energy

The following arrays deal with tabulated  $E^*$  vs  $P(E^*)$  scatterers

NENG	-	Number of energy levels
ENG	-	Energy levels of incident neutron
NETAB1	-	Number of individual $P(E^*)$ values for given incident energy
ETAB1	-	Resultant neutron energy associated with a particular cumulative $P(E^*)$
PTAB1	-	Cumulative $P(E^*)$ 's
NETAB2	-	dummy
ETAB2	-	dummy
PTAB2	-	dummy

16. (Cont.)

- FM - Multiplicity associated with particular non-discrete scatterer
- EA - dummy
- EB - dummy
- TA - Maxwellian coefficient
- TB - Maxwellian coefficient
- TC - Maxwellian coefficient
- NAPP - Number of media scatterer is in
- NMEDE - Medium number scatterer is in
- NELE - Scatterer number with respect to media
- NAE - Tabulated  $E^*$  vs  $P(E^*)$  scatterer number

17. COMMON/MAXMIN/RMAX, RMIN, TMAX, ZMAX, ZMIN, RMAXZ, A

- RMAX - Maximum radius of interest (cm)
- RMIN - Minimum radius of interest (cm)
- TMAX - Maximum time of interest (sec)
- ZMAX - Maximum Z value of interest (cm), source at  $Z = 0.0$ .
- ZMIN - Minimum Z value of interest (cm)
- RMAZ -  $RMAX * RMAX$
- A - Height of burst of source (cm)

18. COMMON/ONE TWO/IRP, ISP, IWANT

- IRP - dummy
- ISP - dummy
- IWANT - Flag which specifies what collisions are to be analyzed.

19. COMMON/PILL/XWT, EN, EA

- XWT - Weight of unbiased neutron
- EN - Neutron energy (MeV) before collision
- EA - Neutron energy (MeV) after collision

20. COMMON/RD/NCOLL, NAME, SPDSQ, U, V, W, X, Y, Z, WATE, SPOLD, UOLD, VOLD, WOLD, XOLD, YOLD, ZOLD, OLDWT, THETM, PSI, ETAUSD, NGROUP, LELEM, NREG, NMED, NAMEX, WATEF, BLZNT, BLZ, LAMBDA, S0, S1, ETATH, FONE, EXTRA1, EXTRA2

The O5R collision parameters associated with each neutron collision

21. COMMON/RECAL/PCOUNT(30), ICOUNT(30), ZCOUNT(30), KCOUNT(30), IPKT, IKT, EPICUT

- PCOUNT - Floating point counters used to check energy conservation, energy of neutrons and gammas produced in a given energy group
- ICOUNT - Integer counters used to indicate number of neutrons and gammas produced, and how many times certain types of collisions occur in a given energy group
- ZCOUNT - Accumulative PCOUNT over a given run
- KCOUNT - Accumulative ICOUNT over a given run

21. (Cont.)

IPKT - Size of PCOUNT and ZCOUNT arrays  
IIKT - Size of ICOUNT and KCOUNT arrays  
EPICUT - Epithermal cutoff

22. COMMON/VTTX/NBATCH, NHIS

NBATCH - Number of batches per energy group  
NHIS - Number of neutron histories per batch

23. COMMON/XTT/T(1000), PP, EG

T - Elapsed time of neutrons  
PP - Weight of photon  
EG - Energy of photon

24. COMMON/XUNITS/IP, JP

IP - Card input unit number  
JP - Printed output unit number

25. COMMON/ZSTOR/RADC(41), NRA, MRAY, TIMC(41), NTIM,  
MTYM, ZADC(41), NZA, MZAY, RADCS(41), ANG(21),  
NAN, MAN, NCOSA, NRADA, NTIMA, NZMA

RADC - Radial bin boundaries (cm)  
NRA - NRADA + 1  
MRAY - MOWER (NRA)  
TIMC - Time bin boundaries (sec)  
NTIM - NTIMA + 1

25. (Cont. )

MTYM	-	MOWER (NTIM)
ZADC	-	Horizontal bin boundaries (cm)
NZA	-	NZMA + 1
MZAY	-	MOWER (NZA)
RADCS	-	$RADCS(I) = RADC(I) * RADC(I)$
ANGC	-	Angular bin boundaries ( $\cos \theta$ )
NAN	-	NCOSA + 1
MAN	-	MOWER (NAN)
NCOSA	-	Number of angular bins
NRADA	-	Number of radial bins
NTIMA	-	Number of time bins
NZMA	-	Number of horizontal bins

#### 4. 6. 3. 3 External Tapes Required

As the program is currently run three external tapes are used, with only one being required at any one time. The program file tape is initially requested and recreated on an internal file being modified as desired. Next, the data tape containing files NPTAPE (file 4), NCONTP (file 3), NXTAP (file 14), and TAPE 15 (file 15) is mounted. After copying these files to internal files it may be removed. Finally, the results file IRESLT (TAPE 16) is mounted. As required, extra reels for TAPE 16 are mounted.

#### 4. 6. 3. 4 Data Files Used

NPTAPE: PHI tape. Generated by a COD678 CODE 8 run. Contains data necessary to employ the Coveyou technique for anisotropic angular scattering. See Ref. (12) for further details.

NCONTP: O5R system data tape. Generated by a COD678 CODE 6 run. Contains cross section data for O5R neutron collision routines. See Ref. (12) for further details.

NXTAP: The file NXTAP contains nuclear data which are required for the analysis of the neutron histories, but which are not available on the O5R system tapes. The data are read as a separate record for each energy supergroup. For each energy supergroup, the complete array contains several types of nuclear data. First is cross section data for gamma production by neutron inelastic scattering in air. These data are in the form of cumulative probability distributions. Next is similar data for ground. The gamma production data are for a particular ground composition, and must be changed whenever a different composition is to be investigated. These data are followed by a set of neutron kerma values for ground. These are used to compute the energy deposition in ground. This is followed by a set of Q values, as discussed in Section VI. 5 of

Ref. ( 1 ). The values on tape are normalized by the total cross section; i. e. ,

$$Q = \frac{\sum Q_i \sigma_i}{\sigma_t}$$

so that, the quantity  $(W_b - W_a) (E + Q)$  is scored at every collision to account for energy deposition by neutron absorption. Finally there follows a set of values for the average energy transfer available to electrons from elastic scattering neutron collisions in air. These are the data shown in Fig. 3 of Ref. (1 ), and are used to score ionization in air.

TAPE 15: The tape 15 was created to eliminate a large number of data cards from the input decks, these data being the same for all runs. The binary file consists of six records, five of which are used in TAUM the other in ROUTIN.

RECORD 1: NVA, NVG

NVA - Number of energy groups represented by data in TAUS in air.

NVG - Number of energy groups represented by data in TAUS in ground.

RECORD 2: (VSTEP (I, 1) I = 1, NVAP1)

NVAPI = NVA + 1

NSTEP: Energy group boundaries ( $v_i$ ), in increasing value ( $v_i < v_{i+1}$ ), in cm/sec.

RECORD 3: ( TAUS (I, J, 1), J = 1, 2), I = 1, NTAUSA)

J = 1, Fermi ages ( $f_{k,j}$ ) for air

J = 2, Slowing down time ( $t_{k,j}$ ) for air

NTAUSA = (NVAPI \* NVA)/2

$f_{k,j}$  - is the Fermi age for going from  $v_k$  to  $v_j$   
 where  $v_k > v_j$ .

$t_{k,j}$  - is the slowing down time corresponding to  
 $f_{k,j}$ .

Then, the  $f$ 's are stored in the following manner:

$f_{2,1}; f_{3,2}; f_{3,1}; f_{4,3}; f_{4,2}; f_{4,1};$   
 $-----; f_{NVA, NVA-1}; -----; f_{NVA, 1};$   
 $f_{NVA+1, NVA}; -----; f_{NVA+1, 1}.$

The  $t$ 's are stored in a similar manner.

RECORD 4: (VSTEP (I, 2) I = 1, NVGP1 )

Same as record 2 except it is for the ground

RECORD 5: (TAUS (I, J, 2), J = 1, 2 ), I = 1, NTAUSG)

Same as record 3 except it is for the ground.

RECORD 6: NSENG, NEENG, ENG, PGE, GE

DIMENSION NSENG (3), NEENG (3), ENG (21),  
 PGE (45, 21), GE (45, 21)

Three gamma production cross sections in file 14 have the  
 gamma energy in the form of tabulated probability distributions which are  
 represented in the above arrays.

NSENG (I) - Starting energy index value for the  $I^{th}$  cross section.

NEENG (I) - Final energy index value for the  $I^{th}$  cross section.

ENG (J) - Upper energy value (MeV) for the incident neutron  
 which belongs to the  $J^{th}$  probability distribution.

(PGE (K, J), K = 1, 45) -  $J^{th}$  accumulative probability distribution.

(GE (K, J), K = 1, 45) - corresponding gamma energy values.



**IRESLT:** O5RNIES results file. Each reel of IRESLT consists of an identification record followed by sets of data records, each set consisting of eight records. These are NRPT \* NEB data sets, where NRPT is the number of batches per results tape reel and NEB is the number of energy groups per batch. The first record consists of:

<b>ID:</b>	Run identification number.
<b>NOREEL:</b>	IRESLT tape reel number.
<b>NZ:</b>	Number of items stored.
<b>NEB:</b>	Number of energy groups.
<b>NBA:</b>	Number of batches.
<b>NTIMA:</b>	Number of time bins.
<b>NRADA:</b>	Number of radial bins.
<b>NCOSA:</b>	Number of angular bins.
<b>NZMA:</b>	Number of horizontal bins.
<b>TIMC:</b>	Time bin boundaries.
<b>RADC:</b>	Radial bin boundaries.
<b>ANGC:</b>	Angular bin boundaries.
<b>ZADC:</b>	Horizontal bin boundaries.
<b>E:</b>	Energy bin boundaries.
<b>NRPT:</b>	Number of batches per reel for IRESLT file.
<b>NHIS:</b>	Number of neutrons per energy band run.
<b>DELT:</b>	Time bin widths.
<b>VOLB:</b>	Volume of the spatial bins.

Each record in a data set consists of one of the arrays dimensioned 10400 which are found in the common block **ENDXX**. The results are stored in these arrays as if they were dimensioned (NTIMA, NRADA, NCOSA + NZMA). The eight records are:

ENDEP  
GENDEP  
XCR  
XCT

Non-thermal

ENDEP  
GENDEP  
XCR  
XCT

Thermal

## 4. 7 INSTRUCTIONS FOR USING THE O5NPT CODE

### 4. 7. 1 O5NPT Input Instructions

The following is a description of the input required for O5NPT.

#### CARD A: TITLE

FORMAT (10A6)

TITLE (dimensioned 10): A 60 character title which will appear on all plots.

#### CARD B: MRUN, IRTT, N2, IFGTP, IFGTIO, IFGTIP, IFGINO, IFGINP

FORMAT (12I5)

MRUN - Number of batches data represent

IRTT - Data set on file KP which contains the results for MRUN batches

N2 - = 4, which is the number of items written on the energy band results tape

IFGTP (dimensioned 5):

IFGTP(1) = 0, plot and/or print out neutron plus gamma ionization results

IFGTP(2) = 0, plot and/or print out neutron ionization results

IFGTP(3) = 0, plot and/or print out gamma ionization results

IFGTP(4) = 0, plot and/or print out radial and horizontal currents

IFGTP(5) = 0, plot and/or print out theta and vertical currents

IFGTIO: Time-dependent results are to be printed out

IFGTIP: Time-dependent results are to be plotted

IFGINO: Time-independent results are to be printed out

IFGINP: Time-independent results are to be plotted

**CARD C: SCALE**

**FORMAT (5E10. 3)**

**SCALE** (dimensioned 5): Scale factors by which the different items are to be multiplied.

**CARD D: N1A(I), N3A(I), N4A(I), A3A(I), A4A(I), DXA(I), XMAXA(I), XMINA(I)**

**FORMAT (3I5, 5X, 5E10. 3)**

5 cards, 1 for each item on results tape

**N1A(I)** - Graph type for item I

1 - X-axis log, Y-axis log

2 - X-axis lin, Y-axis log

3 - X-axis lin, Y-axis lin

4 - X-axis log, Y-axis lin

**N3A(I)** - Number of X-axis decades if logarithmic

**N4A(I)** - Number of Y-axis decades if logarithmic

**DXA(I)** - X-axis interval between tick marks on graph if logarithmic

**XMAXA(I):** Maximum X value allowed for plotting

**XMINA(I):** Minimum X value allowed for plotting

**CARD E: IR1, IRTT, NR, ISP (read in routine SUMOBD)**

**FORMAT (4I3)**

**IR1:** Batch number to start processing energy band result tape with

**IRTT:** Data set on file KP which contains the results for IR1-1 batches

**NR:** Batch number to terminate processing with

**ISP:** = 1, after processing each energy band results tape a data set is written on file KP

**CARD F's: (P(I), I=1, NEB) (read in routine SUMOBD)**

**FORMAT (8F10. 3)**

**P:** Probabilities to be applied to the energy band results so as to simulate a given spectrum

#### 4. 7. 2     O5NPT Output

File 6 is used for output.

First page: Summary of card input

Second page: VCOUNTS: Integer counters normalized to per neutron  
XCOUNTS: Floating point counters normalized to per  
neutron

The VCOUNT and XCOUNT arrays are analagous to the  
KCOUNT and ZCOUNT arrays of Section 4. 6. 2.

All subsequent pages: Normalized results in tabular form containing  
value, its standard deviation, and its percent error

### **4. 7. 3     Structure of the O5NPT Code**

#### **4. 7. 3. 1   Flowcharts**

On the following pages are descriptions of the various routines in O5NPT, excluding the PLOT package routines. Flowcharts are also presented for the more complex routines. Some of the subroutines called by O5NPT are shown in Fig. 4. 26.

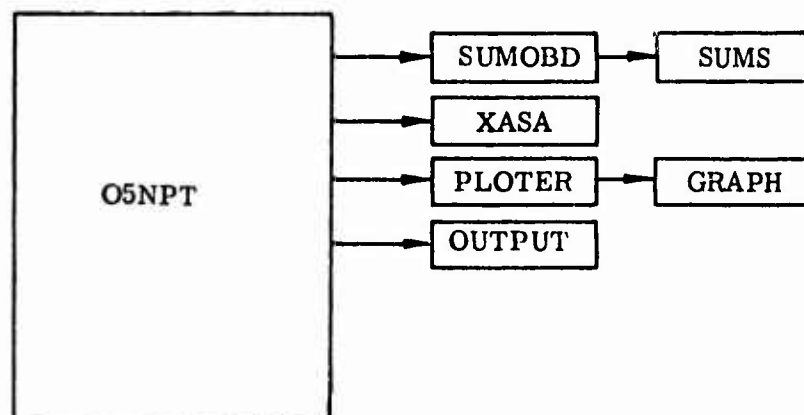


Figure 4.26. Subroutines called by O5NPT

**Main Routine:** O5NPT (Figs. 4. 27-4. 28)

**Function:** Produces the desired information in an orderly fashion calling necessary subroutines.

**Subroutines Called:** OUTPUT, PLOTTER, SUMOBD, XASA

**Labeled COMMON:** CKT, SINGLS



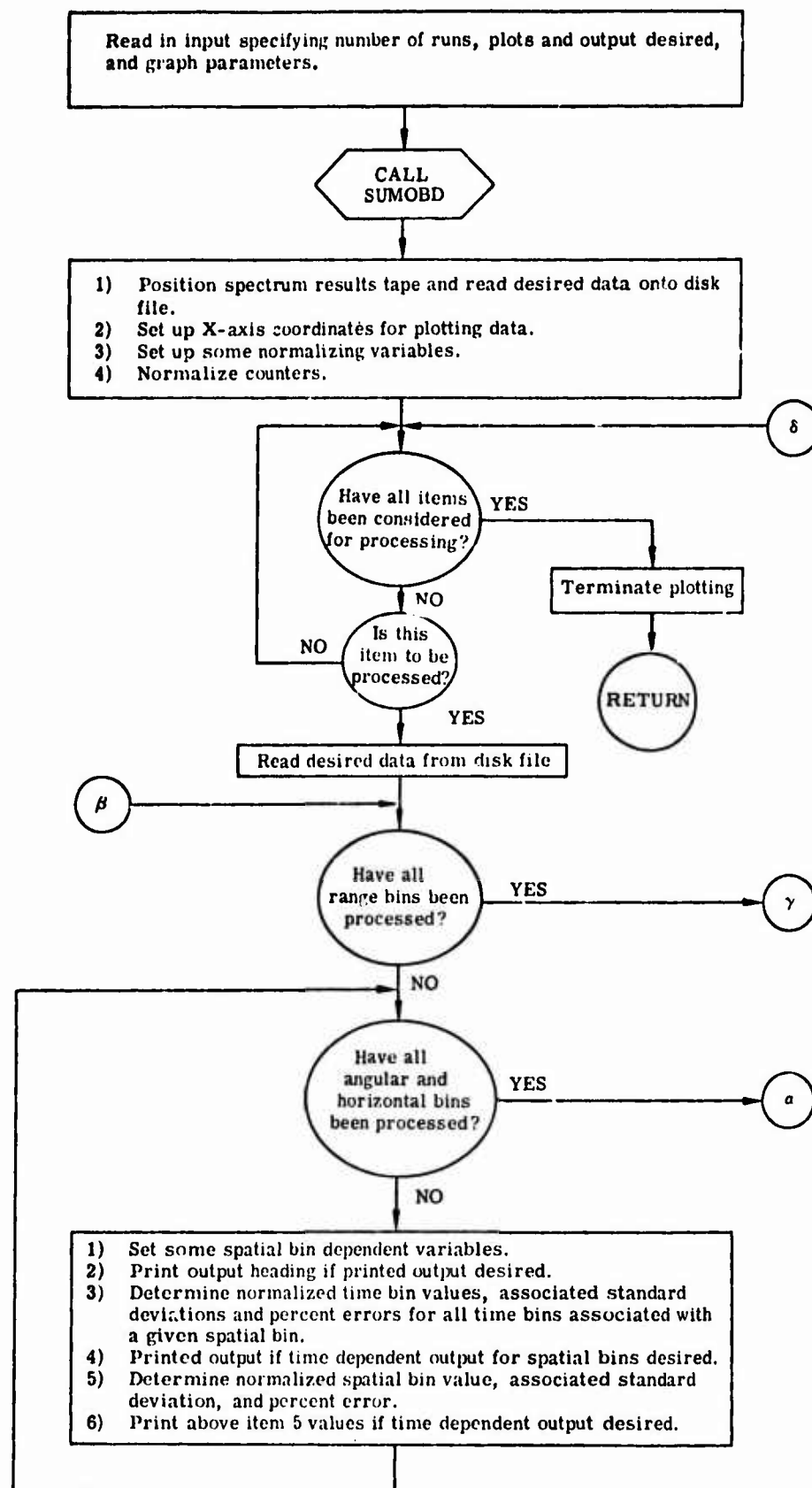


Figure 4. 27. Flowchart for the O5NPT program.

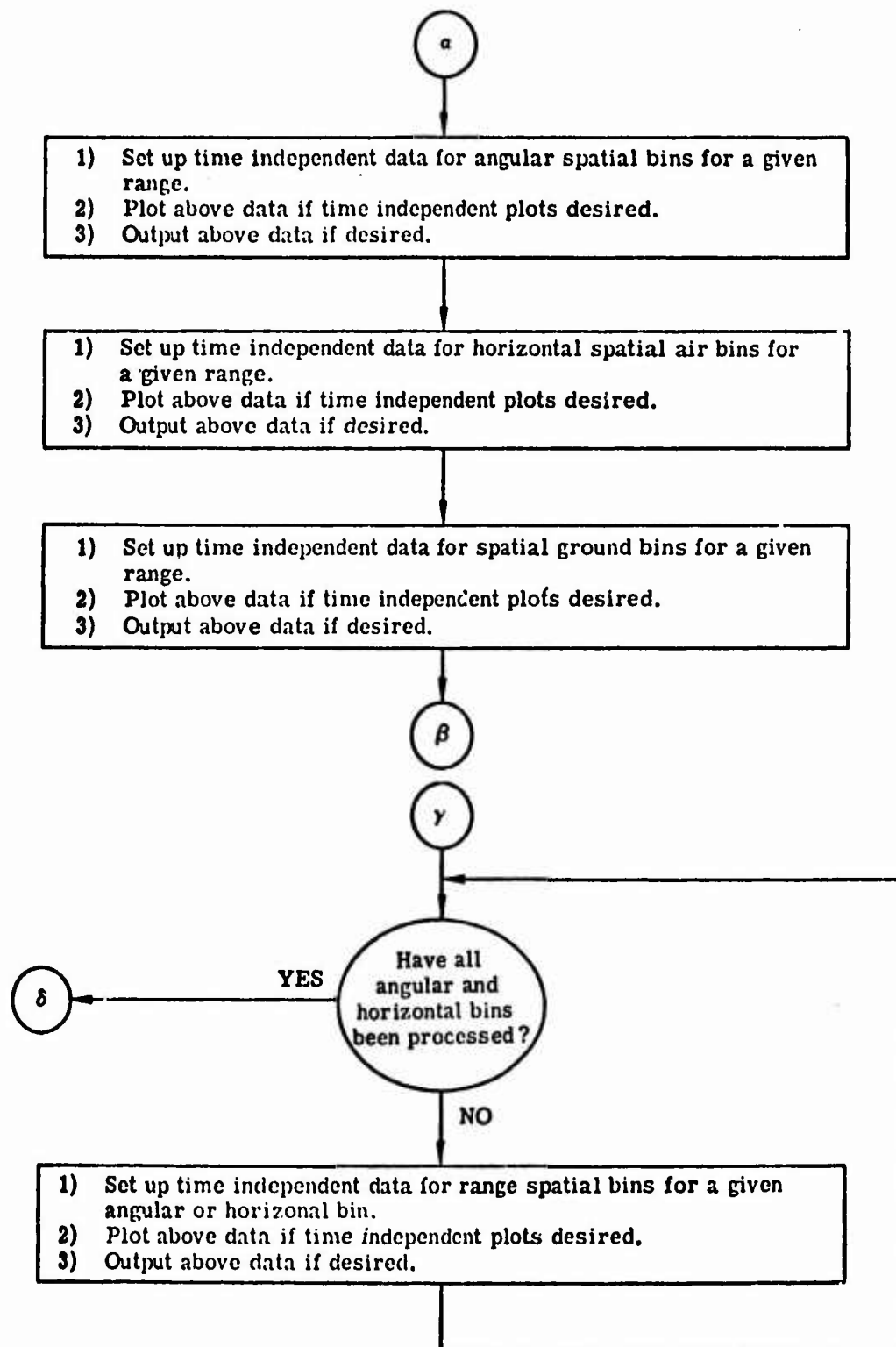


Figure 4. 28. Flowchart for the O5NPT Program.

Subroutine Name:      OUTPUT (NI, NZ, INDX, WORD, VA, SDA,  
VB, SDB, VC, SDC, X, TITLE)

Function:              Put data in tabular form in the output.

Called By:             O5NPT

Input Parameters:      NI        - X - axis type (e. g. , local time, range, etc. )  
                          NZ        - Number of points  
                          INDX     - Flag specifying whether data is result  
                                      of neutrons and gammas, neutrons, or  
                                      gammas  
                          WORD     - Specifies type of current (e. g. , radial,  
                                      theta, etc. )  
                          VA        - Fast data array  
                          SDA       - Standard deviation of VA array data  
                          VB        - Thermal data array  
                          SDB       - Standard deviation of VB array data  
                          VC        - Fast and Thermal data array  
                          SDC       - Standard deviation of VC array data  
                          X         - Independent variable data  
                          TITLE    - Title for output table

Subroutine Name: PLOTTER (NT, N2, XA, SA, INDX, IFY, ITIME)  
(Fig. 4. 29)

Function: Plot desired data in histogram form with error bars on the total curve.

Called By: O5NPT

Subroutines Called: GRAPH and other plotting routines

Input Parameters:

NT	- X-axis type (e. g. local time, range, etc. )
N2	- Number of points
XA	- Histogram X-axis coordinates
SA	- Error bar X-axis coordinates
INDX	- Flag specifying whether data are result of neutrons and gammas, neutrons, or gammas.
IFY	- Flag specifying Y-axis label
ITIME	- =1, Time dependent data =2, Time independent data

Labeled COMMON: CK1F, CMXMN, CPLOT

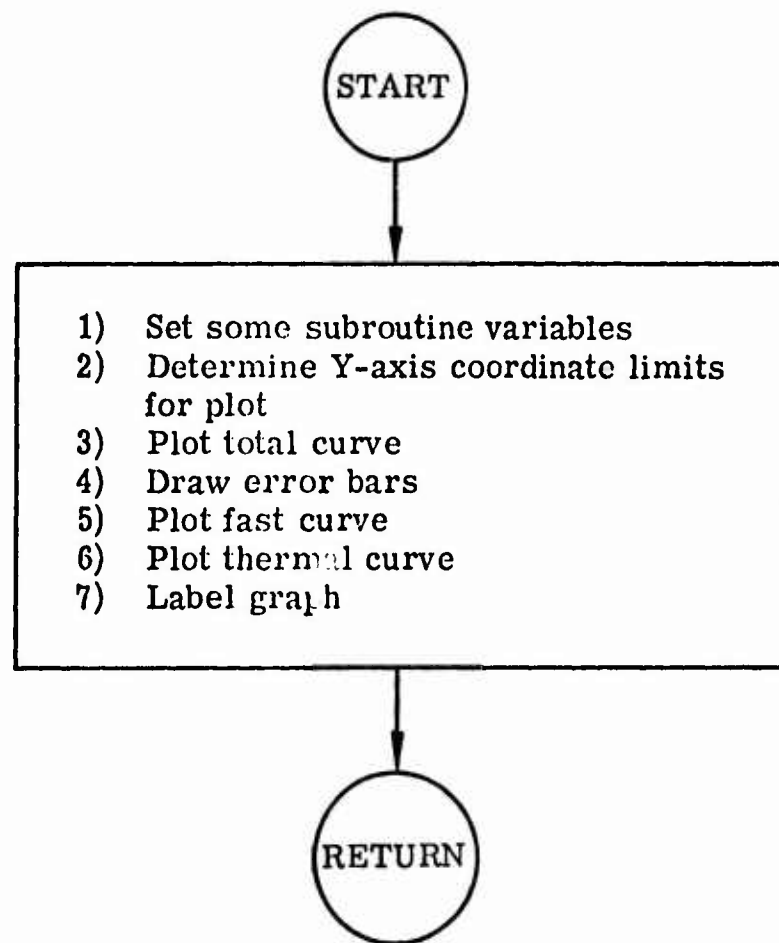


Figure 4. 29. Flowchart for subroutine PLOTTER.

**Subroutine Name:** SUMOBD (Fig. 4. 30)

**Function:** Create file KP (ionization rates and currents for a particular neutron spectrum) using results on file IRESLT (ionization rates and currents for energy bands).

**Called By:** O5NPT

**Subroutines Called:** SUMS

**Labeled COMMON:** CKT, SINGLS, CUNITs

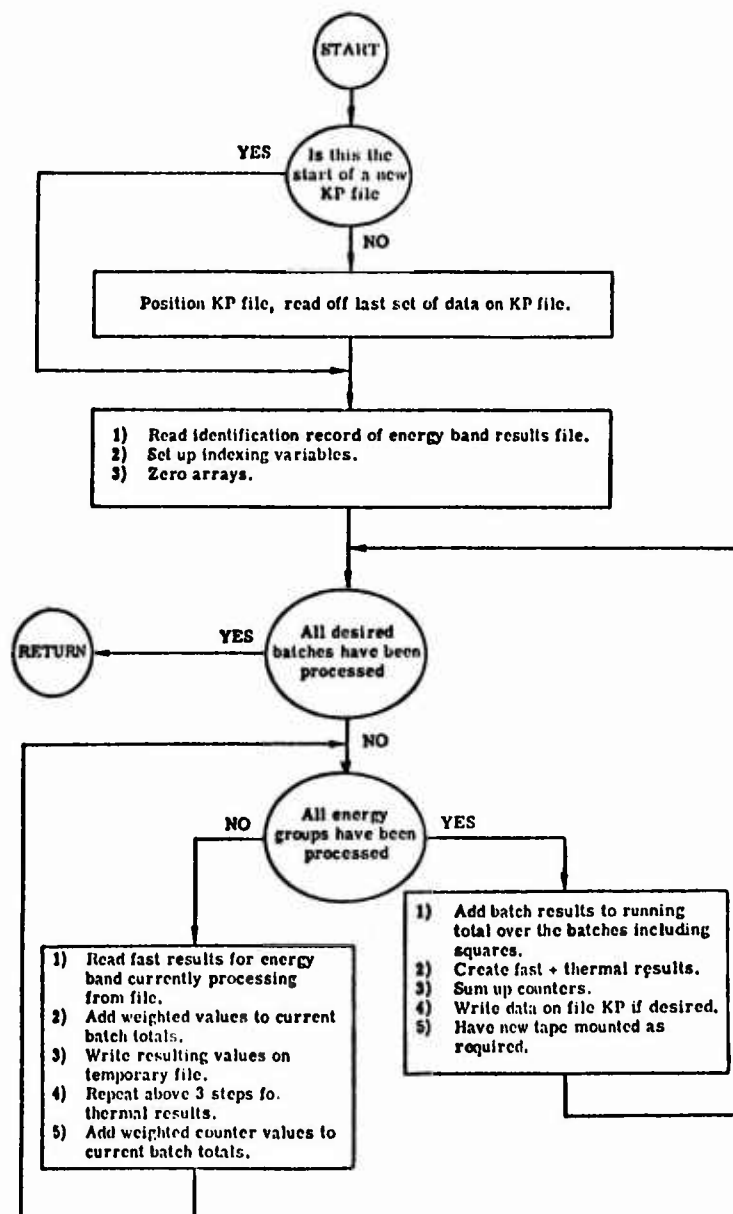


Figure 4. 30. Flowchart for the subroutine SUMOBD.

**Subroutine Name:** SUMS (IMAX, JMAX, KMAX, SEMP, ENDEP, ICOC)

**Function:** Creates the sum over the batches and the sum of the squares over the batches

**Called By:** SUMOBD

**Input Parameter:**

- IMAX: Number of time bins
- JMAX: Number of radial bins
- KMAX: Number of angular plus horizontal bins
- ENDEP: Array of values to be added to  
          accumulative total over the batches
- ICOC: Dummy

**Output Parameter:** SEMP: Array containing the time integrated  
                          values of the ENDEP array

**Labeled COMMON:** SINGLS



Subroutine Name: XASA (AA, AM, IP, NO, XA, SA, KF)

Function: Determine the values to be used for the X-axis when plotting the data.

Called By: O5NPT

Input Parameters:

- AA: Bin boundaries
- AM: X-axis coordinate of the first point to be plotted.
- IP: =1 or 4 log X-axis  
=2 or 3 lin X-axis
- NO: Number of bins
- KF: =1, increment through AA array by 1  
= -1, increment through AA array by -1

Output Parameter:

- XA: Histogram X-axis coordinates
- SA: Error bar X-axis coordinates

#### 4. 7. 3. 2 Common Blocks

In this sub-section we define, briefly, all of the variables which are to be found in the common blocks of O5NPT and subroutines PLOTTER, OUTPUT, SUMOBD, and SUM.

- I.     COMMON/CKT/IKT, IPKT
- IKT     -   Size of KCOUNT and ICOUNT arrays
- IPKT     -   Size of PCOUNT and ZCOUNT arrays
- II.    COMMON/CKIF/KIF
- KIF     -   Indicates the type of line used in plotting a set of data
- KIF = 0     \_\_\_\_\_
- KIF = 1     -----
- KIF = 6     \_\_\_\_\_ - \_\_\_\_\_
- III.   COMMON/CMXMN/XMXL, XMNL, YMAX, YMIN
- XMXL     -   Plots X-axis maximum
- XMNL     -   Plots X-axis minimum
- YMAX     -   Plots Y-axis maximum
- YMIN     -   Plots Y-axis minimum
- IV.    COMMON/CPLOT/YAP(40), YBP(40), YCP(40), SDCP(40)  
        TITLE(10), N1A(5), N3A(5), N4A(5), A3A(5), A4A(5), DXA(5),  
        XMAXA(5), XMINA(5)
- YAP     -   Y coordinates of the fast data to be plotted
- YBP     -   Y coordinates of the thermal data to be plotted
- YCP     -   Y coordinates of the fast and thermal data to be plotted
- SDCP    -   Standard deviation of the fast and thermal data

**TITLE** - A 60 character title to be printed on each plot  
**N1A** - Specifies type of X-axis and Y-axis desired  
**N3A** - Specifies number of decades for X-axis if logarithmic  
**N4A** - Specifies number of decades for Y-axis if logarithmic  
**A3A** - Specifies X-axis plot length  
**A4A** - Specifies Y-axis plot length  
**DXA** - Specifies X-axis tick mark interval for linear X-axis  
**XMAXA** - Maximum X value to be plotted  
**XMINA** - Minimum X value to be plotted

V. COMMON/CUNITS/IP, JP

**IP** - Input unit  
**JP** - Output unit

IV. COMMON/SINGLS/KP, IER, IEW, IERA, IEWA, IET, IRESLT, I1, I2, I3, N2

**KP** - Spectrum results file  
**IER** - Temporary file to be read from, contains spectrum results  
**IEW** - Temporary file to be written on, contains the latest spectrum results. The values for IER and IEW are alternated.  
**IERA** - Temporary file to be read from, contains the current spectrum run sum  
**IEWA** - Temporary file to be written on, contains the new spectrum run sum. The values for IERA and IEWA are alternated  
**IET** - Temporary file to be written and then read. Contains fast results which are to be added to thermal results to arrive at total results  
**IRESLT** - Energy band results file  
**I1** - Size of the F and G arrays

- I2        -    Size of the D and E arrays
- I3        -    2\* (I1 + I2)
- N2        -    Number of items of results data stored (i. e.,  
                   (1) Ionization dose due to neutron ionizations;  
                   (2) Ionization dose due to gammas resulting from  
                   neutron collisions; (3) Radial or horizontal cur-  
                   rents; and (4) Theta or vertical currents)

VII.    COMMON    BSC(360), BSSC(360), ASC(10400), ASSC(10400),  
                   ASA(10400), ASSA(10400), ASB(10400), ASSB(10400), DUM(10400),  
                   BSA(360), BSSA(360), BSB(360), BSSB(360)

In the main routine these arrays are used to store spectrum re-  
 sults which are to be plotted and/or printed out after slight modification.  
 In the subroutine SUMOBD the first 4 arrays are used to store information  
 which is to be written on the spectrum results file, while the next five are  
 used to store information read from the energy band results file. The  
 arrays dimensioned 360 are used to store time independent data, while  
 those dimensioned 10400 are used to store time dependent data.

#### 4. 7. 3. 3 O5NPT Data File Structure

There are two main data files used in O5NPT; they are IRESLT and KP. IRESLT is the input data file and KP is the output data file, along with being the file used for obtaining the information to be plotted. IRESLT has been fully described in the section on O5RNIES data files. The file KP consists of data sets which contain 16 records each. Each data set represents the spectrum results for a given number of batches. The first record consists of: ZCOUNT, KCOUNT, NR, RADC, TIMC, ZADC, ANGC, NRADA, NTIMA, NZMA, NCOSA, NBATCH, NHIS, DELT, VOLB.

ZCOUNT (dimensioned 30): Floating point counters

KCOUNT (dimensioned 30): Integer counters

NR: Number of batches data represents

RADC: Radial bin boundaries

TIMC: Time bin boundaries

ZADC: Horizontal bin boundaries

ANGC: Angular bin boundaries

NRADA: Number of radial bins

NTIMA: Number of time bins

NZMA: Number of horizontal bins

NCOSA: Number of angular bins

NBATCH: =1

NHIS: Number of neutrons per energy band run

DELT: Time bin widths

VOLB: Volume of the spatial bins

The remaining fifteen records consist of D, E, F, G.

D (dimensioned 360): Sum of the time integrated results

E (dimensioned 360): Sum of the squares of the individual batch time integrated results

F (dimensioned 10400): Sum of the time dependent results

G (dimensioned 10400): Sum of the squares of the individual  
batch time dependent results

The results are stored in the F and G arrays as if they were  
dimensioned (NTIMA, NRADA, NCOSA + NZMA). Similarly for the  
D and E arrays (NRADA, NCOSA + NZMA). The results stored in the  
15 records in order of storage is:

Theta and vertical currents - fast

Radial and horizontal currents - fast

Ionization (gammas) - fast

Ionization (neutrons) - fast

Ionization (neutrons and gammas) - fast

Theta and vertical currents - thermal

Theta and vertical currents - fast and thermal

Radial and horizontal currents - thermal

Radial and horizontal currents - fast and thermal

Ionization (gammas) - thermal

Ionization (gammas) - fast and thermal

Ionization (neutrons) - thermal

Ionization (neutrons) - fast and thermal

Ionization (neutrons and gammas) - thermal

Ionization (neutrons and gammas) - fast and thermal

## REFERENCES

1. C. A. Stevens and R. R. Schaefer, "Neutron Induced Electrical Sources," AFWL-TR-69-8, Air Force Weapons Laboratory, Kirtland AFB, New Mexico, 1968.
2. C. A. Stevens, "Neutron Induced Electrical Sources-II," AFWL-TR-69-60, Air Force Weapons Laboratory, Kirtland AFB, New Mexico, 1969.
3. C. A. Stevens and R. E. Dietz, "Late-Time EMP Sources Including Ground Contributions," AFWL-TR-71-8, Air Force Weapons Laboratory, Kirtland AFB, New Mexico, 1970.
4. E. A. Straker and M. L. Gritzner, "Neutron and Secondary Gamma Ray Transport in Infinite Homogeneous Air," ORNL-4464, Oak Ridge National Laboratory, Oak Ridge, Tennessee, 1969.
5. Private Communication from V. W. Pine of AFWL.
6. Written by H. M. Murphy, Jr. of AFWL.
7. H. Kahn, "Applications of Monte Carlo," RM-1237-AEC, RAND Corporation, Santa Monica, California, 1956.
8. H. Goldstein, Fundamental Aspects of Reactor Shielding, Addison-Wesley Publishing Company, Reading, Mass., 1959.
9. J. H. Ray, G. Grochowski, and E. S. Troubetzkoy, "Neutron Cross Sections of Nitrogen, Oxygen, Aluminum, Silicon, Iron, Deuterium, and Beryllium," UNC-5139, United Nuclear Corporation, White Plains, New York, 1965.
10. M. K. Drake, "Neutron and Gamma Ray Production Cross Sections for Silicon," DASA 2099, GA-8628, Gulf General Atomic, San Diego, California, 1968.

11. S. H. Dupree, H. A. Sandmeier, G. E. Hansen, W. W. Engle, Jr., and F. R. Mynatt, "Time-Dependent Neutron and Photon Transport Calculations Using the Method of Discrete Ordinates," LA 4557, Los Alamos Scientific Laboratory, Los Alamos, New Mexico, 1970.
12. D. C. Irving, R. M. Freestone, Jr., and F. B. K. Kam, "O5R, A General-Purpose Monte Carlo Neutron Transport Code," ORNL-3622, Oak Ridge National Laboratory, Oak Ridge, Tennessee, 1965.
13. J. Lindhard, et al., "Integral Equations Governing Radiation Effects (Notes on Atomic Collisions, III)," Mat. Fys. Medd. Dan. Viol. Selsk. 33, No. 10, 1963.